Hierarchical Ordering: Self-Assembly of Block Copolymers in Active Liquid Crystalline Matrices

Von der Fakultät für Mathematik, Informatik und Naturwissenschaften der RWTH Aachen University zur Erlangung des akademischen Grades eines Doktors der Naturwissenschaften genehmigte Dissertation

vorgelegt von

Master of Engineering

Jingbo Wang

aus Suzhou, China

Berichter: Universitätsprofessor Dr. rer. nat. Martin Möller

Universitätsprofessor Dr. rer. nat. Ulrich Simon

Tag der mündlichen Prüfung: 16. November 2012

Diese Dissertation ist auf den Internetseiten der Hochschulbibliothek online verfügbar.

Content

Acknowledgements i

Summary iii

Chapter 1 Introduction 1

1.1. Introduction 1

1.2. Contents of the thesis 3

1.3. References 4

Chapter 2 Literature Reviews 7

2.1. Phase behavior of coil-coil block copolymer in bulk and thin films 7

2.2. Hierarchical ordering in block copolymers thin film 11

2.3. Techniques to investigate hierarchical ordering in block copolymer thin films 15

2.4. Applications of block copolymer complex thin films 19

2.5. References 20

Chapter 3 Structural and Electrical Properties of Asymmetrically Substituted Sexithiophene Monolayers 25

3.1. Introduction 25

3.2. Experimental section 28

3.3. Results and discussions 30

3.4. Conclusions 42

3.5. References 43

Chapter 4 Thin Film Structure of Block Copolymer-Surfactant Complexes: Strongly Ionic Bonding Polymer Systems 47

4.1. Introduction 47

4.2. Experimental section 50

4.3. Results and discussions 52

4.4. Conclusions 68

4.5. References 68

Chapter 5 Specific Interaction Induced Precise Deposition of Gold Nanorods on Supramolecular Block Copolymer Thin Film 73

5.1. Introduction 73

5.2. Experimental section 75

5.3. Results and discussions 77

5.4. Conclusions 89

5.5. References 90

Chapter 6 Nanostructured TiO_2 Thin Films Templated from Co-assembly of Fully Miscible Block Copolymer Complex/Polymeric Precursors 93

6.1. Introduction 93

6.2. Experimental sections 95

6.3. Results and discussions 97

6.4. Conclusions 109

6.5. References 109

Chapter 7 Biaxial Alignment of Block Copolymer - Complex Lamellae 113

7.1. Introduction..... 113

7.2. Experimental section..... 114

7.3. Results and discussions..... 116

7.4. Conclusions..... 123

7.5. References..... 123

Chapter 8 Blue Light Emitted Thin Films from Supramolecular Assembly of Oligothiophene/Poly (2-vinylpyridine-b-ethylene oxide) Complex..... 125

8.1. Introduction..... 125

8.2. Experimental section..... 127

8.3. Results and discussions..... 130

8.4. Conclusions..... 147

8.5. References..... 148

Chapter 9 Morphological Investigation of Unique Onion-type Smectic Polymersome from Supramolecular Approach..... 153

9.1. Introduction..... 153

9.2. Experimental sections..... 155

9.3. Results..... 158

9.5. Discussions..... 165

9.5. Conclusions..... 169

9.6. References..... 169

Supporting Information I: Chapter 3 Structural and electrical properties of asymmetrically substituted sexithiophene monolayers..... 172

Supporting Information II: Chapter 4 Thin Film Structure of Block Copolymer-Surfactant Complex: Strongly Ionic Bonding Polymer Systems 179

Supporting Information III: Chapter 6 Nanostructured TiO_2 Thin Films Templated from Co-assembly of Fully Miscible Block Copolymer Complex/Polymeric Precursors 185

Supporting information V: Chapter 7 Biaxial alignment of block copolymer-complex lamellae 189

Support informations IV: Chapter 8 Blue Light Emitted Thin Films from Supramolecular Assembly of Oligothiophene/Poly (2-vinylpyridine-b-ethylene oxide) Complex 195

Support Informations VI: Chapter 9 Morphological Investigation of Unique Onion-type Smectic Polymersome from Supramolecular Approach 196

Lebenslauf 197

Acknowledgements

At the end of the thesis, I would like to put my great acknowledges to the people who help me during my PhD life in Germany. Without your kindly help, I cannot finish my work.

I would like say thanks to Prof. Möller for his interesting topic, and for giving me a big chance in his lab and large freedom in my work.

I appreciate Dr. Ahmed Mourran for his directly supervision of my PhD work, providing me a large freedom to do my work, and training me with SFM. In addition, I also cannot forget his helpful discussion and friendly invitation for dinner at his home with his family.

I appreciate Prof. Wim H. de Jeu for his great help in the training of XRR, the X-ray scattering measurements of in thin films and bulk, and also the helpful discussion about the data processing and paper preparation.

I would like to thank Prof. Dimitri Ivanov and his student for their help in the X-ray scattering measurements and helpful discussion.

Dr. Xiaomin Zhu is appreciated because of his great help in the chemistry part of this PhD thesis, fruitful discussion about the ligand/block copolymer complexation, and providing me very warm help in the daily life.

I thank Dr. Ulrich Ziener, Dr. Helmut Keul, and Dr Jānis Lejnieks for their help in ligand synthesis.

I thank Prof. Dr. Dago M. de Leeuw and his PhD student, Miss Fatemeh Gholamrezaie, for their great work in OFET preparation and mobility measurement.

I appreciate Dr. Heidrun Keul and Mr. Dipl. Thomas Weyand for their help in gold nanorods preparation.

I would like to thank Mr. Stephan Rütten and Dr. Kim-Hô Phan for their training in (Cryo)FESEM and helpful discussion during my daily work.

I appreciate Dr. Matthieu Defaux and Dr. Nicu Goga for their great help in scientific and daily life. I appreciate the friendly atmosphere when we were working together, including Miss Lea Messager.

I really appreciate the atmosphere in room 3.15, I am missing the interesting topics, the friendly environment and help for daily work, which is proving by Kristina

Bruellhoff, Daniel Bünger, Nina Keusgen, Thomas Wormann, ... I enjoy the time with your guys.

I appreciate my Chinese friends in RWTH, they provide me a lot of help in my daily life and scientific work, and I enjoy the time during the parties and launch break with your guys. Thank you very much: Dr. Zhu Xiaomin, Wang Hailin, He Yingchun, Li Lei, Zhang Heng, Wang Huihui, Zhao Yongliang, Zhao Qingxin, and Wu Yaodong.

Finally I would like to put my great acknowledge to my wife, Yuting Zhao. She spends a lot time to support me, trying her best to reduce my pressure from work, and accompanying me for a lot of difficult times. Without her support, I will not finish my work easily. I appreciate that I know her.

Summary

Block copolymers containing incompatible blocks are a well-known example that forms ordered nanodomains with typical dimensions of 10 - 100 nm. Similar to crystalline structures, isotropic grain morphology is typically obtained characterized by a random distribution of nanodomain orientations. Complexation of polymer chains with low molecular weight amphiphile molecules *via* non-covalent interactions is a tool for the construction of nanostructured macromolecular materials. It is demonstrated that through the selective complexation of one of the blocks of the copolymer, a defined nanodomain orientation can be achieved in thin films. In this work we address systematically the influence of different structural parameters on the morphology formation of block-copolymer / amphiphile complexes and the application of well-oriented nanostructures as templates for the preparation of functional materials.

Firstly, we show that the growth of structurally perfect and electrically connected organic monolayers as active semiconductor component of a field effect transistor (FET) remains an important challenge. Here we report on two new asymmetrically substituted sexithiophenes (6T) that form a monolayer on SiO_2 surfaces. Molecule **1** consists of 6T with at one end a branched alkyl chain, and is crystalline. Molecule **2** has the same end group as **1**, and additionally at the other end a linear alkyl chain. It shows thermotropic liquid crystalline (LC) behaviour. Full monolayer coverage is achieved before the start of growth of a multilayer. LC properties promote pre-ordering near the interface as well as exchange of molecules between the growing domains, regulating the domain sizes and their distribution. As a result, the LC compound **2** forms single-molecule islands with a monomodal distribution leading to large domain sizes compared to the non-LC compound **1**. Structural investigations with X-ray reflectivity and grazing-incidence wide-angle X-ray scattering reveal tilted 6T cores in the monolayers. The tilt angle relative to the surface normal is as large as 54° for **2** compared to 28° for **1**. Evidently, interfacial constraints and packing requirements cause rather loosely packed structures. Nevertheless, after annealing monolayers of **2** support a field effect mobility of 1×10^{-2} cm^2/Vs.

A commercially available amphiphile 1,4-bis (2-ethylhexoxy)-1,4-dioxobutane-2-sulfonic acid (AOT) is used to complex PS-P4VP block-copolymers of different

composition and molecular weight. It is demonstrated that the nanostructure formation could be controlled by not only the composition and molecular weight of the block copolymers, but also by the degree of protonation. Microphase-separated morphologies with vertically aligned cylinders or lamellae are observed in thin films. By varying the composition of the blocks and the molar ratio of AOT/pyridine, a structural transition is observed: cylinder of (AOT/P4VP) to lamellae to PS cylinder. Furthermore, the orientation of the nanostructure is also propagated to thick films. The film can be used for nanofabrication. The AOT/P4VP domain can be loaded with gold precursor and converted to gold nano-pattern by plasma treatment.

The surfactant molecules can be removed easily by shortly washing them in basic solution. Different nanoporous structure can be obtained because of the shrinkage of the complex domain. These thin films can be used to direct the self-assembly of gold nanorods with different PEG coating *via* specific interaction between PEO/P4VP. The orientation of the gold nanorods is controlled by the morphology of the thin films, the cylinder leads to perpendicular orientation and the lamellae leads to parallel orientation. Time dependent adsorption of the gold nanorods is confirmed by the FESEM and UV-Vis spectra. The optical properties can be tuned by changing of the immersion time in the nanorods solution, and it can be described by a single component exponential decay model.

A fast non sol-gel technology for the preparation of the nanostructured TiO_2 pattern is developed. The block copolymer complex is mixed with TiO_2 polymeric precursor in solution, the precursor is selectively miscible with AOT/P4VP *via* coordination. During processing, they co-assembly and ordered nanostructure forms after the processing. These nanopatterns can be converted into TiO_2 by using of soft technology, like plasma. Thermal stable nanostructures with different morphologies can be obtained. The key issues controlling the morphology are the amount of the precursors and the degree of complexation, and the composition of the block copolymer. The crystallinity can be tuned by thermal annealing. After plasma treatment rutile form with very low crystallinity is obtained, and it is converted to anatase form after annealing under 400°C for 4h.

We present a simple and convenient method to self-assemble block copolymer lamellae in thin films uniformly. This is done by exploiting the supramolecular liquid-crystalline ordering of the block copolymer in combination with PTFE rubbing

technology. In this way uniform alignment of the block copolymer is obtained in both the vertical and lateral directions. Wedge-shaped mesogens control the self-assembly of the block copolymer, rendering vertical orientation of the microdomains. In addition the vertical lamellae orient parallel to the friction-deposited PTFE layer, leading to long-range lateral ordering.

The functionality can be easily introduced into the thin film *via* supramolecular approach. A new asymmetric oligothiophene molecule is complexed with P2VP-PEO *via* hydrogen bond. LC ordering forms after complexation, similar to that of wedge-shaped molecules, it also enhances the microphase separation, controls the morphology and orientation, and tunes the crystallization of PEO. The optical properties of the complexes are discussed in both of the solution and thin films.

Finally we investigate the self-assembly of these complexes in water. The hydrogen bonding between carboxylic acid/pyridine and ionic bond between sulfonic acid/pyridine group are strong enough to generate stable complex in water, and the structure of the vesicles depends on the degree of complexation, the length of PEO chain, and the geometry of the ligand. A unique onion type vesicle is obtained from the complex of P2VP-b-PEO/wedge-shaped ligand in a wide composition region of PEO. The wall of the onion type vesicle is made from alternative close packing of the P2VP and ligand bilayer, where the hydrophilic P2VP backbone is parallel to the wall and contact with water. The second block PEO forms well defined nanostructure on the wall when there are enough PEO chains in multilamellar vesicle, or disordered structure in the unilamellar vesicle. Actually the packing of the P2VP/wedge-shaped ligands is similar to that of phospholipids in liposome, the packing parameter of the three wedge-shaped ligands is between 0.7-0.9.

Chapter 1 Introduction

1.1. Introduction.

1.1.1 Hierarchical ordering from self-assembly.

Versatile biological systems exist in nature and provide complicated models for functional and responsive materials. Such systems form in aqueous environments via self-assembly,[1, 2] using both competing hydrophobic/hydrophilic interactions and complementary physical interactions, thereby leading to the formation of hierarchical structures, which are progressively rendered at different length scales.[3, 4] The combination of self-assembly and hierarchy is extended to synthetic materials science to tune the properties.[5-10] Switching and responsive properties are achieved by properly choosing the competing and complementary interactions.[6] A well-known example is a block copolymer having two or more covalently bonded blocks with which a rich variety of structures and hierarchies can be obtained and tuned by mediating the degree of polymerization, composition, and the Flory-Huggins parameter.[10, 11]

However, the attractive interactions involved in self-assembly are not necessarily covalent bonds (i.e., permanent interactions), as in coil-coil block copolymers.[10, 11] In practice, the weaker secondary interactions are systematically used in supramolecular chemistry,[12] these interactions can be used to design mesomorphic polymeric structures, that are typically on a nanometer length scale.[13-15] Figure 1 summarizes the possible routes for the bottom-up construction of nanostructures based on self-assembly via supramolecular chemistry.[16] Through the systematic combination of construction units with different sizes, increasingly higher levels of structural hierarchy at different length scales can be rendered for the target system. Because the interactions between host and guest are physical bonds (e.g., hydrogen bonds and ionic bonds), they can be opened and reformed under certain conditions, which provides an important tool for designing responsible materials and mimicking biological systems.[6]

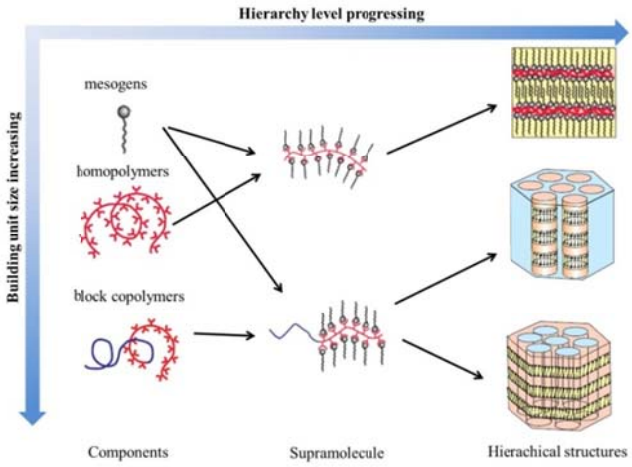

Figure 1. A potential scenario for the hierarchical construction of self-assembled polymeric structures. The images are reorganized based on ref. [7]. Reprinted with permission, Copyright 2002 American Association for the Advancement of Science (AAAS).

In principle, any sufficiently strong secondary interaction can be used for self-assembly.[16] The most commonly employed secondary interactions to create solid supramolecular materials are ionic bonding (electrostatic interactions between charged species), metal-ligand coordination, hydrogen bonding, π-π interactions, and van der Waals forces.[12] Figure 2 shows the approximate bond energies and other relevant information for different types of bonds.[17] The bond energy of the ionic bond is the highest among other non-covalent bonds and the closest in energy to the permanent covalent bond; the hydrogen bond is weaker, approximately one order of magnitude lower than the ionic bond, and the van der Waals interaction is the weakest. Therefore, it is reasonable to expect different materials properties when different non-covalent bonds are chosen. Another important issue in the supramolecular approach is the loss of entropy in the polymer backbone when the mesogen is introduced. The chain is stretched and becomes stiff. However, the energy released from the formation of secondary interactions (mostly ionic bonding, metal-ligand coordination, and hydrogen bonding) is strong enough to compensate for the loss of chain elasticity ($\sim kT$).[18]

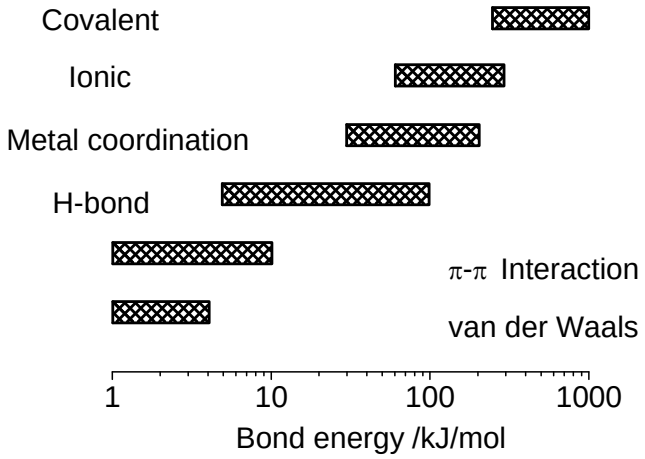

Figure 2. Bond energies and relevant characteristics for different bonding interactions; the values are in absolute terms.[17]

The combination of supramolecular chemistry and block copolymers opens a new era for modern nanotechnologies.[19] The poor long-range order of microphase-separated microdomains limits their application in nanotechnologies. The block copolymer/mesogen complex seems to be a good solution,[19] especially in thin films.[20, 21] There are enormous potential applications for thin films made of a block copolymer/mesogen complex in nanotechnologies related to bulk block copolymers,[22] such as the fabrication of nanostructured metal(oxide) patterns,[23] nanostructured organic semiconductor,[24] etc.

1.2. Contents of the thesis

The objective of this thesis is to understand the phase behaviour of block copolymer/mesogen complexes in thin films and the possible applications of these thin films in nanotechnologies. Most of the secondary interactions used in this thesis are ionic bonds between pyridine and sulfonic acid and hydrogen bonds between carboxylic acid and pyridine. This work begins with the self-assembly behavior of small molecular mesogens.

Chapter 2 gives a short literature review about the self-assembly of block copolymer/mesogen complexes in thin films and the techniques for investigating the thin film structure.

Chapter 3 shows the growth of structurally perfect and electrically connected organic monolayers from two new asymmetrically substituted sexithiophenes. The types of substituents dominate the phase behavior of these two molecules.

Chapter 4 presents the thin film morphology of the block copolymer and the space-demanding surfactant complex via ionic interactions. Factors such as the composition of the block copolymer, the molecular weight, and the degree of protonation are discussed. The potential applications of such thin films in nanotechnology are shown as well.

Chapter 5 shows the template assembly of gold nanorods on the thin films shown in **Chapter 4**. The surfactant is removed, and self-assembly of gold nanorods on the template is directed by specific interactions between PEO and P4VP.

Chapter 6 investigates the co-assembly behavior of the block copolymer/surfactant complex (shown in **Chapter 4**) and the TiO_2 precursor in thin films. The effects of the composition of the block copolymer complex and the ratio between the polymer and precursors on the morphology are discussed.

Chapter 7 presents a new way to enhance the lateral orientation of the block copolymer/ligand complex in a thin film. The combination of liquid crystalline ordering and PTFE rubbing technology allows for the large-scale alignment of microdomains both vertically and laterally.

Chapter 8 shows the self-assembly behaviour of the block copolymer/oligothiophene complex in thin film. The morphology of the thin film is controlled by the oligothiophene, and the optical properties of the thin film are investigated.

Chapter 9 investigates the self-assembly of the block copolymer/ligand complex in water. By properly tuning the ligand and composition of the block copolymer, the formation of a unique onion-type giant vesicle is possible.

1.3. References

[1] G. Whitesides, J. Mathias, C. Seto, *Science* **1991**, *254*, 1312.

[2] G. M. Whitesides, B. Grzybowski, *Science* **2002**, *295*, 2418.

[3] W. H. Binder, V. Barragan, F. M. Menger, *Angew. Chem. Int. Edit.* **2003**, *42*, 5802.

[4] P. Brion, E. Westhof, *Annu. Rev. Biophys. Biomol. Struc.* **1997**, *26*, 113.

[5] M. Muthukumar, C. K. Ober, E. L. Thomas, *Science* **1997**, *277*, 1225.

[6] J. Ruokolainen, R. Mäkinen, M. Torkkeli, T. Mäkelä, R. Serimaa, G. t. Brinke, O. Ikkala, *Science* **1998**, *280*, 557.

[7] O. Ikkala, G. ten Brinke, *Science* **2002**, *295*, 2407.

[8] T. Kato, *Science* **2002**, *295*, 2414.

[9] I. W. Hamley, *Angew. Chem. Int. Edit.* **2003**, *42*, 1692.

[10] F. S. Bates, G. H. Fredrickson, *Phys. Today* **1999**, *52*, 32.

[11] I. W. Hamley, *The physics of block copolymers* Oxford University Press Oxford 1998.

[12] J.-M. Lehn, *Supramolecular Chemistry*, VCH, Weinheim, 1995.

[13] J. A. A. W. Elemans, A. E. Rowan, R. J. M. Nolte, *J. Mater. Chem.* **2003**, *13*, 2661.

[14] T. Kato, J. M. J. Frechet, *Macromolecules* **1989**, *22*, 3818.

[15] R. P. Sijbesma, F. H. Beijer, L. Brunsveld, B. J. B. Folmer, J. H. K. K. Hirschberg, R. F. M. Lange, J. K. L. Lowe, E. W. Meijer, *Science* **1997**, *278*, 1601.

[16] O. Ikkala, G. ten Brinke, *Chem. Comm.* **2004**, 2131.

[17] M. R. Hammond, R. Mezzenga, *Soft Matter* **2008**, *4*, 952.

[18] X. Zhu, U. Beginn, M. Möller, R. I. Gearba, D. V. Anokhin, D. A. Ivanov, *J. Am. Chem. Soc.* **2006**, *128*, 16928.

[19] W. van Zoelen, G. ten Brinke, *Soft Matter* **2009**, *5*, 1568.

[20] K. Albrecht, A. Mourran, X. Zhu, T. Markkula, J. Groll, U. Beginn, W. H. de Jeu, M. Moeller, *Macromolecules* **2008**, *41*, 1728.

[21] J. Kao, J. Tingsanchali, T. Xu, *Macromolecules* **2011**, *44*, 4392.

[22] C. Park, J. Yoon, E. L. Thomas, *Polymer* **2003**, *44*, 6725.

[23] J. Chai, J. M. Buriak, *ACS Nano* **2008**, *2*, 489.

[24] B. J. Rancatore, C. E. Mauldin, S.-H. Tung, C. Wang, A. Hexemer, J. Strzalka, J. M. J. Fréchet, T. Xu, *ACS Nano* **2010**, *4*, 2721.

Chapter 2 Literature Reviews

2.1. Phase behavior of coil-coil block copolymer in bulk and thin films

2.1.1. Bulk structure

Block copolymers are polymers comprising more than one chemically distinct block via covalent bonding. The number of the blocks defines the molecular architecture of block copolymers: diblock (two distinct blocks), triblock (three distinct blocks), and multiblock (more than three distinct blocks) copolymers. In most cases, block copolymers are prepared by living polymerization technology and possess a varied molecular structure and molecular weight, having a typical polydispersity index between 1 and 1.2.[1] In the present thesis, we focus mainly on the diblock copolymer; therefore, in the following chapters, the block copolymer is referred to diblock copolymer.

The thermodynamics of a polymer mixture can be described by Eq. 2.1:[2]

$$\frac{\Delta G_m}{RT} = \frac{\varphi_A}{N_A} ln\varphi_A + \frac{\varphi_B}{N_B} ln\varphi_B + \varphi_A \varphi_B \chi \quad (2.1)$$

where R is the gas constant; T is the absolute temperature; N_A, N_B, φ_A and φ_B are the degree of polymerization and volume fraction of components A and B, respectively; and χ is the Flory-Huggins interaction parameter. For polymers, the contribution of entropy (the first two terms on the right side) is limited. Therefore, the miscibility of a mixture largely depends on the value of χ, which is defined in Eq. 2.2:[2]

$$\chi = \frac{1}{kT}[\varepsilon_{AB} - \frac{1}{2}(\varepsilon_{AA} + \varepsilon_{BB})] \quad (2.2)$$

where ε_{il} is the constant energy between the i^{th} and j^{th} components and k is the Boltzmann constant. In this equation, χ is temperature dependent (χ ~a+b/T); therefore, two components are miscible when χ is <0.05 or at very high temperatures.

Covalent bonding in block copolymers is different from that in polymer mixtures in which macrophase separation is prevented; instead, nanostructures with a periodicity of 10-100 nm are always observed due to microphase separation of the two blocks. Microphase separation is defined by the strength of the repulsion as characterized by

the product of χN (where N is the degree of polymerization).[3] Two regimes are discernible based on the value of χN as follows:

χN <10: the interaction between blocks is sufficiently weak, and individual chain statistics are unperturbed; therefore, the interface is broad. This regime is referred to as the *weak segregation limit* (WSL).

χN >100: the interaction is strong, and the interface is narrow; the system wants to minimize the total area of the interface under the constraint of incompressibility and with the entropic penalty of a stretched chain, thereby leading to perturbed chains and domains. This regime is referred to as the *strong segregation limit* (SSL).

The change in volume fraction of the two blocks alters the morphology. As shown at the bottom of Figure 1, when block A is the minor phase, a body-centered cubic spherical structure is observed; a slight increase in A switches the morphology to a hexagonal packed cylinder. A lamellar phase exists in symmetric copolymers for which a further increase in A reverses the change observed in the morphology. A gyroid phase is observed between the cylinder and lamellar phases. Such phase behavior is successfully predicted by self-consistent mean field theory (SCMF), and it is proven experimentally.[4]

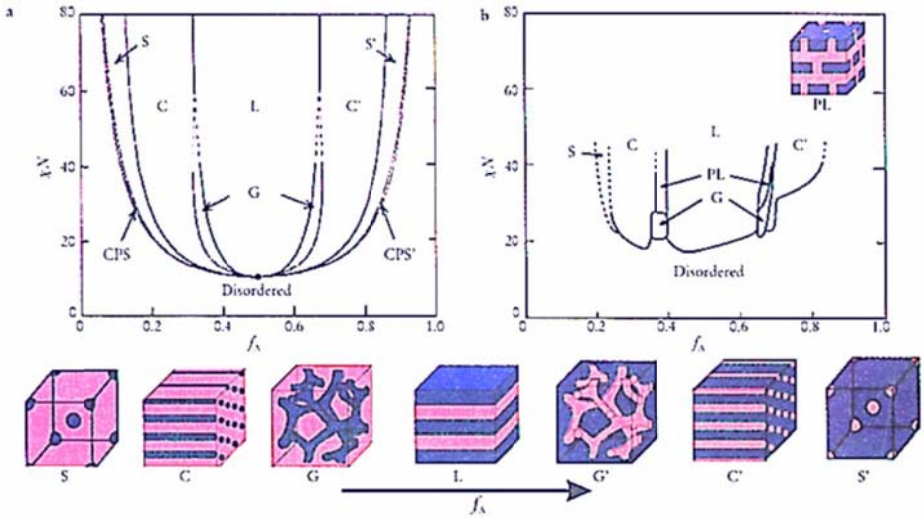

Figure 1. Phase behaviour of block copolymer: equilibrium morphology predicted by SCMF theory (left) and experimental phase diagram of poly (styrene-b-isoprene).[4]

Reprinted with permission, Copyright 1996 American Chemical Society.

2.1.2. Thin film structure

When the block copolymer is confined to a thin film on a surface, the morphology is generally similar to that of the bulk, but two new factors need to be considered: the film thickness and the preferential interaction of one block with the air/polymer interface and the polymer/substrate interface.[5] The reduced film thickness suppresses the formation of certain bulk morphologies (e.g., gyroids), whereas preferential wetting of distinct blocks on the interface has the important consequence of affecting the orientation of the microstructure. For example, the lamellar domains of poly (styrene-b-methyl methacrylate) (PS- PMMA) on silicon oxide are parallel to the surface, with PMMA and PS wetting the substrate surface and air interface, respectively. Such an asymmetric wetting is because of the different affinity of different blocks with interfaces: the polar PMMA block wets the hydrophilic silicon oxide surface, and the nonpolar PS block segregates at the air interface to reduce the surface energy.[6-8] Another important consequence of preferential wetting is the topographical structure of the thin films: a series of lamellae of alternating blocks join the two interfaces if the film thickness is commensurate with the block copolymer periodicity (L_0), but when the film thickness is incommensurate with the periodicity (thickness $\neq$(n+1/2) L_0), islands (holes) form on the top to minimize the total energy by quantizing the local film thickness.[6-8]

In thin films, the morphology and orientation of microdomains depend on the film thickness (Figure 2). The equilibrium bulk morphology of this SBS triblock copolymer is cylindrical; however, surface effects can cause significant deviations from the predicted bulk structure. On the thinnest part of the film, a disordered structure (dis) is observed, which might be caused by the wetting layer or by suppression of microphase separation due to confinement. Increasing of the film thickness facilitates phase separation, with a morphology sequence that proceeds from a perpendicular cylinder ($C_{\perp}$) –> parallel cylinder($C_{/\!/,1}$) –> a perforated lamellae (PL) –> parallel cylinder ($C_{/\!/,1}$) with an elongated cross-section and necks –> perpendicular cylinder ($C_{\perp}$) –> two layers of parallel cylinder ($C_{/\!/,2}$). Such a morphology sequence is confirmed by simulation technology.[9]

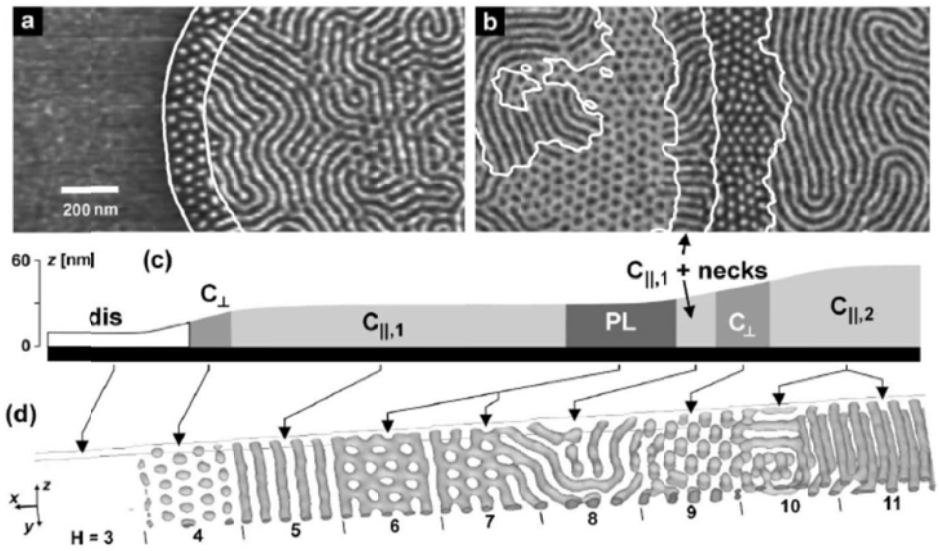

Figure 2. (a) and (b) Tapping mode scanning force microscopy phase images of thin poly(styrene-b-butadiene-b-styrene) (SBS) films on silicon substrates after annealing in chloroform vapor; (c) Schematic height profile of (a) and (b); (d) Simulation results with film thickness increasing from left to right.[9] Reprinted with permission, Copyright 2002 by The American Physical Society.

2.1.3. Directing self-assembly of block copolymers in thin film

The preferential wetting of the distinct blocks on the interfaces leads to parallel orientation of the microdomains mostly,[6-8] which limits the application of block copolymers in one of the important fields - nanolithography.[10, 11] Strategies have been devised to overcome interactions with the surface and to induce a perpendicular orientation of cylinders or lamellae relative to the substrate.[10] Some success has been achieved through techniques such as a neutral brush,[12] solvent annealing,[13] zone casting,[14] electric field alignment,[15] optical alignment,[16] topographical or chemical substrate patterning,[17] and surfactant-[18] and nanoparticle-assisted orientational order.[19]

A neutral brush is widely used to achieve vertical orientation of the block copolymer.[12, 20-22] Random copolymers with chemical structures similar to that of block copolymers (e.g., poly (styrene -*r*- methyl methacrylate) for PS-PMMA) are used to formulate neutral surface layers on a SiO_2 surface. To enhance adhesion between the random copolymer and the substrate, reactive groups are introduced in the side chain or to the end group for purpose. The neutrality of the surface is

controlled by the composition of the random copolymer brush. The optimal condition for the neutrality is a mole fraction of PS in poly (styrene -*r*- methyl methacrylate) for PS-PMMA of 0.64 and 0.55 for cylindrical and lamellar microdomains, respectively.[21] However, the vertical orientation of the microdomain obtained from this method is quite sensitive to the film thickness; at the neutral wetting point, the orientation of the lamellar domain changes from a random orientation ($1.5L_0$) -> perpendicular orientation ($1.75L_0$) -> random orientation ($2L_0$) -> perpendicular orientation ($2.25L_0$) -> random orientation ($2.5L_0$), where L_0 is the periodicity of the lamellae.[22]

2.2. Hierarchical ordering in block copolymers thin film

Hierarchical ordering with more than one characteristic length scale has been found in copolymers whose macromolecules consist of more than two types of monomer units.[23-27] A well-known example is a copolymer with side chain liquid crystal (LC) units, wherein ordering of the mesogenic moieties concurs with microphase separation. In such a system, the LC field will affect mesophase formation and domain orientation, whereas in thin films, thermally stable morphologies can be generated that consist of either lamellae or cylinders oriented perpendicular to the surface.[27]

2.2.1. Hierarchical ordering in thin films of side chain liquid crystalline block copolymers with covalent bonded mesogen

The common way to prepare the side chain liquid crystalline block copolymers is via living copolymerization of two or more monomers with at least one monomer bearing mesogenic group.[23-28] The mesogen is bonded to the polymer backbone with covalent bond. By proper choosing of the amount and type of the mesogen, different type of LC behavior (*i.e.,* nematic, smectic) can be introduced into the block copolymer,[29] and also the morphology (such cylinder, lamellae) can be varied.[27] Similar to that of the coil-coil block copolymers, morphologies of cylinder and lamellae are predicted by simulation[30] and are observed experimentally,[27] but some other moprhologies, such as spherical phase is supressed by the confinement of the

smectic LC field. In addition the lamellar phase dominates the phase dirgram, which is believed to be the effect of the smectic ordering.[24, 30]

In most of the cases the mesogen is amphiphilic, therefore it can wet both of the substrate and air interfaces, and the parallel oriented layers (smectic) drive the block copolymer microdomains vertically to the substrates.[23-28] However, it is also found that the microdomains can orient parallel to the substrate if the mesogen is sparse on the side chain (Figure 3), the normal vertical orientation is achieved when the graft density reach 100%. This means that the orientation of the microdomains is determined by the interactions of the mesophase with the interface of the LC block/coil block and the substrate. Higher graft density of mesogen leads to stronger preferences for the anchoring of the LC relative to LC block/coil block and the substrate. By essentially manipulating the strength of these interactions the morphology of the thin film can be controlled, allowing a transition of poorly oriented cylinder (55%) –> parallel cylinder –> perpendicular cylinder (100%) morphologies.[26]

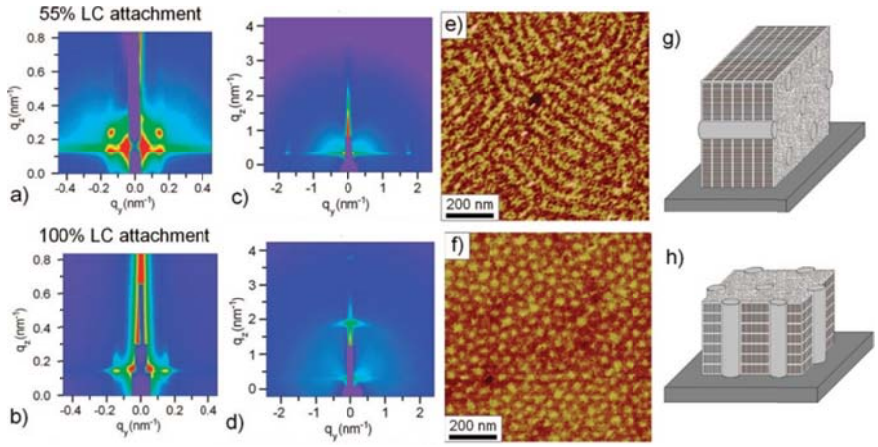

Figure 3. Comparison of the parallel cylinder morphology (55% LC attachment) and the perpendicular cylinder morphology (100% LC attachment). GISAXS images of (a) 55% LC attachment and (b) 100% LC attachment; GIWAXS of (c) 55% LC attachment and (d) 100% LC attachment; SFM images of (e) 55% LC attachment and (f) 100% LC attachment; schematics of the observed morphologies with the cylinder axis and the smectic layer normal parallel (g) and perpendicular (h) to the substrate.[26] Reprinted with permission, Copyright 2008 American Chemical Society.

2.2.2. Hierarchical ordering in thin films of side chain liquid crystalline block copolymers with non-covalently bonded mesogens

Polymer chemistry allows for tuning of the molecular structure of the side chains of liquid crystalline block copolymers by varying the type and volume ratio of monomers and mesogens.[23, 25-28] However, this method encounters several problems: 1) complicated chemistry to synthesize the mesogen monomer because not all of the monomer is available; 2) not all of the monomer can be (co)polymerized with normal living polymerization techniques, and more efforts are necessary to find appropriate living polymerization techniques to synthesize well-defined block copolymers; and 3) each composition must be freshly synthesized, which is a difficult and inflexible requirement. The combination of block copolymer and supramolecular chemistry is a good solution: 1) a block copolymer with only one composition is necessary because the morphology is tuned by the amount of ligand and by the interaction between the ligand and block copolymer; 2) the LC phase is introduced by supramolecular chemistry, thus avoiding complicated synthetic chemistry; and 3) functionality is easily introduced by the ligand.[31-33] The focus of this chemistry has initially been on the bulk structure of the block copolymer/ligand complex,[34-38] but it is gradually turning to the structure of thin films because of the promising applications of thin films in nanotechnology.[39-43]

The most widely used mesogens in the literature are simple linear surfactants (e.g., 3-pentadecylphenol (PDP)).[42, 44, 45] PDP bonds to the polymer backbone via hydrogen bonding between the hydroxyl group of the phenol and the pyridine group of poly (4-vinylpyridine). In the solid state, the complex forms a smectic phase, and the periodicity of the smectic layer is approximately 4 nm depending on the degree of complexation (x) as x^{-1}.[46] The same organization of PDP in thin films of PS-P4VP(PDP) is observed. P4VP(PDP) forms layers with a periodicity of ~4 nm, and orients itself parallel to the surface, thus driving the vertical orientation of block copolymer domains (with a periodicity of ~40 nm). The most promising result is that different hierarchical structures can be obtained with the same block copolymer simply by adjusting of the ratio of PDP to P4VP.[44]

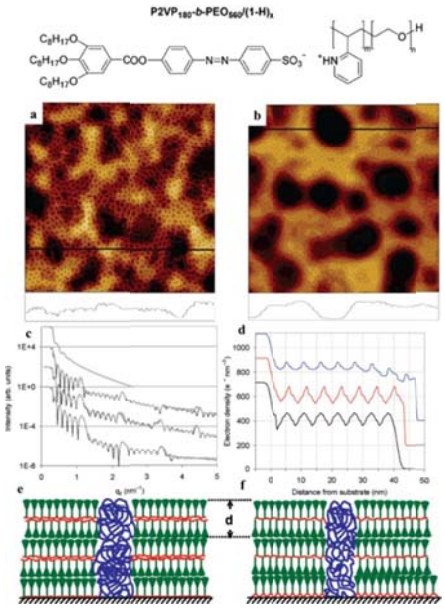

Figure 4. Hierarchical ordering of complex thin films: SFM topographic images of (a) 0.25 of protonation and (b) 0.50 of protonation; (c) X–ray reflectivity data 0f 0, 0.25, 0.5, and 1.0 of protonation (from top to bottom), open circles represent experimental data and solid lines the fits; (d) density profiles corresponding to the fits shown in (c), the curves are displaced by 135 e^{-}/nm^3 for clarity; schematics of the observed morphologies of (e) 0.25 and (f) 0.50 of protonation in thin films.[40] Reprinted with permission, Copyright 2008 American Chemical Society.

The wedge-shaped ligand with a sulfonate group (top of Figure 4) at the tip is an interesting example that forms a complex with block copolymer.[47] The pyridine salt of the ligand (which mimics the monomer) has a lamellar phase at low temperature, which transforms into a columnar phase at higher temperatures.[48] This ligand has been complexed with P2VP via ionic bonding;[48, 49] here, the contour length of the homopolymer chain defines the shape of the complex (either spheres or rods), whereas the degree of protonation determines the morphology (either smectic or columnar). In addition, incorporation of such a ligand into a miscible diblock copolymer, such as P2VP-PEO,[40] greatly increases the segregation between blocks. In thin films (Figure 4), smectic ordering of the ligand occurs in layers that are orthogonal to the interfaces of a block (Figure 4a-d). This allows for effortless alignment of the block copolymer microstructure, e.g., cylinders or lamellae, perpendicular to the air/substrate interfaces.

2.3. Techniques to investigate hierarchical ordering in block copolymer thin films

2.3.1. Optical Microscopy (OM)

OM is a very old technology[50] that is limited by the type of probe used (i.e., visible light), and the resolution is limited to the micrometer scale; therefore, its use in detecting the nanostructure in microphase separation is limited. However, OM is very powerful when visualizing the structure of late-stage islands (i.e., holes) in thin films via interference OM.[51] In addition, this technique can be used to identify the LC phase in the block copolymer/ligand complex by using cross-polarized light.[38, 48, 52]

2.3.2. Scanning Force Microscopy (SFM)

The most popular method for imaging the structure of surfaces is SFM operating under the tapping mode.[53] Figure 5 shows the generic scheme of tapping mode SFM. Generally, a sharp probe is driven by a piezoelectric system and oscillates just above the surface of a sample. The tip tracks the topography of the surface, and its oscillation frequency changes with the properties of the material (e.g., relatively harder or softer features on the surface), thereby generating so-called phase contrast images. This technique provides a unique advantage for simultaneous detection hierarchical ordering (*e.g.*, LC ordering and phase separation). As shown in Figure 4, a terrace is observed on the topographic images, which has a height of approximately 5.9 nm that corresponds to the periodicity of the smectic ordering. Meanwhile, features corresponding to microphase separation are visible on the same image. PEO forms a cylindrical microstructure with a long-range distance of approximately 46 nm, perpendicular to the substrate.[40]

Another merit of this technique is that the tip can penetrate the surface and reveal the morphology beneath the surface. For example, there is no feature corresponding to microphase separation in the complex thin film under soft tapping mode, but a clear contrast is obtained using the hard tapping mode.[40] The ligand forms a thin, amorphous top layer, which prevents imaging of the morphology at lower force; however, this structure is visible if a large force is applied, and the thin layer is penetrated. The strong phase contrast originates from the contrast between amorphous PEO at room temperature and the P2VP/ligand, which has an LC nature.

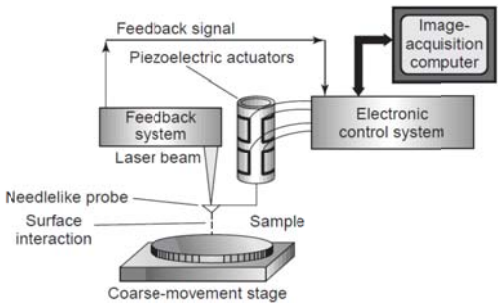

Figure 5. Generic scheme of SFM with its main components.[53] Reprinted with permission, Copyright 2000 John wiley &Sons.

2.3.3. Scanning Electron Microscopy (SEM)

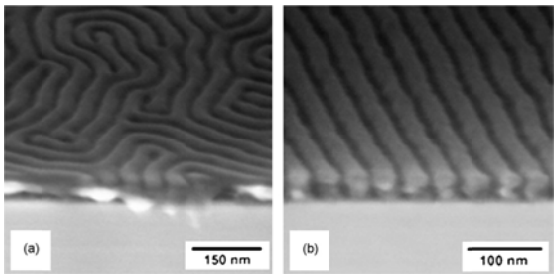

Figure 6. SEM micrograph of perpendicular PS-PMMA lamellae on: (a) an unpatterned substrate and (b) a chemically patterned substrate with $L_s = L_0$.[17] Reprinted with permission, Copyright 2003 Nature Publishing Group.

.

SEM is also used to image the surface morphology of block copolymer thin films. However, this method is limited by the weak contrast between blocks, whose components are always carbon and hydrogen; therefore, additional sample preparation techniques, *e.g.*, selective etching, are required.[50] For example, in PS-PMMA, the PS domains remain intact while the PMMA block is etched by exposure to UV light and by washing in acetic acid; the topographic contrast is drastically enhanced, and observation of the morphology is possible (Figure 6).[17] The most promising feature of this technique is the directly visualization of the orientation of the microdomains. As shown in Figure 6, the perpendicular orientation of the lamellae is clear visible on the cross-section of the thin film, after removing of PMMA block.[17]

2.3.4. Transmission Electron Microscopy (TEM)

TEM is another popular electron microscopy technique in block copolymer science. Instead of using the secondary electrons for the signal as in SEM, TEM instead uses the transmitted electrons as the source of the signal. The contrast of the images are formed directly by the occlusion and absorption of electrons by the sample. As with SEM, additional sample preparation techniques are necessary (*e.g.*, staining) to enhance the contrast.[50] Samples can be prepared by floating thin films from the substrate to a water surface or by obtaining cryo-microtome sections of the thin film with the substrate; in both cases, the sample is transferred to copper grids for imaging. The former method is always used to observe the morphology of the thin film,[44] and the later can be used to identify the orientation of the microdomains in thin films.[54]

2.3.5. Grazing incidence small (wide) angle X-ray scattering (GISAXS/GIWAXS) and X-ray Reflectivity (XRR)

Reflection involves the presence of an evanescent wave parallel to the interface, both below and above the critical angle.[56, 57] Depending on the signal used, different X-ray diffraction techniques are named: XRR uses the reflection X-ray beam, while GISAXS/GIWAXS use the evanescent wave.

Briefly, XRR reflects an X-ray beam from a flat surface to measure the intensity of the reflected X-ray in the specular direction (Figure 7, when $\alpha_2=\alpha_1$). The deviation of the reflected intensity from the value predicted by the Fresnel reflectivity law can be used to analyze the electron density profile of the interface normal to the surface[56]. To detect the hierarchical ordering in block copolymer thin films, XRR provides information about the layers parallel to the substrate, which correspond to the alternate stacking of smectic layers.[40, 55] As shown in Figure 4, the average periodicity of smectic layers (~5.6 nm) is detected by XRR, which is very close to the periodicity detected by SFM in thin films (5.9 nm).[40] In addition, this technique provides information about the thickness of the layer of the block copolymer lamellae parallel to the surface.[56]

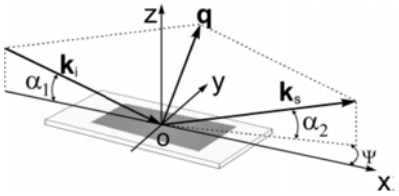

Figure 7. General X–ray diffraction geometry. For XRR, α_2 and α_1 are varied together while setting $\alpha_2=\alpha_1$ for $\Psi=0$, which results in $q \equiv q_z$. For GIWAXS and GISAXS, α_1 is set either below or close to the critical angle of total reflection. As a result, an evanescent wave is generated, and 2D surface diffraction can be performed by varying Ψ for specific values of α_2.[55] Reprinted with permission, Copyright 2005 American Chemical Society.

In GISAXS and GIWAXS, the X-ray beam is incident on the surface of a sample at a small grazing angle below the critical angle of total reflection. Under these conditions, only an evanescent wave is generated that propagates along the film/air interface and penetrates into the film. The penetration depth can be varied by changing the incident angle. The evanescent wave can be considered to be the incident beam for 2D X-ray diffraction, and the geometry of GISAXS and GIWAXS techniques is shown in Figure 7.[55] The scattering vector is given by $q_x = (2\pi/\lambda)(\cos\Psi\cos\alpha_2 - \cos\alpha_1)$, $q_y = (2\pi/\lambda)(\sin\Psi\cos\alpha_2)$, and $q_z = (2\pi/\lambda)(\sin\alpha_1 + \sin\alpha_2)$.[57]

GISAXS and GIWAXS provide information about both the lateral and normal ordering inside a thin film. Different lateral ordering generates signals on different positions of a 2D pattern: when the structure is parallel to the substrate (*i.e.*, the smectic layer laying down), intensive stripes with regular spacing along the q_z direction are expected, whereas a perpendicular structure generates a rod-shaped signal normal to the surface. Combining these two techniques provides unique information about the structure and orientation of the hierarchical ordering in block copolymer thin films. In Figure 3, when the LC attachment is approximately 55%, GISAXS shows a typical pattern of a flat hexagonal packed cylinder (Figure 3a), and rods normal to the surface appear on GIWAXS pattern (Figure 3c), indicative of the perpendicular orientation of the smectic phase, which confirms the observations from SFM (Figure 3e).[26]

2.3.6. Ellipsometry

Ellipsometry is an optical technique which can be used to determine the thickness of block copolymer thin films. Upon analysis of the change in the polarization of light, this technique can detect both the amplitude and phase shift of reflected waves. Measurements at different wavelengths with spectroscopic ellipsometry enables probing of complex refractive indices.[58]

2.4. Applications of block copolymer complex thin films

In general, block copolymer complex thin films can be used in all of the same applications as normal coil-coil block copolymer thin films, as a template, mask, porous media, etc.[10, 11] Here, several applications that reflect the unique properties of block copolymer complex thin films are illustrated.

2.4.1. Nano-objects

The ligand in block copolymer complex thin films can be easily removed by washing in a selective solvent without disturbing the nanostructure.[41, 59] Depending on the initial morphology of the thin film and the orientation of the microdomains, different types of nanostructures can be generated.[41] For example, the LC complex forms a cylinder embedded in an amorphous matrix; removing the ligand leads to the formation of a nanoporous block copolymer thin film, with channels vertically oriented throughout the film, which is promising for ultrafiltration[60] and control releasing.[61]

2.4.2. Nanofabrication

This application is based on the formation of nano-objectives with various morphologies.[59] These nanostructures can be used to template functional inorganic nanostructures.[62] Beginning with PS-P4VP(PDP) thin films, removal of PDP results in nanorods with a PS core and a P4VP corona; amorphous $PbTiO_3$ is coated to this template using a pulsed laser deposition technique. The template is removed by heating to above 565°C, and nanostructured crystalline $PbTiO_3$ forms, which possesses ferroelectric properties.[59] Various metal nanopatterns can be fabricated using this technology.

2.4.3. Organic Thin Film Transistors (OFETs)

Recently it was found that the concept of a block copolymer/ligand supramolecular complex can be used to fabricate OFETs, which can solve the dewetting problem in the organic semiconductor industry.[63] For example, a quaterthiophene oligomer is attached to the side chains of P4VP *via* hydrogen bonding. In thin films, the quaterthiophenes self-assemble into microdomains tens of nanometers in size and orient themselves normal to the surface. Such supramolecules exhibit the same field-effect mobilities as that of the quaterthiophene alone (10^{-4} $cm^2/(V \cdot s)$).

2.5. References

[1] N. Hadjichristidis, M. Pitsikalis, H. Iatrou, *Adv. Polym. Sci.* **2005**, *189*, 1.

[2] G. Strobl, *The physics of polymer*, Springer, Berlin Heidelberg 2007.

[3] F. S. Bates, G. H. Fredrickson, *Annu. Rev. Phys. Chem.* **1990**, *41*, 525.

[4] M. W. Matsen, F. S. Bates, *Macromolecules* **1996**, *29*, 1091.

[5] M. J. Fasolka, A. M. Mayes, *Annu. Rev. Mater. Res.* **2001**, *31*, 323.

[6] S. H. Anastasiadis, T. P. Russell, S. K. Satija, C. F. Majkrzak, *Phys. Rev. Lett.* **1989**, *62*, 1852.

[7] T. P. Russell, G. Coulon, V. R. Deline, D. C. Miller, *Macromolecules* **1989**, *22*, 4600.

[8] D. G. Walton, G. J. Kellogg, A. M. Mayes, P. Lambooy, T. P. Russell, *Macromolecules* **1994**, *27*, 6225.

[9] A. Knoll, A. Horvat, K. S. Lyakhova, G. Krausch, G. J. A. Sevink, A. V. Zvelindovsky, R. Magerle, *Phys. Rev. Lett.* **2002**, *89*, 035501.

[10] A. P. Marencic, R. A. Register, *Annu. Rev. Chem. Biomol. Eng.* **2010**, *1*, 277.

[11] H. I.W, *Prog. Polym. Sci.* **2009**, *34*, 1161.

[12] I. In, Y.-H. La, S.-M. Park, P. F. Nealey, P. Gopalan, *Langmuir* **2006**, *22*, 7855.

[13] S. H. Kim, M. J. Misner, T. Xu, M. Kimura, T. P. Russell, *Adv. Mater.* **2004**, *16*, 226.

[14] C. Tang, A. Tracz, M. Kruk, R. Zhang, D.-M. Smilgies, K. Matyjaszewski, T. Kowalewski, *J. Am.Chem.Soc.* **2005**, *127*, 6918.

[15] T. Thurn-Albrecht, J. Schotter, G. A. Kästle, N. Emley, T. Shibauchi, L. Krusin-Elbaum, K. Guarini, C. T. Black, M. T. Tuominen, T. P. Russell, *Science* **2000**, *290*, 2126.

[16] Y. Morikawa, S. Nagano, K. Watanabe, K. Kamata, T. Iyoda, T. Seki, *Adv. Mater.* **2006**, *18*, 883.

[17] S. Ouk Kim, H. H. Solak, M. P. Stoykovich, N. J. Ferrier, J. J. de Pablo, P. F. Nealey, *Nature* **2003**, *424*, 411.

[18] J. G. Son, X. Bulliard, H. Kang, P. F. Nealey, K. Char, *Adv. Mater.* **2008**, *20*, 3643.

[19] Y. Lin, A. Boker, J. He, K. Sill, H. Xiang, C. Abetz, X. Li, J. Wang, T. Emrick, S. Long, Q. Wang, A. Balazs, T. P. Russell, *Nature* **2005**, *434*, 55.

[20] E. Han, K. O. Stuen, M. Leolukman, C.-C. Liu, P. F. Nealey, P. Gopalan, *Macromolecules* **2009**, *42*, 4896.

[21] S. Ham, C. Shin, E. Kim, D. Y. Ryu, U. Jeong, T. P. Russell, C. J. Hawker, *Macromolecules* **2008**, *41*, 6431.

[22] H. S. Suh, H. Kang, P. F. Nealey, K. Char, *Macromolecules* **2010**, *43*, 4744.

[23] C. Osuji, Y. Zhang, G. Mao, C. K. Ober, E. L. Thomas, *Macromolecules* **1999**, *32*, 7703.

[24] M. Anthamatten, P. T. Hammond, *J, Polym, Sci, Part B: Polym, Phys,* **2001**, *39*, 2671.

[25] I. W. Hamley, V. Castelletto, Z. B. Lu, C. T. Imrie, T. Itoh, M. Al-Hussein, *Macromolecules* **2004**, *37*, 4798.

[26] E. Verploegen, T. Zhang, Y. S. Jung, C. Ross, P. T. Hammond, *Nano Lett.* **2008**, *8*, 3434.

[27] W. H. de Jeu, Y. Séréro, M. Al-Hussein, *Adv. Polym. Sci.* **2006**, *200*, 71.

[28] G. Mao, C. K. Ober, *Acta Polymer.* **1997**, *48*, 405.

[29] J. C. Dubois, P. Le Barny, M. Mauzac, C. Noel, *Acta Polymer.* **1997**, *48*, 47.

[30] M. Shah, V. Pryamitsyn, V. Ganesan, *Macromolecules* **2007**, *41*, 218.

[31] M. R. Hammond, R. Mezzenga, *Soft Matter* **2008**, *4*, 952.

[32] O. Ikkala, G. ten Brinke, *Chemical Communications* **2004**, 2131.

[33] W. van Zoelen, G. ten Brinke, *Soft Matter* **2009**, *5*, 1568.

[34] J. Ruokolainen, R. Mäkinen, M. Torkkeli, T. Mäkelä, R. Serimaa, G. t. Brinke, O. Ikkala, *Science* **1998**, *280*, 557.

[35] O. Ikkala, G. ten Brinke, *Science* **2002**, *295*, 2407.

[36] W.-T. Chuang, H.-S. Sheu, U. S. Jeng, H.-H. Wu, P.-D. Hong, J.-J. Lee, *Chem. Mater.* **2009**, *21*, 975.

[37] K. K. Tenneti, X. Chen, C. Y. Li, X. Wan, X. Fan, Q.-F. Zhou, L. Rong, B. S. Hsiao, *Macromolecules* **2007**, *40*, 5095.

[38] J. T. Korhonen, T. Verho, P. Rannou, O. Ikkala, *Macromolecules* **2010**, *43*, 1507.

[39] W. van Zoelen, E. Polushkin, G. ten Brinke, *Macromolecules* **2008**, *41*, 8807.

[40] K. Albrecht, A. Mourran, X. Zhu, T. Markkula, J. Groll, U. Beginn, W. H. de Jeu, M. Moeller, *Macromolecules* **2008**, *41*, 1728.

[41] J. W. Lee, C. Lee, S. Y. Choi, S. H. Kim, *Macromolecules* **2009**, *43*, 442.

[42] J. Kao, J. Tingsanchali, T. Xu, *Macromolecules* **2011**, *44*, 4392.

[43] H.-S. Sun, C.-H. Lee, C.-S. Lai, H.-L. Chen, S.-H. Tung, W.-C. Chen, *Soft Matter* **2011**, *7*, 4198.

[44] S.-H. Tung, N. C. Kalarickal, J. W. Mays, T. Xu, *Macromolecules* **2008**, *41*, 6453.

[45] W. van Zoelen, T. Asumaa, J. Ruokolainen, O. Ikkala, G. ten Brinke, *Macromolecules* **2008**, *41*, 3199.

[46] J. Ruokolainen, G. ten Brinke, O. Ikkala, M. Torkkeli, R. Serimaa, *Macromolecules* **1996**, *29*, 3409.

[47] X. Zhu, B. Tartsch, U. Beginn, M. Möller, *Chem. – A Europ. J.* **2004**, *10*, 3871.

[48] X. Zhu, U. Beginn, M. Möller, R. I. Gearba, D. V. Anokhin, D. A. Ivanov, *J. Am. Chem. Soc.* **2006**, *128*, 16928.

[49] K. Albrecht, M. Gallyamov, X. Zhu, M. Moeller, *Macromolecular Chem. Phys.* **2007**, *208*, 1409.

[50] L. C. Sawyer, D. T. Grubb, G. F. Meyers, *Polymer Microscopy (3rd Ed.)*, Springer, 2007.

[51] Y. V. Khandurina, V. L. Alexeev, G. A. Evmenenko, A. T. Dembo, V. B. Rogacheva, A. B. Zezin, *J. Phys. II France* **1995**, *5*, 337.

[52] M. C. Luyten, G. O. R. Alberda van Ekenstein, G. ten Brinke, J. Ruokolainen, O. Ikkala, M. Torkkeli, R. Serimaa, *Macromolecules* **1999**, *32*, 4404.

[53] S. Magonov, *Encyclopedia of Analytical Chemistry*, John wiley &Sons, Chichester 2000.

[54] T. Xu, A. V. Zvelindovsky, G. J. A. Sevink, K. S. Lyakhova, H. Jinnai, T. P. Russell, *Macromolecules* **2005**, *38*, 10788.

[55] M. Al-Hussein, Y. Séréro, O. Konovalov, A. Mourran, M. Möller, W. H. de Jeu, *Macromolecules* **2005**, *38*, 9610.

[56] R. T.P, *Mater. Sci. Rep.* **1990**, *5*, 171.

[57] M. Tolan, *X-Ray Scattering from Soft-Matter Thin Films*, Springer, 1999.

[58] RMA Azzam, NM Bashara, *Ellipsometry and polarized light*, North-Holland, Amsterdam 1989.

[59] W. van Zoelen, A. H. G. Vlooswijk, A. Ferri, A.-M. Andringa, B. Noheda, G. ten Brinke, *Chem. Mater.* **2009**, *21*, 4719.

[60] S. Y. Yang, I. Ryu, H. Y. Kim, J. K. Kim, S. K. Jang, T. P. Russell, *Adv. Mater.* **2006**, *18*, 709.

[61] E. A. Jackson, M. A. Hillmyer, *ACS Nano* **2010**, *4*, 3548.

[62] B. K. Kuila, M. Stamm, *J. Mater. Chem.* **2011**, *21*, 14127.

[63] B. J. Rancatore, C. E. Mauldin, S.-H. Tung, C. Wang, A. Hexemer, J. Strzalka, J. M. J. Fréchet, T. Xu, *ACS Nano* **2010**, *4*, 2721.

Chapter 3 Structural and Electrical Properties of Asymmetrically Substituted Sexithiophene Monolayers

3.1. Introduction

During the last decades, functionalized oligothiophenes have attracted much attention as active components in organic electronic devices. Applications include organic light-emitting diodes (OLEDs),[1, 2] organic thin film transistors (OFETs),[3-7] sensors,[8, 9] and electrochromic devices.[10, 11] These possibilities are directly related to the transverse π-π coupling between neighboring thiophene molecules.[12] Therefore the well-established chemistry of oligothiophenes with their physical and chemical properties is crucial for application in OFETs and organic photovoltaics (OPV). [13] Considerable structure variation of oligothiophenes is possible, allowing fine tuning of the electronic and optical properties over a wide range. The structure of oligothiophenes in the solid state is controlled by chemical details of the oligomers (e.g. the type of substituents, the number of the thiophene rings) and the processing conditions.[14-17] Upon deposition by vacuum evaporation or from solution, oligothiophenes form polycrystalline films lead to a fairly good performance in OFETs.[18] To improve OFET properties, proper alignment of the molecules is desired, either directly in the crystalline state or via a mesomorphic intermediate state.

The problems of polycrystalline thin films arise from structural defects as well as from grain boundaries. Both act as trap for the charge carriers and reduce the performance of the device. Introducing liquid crystalline (LC) ordering into oligothiophenes potentially provides a solution to circumvent structural defects. An LC structure can provide self-healing of structural defects leading to the formation of large ordered domains.[14] In this context, smectic LC order is most appealing due to the anisotropic two-dimensional (2D) charge transport within the layers, which depends mainly on the lateral molecular distance. [19] Unsubstituted oligothiophenes are usually crystalline and the magnitude of the π-coupling between cofacially aligned thiophene rings essentially depends on the intermolecular distance of about 3 Å.[17] In order to obtain LC phases, different substituents have been introduced symmetrically at α, ω positions of the rigid thiophene core. The interplay between rigid core and

flexible substituents directly influences the self-assembly of the oligomers. The phase behaviors, including the transition temperatures determining the LC window, originate from a balance between length and structure of the core and length of the substituents (linear *vs*. branched).[14, 20-22] By proper tuning the structure of the substituents, LC ordering has been introduced into long oligothiophenes, and excellent charge carrier mobilities up to 0.18 $cm^2/V/s$ have been reported in septithiophenes.[14]

Asymmetry can be introduced into an oligothiophene system by attaching different kinds of substituents at the α, ω positions.[23-26] Asymmetric oligomers compared to symmetric oligomers leads to additional frustration in the packing of the molecules, promoting LC phases over crystalline ones. Thus the LC temperature window can be extended, as desired for fabrication of high-performance OFETs. By carefully tuning the type of substituent, smectic ordering has been obtained at room temperature and for an asymmetrically substituted quaterthiophene mobilities have been achieved up to 0.1 $cm^2/V/s$.[26] On the other hand, any asymmetry should not be too large as otherwise the molecular ordering - crucial for the mobilities of charge carriers - could be hindered.

Compared to symmetrically substituted oligothiophenes, work on asymmetric ones has so far been limited to relatively short oligomers (≤ 6 thiophene rings)[23-27] as chemistry of oligothiophene with long thiophene cores is difficult.[13] In contrast, solution-processable symmetric oligomers up to 13 thiophene rings have been reported.[28] Hence it is challenging to prepare asymmetric oligothiophenes with a long thiophene core. In particular, obtaining smectic ordering in combination with solution processability requires a carefully designed balance between the influence of the rigid core and the asymmetric substituents.

Previously we have shown that LC ordering can be obtained by introducing a specially designed branched alkyl substituent, 2-octyldodecyl, at *α*, *ω* positions of septithiophene, abbreviated as **7T**.[30] The solubility of **7T** in various organic solvents is relatively high, resulting in good processability from solution. In submonolayers as well as monolayers, the molecules self-assemble into domains with rectangular symmetry. Interestingly, inside these domains supramolecular fine structure is found with a periodicity of 250 Å. The formation of additional layers on top is suppressed

until completion of the first monolayer. The performance of a monolayer OFET built from **7T** has been investigated; the resulting mobility was 0.01 $cm^2/V/s$.

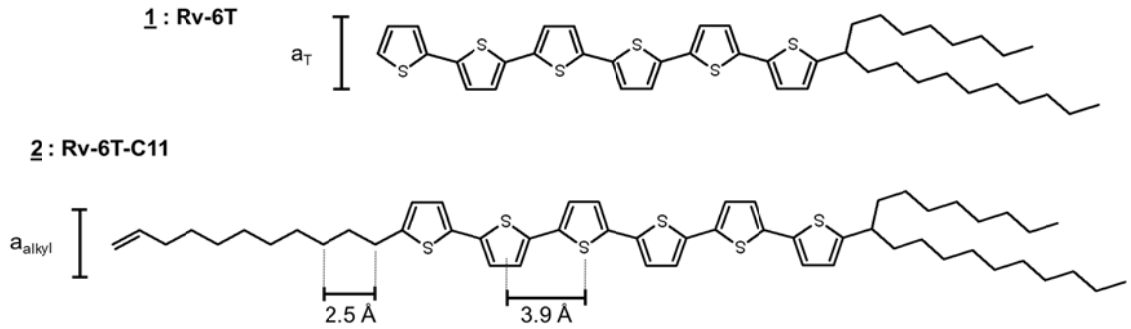

Scheme 1. Molecular structure of compounds **1** and **2**: the length of sexithiophene is 22.2 Å[29] when taking into account the van der Waals radius of the terminal H atoms. The octyldodecyl chain has a length of 15.3 Å when taking into account the van der Waals radius of the terminal CH_3 groups. Molecule **1** has a total length of about 37.5 Å compared to 52.8 Å of molecule **2**. The van der Waals diameter of a compact alkyl chain is of about $a_{alkyl} \sim$ 4-5 Å while it is 3-5 Å for oligothiophenes.

Note that the van der Waals diameter of a compact thiophene is about 3 to 3.5 Å while alkyl is of about 4 to 5 Å per chain. The packing frustration due to the branched aliphatic chains could be alleviated in a 3D-crystal by interdigitation of the alkyl chains and tilting of the oligothiophene core. However, in two-dimension, the lack of interdigitation give rise to a monolayer of tilted molecules different from the bulk phase. Despite that, a physisorbed monolayer of **7T** showed electrical connectivity and a mobility of charge carriers with similar magnitude as covalently bound monolayers of the "SAMFET".[7, 10] Here we present two new asymmetric oligothiophenes with a sexithiophene core, at one side substituted with the 2-octyldodecyl group just mentioned and at the other side by H or a linear C_{11} alkenyl chain, respectively (abbreviated as compound **1** and **2**, see Scheme 1). The design principle is based on the established properties of the 2-octyldodecyl group (enhanced solution processablity, unique monolayer formation) observed in symmetric systems.[30] Obviously, due to the asymmetry, frustration increases and the compromise between the effects of the rigid thiophene core and the flexible alkyl chains leads to reduced phase transition temperatures. Thus versatile LC phases are

found in these new oligothiophenes, which is a prerequisite for potential high performance. The experimental work presented here seeks to understand: (i) the impact of end groups on the formation of monolayer (wetting) and (ii) the role of the mesophase on the growth of the monolayer (domain size). Therefore, we use two molecules with identical conjugation length (6T) with different terminal groups. In the following we discuss the phase behavior of these new asymmetric oligomers in bulk, monolayer formation, as well as structural analysis, optical properties, and finally the field effect mobility in a monolayer transistor.

3.2. Experimental section

3.2.1. Materials.

α-(2-octyldodecyl)-sexithiophene (denoted as compound **1**) was prepared according to the procedure given in a previous publication.[31] The synthesis of molecule **2** is described in detail in the supporting information. Chlorobenzene (99.9%, CHROMASOLV) was purchased from Sigma-Aldrich.

3.2.2. Film preparation.

Silicon wafers (Si-Mat GmbH, Germany) were cut into pieces of about 1×1 cm^2, cleaned by sonication in isopropanol for 5 min, and dried with air. The silicon substrates were used immediately after activation in UV/O_2 for 12 min. the compound was dissolved into chlorobenzene by stirring in the brawn GC vial overnight, and filtrated through a 0.2 μm PTFE syringe filter. In some cases the solution was heated up to 40°C to improve the solubility of the oligomer. Samples were spin coated at a spinning rate of 500 rpm for 5 min (Convac 1001S, Germany). The surface coverage was controlled by changing the concentration of the solution. For the optical measurements films were prepared on quartz following the same procedure.

3.2.3. Characterizations.

Differential scanning calorimeter DSC measurements were performed using a Netsch DSC 404 instrument purged with N_2. For each measurement, a sample of about 5 mg was sealed in an aluminum pan while an identical pan was used as

reference. Each sample was heated into the isotropic phase and kept for 2 minutes to erase any thermal history. Subsequently each Compound sample was cooled and reheated between 0 and 300°C (for Compound **1** between 0 and 240°C) at a rate of 10°C/min. To obtain the enthalpy of transitions for overlapping peaks, deconvolution was performed with the peak fit module of Origin 7.5. The peaks were fitted by Gaussians while the number of peaks and their positions were determined from the second derivative.

Polarized Optical Microscopy (POM) was done using a Carl Zeiss Axioplan-2 imaging polarizing microscope equipped with a Mettler Toledo FP 82HT hot stage and a FP 90 processor. The micrographs were recorded with a Carl Zeiss AxioCam MRc digital camera.

Field Emission Scanning Electron Microscope (FESEM) experiments were performed using a Hitachi S4800 high resolution Field Emission Scanning Electron Microscope (accelerating voltage 1.5kV). Data analysis was performed by using Image J, version 1.38.

The Scanning force microscopy (SFM) was done by tapping mode (NanoScope V, Digital Instruments Veeco Instruments, Santa Barbara, CA) under ambient conditions. Standard silicon cantilevers with a spring constant of 5~37 N/m and an oscillation frequency of ~75 kHz were used. Data were processed using of Digital Instruments software: NanoScope Analysis, version 1.12.

X-ray reflectivity (XRR) was performed at JCNS-2 and PGI-4, Forschungszentrum Jülich using a D8 Advance x-ray reflectometer from Bruker AXS (Karlsruhe, Germany). A Cu X-ray tube with a line source (focal spot 12×0.04 mm^2) provided Cu K_α radiation with λ=0.1542 nm. A parabolic graded multilayer system (Göbel mirror) converted the divergent beam into an almost parallel beam (divergence <0.03°) and suppressed the Cu K_β radiation. The scattering plane was vertical and the sample remained horizontal. After reflection at the sample stage the intensity was collected by a NaI scintillation detector. The intensity was measured as a function of the scattering vector $q_z = (4\pi/\lambda)\sin\theta$, in which 2θ was the scattering angle. The latter was fixed at twice the incident angle θ, which sets q_z along the film normal. The measured intensity was corrected for the footprint of the X-ray beam, which overilluminates the sample below θ=0.8°. The experimental data were fitted to a multilayer model

representing the internal structure of the monolayer using the recursive Parratt formalism.[32]

Grazing incidence wide angle X-ray scattering (GIWAXS) measurements were performed at the synchrotron beamline BW4 of the DORIS III storage ring (HASYLAB at DESY) in Hamburg. The sample-detector distance and the incident angle were set to 110 mm and 0.2°, respectively. The scattering signal was recorded by a 2d detector (MARCCD, 2048x2048 pixels) and the small angle scattering blocked by a rod-like beam stop. Detailed GIWAXS setting description can be found elsewhere.[33] The absorption spectra of asymmetric substituted sexithiophene were measured in both of solution and thin films on a JASCO V-610 UV-Vis spectrometer (JASCO GmbH, Germany). For solution the concentration was 10^{-5} mmol/L. Fluorescence emission spectra in solution were measured with a FLUROMAX-4P Spectrometer (HORIBA Jobin Yvon GmbH). The solutions were excited at the wavelength of the respective UV/Vis absorption maxima. Electrical characterization of the field effect transistors all carried out in a probe station under high vaccum (10^{-6} mbar) with a Keithly 4200-SCS Semiconductor Characterization System.

3.3. Results and discussions

3.3.1. Phase behavior in bulk

The thermal transitions of compounds **1** and **2** have been investigated by differential scanning calorimetry (DSC) (Figure 1); the extracted parameters are listed in Table 1. As shown by both experiment and theory, non-substituted α-sexithiophene displays versatile phase transitions including a crystalline phase and at least two mesophases at high temperature.[29, 34] Introducing a branched 2-octyldodecyl group at the α-position of the sexithiophene drastically reduces the possibility of phase transitions while the highest transition temperature is now below ~200°C. The phase behavior of the mono-substituted compound **1** is simple: during cooling and reheating to the isotropic state only a single peak is observed (Figure 1a). The value of the enthalpy is large (Table 1), which is typical for crystallization. Hence, we conclude that only a phase transition crystalline-isotropic (melting) is present. When the ω-position of sexithiophene core is substituted with a 11-undecen-1-yl group (compound **2**), the highest transition temperature is further reduced to ~30 °C below the melting

point of **1**. In addition a rich pattern of reversible phase transitions is observed upon heating and cooling (Figure 1b). Not surprisingly, in the double substituted asymmetric compound the balance between the effects of the rigid sexithiophene core and the flexible alkyl groups differ from the mono-substituted one. Upon cooling **2** down from the isotropic state four peaks are observed, indicating multiple phases. When heated back to the isotropic state, two peaks are clearly seen while two other ones appear only as shoulders which show again four transitions. To obtain the enthalpy of each transition, peak deconvolution was applied, based on the second heating curve (see supporting information, Figure S1). The extracted parameters are summarized in Table 1. The transitions are thermally reversible and show limited undercooling, indicating fast transformations from one mesophase to another. Upon cooling down from the isotropic melt, the enthalpy values for the first three transitions are between 3-10 kJ/mol, signifying the formation of three different LC phases. The much larger enthalpy associated with the last peak indicates most probably crystallization. From polarized optical microscopy (POM), these transitions appear to be between different smectic phases (see supporting information Figure S2). Tentatively we assign the following phase sequence upon cooling: I→Sm-B→Sm-E→Sm-H→Cr. The transition temperatures observed with POM are consistent with the DSC measurements.

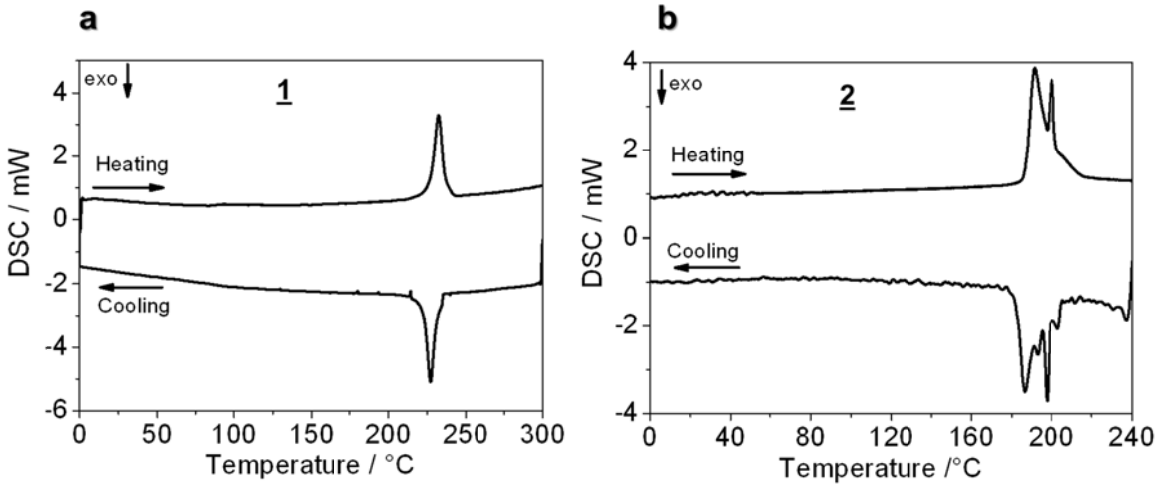

Figure 1. DSC thermograms of (a) molecule **1** and (b) molecule **2**.

Table 1. Transition temperatures and attendant enthalpies of the asymmetricexithiophene oligomers (Cr=crystalline phase; LC=liquid-crystalline phase; I=isotropic phase).

Compound	Process	Transition peak temperature (°C) and (enthalpies (kJ/mol))
1	cooling	I 227 (–32.9) Cr
	heating	Cr 232 (31.4) I
2	cooling	I 201 (–3.9) LC 198 (–7.0) LC 193 (–9.4) LC 187 (–17.1) Cr
	heating	Cr 191 (17.5) LC 196 (6.1) LC 200 (4.8) LC 201 (12.7) I

3.3.2. Monolayer growth and morphology

The solubility of oligothiophenes in different organic solvents - crucial for convenient processing - is enhanced by the introduction of bulky branched substituents to α,ω positions.[30] In fact, even one branched substituent is enough to increase the solubility of the sexithiophenes in chlorobenzene. Compound **1** has a saturation concentration of 0.7 g/L at room temperature and about 1.4 g/L at 40 °C which is higher for both non-substituted insoluble sexithiophene and for symmetrically substituted sexithiophenes (e.g. dihexylsexithiophene, almost insoluble). Introducing a linear 11-undecen-1-yl group at the ω position increases the solubility further: **2** saturates at 0.9-1.0 g/L at room temperature sufficient for monolayer formation.

Thin films of compounds **1** and **2** were prepared by spin casting solutions in chlorobenzene onto a silicon wafer. Figure 2 shows representative (sub)monolayers morphologies of each compound. Both form unique elliptically shaped crystals (Figure 2- 1a, 1b, 2a and 2b) that are not connected. Such type of morphology has not been observed in symmetric di-substituted oligothiophenes with either linear or branched alkyl groups.[30, 35] For these molecules mostly square crystals have been found with a broad size distribution. Obviously, the new morphology must be attributed to the asymmetric substitution of the oligothiophene, which leads to an increased mismatch between the volume of the bulky branched alkyl substituent and the rigid thiophene core. This, in turn, induces an anisotropic stress in the domains, leading to different growth rates of the crystals along dissimilar directions. The presence of the branched tail suppresses any 3D growth of the crystals until the

surface coverage reaches a full monolayer. At earlier stages still 3D nuclei are formed but they do not grow into crystals. At this stage we do not have a more detailed explanation of this unique property.

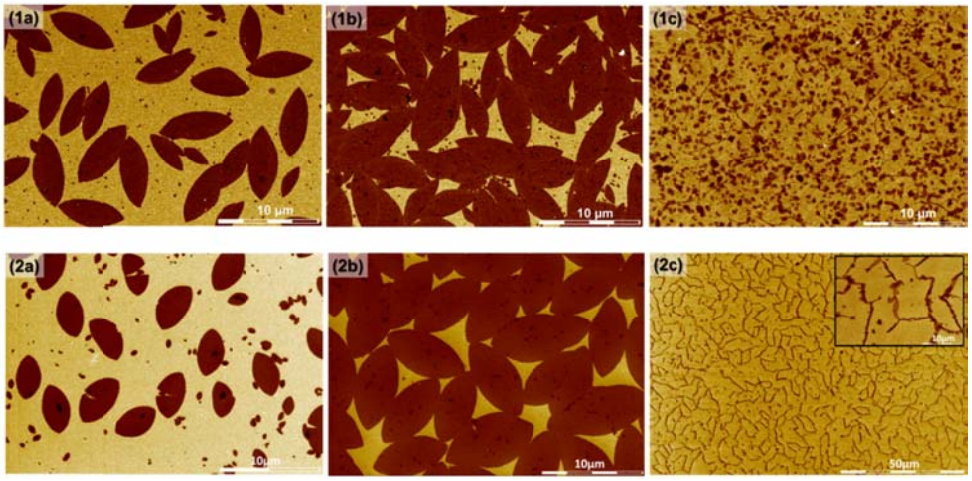

Figure 2. Field-emission scanning electron (FE-SEM) micrographs depict the morphology of **1** and **2** through the growth of a monolayer. (*Top*) Morphology of **1** depending on the concentration: (**1**a) 0.3 g/L, (**1**b) 1.0 g/L, and (**1**c) 1.2 g/L; (*bottom*) Morphology of **2**: (**2**a) 0.3 g/L, (**2**b) 0.7 g/L, (**2**c) 1.0 g/L. Figure **2**c is an image of a monolayer of **2** on a large scale, notice the homogeneity and the relatively large domain sizes. In contrast, **1** forms a monolayer with a high density of grain boundaries. The difference can be appreciated by comparing images of the same scale i.e. the insert of Figure **2**c and Figure **1**c.

The uniform contrast of the elliptic islands seen in the FE-SEM images indicates a homogeneous height distribution of the crystals. As probed with SFM, the height values are slightly different for **1** and **2**. For **1** the height of the islands is about 38 ± 4 Å (**Figure 3- 1a**), for **2** the value is about 35 ± 4 Å (Figure 3- 2b). XRR has the same tendency but gives somewhat larger values of 46.1 and 42.8 Å, respectively (see next section). The difference between SFM and XRR height values can be understood by an oil-like layer on the film/air interface formed by the branched tails. Due to such soft layer the force applied by the SFM cantilever during tapping is sufficient to penetrate the topmost layer, this can be the reason to underestimate the thickness.[36] Reducing the force during tapping causes somewhat larger thickness values, however this effect cannot be eliminated completely due to the softness of the oil-like layer.

For **1** the layer thickness is approximately 1.2 times the molecular length assuming a fully extended linear structure. The difference can be explained by an interdigitated anti-parallel packing arrangement. The branched tails orient alternatively up and down, adhered to a central thiophene sublayer stabilized by strong π-π interactions. For asymmetric molecules this stacking model is energetically favorable due to reducing steric hindrance between branched tails. Meng et al. reported a similar way of packing for asymmetrically substituted quaterthiophene.[24] This model will be further refined in the next section in combination with results from x-ray reflectivity (XRR) and grazing-incidence wide angle x-ray scattering (GIWAXS) data. A model for the structure of the monolayer of compound **2** will be proposed as well.

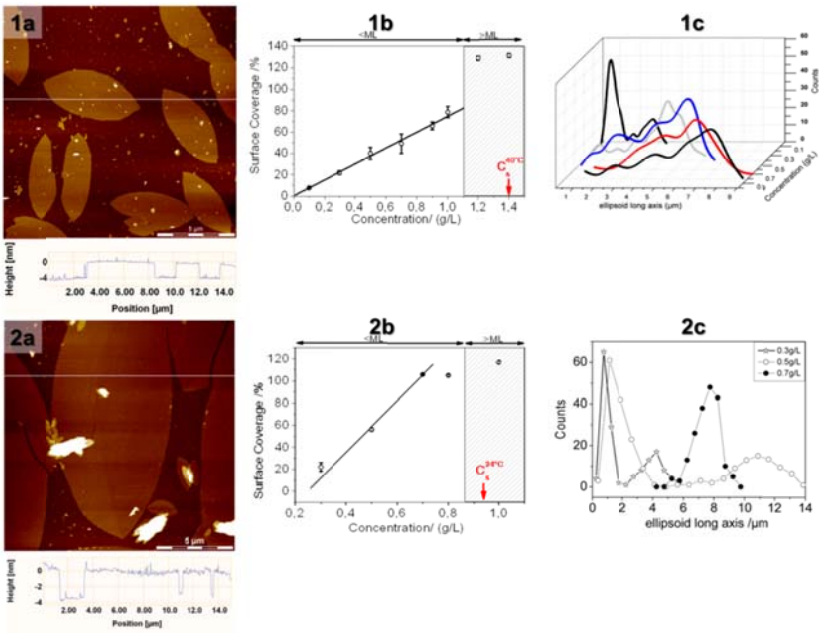

Figure 3. Scanning Force Microscopy (SFM) height image of **1** (1a) and **2** (2a) of submonolayer coverage the graph below each image is a cross section profile along the horizontal line as indicated. Graphs (1b) and (2b) are plots of the surface coverage as function of the solution concentration respectively for **1** and **2**. Cs indicates the concentration and temperature at which the solution saturates. Graphs (1c) and (2c) are the size distribution of the long axis of the elliptical islands depending on the concentration.

As expected, increasing the concentration leads to a larger surface coverage. The monolayer grows linearly with concentration (Figure.3- 1b and 2b). In both cases a

good linear fit is obtained (R^2=0.99). However, the slope of **2** is roughly three times larger than for **1**, indicating a much faster growth of compound **2**. As in **2** the ω position is substituted by a linear C_{11} alkenyl chain whose physical nature is similar to the branched tail, it is less asymmetric than **1**. Therefore any stress induced by the asymmetry will be smaller, packing the molecules will be easier, and the growth rate increases.

Interestingly, the distribution of the long axes of the elliptical crystals is bimodal when deposited from solution at low concentration (Figure 3- 1c and 2c). For **1** at highly diluted solution, the long axes of the two types of islands are 0.8±0.2 μm and 2.8±0.3 μm, respectively. Upon increasing the concentration, both maxima shift to larger values while the smaller islands start to disappear (Figure 3- 1c). Compound **2** starts in a similar way, but at high concentration islands with homogeneous size distribution (centered on 8 μm) are found. Moreover, this peak value is somewhat smaller than the largest size at lower concentration (Figure 3- 2c, circles and filled circles)

Finally, after formation of a complete monolayer, 3D growth is observed in both compounds. However, some details of the 3D layer are different for **1** and **2**. Compound **1** forms 3D layers over the whole area, some of layers follow the direction of grain boundaries in the monolayer (line-like structure in Figure 2- 1c), but most of the layers nucleate and grow on the top of the grains. Compound **2** is different because the 3D crystals develop mainly at the grain boundaries of the monolayers. Line-like structure and the curvature of the lines following the shape of the elliptical domains boundaries can be deduced from (Figure 2- 2c).

3.3.3. X-Ray investigations of the layer structure

X-ray reflectivity (XRR) provides information on the thickness and the electron density profile of the monolayer averaged along the surface normal,[37] which is not directly accessible with SFM and/or FESEM. Figure 4 shows the measured XRR data together with a model fit and the resulting density profile both for compound **1** and **2**. The films have been modeled as a sandwich structure with three sublayers: a middle thiophene layer with the highest electron density between two layers of alkyl substituents with a lower electron density at the silicon/film and the film/air interface. Each sublayer is characterized by three parameters: thickness, electron density and

interface roughness. The thickness and electron density of the native SiO_2 film on the Si wafer were predetermined and kept constant during the fitting process. With this model, good agreement with the experimental data is obtained for the parameters listed in the supporting information (Table S1). The sublayer thicknesses of the alkyl tails at the silicon/film interface and at the film/air interface are close to each other, all about 10 Å. This suggests similar surface structures, presumably consisting of the branched alkyl group. As the thickness is substantially smaller than the length of the chain (about 15 Å), there must be either considerable disorder or a strong tilt. The thicknesses of the central layers are also not very different: 24.0 Å and 23.4 Å for **1** and **2**, respectively, slightly larger than the length of a 6T molecule (about 22 Å).[29] This situation can be contrasted with symmetrically substituted **7T** for which the thickness of the central oligothiophene layer was found to be 20.5 Å, smaller than the length of **7T** itself.[30]

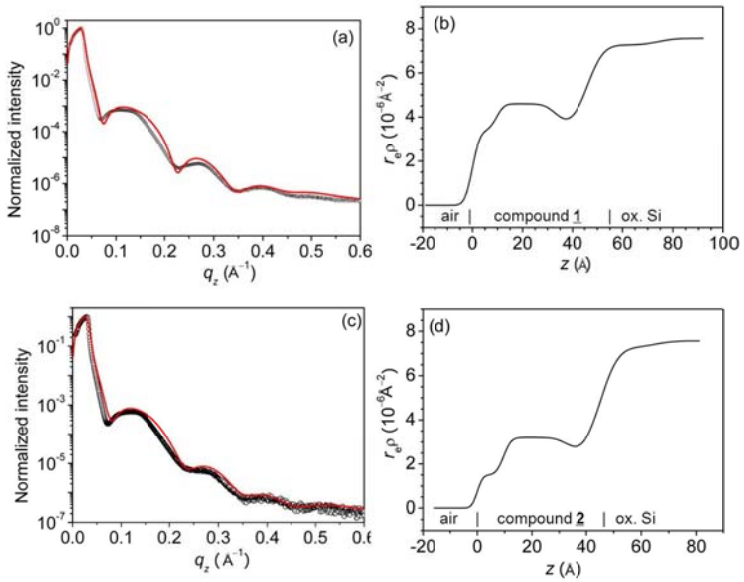

Figure 4. Plots of reflected intensity *vs.* scattering vector q_z and corresponding profiles along the surface normal for films of compound **1** **(R_v-6T-H)** (a, b) and **2** (**R_v-6T-C_{11}**) (c, d). In (a, c) dots are data points while the red curve represents the fit (model details in Table S1). In (b, d) vertically the scattering length density $r_e\rho$ is plotted, in which r_e is the Thomson scattering length and ρ the number density; z is the distance from the film surface.

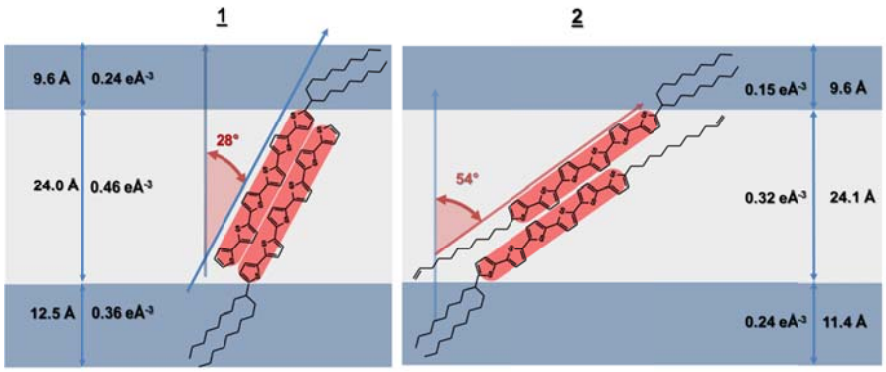

Figure 5. Thickness and electron density of the sublayers as extracted from XRR and possible model interpretation.

In Figure 5 a possible model in presented in which for both compounds the outer layers consist of the bulky branched alkyl chains is presented. For molecule **1** the necessary space required to pack these chains is obtained by interdigitation of the central 6T core which is in agreement with a value of the middle layer thickness larger than the length of 6T. Some tilt must be involved in order to accommodate for the difference in cross sections of the different groups. According to the results from grazing-incidence wide-angle x-ray scattering (GIWAXS) the tilt angle of the 6T core is about 28°. For molecule **2** a similar surface packing of the branched alkyl chains can be obtained if the linear alkyl chains at the other end of the molecules are incorporated in the middle layer. This construction can account for the similar model results for the outer layers. As in **2** the combination linear C_{11}+6T (about 15+22 Å) is considerably larger than only 6T in the case of **1**, the tilt angle in the middle layer must be larger, as confirmed by GIWAXS. In addition, inclusion of the linear alkyl chains in the thiophenes of the middle layer would reduce the electron density of **2** compared to the pure thiophene packing in **1**. This is reflected an overall lower electron density of **2** as observed by XRR.

Though the overall picture from the XRR seems to be reasonable, there are some problems in the details. First the model so far is symmetric. However, for both compounds the bottom layer is somewhat expanded compared to the top layer, in combination with a slightly larger electron density. An obvious solution is to assume that the branched alkyl chain is more stretched and closer packed in the bottom layer, due to the smaller affinity to the SiO_2 substrate as compared to the air interface. Second, the length of a 6T molecule of about 22 Å, would allow the 6T in the middle

layer to organize homeotropically. We conclude that the packing between the central 6T cores depends in a complicated way on the interaction with the branched alkyl chains, which is not fully incorporated in the model.

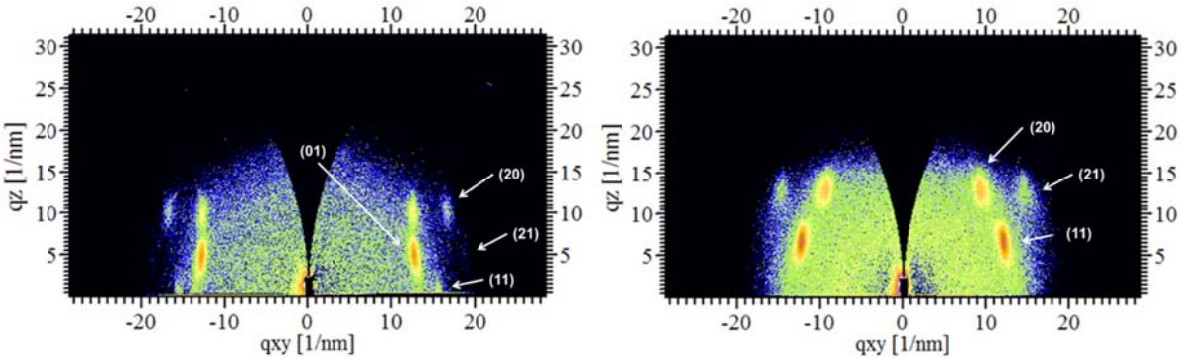

Figure 6. Two-dimensional GIWAXS data of sample **1** (a) and **2** (b), respectively, including the assignment of the various peaks. The peak positions are summarized in Table S2 added to the supplementary information.

To obtain detailed information on molecular ordering of organic molecules such as conjugated polymers or monolayers GIWAXS can be used advantageously especially, the arrangement regarding the substrate is probed by GIWAXS.[38] Two-dimensional GIWAXS data are shown in Figure 6 in reciprocal space with q_z being along the surface normal and q_{xy} in the sample plane. The interpretation of the various peaks - attributed to the packing of the central 6T layer - is also indicated. The outer layers of alkyl chains are expected to be largely disordered and to contribute only to the general background. The general scattering features can be understood in analogy to the interpretation of scattering data of hexagonal Langmuir monolayers of fatty acids by Kaganer et al.[37] However, we assumed a centered rectangular packing with two molecules per unit cell, similar to the known centered orthorhombic structure of oligothiophenes.[38] For compound **1** we calculate from $tan\theta = q_z^{11} \Big/ \sqrt{(q_{xy}^{11})^2 - \left(\frac{1}{2} q_z^{11}\right)^2}$ a tilt angle of 28° and for compound **2** from $tan\theta = q_z^{20} / q_{xy}^{20}$ a value of 54.5°.[37] For **1** the lattice vectors are given by a=7.6 nm and b=9.5 nm, leading to an area per molecule of $a \times b/2$=19 Å^2. For **2** we find in a similar way $a \times b/2$=38.4 Å^2. In agreement with the previous discussion we find that

compound **2** is much looser packed than **1**. Using n= 252, the number of electrons of 6T, and the thickness of the 6T middle layer from XRR, for **1** an electron density of 0.55 $eÅ^{-3}$ can be calculated for **1**. Projected on the layer normal this gives 0.49 $eÅ^{-3}$, in agreement with the electron density of 0.46 $eÅ^{-3}$ from XRR.

For compound **2** the situation is somewhat more complicated. If we use the suggested model of Figure 5b, including the electron density of C_{11} in the middle layer leads to n=252+89=341 electrons. Using again half of the area per unit cell and the thickness of the middle layer from XRR, the electron density would be 0.37 $eÅ^{-3}$. Projected on the layer normal this leads to 0.21 $eÅ^{-3}$, considerable smaller than the value 0.32 $eÅ^{-3}$ from XRR. As a consequence, the model shown in Figure 5b must be oversimplified and thus somewhat too extreme.

We conclude that the X-ray results - including the anisotropy of the GIWAXS peaks not touched upon yet - deserve a more extensive discussion that exceeds the scope of this article and thus will be given elsewhere. For the present purpose the most important result is the GIWAXS provides proof of a tilted ordered 6T core in the center of the monolayer. This structure deviates from earlier results for bulk[38] and thicker layers[36] of substituted oligothiophenes.

3.3.4. UV-Visible Spectroscopy

In Figure 7 the absorption spectra of a monolayer and in solution of molecules **1** and **2** recorded at room temperature are presented. In solution, the position of the strong absorption band is centered on 443 nm (2.79 eV) and it is rather independent on the substituents.[39] The monolayers reveal distinct absorption spectra with an intense band followed by one or two less pronounced shoulders at long-wavelength side. The strong absorption band of molecule **1** is centered on 373 nm (3.33 eV) while for **2**, it is at 422 nm (2.93 eV). Apart from the difference in the absorption maximum, the optical spectra are similar with a blue shift compared to the solvated molecules.[40-42] The shift of the intense peak is determined by the intermolecular coupling strength. Indeed, thin films of unsubstituted sexithiophene in which the long molecular axis is perfectly aligned along the surface normal shows an intense absorption band at 364 nm (3.4 eV) and it is polarized parallel to the long axis of the molecules. Therefore misalignments such as tilting the molecules relative to the surface plane, which is the case here, loosen the packing and reduce the intermolecular coupling causing a red

shift of that band relative to the densest packing.[36] We note that the shoulders at the long wavelength side retain their spectral position. These peaks are found in the optical spectra of sexithiophene irrespective of the substituents and were attributed to the (0-0) transition of an isolated molecule.[39] This observation can account for the absorption spectrum of the monolayer acquired at normal incidence. A red shift with respect the monolayer of **1** is accompanied with enhanced absorption consistent with the structural analysis of the monolayer in which molecule **1** is less tilted and more densely packed than **2** (see above).

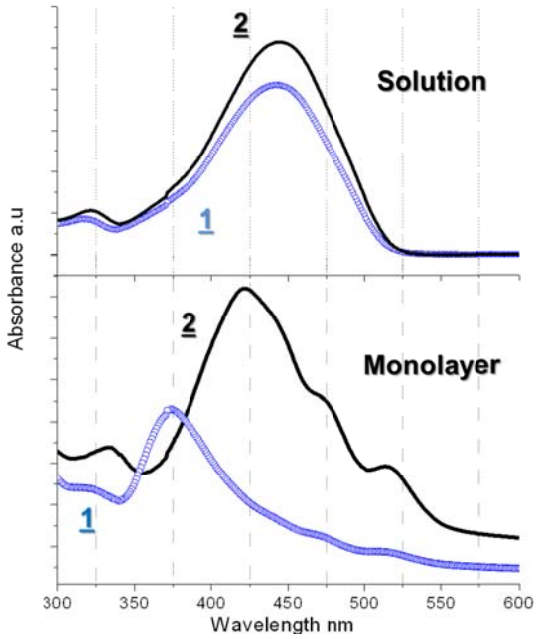

Figure 7. UV/Vis spectra of compound **1** and **2**, in chlorobenzene solution and on a monolayer, recorded at room temperature at normal incidence.

3.3.5. OFET Performance

We investigated the electrical transport of **1** and **2** in monolayer field-effect transistors. The molecules are oriented parallel to each other with the long molecular axes more or less perpendicular to the substrate plane. This configuration is highly favorable for charge transport, because it favors the overlap between π-orbitals.

Transistors were fabricated by spin coating of compound **1** or **2** on electrodes at concentrations that give full monolayer surface coverage. A ring geometry was chosen to prevent parasitic leakage currents. The pristine transistors exhibited very little hysteresis and a mobility of about 3×10^{-3} cm^2/Vs. Scaling of the mobility with

channel length shows only a small contact resistance, which is confirmed by the linear mobility that is comparable to the saturated mobility.

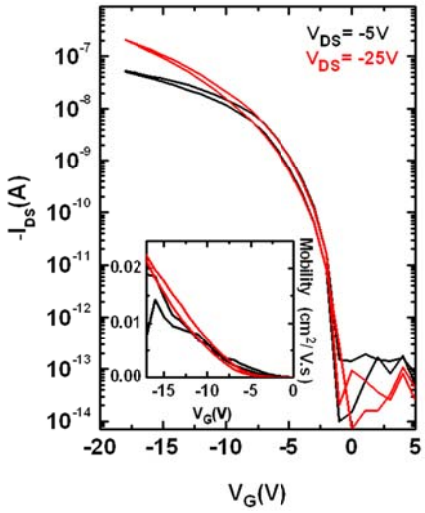

Figure 8. Linear and saturated transfer characteristic of spin-coated monolayer field-effect transistor of compound **2** after annealing for an hour at 140 ^{0}C. The channel length is 40 µm and channel width is 1000 µm. The inset shows the linear and the saturated mobility.

The transistors were subsequently annealed for an hour to remove any residual solvent. Upon annealing at 80 $^\circ$C, the mobility of molecule **1** decreases and a significant increase in contact resistance is observed. There is hardly any change in transfer characteristics for molecule **2.** The transistors were subsequently annealed for an hour at 140 $^\circ$C. The charge transport of the transistors of molecule **1** deteriorates. In most transistors the current was orders of magnitude lower than before annealing. The transfer curve of **2**, presented in Figure 8, shows no hysteresis, a threshold voltage of 0 V and a current modulation of six decades. The inset shows that the linear mobility is equal to the saturated mobility. The value increases with gate bias up to about 1×10^{-2} cm^2/V/s at a gate bias of -20V. The saturated mobility is comparable to the linear mobility. The transport is bulk dominated, the contact resistance can be disregarded. The mobility value of compound **2** is similar to that of 5T monolayer SAMFETs (2×10^{-2} cm^2/V/s) and of 7T spin-coated monolayer (1×10^{-2} cm^2/V/s).

The mobility is thermally activated. The activation energy has been extracted as 80 meV for **1** and 100 meV for **2**. The activation energies are similar to those extracted for a **5T** SAMFET of 80 meV and for a **7T** spin-coated monolayer of around 60-90 meV. The values obtained might indicate that the charge transport in all compounds is limited by grain boundaries.

3.4. Conclusions

We have investigated the electric behavior of monolayers of two new asymmetrically substituted sexithiophene (6T). Both molecules have at one thiophene end a branched alkyl chain. For molecule **1** this is all; molecule **2** the bifunctional 6T has at the other end additionally a linear alkyl chain. In the latter case the asymmetry of the substituents and a mismatch in the cross-sectional area (thiophene/alkyl) induces LC behavior. Growing a monolayer from solution leads to anisotropic domains (ellipsoids) attributed to the asymmetry and bulkiness of the tails. Furthermore full monolayer coverage is achieved before a multilayer starts to develop. This can occur if the interaction adsorbate/substrate is somewhat larger (or comparable) than the intermolecular interactions. This seems to be the case here - at least for the first layer - and is attributed to the end groups decoupling the two-dimensional lateral growth from that perpendicular to the substrate. The thermotropic LC 6T (**2**) forms islands with a monomodal distribution that leads to large monodomain sizes compared to non-LC compound (**1**). This is attributed to the importance of the LC properties near the interface that promote preordering and exchange of molecules between growing domains, thus regulating the domain sizes and their distribution.

XRR and GIWAXS on monolayer samples reveal tilted central thiophene cores. The tilt angle relative to the surface normal is 54° for **2** compared to 28° for **1**. The interfacial constraints and packing requirements cause the formation of a tilted monolayer with loosely packed oligothiophenes. Still the monolayer supports a field-effect mobility as high as found in SAMFET's of 5T or 6T. However, comparing device performance of **1** and **2** the field-effect mobility is substantially lower than in an unsubstituted 6T with small tilt angle.

3.5. References

[1] D. Fichou, *J. Mater. Chem.* **2000**, *10*, 571.

[2] I. F. Perepichka, D. F. Perepichka, H. Meng, F. Wudl, *Adv. Mater.* **2005**, *17*, 2281.

[3] F. Garnier, R. Hajlaoui, A. Yassar, P. Srivastava, *Science* **1994**, *265*, 1684.

[4] B. S. Ong, Y. Wu, P. Liu, S. Gardner, *J. Am. Chem. Soc.* **2004**, *126*, 3378.

[5] S. G. J. Mathijssen, E. C. P. Smits, P. A. van Hal, H. J. Wondergem, S. A. Ponomarenko, A. Moser, R. Resel, P. A. Bobbert, M. Kemerink, R. A. J. Janssen, D. M. de Leeuw, *Nat. Nanotech.* **2009**, *4*, 674.

[6] H. Sirringhaus, T. Kawase, R. H. Friend, T. Shimoda, M. Inbasekaran, W. Wu, E. P. Woo, *Science* **2000**, *290*, 2123.

[7] S. A. Ponomarenko, O. V. Borshchev, T. Meyer-Friedrichsen, A. P. Pleshkova, S. Setayesh, E. C. P. Smits, S. G. J. Mathijssen, D. M. de Leeuw, S. Kirchmeyer, A. M. Muzafarov, *Organometallics* **2010**, *29*, 4213.

[8] B. J. Holliday, T. M. Swager, *Chem. Comm.* **2005**, 23.

[9] H. Röckel, J. Huber, R. Gleiter, W. Schuhmann, *Adv. Mater.* **1994**, *6*, 568.

[10] E. C. P. Smits, S. G. J. Mathijssen, P. A. van Hal, S. Setayesh, T. C. T. Geuns, K. A. H. A. Mutsaers, E. Cantatore, H. J. Wondergem, O. Werzer, R. Resel, M. Kemerink, S. Kirchmeyer, A. M. Muzafarov, S. A. Ponomarenko, B. de Boer, P. W. M. Blom, D. M. de Leeuw, *Nature* **2008**, *455*, 956.

[11] S. Tan, J. Zhai, H. Fang, T. Jiu, J. Ge, Y. Li, L. Jiang, D. Zhu, *Chem. Eur. J.* **2005**, *11*, 6272.

[12] C. D. Dimitrakopoulos, D. J. Mascaro, *IBM J. Res. Dev.* **2001**, *45*, 11.

[13] A. Mishra, C.-Q. Ma, P. Bäuerle, *Chem. Rev.* **2009**, *109*, 1141.

[14] A. Kreyes, S. Ellinger, K. Landfester, M. Defaux, D. A. Ivanov, A. Elschner, T. Meyer-Friedrichsen, U. Ziener, *Chem. Mater.* **2010**, *22*, 2079.

[15] A. R. Murphy, P. C. Chang, P. VanDyke, J. Liu, J. M. J. Fréchet, V. Subramanian, D. M. DeLongchamp, S. Sambasivan, D. A. Fischer, E. K. Lin, *Chem. Mater.* **2005**, *17*, 6033.

[16] P. Leclère, M. Surin, P. Viville, R. Lazzaroni, A. F. M. Kilbinger, O. Henze, W. J. Feast, M. Cavallini, F. Biscarini, A. P. H. J. Schenning, E. W. Meijer, *Chem. Mater.* **2004**, *16*, 4452.

[17] S. Nagamatsu, K. Kaneto, R. Azumi, M. Matsumoto, Y. Yoshida, K. Yase, *J. Phys. Chem. B* **2005**, *109*, 9374.

[18] M. Mas-Torrent, C. Rovira, *Chem. Rev.* **2011**, *111*, 4833.

[19] P. Vlachos, B. Mansoor, M. P. Aldred, M. O'Neill, S. M. Kelly, *Chem. Comm.* **2005**, 2921.

[20] C. Reese, M. E. Roberts, S. R. Parkin, Z. Bao, *Adv. Mater.* **2009**, *21*, 3678.

[21] S. Ellinger, A. Kreyes, U. Ziener, C. Hoffmann-Richter, K. Landfester, M. Möller, *Eur. J. Org. Chem.* **2007**, *2007*, 5686.

[22] M. Surin, P. Leclère, S. De Feyter, M. M. S. Abdel-Mottaleb, F. C. De Schryver, O. Henze, W. J. Feast, R. Lazzaroni, *J. Phys. Chem. B* **2006**, *110*, 7898.

[23] M. Melucci, L. Favaretto, C. Bettini, M. Gazzano, N. Camaioni, P. Maccagnani, P. Ostoja, M. Monari, G. Barbarella, *Chem. Eur. J.* **2007**, *13*, 10046.

[24] Q. Meng, X.-H. Sun, Z. Lu, P.-F. Xia, Z. Shi, D. Chen, M. S. Wong, S. Wakim, J. Lu, J.-M. Baribeau, Y. Tao, *Chem. Eur. J.* **2009**, *15*, 3474.

[25] J. Leroy, N. Boucher, S. Sergeyev, M. Sferrazza, Y. H. Geerts, *Eur. J. Org. Chem.* **2007**, *2007*, 1256.

[26] M. Funahashi, J. I. Hanna, *Adv. Mater.* **2005**, *17*, 594.

[27] S. R. g. González, J. s. Orduna, R. Alicante, B. n. Villacampa, K. A. McGee, J. o. Pina, J. Seixas de Melo, K. M. Schwaderer, J. C. Johnson, B. A. Blackorbay, J. J. Hansmeier, V. F. Bolton, T. J. Helland, B. A. Edlund, T. M. Pappenfus, J. T. López Navarrete, J. Casado, *J. Phys. Chem. B* **2011**, *115*, 10573.

[28] A. Kreyes, M. Amirkhani, I. Lieberwirth, R. Mauer, F. Laquai, K. Landfester, U. Ziener, *Chem. Mater.* **2010**, *22*, 6453.

[29] A. Pizzirusso, M. Savini, L. Muccioli, C. Zannoni, *J. Mater. Chem.* **2011**, *21*, 125.

[30] M. Defaux, F. Gholamrezaie, J. Wang, A. Kreyes, U. Ziener, D. V. Anokhin, D. A. Ivanov, A. Moser, A. Neuhold, I. Salzmann, R. Resel, D. M. de Leeuw, S. C. J. Meskers, M. Moeller, A. Mourran, *Adv. Mater.* **2012**, *24*, 973.

[31] S. Destri, M. Mascherpa, W. Porzio, *Adv. Mater.* **1993**, *5*, 43.

[32] M. Lu, S. Nagamatsu, Y. Yoshida, M. Chikamatsu, R. Azumi, K. Yase, *Chem. Lett.* **2010**, *39*, 60.

[33] E. Barrena, S. Kopta, D. F. Ogletree, D. H. Charych, M. Salmeron, *Phys. Rev. Lett.* **1999**, *82*, 2880.

[34] M. Tolan, *X-Ray Scattering from Soft-Matter Thin Films*, Springer, 1999.

[35] M. A. Ruderer, S. M. Prams, M. Rawolle, Q. Zhong, J. Perlich, S. V. Roth, P. Müller-Buschbaum, *J. Phys. Chem. B* **2010**, *114*, 15451.

[36] B. Servet, G. Horowitz, S. Ries, O. Lagorsse, P. Alnot, A. Yassar, F. Deloffre, P. Srivastava, R. Hajlaoui, *Chem. Mater.* **1994**, *6*, 1809.

[37] V. M. Kaganer, I. R. Peterson, R. M. Kenn, M. C. Shih, M. Durbin, P. Dutta, *J. Chem. Phys.* **1995**, *102*, 9412.

[38] G. Horowitz, B. Bachet, A. Yassar, P. Lang, F. Demanze, J.-L. Fave, F. Garnier, *Chem. Mater.* **1995**, *7*, 1337.

[39] A. Yassar, G. Horowitz, P. Valat, V. Wintgens, M. Hmyene, F. Deloffre, P. Srivastava, P. Lang, F. Garnier, *J. Phys. Chem.* **1995**, *99*, 9155.

[40] D. Oeter, H. J. Egelhaaf, C. Ziegler, D. Oelkrug, W. Göpel, *J. Chem. Phys.* **1994**, *101*, 6344.

[41] K. Hamano, T. Kurata, S. Kubota, H. Koezuka, *Jpn. J. Appl. Phys.* **1994**, *33*, L1031.

[42] D. Oelkrug, H. J. Egelhaaf, J. Haiber, *Thin Solid Films* **1996**, *284–285*, 267.

[43] S. Ellinger, U. Ziener, U. Thewalt, K. Landfester, M. Möller, *Chem. Mater.* **2007**, *19*, 1070.

[44] L. G. Parratt, *Phys. Rev.* **1954**, *95*, 359.

[45] J. Perlich, J. Rubeck, S. Botta, R. Gehrke, S. V. Roth, M. A. Ruderer, S. M. Prams, M. Rawolle, Q. Zhong, V. Körstgens, P. Müller-Buschbaum, *Rev. Sci. Instrum.* **2010**, *81*, 105105.

Chapter 4 Thin Film Structure of Block Copolymer-Surfactant Complexes: Strongly Ionic Bonding Polymer Systems

4.1. Introduction

A distinctive feature of block copolymers (bcp) is their ability to self-assemble into mesophases whose structure and periodicity are defined by the Flory-Huggins Parameter χ, the composition, and the molecular masse of individual blocks.[1-3] This property has been extensively explored to tailor thin films, allowing to generate dense periodic arrays with sub-100 nm features.[4] Such an attribute can be considered as an alternative to e-beam lithography, and has been successfully integrated in manufacturing processes of microelectronic devices such as high-density storage media, plasmonic devices, nanowire polarizer grids, silicon capacitors, etc.[5] The thin films used for these applications require a certain degree of control of the orientational and positional order of the mesostructures.[4, 6] Because of the large interfacial area of thin films, the orientation of the domains depends largely upon the relative surface energies of the blocks as well as -in case of incommensurability- upon the structural frustration between the intrinsic periodicity of the bulk structure and the film thickness.[7] These confinement and surface effects can result in morphologies that are absent in the bulk. [8]

Morphologies of bcp's can be controlled rather well for solution-cast thin films. However, to obtain a uniform orientation of the microdomains normal to the film surface - as required in certain applications - remains a challenge.[4, 6] Strategies have been devised to overcome the surface interactions and induce perpendicular orientation of cylinders or lamellae relative to the substrate.[6, 9] Some success has been achieved through techniques such as solvent annealing,[10] zone casting,[11, 12] electric field alignment,[13] optical alignment,[14] topographical or chemical substrate patterning,[15] and surfactant[16] or nanoparticle-assisted orientational order.[17]

Hierarchical structures with more than one characteristic length scale have been found in copolymers whose macromolecules consist of more than two types of monomer units.[18-22] A well-known example is a copolymer with side chain liquid

crystal (LC) units, wherein ordering of the mesogenes moieties concur with microphase separation. In such a system, the LC field will affect mesophase formation and domain orientation, whereas in thin films thermally stable morphologies can be generated consisting of lamellae or cylinders oriented perpendicular to the surface. [22]

An interesting example of a copolymer with mesogenic side chains is provided by specific interactions between an oligomer or a surfactant and a block of a diblock copolymer. These have been neatly used to generate a variety of mesomorphic structures characterized by two periodic scales (structure-*within*-structure).[23-25] The copolymer self-assembles and sets a large period of about 100 nm, while the LC organization of the surfactant occurs at a much smaller scale of a few nm. The obvious advantage of such bcp-complex systems is that the composition of one of the blocks can easily be adjusted by varying the amount of side chains. An additional peculiarity is that a non-covalent bond of the side groups can be used with a strength variable from very strong (ionic bond), to very weak (hydrogen bond).[26-28] Complexes based on hydrogen bonding are particularly interesting since the binding is thermally reversible, selective and directional.[23, 24] Such interchangeable physical interactions can play a crucial role in the formation of mesophases and in the occurrence of an order-disorder transition.[29] Unlike hydrogen bonds, ionic interactions are stronger and the oligomers are tightly bound to the polymer backbone. Mesostructure based on ionic interactions are thermally stable and in some cases the complex even decomposes before reaching the isotropic phase.[29-33] Surfactants with sulfonic acid head group have been widely combined with poly (vinylpyridine)s.[27, 28, 31-33] In that case the nitrogen in the pyridine ring acts as a weak base and charge transfer takes place from acid to one electron pair. For diblock copolymers, incorporation of sulfonated oligomers such as dodecylbenzene sulfonic acid,[28-30] eventually combined with a wedge-shaped mesogen,[27] resulted in the formation of mesophases with a hierarchical order at two different length scales.

Ionic bonding of a sterically demanding mesogen to a polymer backbone provides an additional degree of control over the macromolecular conformations and their subsequent self-assembly.[27, 32, 33] Recently, we have complexed Poly (2-vinylpyridine) (P2VP) with a wedge-shaped ligand consisting of a sulfonated group at the tip and a large non-polar body.[32, 33] In that situation the contour length of the homopolymer chain defines the shape of the complex (spheres or rods) while the degree of protonation sets the morphology (smectic or columnar). In addition,

incorporation of such a ligand to a miscible diblock copolymer, Poly (2-vinylpyridine-b-ethylene oxide) (P2VP -b- PEO),[34] greatly increases the segregation between blocks.[27] In thin films, smectic ordering of the ligand takes place with the layers that are orthogonal to the block interfaces. This allows effortless alignment of the bcp microstructure, e.g. cylinder or lamellae, perpendicular to the air/substrate interfaces.

In this work we extend the above ideas to ionic bonding of a widely studied surfactant, sodium bis (2-ethylhexyl) sulfosuccinate (AOT), with the diblock copolymer poly (styrene - b- 4-vinylpyridine) (PS-b-P4VP). The solid state structure of pure AOT has been established only recently: it self-assembles in a hexagonal columnar phase with three molecules in a column cross-section.[35] Furthermore, unlike the ligands discussed so far,[23, 26-28, 32, 33] AOT has two branched aliphatic chains that prevents crystallization. The binding strength of the sulfonate head to the pyridine is still essential the same as described above. Furthermore, the bcp-AOT complex does not support uncomplexed ligands because AOT acid form (AOT-H) contains ester groups that are labile (easily cleaved). Consequently, the system bcp-AOT is appealing because it alleviates (1) any difficulties associated with crystallization of the side chains, and (2) the presence of free ligands. Still, the truncated wedge-tail is appropriate to study the impact of steric hindrance on the organization of the bcp-AOT complex.

In the following, we show that protonation of the P4VP homopolymer or the diblock copolymer PS-b-P4VP with AOT leads to a mesomorphic multilayer structure in which the surfactant determines the layer thickness. In thin films the segregation between the blocks generates nanostructures with an in-plane periodicity defined by the molecular masse of the copolymer and by the stoichiometry of the complex. By varying the composition of the blocks and the molar ratio AOT/pyridine, the following structural transitions are observed: cylinders of (AOT/P4VP) → lamellae → PS cylinders. Interestingly, in all morphologies, the bcp microdomain structure stays orthogonal to the air substrate interface. Finally, we show that hydrolysis of AOT results in pores with a variable geometry useful for templating a two-dimensional inorganic structure.

4.2. Experimental section

4.2.1. Materials.

Four PS-b-P4VP diblock copolymers were investigated: PS_{390}-$P4VP_{140}$ (PDI=1.08), PS_{350}-$P4VP_{260}$ (PDI= 1.07), PS_{190}-$P4VP_{100}$ (PDI=1.12), PS_{120}-$P4VP_{50}$ (PDI=1.03), in which the subscript indicates the degree of polymerization of each block. They were synthesized via sequential anionic polymerization, as described elsewhere.[36] Sodium bis(2-ethylhexyl) sulfosuccinate (98%), iodine beads (>99.9), hydrazine hydrate (reagent grade, N_2H_4 50-60%), diisopropyl ether (p.a.), chloroform (p.a.), benzene (p.a.), isopropanol (p.a.), ion-exchange resin (Amberlyst 15, acid form), and Gold(III) chloride hydrate ($HAuCl_4$, p.a., Au ≥ 49%), were purchased from Sigma-Aldrich. Silicon wafers (100) were supplied by Si-Mat GmbH. Copper grids, 200mesh, with silicon oxide coating, and naked copper grins, 100mesh, were supplied by Plano GmbH, Germany.

4.2.2. Polymer complex and thin film preparation.

The procedures for preparation of polymer complex were similar as discussed in a previous paper.[27] 100mg of AOT-Na was dissolved into 10ml of diisopropyl ether and stirred with 1g of Amberlyst 15 for 1h; after this treatment, AOT-Na converted to its sulfonic acid form (denoted as AOT-H) with a yield of ~100%.[31, 33] The desired amounts of P4VP homopolymer or PS-b-P4VP block copolymer were dissolved into chloroform according to the desired degree of neutralization (DN, nominal ratio between AOT-H molecules versus 4-vinylpyridine repeat units). The solution of AOT-H was filtrated through a 1μm PTFE syringe filter, and the ion-exchange resin was washed at least three times with 10 ml of diisopropyl ether. While stirring, the AOT-H solution was added to PS-b-P4VP solution. The total concentration of the mixed solution was controlled to within less than 1mg/ml, and stirred overnight. Subsequently, the solvent was removed by a rotor evaporator at 60°C. The complex was dissolved into chloroform again to make a stock solution of 30 mg/ml.

Silicon wafers or glass substrates were cleaned by sonication in isopropanol for 5 min, dried in an air stream, and activated in UV/O_2 for 12 min. These treatments provided a clean silicon surface with a water contact angle of < 5°. Before spin coating, the stock solution was diluted to the desired concentration and filtered through a 0.2 μm PTFE syringe filter. Thin films of the complexes were prepared by

placing drop of 50 μL onto a cleaned silicon wafer and spin coated at a spinning rate of 2500 rpm for 30s (Convac 1001S, Germany). The film thickness was controlled by the concentration of the solution. All films had approximately the same thickness (300 Å), as determined by ellipsometry (MM-SPEL-VIS, OMT GmbH, Germany). Vapor annealing was performed by exposing the films to saturated benzene vapor in a closed vessel at room temperature. After the solvent annealing, the solvent was allowed to evaporate slowly.

4.2.3. Fabrication of nanoporous film.

Nanoporous film or nano-objects was prepared by washing of the polymer films in 0.33 mol/L NH_3 solution for 30 s. Subsequently, the films were rinsed with MilliQ water and dried in an air stream. Free-standing films were prepared by floating thin film on 0.1mol/L KOH solution, rinsing the film with Milli Q water, and then transferring onto a copper grid.

4.2.4. Gold salts deposition.

To load the complex with gold salts, the polymer film were coated on a glass substrate and immersed into 1 g/L of aqueous $HAuCl_4$ solution for 3 h. Subsequently, the films were thoroughly rinsed with Milli Q water, and dried in an air stream. Reduction of the gold salt was performed by either exposing the film to hydrazine vapor in a closed vessel for 1 min, or in oxygen plasma (Plasma System 100, PVA Tepla AG). Typical conditions were: 100 W, 0.89 mbar, and 30 min.

4.2.5. Thin film characterization.

IR spectra (resolution 4 cm^{-1}) were recorded using a Nicolet NEXUS 670 Fourier Transform IR spectrometer. Samples were prepared by drying several droplets of 30 g/L solution onto KBr plates at room temperature. For each spectrum more than 200 scans were averaged to enhance the signal to noise ratio. The morphology of the film was investigated by a tapping model SFM (NanoScope V, Digital Instruments Veeco Instruments Santa Barbara, CA) under ambient conditions. Commercial available standard silicon cantilevers (PPP-SEIH-W from Nanosensors) with a spring constant of 5~37 N/m and an oscillation frequency of ~125 kHz were used. The data were

processed using NanoScope software Analysis, v-1.10. Transmission Electron Microscopy (TEM) images were acquired using a Zeiss Libra120 with an accelerating voltage of 120 kV. For TEM studies, a droplet of the polymer complex solution was put onto a copper grid. The excess of the solution was absorbed by a filter paper. Subsequently, grids plus sample were annealed in benzene. In order to enhance the contrast the films were stained in iodine vapor for about 2 h. Scanning Electron Microscope (SEM) experiments were performed using a Hitachi S4800 high-resolution Field Emission Scanning Electron Microscope with an accelerating voltage of 1.5kV. The optical properties of the gold patterns on glass support were measured with a JASCO V-610 UV-Vis Spectrometer.

Small and Wide Angle X-Ray scattering was recorded by a powder diffractometer (STADI MP vertical from STOE, Darmstadt, Germany) with a focusing Ge-monochromator (Johansson-type) and a position-sensitive detector. The experiments were performed on flat samples in a transmission geometry. X-Ray Reflectivity (XRR) experiments were performed using a Bruker-Axs D8 Advance. The X-ray intensity was corrected for sample size effects at small incidence angles. The data were analyzed using an iterative matrix formalism derived from the Fresnel equations. During fitting to the multilayer model thickness, electron density, and interface roughness were allowed to vary for each layer.[37] The thickness, electron density, and roughness of the native SiO_2 layer were predetermined from a bare Si wafer and left fixed for the later fits.

4.3. Results and discussions

We first present the results of the FTIR, which substantiate complexation of the pyridine with the sulfonic acid (AOT-H). Second, on the basis of the X-ray scattering data we discuss the impact of the degree of protonation on the bulk organization of the homopolymer and a copolymer. Subsequently, a structural characterization of the different thin films morphologies is presented based on scanning force microscopy and X-ray reflectivity. The discussion ends with a practical example in which the structure has been used to produce a template with pores of defined geometry.

4.3.1. Bulk organization

4.3.1.1. FTIR.

The transformation of AOT-Na to AOT-H, and the formation of the P4VP(AOT) complex have been characterized by FTIR. As shown before,[27, 31, 33] ion-exchange resin is very effective for the preparation of molecules with sulfonic acid group. The yield is very high, close to 100%. Results of FTIR measurements (see Supporting Information, Figure S1) show that AOT-Na has two characteristic peaks at 1051 cm^{-1} and 1247 cm^{-1}, corresponding to symmetric and asymmetric stretching vibrations of SO_3 in the sulfonic acid sodium salt. After stirring with ion-exchange resin for 1 h, these two peaks disappear, while two new peaks appear at 1038 cm^{-1} and 1166 cm^{-1}. These are identified as the symmetric and asymmetric stretching vibration of SO_3 in sulfonic acid. Further increase of the treatment time does not change the spectra, which means that AOT-Na has completely transformed to AOT-H.[38] P4VP and PS-P4VP have an absorption band at ca.1599 cm^{-1}, assigned to the aromatic carbon-carbon stretching vibration of the phenyl group (1600-1601 cm^{-1}), and a carbon-nitrogen stretching vibration of the unprotonated pyridine ring (1596-1597 cm^{-1}).[38] After incorporation of AOT-H, the intensity of the latter band decreases, and a new distinct band corresponding to the protonated pyridine ring appears at 1637 cm^{-1}.[39] Increasing the DN increases the intensity of the later band and decreases the intensity of the one at 1599 cm^{-1}. In addition, a small shift of this band from 1599 cm^{-1} to 1601 cm^{-1} is observed. At DN=1.0, only one band at 1601 cm^{-1} is found corresponding to the aromatic carbon-carbon stretching vibration of phenyl group, indicating that at this condition all the free pyridine rings are protonated. (See Supporting Information, Figure S2-S5) However, quantitative analysis of the FTIR spectra is difficult, because it requires curve fitting while the needed adsorption cross sections of pyridine before and after protonation are unknown. Moreover, for the band at about 1599 cm^{-1}, it is difficult to separate the contribution from the aromatic carbon-carbon stretching vibration of the phenyl group from that of the carbon-nitrogen stretching vibration of the unprotonated pyridine ring.

4.3.1.2. X-ray Scattering.

The X-ray scattering of the fully neutralized homopolymer P4VP(AOT) (DN=1.0) displays in the small-angle region a peak at scattering vector q^*=0.216 $Å^{-1}$, corresponding to a periodicity of 29 Å, and a much weaker second-order one at

q=0.43 Å^{-1}. If the DN is reduced to 0.5, the q*-value shifts to a slightly larger number. Further decreasing the DN does not change the position of the first-order peak, but the second-order one become weaker and vanishes at DN=0.25. In all cases the scattering is rather weak and even at typical measurement times of a couple of hours the intensity is still quite small. This can be attributed to the limited contrast in electron density. The mass densities of AOT and P4VP are 1.13[40] and 1.11 g/cm^3,[41] respectively, and differ only little. In addition we note that the X-ray peak is broader at low DN-values. We fitted the peaks to both a Gaussian and a Lorentzian lineshape. In all cases - apart from DN=1.0 - the Lorenzian fit is significantly better. The corresponding correlation lengths are 22, 25 and 29 Å for DN= 0.5, 0.33 and 0.25, respectively. From these correlation lengths we can conclude that structure extends over a relatively small range. For DN=1.0 a Gaussian fit is somewhat better than a Lorentzian one, which in principle indicates that the corresponding close packing leads to enhanced ordering.

As example of a complexed diblock copolymer the composition PS_{390}-$P4VP_{140}$ (DN=1.0) has been selected. The organization of the $P4VP_{140}(AOT)_{1.0}$ complex in the bcp is very similar as in the corresponding homopolymer, as shown in Figure 1a. The period is slightly larger than that of the corresponding homopolymer-complex. Interestingly the X-ray peak of the block copolymer with DN=1.0 is broader than for the homopolymer. The quality of the data does not allow a full lineshape analysis, but evidently introduction of the PS block leads to some interruption of the order.

The simplest interpretation compatible with the data is a lamellar (smectic) mesophase. However, due to the limited contrast only a faint second-order peak is observed. Hence we cannot fully exclude the presence of weak peaks at other positions like q*√3, which would be evidence of a hexagonal (columnar) structure. Such structures have been observed in related surfactant-polymers complexes.[42] From Figure 1b, the smectic mesophase has a lamellar period $L=2\pi/q^*$ around 28-29 Å for the homopolymer and slightly larger for the block copolymer (around 31 Å). At large angles the scattering data show regardless of the DN a broad peak at q=1.6 Å^{-1}, indicative of liquid-like order inside the smectic layers. Evidently the ligands do not display strong lateral positional correlations.

AOT has a small ionic head group with a diameter of about 5 Å and relatively short (about C6) but bulky hydrocarbon tails of fully stretched length 12 Å.[43] Hence the thickness of a bilayer of free AOT is about 35 Å, which is comparable, but somewhat

larger, than the lamellar period of the homopolymer complex. Evidently the AOT self-assemble into layers with a partial interpenetration of side chains. Furthermore, Figure 1b shows that *L* increases slightly from 28.0 Å for DN = 0.25 to 29.3 Å at full protonation. This behavior differs from conventional LC side chain polymers.[44] In that situation the lateral smectic interactions are dominant and increasing the number of side groups leads to a decrease of the layer spacing due to stretching of the polymer backbone. We assume that in our situation at low degree of protonation the ligand is evenly distributed along a Gaussian conformation of P4VP chains. For high DN, further stretching of the side chains may reduce interpenetration and enhance the inter-smectic order, leading to a slightly larger period. This would compensate for the reduction of *L* due to backbone stretching. The delicate balance of two interacting effects can be expected to depend on the overall morphology. Hence one would not expect *L* to be exactly the same for bcp and homopolymer.

An alternative explanation[30] of the absence of a decreasing smectic period with increased DN - heterogeneity in the complex composition - cannot apply in our situation. As discussed above, in the present case a dynamic complexation equilibrium drives the system to an identical degree of complexation of all polymer chains.[33] Note that any entropic penalty associated with stretching of the P4VP backbone becomes significant only at saturation.[32] Rigorous modeling would require knowledge of the bilayer thickness for ligands including the pyridine salt.

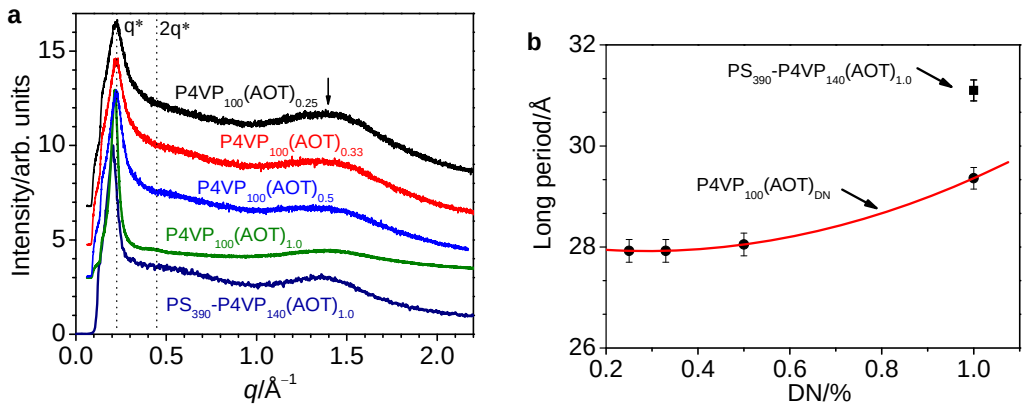

Figure 1. (a) Room temperature WAXS of $P4VP_{100}(AOT)_{DN}$ complex and PS_{390}-$P4VP_{140}(AOT)_{1.0}$. (b) the long period depending on the degree of neutralization (See SI S7 for details).

4.3.2. Thin film morphology

Thin films PS-P4VP(AOT)$_{DN}$ (about 300 Å) with different degree of neutralization were deposited on silicon oxide from a chloroform solution, and annealed in benzene vapor for 24h. The films were optically smooth and homogenous before and after annealing, except for the low molecular weight sample, which started to dewet from the SiO_2 support. Though we focus on thin films, for consistency also thicker films up to three fold the bcp periodicity were checked. No difference in morphology was found.

Table 1. Summarization of the morphology of thin films

bcp	DN	f_{comp} (%)*	Morphology
PS_{390}-$P4VP_{140}$	0	27	*CYL*
	0.25	44	*Mixed*
	0.33	47	*Comp-CYL*
	0.5	54	*LAM*
	1	66	*LAM*
PS_{350}-$P4VP_{260}$	0	51	*LAM*
	0.25	62	*LAM*
	0.33	65	*LAM*
	0.75	76	*LAM*
	1	80	*PS-CYL*
PS_{120}-$P4VP_{50}$	0	30	*CYL*
	0.75	65	*LAM /Comp-CYL*
	1	70	*LAM*
PS_{190}-$P4VP_{100}$	0	0.36	*LAM*
	0.5	64	*LAM/Comp-CYL*
	1	73	*LAM*

$f_{comp} = \frac{N_{P4VP} M_{4VP} + DN N_{P4VP} M_{AOT}}{N_{PS} M_S + N_{P4VP} M_{4VP} + DN N_{P4VP} M_{AOT}}$, where M_{4VP}, M_S, M_{AOT}, are molar masse of 4-vinylpyridine, styrene, and AOT-H, respectively.

Depending on the composition of the bcp(AOT) complex, two morphologies are identified: cylinders of the P4VP(AOT) complex in a matrix of PS for weight fraction f_{comp}=0.45 and the inverse for f_{comp}=0.8, whereas a lamellar structure is observed for $0.55 \leq f_{comp} \leq 0.77$. Interestingly, the lamellae or cylinders are consistently orthogonal to the air/SiO_2 interface.

We shall proceed with a detailed account of the thin films morphology of bcp-complex, in dependence of the degree of protonation and molecular weight. Table 1 summarizes the composition of the studied copolymers: The subscript indicates the degree of polymerization of each block, DN is the degree of neutralization, f_{comp} the weight fraction of the P4VP(AOT), and the last column list the observed thin film morphologies.

4.3.2.1. PS_{390}-$P4VP_{140}(AOT)_{DN}$.

Without AOT the bcp self assembles into a structure with P4VP cylinders parallel to the SiO_2/air interface. The bcp-complex is different, Figure 2 depicts the film morphology depending on mass fraction of the $P4VP(AOT)_{DN}$. For a weight ratio of 44% of the complex, three structures coexists "sphere"-like or "cylinder", lamellae and, featureless domain in between (Figure 2a). Most likely, the low degree of protonation leads to structures with different orientations relative to the surface plane. For higher weight ratios, *i.e.* 47%, a hexagonally ordered structure evolves with a mean spacing of 420 Å (c.f. Figure 2b). The mass ratio suggest cylinders of the P4VP(AOT) complex embedded in a PS matrix. Two observations support this assumption: the cylinders exhibit a well-defined depth of 25 Å, inferred to the organization of the $AOT(P4VP)_{0.33}$ complex. The absence of steps with a height commensurate with the bcp periodicity suggests a perpendicular orientation of the cylinder relative to the substrate plane. Furthermore, increasing the weight fraction of the complex to 54% leads to interconnected lamellae with few P4VP(AOT) cylinders normal to the substrate plane. For this bcp, the highest weight fraction of the complex is 66% corresponding to DN=1.0. In that case the lamellar structure is preserved while contour length and branching are reduced. This is clearly seen by comparing the surface morphology of 54% in Figure 2c and 66% in Figure 2d. The average height distribution indicates that the lamellae or cylinders have a fairly well-defined surface profile of 24 ± 5 Å (cf. cross-section profile, and SI S8).

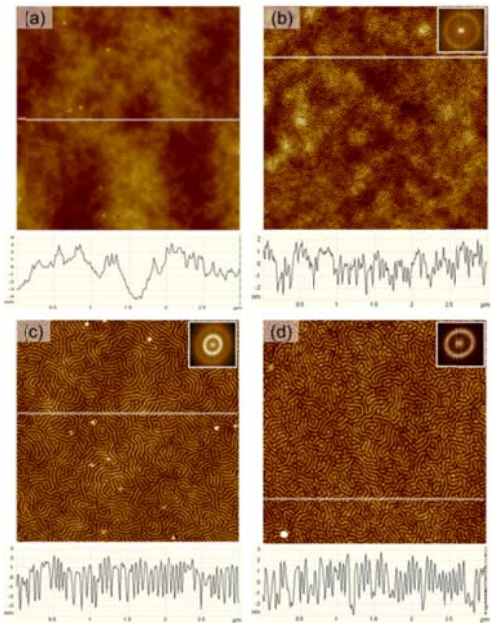

Figure 2. AFM height images of PS_{390}-$P4VP_{140}(AOT)_{DN}$ (a) weight fraction of the $P4VP(AOT)_{0.25}$ is f_{comp}= 0.44 in this case each fourth 4VP monomer is protonated DN=0.25; (b) correspond to f_{comp}= 47% and DN=0.33; (c) correspond to f_{comp}= 54% and DN=0.5; (d) correspond to f_{comp}= 66% and DN=1.0. The average periodicity assessed from the power spectral density over 3x3 μm^2 was 420 Å, 470 Å and 500 Å, for DN= 0.33, 0.5, and 1.0, respectively. The scan size is 3×3 μm^2, and the graph below each image is a cross section profile along the horizontal line as indicated.

WAXS data indicate for the 100% protonated copolymer a smectic structure with a period of about 31 Å. This bulk period is somewhat larger than the depth of the surface profile. The difference may be due to the indenting force of the SFM probe which reduces the height. Thus, the surface profile is the result of a layer structure of P4VP (AOT) at the air / film.

4.3.2.2. PS_{350}-$P4VP_{260}(AOT)_{DN}$.

The bcp, without AOT forms lamellae parallel to the air/SiO_2 interface. The surface morphology of such films often shows islands or holes with a depth commensurate with the bcp periodicity.[1] This is not case for the present bcp-AOT complex. SFM investigations summarized in Figure 3 show that, regardless of the fraction of the complex, the films display an in-plane periodicity without holes or islands. This suggests that the bcp microdomains are orthogonal to the air/SiO_2 interface. Increasing the weight fraction of the complex from 60% to 76% affects mainly the

connectivity between the lamellae. This can be appreciated qualitatively by comparing Figure 3a or 3b to 3c in which the numbers of junction between lamella and their contour length are reduced. Further increasing of the complex weight fraction to 0.8 leads to hexagonally ordered isolated dots, which we assign to PS cylinder embedded in P4VP(AOT)$_{1.0}$ layer (Figure 3d). The common feature is the height distribution, which shows a well-defined depth of 24 ± 5 Å (cf. cross-section profile and S8). Interestingly, this value is somewhat smaller than *L* the bulk period. Thus, again this observation enforces the peculiar organization of P4VP(AOT)$_{1.0}$ at the air/film surface (see X-ray reflectivity section below).

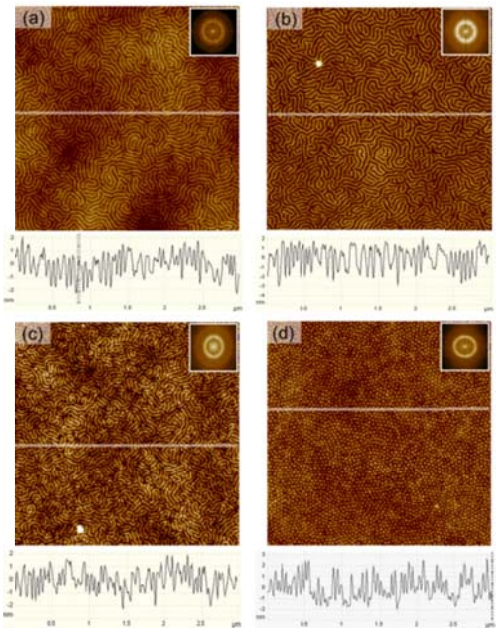

Figure 3. AFM height images of PS$_{350}$-P4VP$_{260}$(AOT)$_{DN}$; (a) corresponds to f_{comp}= 0.6, in this case each fourth 4VP monomer is protonated DN=0.25; (b) corresponds to f_{comp}= 65% and DN=0.33; (c) corresponds to f_{comp}= 76% and DN=0.75; (d) corresponds to f_{comp}= 80% and DN=100%. The average periodicity assessed from the power spectral density over 3x3 μm^2 is 490 Å, 510 Å, 470 Å, 460 Å, for DN=0.25, 0.33, 0.75, and 1.0, respectively. The scan size is 3×3μm^2, and the graph below each image is a cross section profile along the horizontal line as indicated.

4.3.2.3. PS$_{120}$-P4VP$_{50}$(AOT)$_{DN}$.

Irrespectively of the AOT composition, these films of low molecular masse are unstable and dewet upon vapor annealing (cf. Figure 4). Because the weight fraction of P4VP in the neat bcp is 30%, P4VP forms cylinders embedded in a PS matrix. In

thin films, the surface structure starts to evolve only for weight fractions of the complex above 64%. Below this value the films exhibit a localized structure which might indicate mixed orientation (not shown). The bcp with 64 % of the complex shows an ill-defined morphology, it might be coexisting lamellae and cylinder, but it is difficult to assign. The phase image indicates that the system is microphase separated with an average period of 290 Å. A higher weight fraction of the complex of ca. 70% leads to a lamellae structure orthogonal to the SiO_2/air interface. The structure has a mean periodicity of 250 Å.

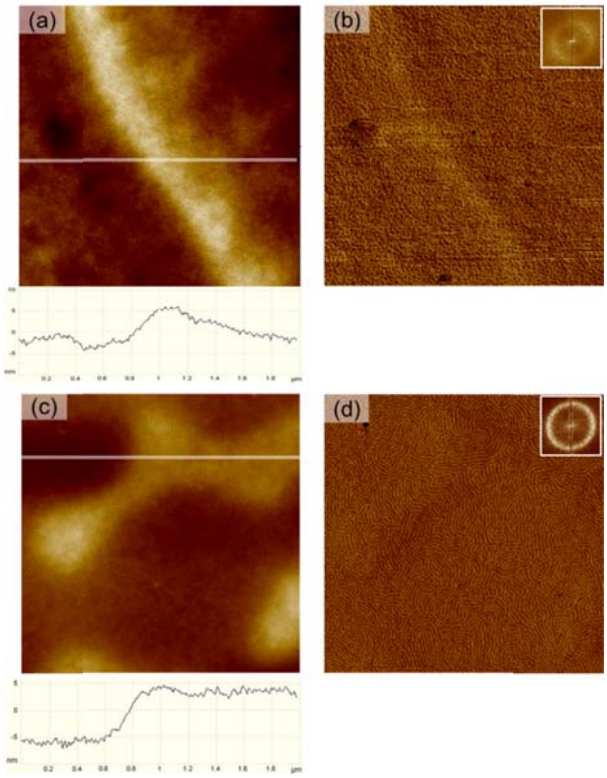

Figure 4. Height and phase SFM images of PS_{120}-$P4VP_{50}$(AOT) (a) topography and (b) phase for a bcp-complex with weight fraction of 64% equivalent to protonation of three 4VP unit out of four i.e. DN=0.75; (c) topography and (d) phase for f_{comp}= 70% and DN=1.0. The scan size is 2×2 μm^2, and the graph below each image is a cross section profile along the horizontal line as indicated.

4.3.2.4. PS_{190}-$P4VP_{100}$(AOT)$_{DN}$.

This composition shows a lamellae structure, but the total molecular weight is almost twice as low as the previous bcp PS_{350}-$P4VP_{260}$. If the weight fraction of the complex is smaller than 63%, the surface morphology exhibit localized structures

coexisting with a featureless layer. Most likely this indicates a mixed orientation. Ordered structures evolve only at 63% weight fraction of P4VP(AOT), for which the dominant structure is lamellae coexisting with cylinders (cf. Figure 5a). Rather well-defined lamellae with improved ordering are observed for 73 wt% (cf. Figure 5b). In contrast to previous films, the surface profile is smooth, suggesting a specific organization of P4VP(AOT) complex. This observation will be discussed in more detail in the next section.

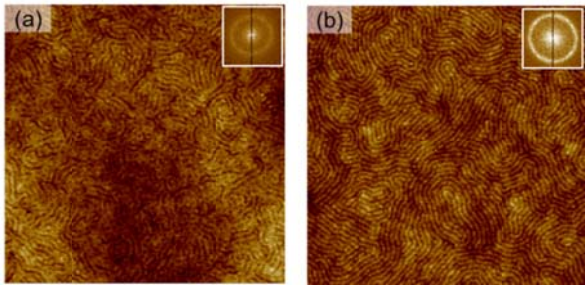

Figure 5. AFM height images of PS_{190}-$P4VP_{100}(AOT)_{DN}$; (a) corresponds to f_{comp}= 63% in this case each second 4VP monomer is protonated DN=0.5; (b) correspond to f_{comp}= 73% and DN=1.0. The average periodicity assessed from the power spectral density over 2x2 μm^2 is 380 Å, 300 Å, for DN=0.5, and 1.0, respectively. The scan size is 2×2 μm^2.

4.3.3. Intermediate conclusions

To elucidate the influence of interfacial constraints on the surface structure, let us first consider the surface energy of each component in the system. Both pyridine and AOT have a high affinity for the silanol groups present at the surface of silicon oxide.[45, 46] On the other side, at the air interface, PS and AOT have a similar critical surface tension, γ_{PS} ~ 33 mN/m;[47] γ_{AOT} ~ 34 mN/m,[48] which ensures non-selective wetting of the air interface. To exclude any effect related to the confining interfaces,[8, 49] thicker films have also been studied. Up to threefold the block copolymer periodicity the surface structure turns out to be identical regardless of thickness (see SI, Figure S9). Second, WAXS provides clear evidence of bulk mesomorphic behavior of the P4VP(AOT) complex. Furthermore, the in-plan periodicity and the cross-section profile assessed by SFM imply smectic organization of the AOT-complex orthogonal to the PS interface. Finally, the question arises whether the

layering persist over the film depth. This issue has been addressed by X-ray reflectivity (see below).

Regarding the structural transition of the bcp-complex, we note that, a comb architecture requires more space compared to a coil, which tends to curve the interface away from the comb region. For the present bcp-AOT complex, the comb blocks form cylinders at a nearly symmetric mass fraction i.e. f_{comp}=45%. A cylindrical phase for such a composition is unusual. In bulk, for a copolymer with a symmetric composition, curving of the interface requires a conformational asymmetry of the blocks.[50] In principle, steric stiffening due to complexation provides such a conformational asymmetry that may introduce spontaneous curvature.[51] However, incorporation of AOT will also reduce the interfacial tension and thus the effective interaction parameter between PS/P4VP(AOT).[52, 53] In summary, steric stiffening may induce extra P4VP stretching which is partly compensated by lowering the interfacial tension at the coil/comb interface. In our experiments, the lamellae of the high molecular mass bcp-complex show a remarkable connectivity and short contour lengths. This suggest that it is energetically favorable (less costly) to curve the interface to create junctions between the lamellae. We attribute this behavior to a balance between interfacial tension reducing the interfacial area between the blocks and chain stretching favoring domains of uniform thickness in order to avoid packing frustration. However, at present, it is neither clear how effectively the surfactant (AOT) reduces the incompatibility between the blocks, nor to what extend it affects the conformational asymmetry between P4VP(AOT) and PS. Furthermore, our observations were made for thin films, in which additional interfacial interactions come into play.

4.3.4. X-Ray Reflectivity.

The XRR intensities for two representative morphologies, PS cylinders and lamellae, are shown in Figure 6a and b, respectively, as function of the scattering vector q. The Kiessig fringes at low q-values correspond to the total film thickness which is similar for both samples: 299 Å for the cylindrical forming bcp-complex (a) and 276 Å for the lamellar forming one (b). For the first sample (Figure 6a) the solid line represents a fit to a three-layer model leading to the density profile shown in the

inset. The essential elements are an ordered top and bottom layer of high density and a homogenous middle layer. Two aspects are remarkable. First, inclusion of a separate bottom layer is essential to fit the change in slope of the reflectivity curve around q=0.2-0.3 Å^{-1}. The additional top layer has a minor influence on the quality of the fit and its incorporation hardly affects the conclusions from the model. Second, replacing the homogeneous middle layer by a stack of layers of alternating density (smectic period), does hardly improve the quality of the fit. In fact the two densities converge to very close values with a small difference that cannot be considered to be significant within the given accuracy. Hence we conclude that no conclusive evidence for smectic layers parallel to the substrate is found. Given the small density contrast between P4VP and AOT (as also concluded from the bulk X-ray intensities), this cannot be considered as evidence of the absence of such a structure. The dense bottom layer with a thickness of ca. 12 Å is assigned to a monolayer of predominantly comb-like P4VP(AOT). The comb polymer is forced (constrained) to be ordered on the substrate surface, with polar parts contacting SiO_2 and alkyl tails oriented towards the bulk of the sample. The thickness of the bottom and top layer are commensurate with the bulk smectic period and also in agreement with the height profile from SFM. Films of other compositions with a lower DN have been also measured by XRR. The results are very similar to Figure 6a and the analysis shows that regardless the film morphology the data can be rationalized with the model described above for DN=1.0.

We now come to Figure 6b, describing the block copolymer PS_{190}-$P4VP_{100}(AOT)_{1.0}$ with a low molecular weight, which behaves somewhat differently. Similar as in Figure 6a the slope of the curve changes in the q range of 0.2-0.3 Å^{-1}, leading again to an adsorbed bottom layer in the model. However, in addition, irregular changes of the fringes occur in the same region. To fit this part of the curve now a stack of alternating layers is required, representing smectic ordering of the $P4VP(AOT)_{1.0}$ complex parallel to the substrate. The full model requires an absorbed bottom layer, ten smectic layers parallel to the substrate, and a special 'top stack' of two layers. The results are listed in Table 3. The smectic layer period is 25.9 Å, close to the bulk value, and the thickness of the adsorbed bottom layer is again about half the smectic period. The top layer is clearly different from that of the previous block copolymer with high molecular weight. The resulting two separate top layers are somewhat ill defined, while each of the two layers has a thickness close to half the smectic period. They are needed to fit the rather gradual decrease of electron density

upon approaching the air interface. The model agrees with the results of AFM that indicate a fuzzy morphology without well-defined height values of the smectic system.

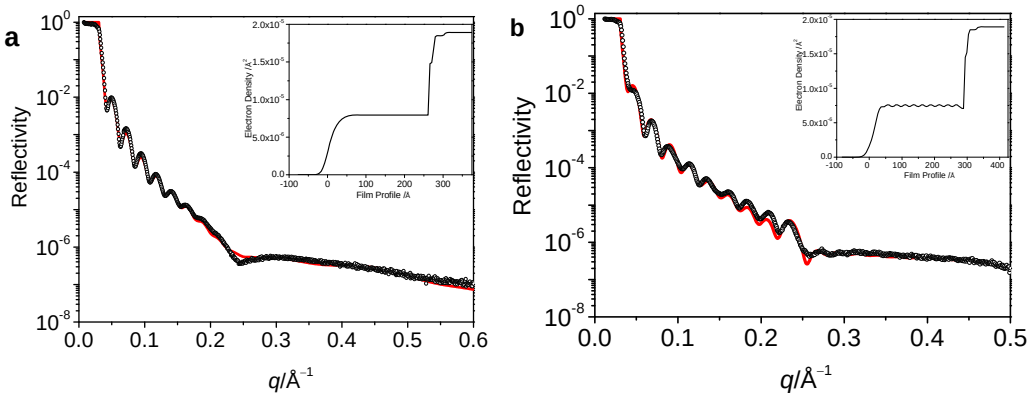

Figure 6. XRR intensity plotted as function of the scattering vector *q*. (a) PS_{350}-$P4VP_{260}(AOT)_{1.0}$ (PS cylinder) and (b) PS_{190}-$P4VP_{100}(AOT)_{1.0}$ (lamellae). The solid red lines are fits to the data points using a three layer model for (a) and a multilayer stack for (b). The inset gives the fitted density profiles normal to the substrate. The results of the fits are summarized bellow in Table2 and 3.

Table 2. Structural details inferred from the fit of XRR data of film of PS_{350}-$P4VP_{260}(AOT)_{1.0}$.

Model	Thickness/ Å	Roughness/ Å	Electron density/ eÅ^{-3}
Top layer	26.5	12.4	0.19
Middle layer	237	19.9	0.29
Bottom layer	12.2	0.1	0.54
SiO_2	29	2.6	0.66

Regarding the difference between Figure 6a and 6b, we note that in general in smectic block copolymers the smectic layers have a tendency to be perpendicular to the block interfaces.[22] Due to the comb geometry this situation leads to a natural continuity of the backbone polymer at the block interfaces. For films of PS_{190}-$P4VP_{100}(AOT)_{1.0}$ (Figure 6b) this situation is realized with PS lamellae along the film normal. For the other case of Figure 6a any orientation of smectic layer is unclear as discussed above.

Table 3. Layered structure details of PS_{190}-$P4VP_{100}(AOT)_{1.0}$ from fitting the XRR data.

Model		Thickness/ Å	Roughness/ Å	Electron density/ eÅ^{-3}
Top layer		15.5	12.4	0.12
Second layer		12.2	7.4	0.19
Smectic	layer 1	7.8	7.9	0.30
layer stack	layer 2	18.1	7.5	0.25
Bottom layer		11.9	0.1	0.52
SiO_2		29	2.6	0.66

4.3.5. Templating from PS-P4VP$(AOT)_{DN}$.

The present complexes with low a molecular weight surfactant allow controlled orientation of microdomains structures, which may provide ideal templates. Indeed, the selective dissolution of AOT with NH_3 solution allows to generate porous polymer films. Three morphologies, PS cylinder, lamellae, and P4VP/AOT cylinder have been selected to demonstrate the process. Figure 7 shows the film structures after simple dipping the samples for 30s in a NH_3 solution.

For films in which the complex forms cylinders in a PS matrix, dissolution of the AOT lead to ca. 200 Å cylindrical pores connecting the two side of the film (cf. Figure 7a). Stripping the film from the Si support gives freestanding films that can be transferred on a bare TEM cupper grid. Figure 7b shows the TEM image, in which the contrast is reversed compared to unwashed sample (Supporting Information, S10). This indicates that the cylinder cores have a lower electron density compared to the situation before NH_3 treatment. Similarly for a lamellae morphology, dissolution of AOT leads to interconnected lamella or a labyrinth-like structure (cf. Figure 7c). The insert in Figure 7c confirms the orthogonal orientation of the lamellae relative to the SiO_2/air interface. For films in which the complex constitutes the continuous matrix, dissolution of AOT leads to PS pillars (cf. Figure 7d). The insert in Figure 7d shows an area where the film has been scratched mechanically to inspect the profile of pillar. Because polystyrene is glassy, the hydrolysis of AOT does not affect the periodicity of the structures. Therefore any change in the inter-polystyrene structure is

exclusively associated with a contraction (collapse) of the P4VP chains. For a given morphology such as pillars, we can estimate a contraction of the chains of about 65%.

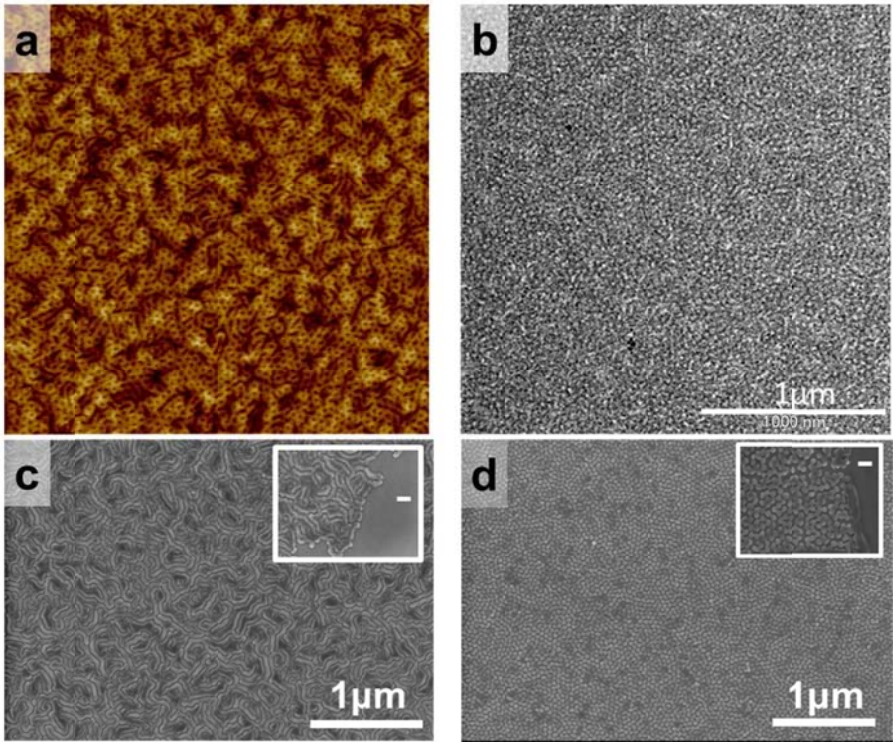

Figure 7. Morphology of PS-P4VP(AOT) complex thin films after NH_3 solution washing: (a) AFM topography the scan size is $3\times3\mu m^2$ and (b) TEM images of PS_{390}-$P4VP_{140}(AOT)_{0.33}$; (c) FESEM image of PS_{390}-$P4VP_{140}(AOT)_{0.5}$; (d) FESEM image of PS_{350}-$P4VP_{260}(AOT)_{1.0}$ The inset is a magnified view with a scale bar representing 100 nm.

It is interesting to note that the P4VP chains are bounded to the glassy PS and the properties of the nanostructure is pH sensitive.[54] In addition, other functionalities can be easily introduced by incorporating other species, susceptible to specifically interact with P4VP chain such as, anionic dyes [55]or inorganic salts, as illustrated below.

If films of PS-P4VP$(AOT)_{DN}$ are immersed in a aqueous solution of $HAuCl_4$, the P4VP is protonated and forms a complex with auric acid $AuCl_4^{-1}$ ions through coordination and electrostatic interaction.[56] This allows a high amount of gold precursor to be incorporated. Subsequently, treatment of the sample with O_2 plasma converts the salt to gold while striping-off the polymer templates. This results in a well-defined array of gold dots.

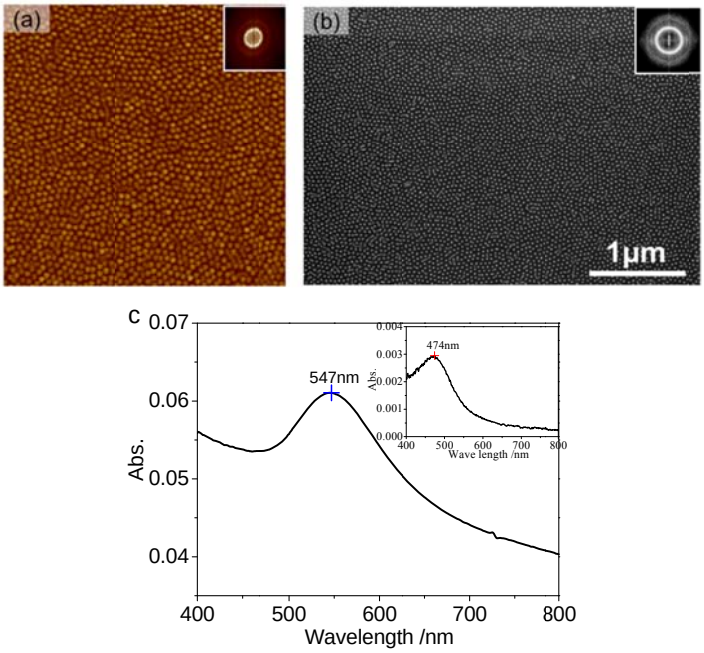

Figure 8. Morphology and optical properties of gold patterns from PS-P4VP(AOT) supramolecular template: (a) AFM and (b) SEM images of gold dots prepared by templating PS_{390}-$P4VP_{140}(AOT)_{0.33}$; (c) UV-Vis spectra of the gold patterns, the insert shows the SPR peak of gold with a diameter of ca.100 Å and a periodicity of ca. 800 Å prepared through solution loading of gold salt-block copolymer micelles.[57] The scan size of the AFM image is 2×2 μm^2.

Figure 8 shows a two-dimensional pattern of gold dots obtained after plasma treatment. AFM and SEM micrographs (Figure 8a and b) allows to assess the regularity and uniformity of the pattern. The gold dots have an average periodicity of about 440 Å, with a mean diameter and height of about 200 Å, and 300 Å, respectively. However, if one takes the radius of the AFM tip into account (~ 100 Å), the diameter of the gold dots is of the order of 100 Å, in agreement with the size inferred from SEM micrographs. Accordingly the pattern consists of gold pillars with an aspect ratio of ~3. Additional information might be gained by recording the surface plasmon resonance (SPR) of such an array. Figure 8c shows the UV-Vis spectra of the gold dots prepared on a glass substrate. The pattern displays a pronounced SPR peak around 547nm. Spherical gold nanoparticles with a diameter of 100 Å made from PS_{1350}-$P2VP_{400}/HAuCl_4$ [57]on a glass substrate have an SPR peak at 474nm. The red shift of 70nm is most likely due to the size increase of gold nanoparticles. If a

lamellae morphology is loaded, removal of the polymer and reduction the gold yield interconnected gold nanoparticle (see SI, Figure S11).

4.4. Conclusions

In the solid state AOT–sodium salt is known to form a hexagonal columnar phase. Ionic bonding of AOT-acid and monomers of a P4VP backbone retains the mesomorphic properties. However, instead of a columnar phase, $P4VP(AOT)_{DN}$ complexes form a layered smectic structure. Formation and stability of the complex is provided by a large heat of protonation that overcomes the elasticity of the chain. The steric requirements of the complex impose a comb-like chain structure.

Incorporation of AOT in a diblock copolymer PS-b-P4VP has a minor effect on the smectic structure. However, incompatibility between the blocks drives the system to microphase separate. In such a situation, the degree of neutralization determines the morphology of the blocks and alleviates the interfacial constraints present in thin films. This allows to generate lamellar or cylindrical structures whose orientation is perpendicular to the air/substrate interface.

Thin films of the complex can be used as template for nanofabrication. Various structures like gold rods or nanowires can be made via simple post loading method and plasma treatment or gold-bcp hybrid films can be made via simple loading without any additional treatments.

4.5. References

[1] I. W. Hamley, *The Physics of Block Copolymers*, Oxford University Press, Oxford, U.K. 1998.

[2] L. Leibler, *Macromolecules* **1980**, *13*, 1602.

[3] F. S. Bates, G. H. Fredrickson, *Annu. Rev. Phys. Chem.* **1990**, *41*, 525.

[4] I. W. Hamley, *Prog. Polym. Sci.* **2009**, *34*, 1161.

[5] H. C. Kim, S. M. Park, W. D. Hinsberg, *Chem. Rev.* **2010**, *110*, 146.

[6] A. P. Marencic, R. A. Register, *Annu. Rev. Chem. Biomol. Eng.* **2010**, *1*, 277.

[7] M. J. Fasolka, A. M. Mayes, *Annu. Rev. Mater. Res.* **2001**, *31*, 323.

[8] A. Knoll, A. Horvat, K. S. Lyakhova, G. Krausch, G. J. A. Sevink, A. V. Zvelindovsky, R. Magerle, *Phys. Rev. Lett.* **2002**, *89*, 035501.

[9] S. Sakurai, *Polymer* **2008**, *48*, 2781

[10] S. H. Kim, M. J. Misner, T. Xu, M. Kimura, T. P. Russell, *Adv. Mater.* **2004**, *16*, 226.

[11] C. Tang, A. Tracz, M. Kruk, R. Zhang, D.-M. Smilgies, K. Matyjaszewski, T. Kowalewski, *J. Am. Chem. Soc.* **2005**, *127*, 6918.

[12] C. Tang, W. Wu, D.-M. Smilgies, K. Matyjaszewski, T. Kowalewski, *J. Am. Chem. Soc.* **2011**, *133*, 11802.

[13] T. Thurn-Albrecht, J. Schotter, G. A. Kästle, N. Emley, T. Shibauchi, L. Krusin-Elbaum, K. Guarini, C. T. Black, M. T. Tuominen, T. P. Russell, *Science* **2000**, *290*, 2126

[14] Y. Morikawa, S. Nagano, K. Watanabe, K. Kamata, T. Iyoda, T. Seki, *Adv. Mater.* **2006**, *18*, 883.

[15] S. O. Kim, H. H. Solak, M. P. Stoykovich, N. J. Ferrier, J. J. de Pablo, P. F. Nealey, *Nature* **2003**, *424*, 411

[16] J. G. Son, X. Bulliard, H. Kang, P. F. Nealey, K. Char, *Adv. Mater.* **2008**, *20*, 3643.

[17] Y. Lin, A. Boker, J. He, K. Sill, H. Xiang, C. Abetz, X. Li, J. Wang, T. Emrick, S. Long, Q. Wang, A. Balazs, T. P. Russell, *Nature* **2005**, *434*, 55.

[18] C. Osuji, Yuanming Zhang, G. Mao, C. K. Obe, E. L. Thomas, *Macromolecules* **1999**, *32*, 7703.

[19] M. Anthamatten, P. T. Hammond, *J. Polym. Sci. Part B: Polym. Phys.* **2001**, *39*, 2671

[20] I. W. Hamley, V. Castelletto, Z. B. Lu, C. T. Imrie, T. Itoh, M. Al-Hussein, *Macromolecules* **2004**, *37*, 4798

[21] E. Verploegen, T. Zhang, Y. S. Jung, C. Ross, P. T. Hammond, *Nano Lett.* **2008**, *8*, 3434

[22] W. de Jeu, Y. Séréro, M. Al-Hussein, *Adv. Polym. Sci.* **2006**, *200*, 71.

[23] O. Ikkala, G. ten Brinke, *Science* **2002**, *295*, 2407.

[24] J. Ruokolainen, R. Mäkinen, M. Torkkeli, T. Mäkelä, R. Serimaa, G. t. Brinke, O. Ikkala, *Science* **1998**, *280*, 557.

[25] W. van Zoelen, E. Polushkin, G. ten Brinke, *Macromolecules* **2008**, *41*, 8807.

[26] W. van Zoelen, T. Asumaa, J. Ruokolainen, O. Ikkala, G. ten Brinke, *Macromolecules* **2008**, *41*, 3199.

[27] K. Albrecht, A. Mourran, X. Zhu, T. Markkula, J. Groll, U. Beginn, W. H. de Jeu, M. Moeller, *Macromolecules* **2008**, *41*, 1728.

[28] H.-L. Chen, J.-S. Lu, C.-H. Yu, C.-L. Yeh, U.-S. Jeng, W.-C. Chen, *Macromolecules* **2007**, *40*, 3271

[29] M. Gopinadhan, E. S. Beach, P. T. Anastas, C. O. Osuji, *Macromolecules* **2010**, *43*, 6646.

[30] O. Ikkala, J. Ruokolainen, G. ten Brinke, M. Torkkeli, R. Serimaa, *Macromolecules* **1995**, *28*, 7088.

[31] X. Zhu, B. Tartsch, U. Beginn, M. Möller, *Chem. – Eur. J.* **2004**, *10*, 3871.

[32] K. Albrecht, M. Gallyamov, X. Zhu, M. Moeller, *Macromol. Chem. Phys.* **2007**, *208*, 1409.

[33] X. Zhu, U. Beginn, M. Möller, R. I. Gearba, D. V. Anokhin, D. A. Ivanov, *J. Am. Chem. Soc.* **2006**, *128*, 16928.

[34] C.-L. Yeh, T. Hou, H.-L. Chen, L.-Y. Yeh, F.-C. Chiu, A. J. Müller, N. Hadjichristidis, *Macromolecules* **2011**, *44*, 440.

[35] G. Ungar, V. Tomašić, F. Xie, X.-b. Zeng, *Langmuir* **2009**, *25*, 11067.

[36] P. Eibeck, Vol. PhD, University of Ulm, Ulm 1999.

[37] M. Tolan, Ed. *X-Ray Scattering from Soft-Matter Thin Films*, Springer Berlin / Heidelberg, 1999.

[38] G. Socrates, *Infrared and Raman Characteristic Group Frequencies*, John Wiley & Sons, 2004.

[39] H. Kosonen, S. Valkama, J. Ruokolainen, M. Torkkeli, R. Serimaa, G. t. Brinke, O. Ikkala, *Eur. Phys. J. E* **2003**, *10*, 69.

[40] O. Ghosh, C. A. Miller, *J. Phys. Chem.* **1987**, *91*, 4528.

[41] J. E. Mark, *Polymer Data Handbook*, Oxford University Press, 1999.

[42] S. G. Starodubtsev, T. V. Laptinskaya, A. S. Yesakova, A. R. Khokhlov, E. V. Shtykova, K. A. Dembo, V. V. Volkov, *Polymer* **2010**, *51*, 122.

[43] E. Y. Sheu, S. H. Chen, J. S. Huang, *J. Phys. Chem.* **1987**, *91*, 3306.

[44] R. Napolitano, B. Pirozzi, *Makromol. Chem.* **1986**, *187*, 1993.

[45] W. R. Birch, M. A. Knewtson, S. Garoff, R. M. Suter, S. Satija, *Colloid Surf. A: Physicochem. Eng. Asp.* **1994**, *89*, 145.

[46] J. P. Spatz, M. Möller, M. Noeske, R. J. Behm, M. Pietralla, *Macromolecules* **1997**, *30*, 3874.

[47] A. Zisman W, in *Contact Angle, Wettability, and Adhesion*, Vol. 43, AMERICAN CHEMICAL SOCIETY, 1964, 1.

[48] E. F. Hare, W. A. Zisman, *J. Phys. Chem.* **1955**, *59*, 335.

[49] Y. Tsori, D. Andelman, *Eur. Phys. J. E* **2001**, *5*, 605.

[50] F. S. Bates, G. H. Fredrickson, *Macromolecules* **1994**, *27*, 1065.

[51] F. S. Bates, M. F. Schulz, A. K. Khandpur, S. Forster, J. H. Rosedale, K. Almdal, K. Mortensen, *Faraday Discuss.* **1994**, *98*, 7.

[52] E. Polushkin, G. O. R. Alberda van Ekenstein, M. Knaapila, J. Ruokolainen, M. Torkkeli, R. Serimaa, W. Bras, I. Dolbnya, O. Ikkala, G. ten Brinke, *Macromolecules* **2001**, *34*, 4917.

[53] I. Vukovic, S. Punzhin, Z. Vukovic, P. Onck, J. T. M. De Hosson, G. ten Brinke, K. Loos, *ACS Nano* **2011**, *5*, 6339.

[54] S. P. Nunes, R. Sougrat, B. Hooghan, D. H. Anjum, A. R. Behzad, L. Zhao, N. Pradeep, I. Pinnau, U. Vainio, K. V. Peinemann, *Macromolecules* **2010**, *43*, 8079.

[55] R. Křenek, V. Cimrová, M. Stamm, *Macromol. Symp.* **2008**, *268*, 86.

[56] J. P. Spatz, A. Roescher, S. Sheiko, G. Krausch, M. Möller, *Adv. Mater.* **1995**, *7*, 731.

[57] R. Glass, M. Arnold, J. Blümmel, A. Küller, M. Möller, J. P. Spatz, *Adv. Fun. Mater.* **2003**, *13*, 569.

Chapter 5 Specific Interaction Induced Precise Deposition of Gold Nanorods on Supramolecular Block Copolymer Thin Film

5.1. Introduction.

Block copolymer/nanoparticle composites attract intensive attention because of their interesting properties and various potential applications.[1-6] The ability to organize the nanoparticles into ordered 2D arrays greatly extends the range of the nanoparticle-based nanocomposites. Depending on the composition and molecular weight of the block copolymer, and the Florry-Hygenious interaction parameters, block copolymers spontaneously organize into long range ordered periodic nanoscale structures with a variety of promising morphologies (e.g., lamellae, cylinders, and spheres),[7] providing suitable template to direct the 2D nanoparticle assemblies.[5] In order to control the selectivity of the nanoparticles toward one of the blocks, the surface properties of the nanoparticles or block copolymer thin films need to be carefully tuned to introduce some interactions (i.e., chemical forces, hydrophobic/hydrophilic interaction), and some successes have been achieved in the literature.[8-13] The driving forces are mainly chemical interaction and capillary forces, and the nanoparticles are introduced *via* co-assembly of nanoparticles/block copolymer,[14-16] *in situ* synthesis,[17] and post loading.[12, 18, 19] For example, Son *et al.* reported a simple method to control the location of the nanoparticles on block copolymer thin film.[12] The topographical contrast of the block copolymer is enhanced by surface reconstruction of the thin films in selective solvent. By combination of the surface topography and capillary force, various types of nanoparticles and nanorods can be incorporated into grooves selectively, the particles oriented along the block copolymer grooves, and the anisotropic shape of the nanoparticles can enhance the alignment of the particles.

Another important issue in nanoparticle/block copolymer composite thin film is the controlling of the orientation of the microdomains of block copolymers, for which the vertical orientation is required. However, the strong preferentially interaction of one block with substrates and air interface leads to the parallel orientation of the

microdomains.[7] Various methods are developed to achieve vertical orientation of the block copolymer microdomains.[20-22] Liquid crystalline ordering (LC field) can also be used to direct the vertical orientation of the microdomains. In such a system, the LC field will affect mesophase formation and domain orientation, whereas in thin films thermally stable morphologies can be generated consisting of lamellae or cylinders oriented perpendicular to the surface.[23-25] Recently it has been shown that block copolymer/small molecular mesogens complex[26, 27] *via* secondary interactions can also be used to control the vertical orientation of the microdomains.[28-31] In thin films, smectic ordering of the ligand takes place with the layers that are orthogonal to the block interfaces. This allows effortless alignment of the block copolymer microstructure, e.g. cylinder or lamellae, perpendicular to the air/substrate interfaces.

To date, most of the researches about block copolymer/nanoparticles are concentrated on spherical particles,[12, 16, 19, 32] and the size of the particles are mostly less than that of the size of block copolymer domains,[33] less attention has been paid to the block copolymer/nanorods,[12, 14, 18, 34] although it has particular importance. The difficulty comes from the anisotropic shape of the nanorods, especially when the sizes of both of the longitudinal and transverse directions are comparable to that of block copolymer domain size.[12, 14, 18, 34]

Gold nanorods are especially attractive because of its anisotropic profiles, which introduced unique optical properties. Two different resonance modes are observed: longitudinal SPR and transverse SPR corresponding to resonance parallel and perpendicular to the long axis, respectively.[35] The longitudinal SPR always locates at the region closed to that of near infrared region, and it can be finely tuned as a function of aspect ratio, the distance between two particles, the size, and the physical environment. In addition, gold nanorods also have the ability to assemble into aligned configurations, a property, which gives rise to optical anisotropies that provided useful to a number of potential applications.

In this paper we describe a new way to direct the assembly of the gold nanorods on the surface of the block copolymer thin films. The thin film templates are prepared from poly (styrene-b-4-vinyl pyridine)/Aerosol OT complex (PS-P4VP $(AOT)_{DN}$, *DN* denoted the molar ratio between pyridine units and sulfonic acid group). The morphology and orientation of the block copolymer thin films are directed by the hierarchical ordering of the block copolymer/ mesogen complex. The ligand can be washed out in a basic solution, without disturbing the nanostructure. Such a porous

template is perfect for the directing the assembly of the poly (ethylene glycol) (PEG) coated nanorods. The selectivity between the nanoparticles and blocks is tuned by the specific interaction between P4VP/PEG, and the orientation of the nanorods in the template is controlled by the morphology of the templates. This method circumvents the unexpected aggregation of the nanorods, leading to high surface coverage of the gold nanorods in the thin film.

5.2. Experimental section.

5.2.1. Sample preparation.

The procedures for the preparation of the block copolymer thin films are reported elsewhere. (Chapter 4) Generally, the thin films were spin casted from 0.6wt% of PS_n-$P4VP_m(AOT)_{DN}$ (n, m and *DN* are the degree of polymerization of PS, P4VP and molar ratio of AOT/pyridine, respectively) chloroform solutions under 2000rpm, annealed in benzene vapor for 24h, washed in 0.3mmol/L NH_3 water solution for 30s, and thoroughly rinsed with MilliQ water for several times, dried with compressed air. The treatment did not change the morphology of the block copolymer thin film, but removed the AOT, and made the P4VP exposed to the surrounding environment. The thickness of films used in this research is 30nm, and three block copolymer templates are used: vertically oriented cylindrical holes from PS_{390}-$P4VP_{140}(AOT)_{0.33}$, the diameter of the hoes is 25±2nm, the period is 41nm; PS_{390}-$P4VP_{140}(AOT)_{0.5}$, vertically oriented lamellae holes, the width of the P4VP domains is 18±1nm, and the period is 47nm; and PS_{710}-$P4VP_{340}(AOT)_{0.5}$, vertically oriented lamellae, the width of the P4VP domains is 28±1nm, and the period is 71nm. The PEG modified gold nanorods are prepared in our lab, and the details are published elsewhere.[36] The molecular weight of the PEG is 3000, and the end groups are varied to obtain different surface properties. The properties of these nanorods are listed in Table 1.

The nanorods are loaded into the block copolymer template via spin coating or adsorption. The spin coating (Convac 1001S, Germany) are done by putting a drop of the gold nanorods solution on the thin film after removing of the AOT, the speed is 2000rpm and time is 60s. The adsorption is done by immersing the polymer thin films into the gold nanorods solution for desired time, after that taking the film out, washing thoroughly in MilliQ water immediately, and dried with compress air.

Table 1. Properties of the gold nanorods[36]

Surface Modification	Dimension L×D nm	Aspect Ratio	Zeta Potential /mv	I_{LSPR}/I_{TSPR}
CTAB	50×15	3.3	+49.6	/
PEGCOOH			-23.2	2
$PEGNH_2$			+21.3	2
PEGOH			-4.5	3
PEGOH	65×13	5.2	-6.1	15

5.2.2. Sample characterization.

Scanning Force Microscope (SFM) was performed on a tapping model SFM (NanoScope V, BrukerAXS) under ambient condition. Commercial available standard silicon cantilevers (POINTPROBE FM-W, Nanoworld) with a spring constant of ~2.5 N/m and an oscillation frequency of ~75 kHz were used. Field Emission Scanning Electron Microscope (FESEM) experiments were performed on a Hitachi S4800 high resolution Field Emission Scanning Electron Microscope with an accelerating voltage of 1 or 1.5kV. The films were without any coating of metal, which may generate artifacts. FESEM image analysis was processed with a freeware, Image J (1.38X). As showed in Figure 1, the images were firstly smoothed in order to reduce the noise, manually threshold to define the area interested, and then binary and integrated. The adsorption of the gold nanorods in thin films was measured with a JASCO V-610 UV-Vis Spectrometer (JASCO GmbH, Germany). Thin films on glass were used, and the illuminated area is about 10×8mm.

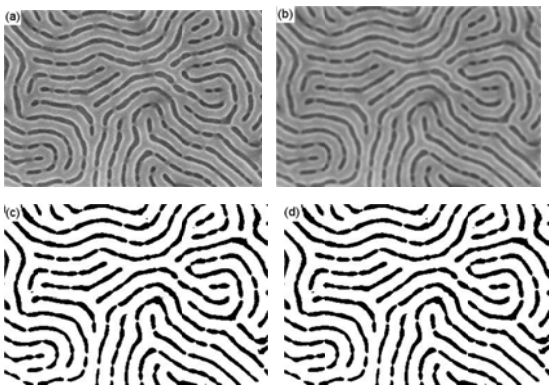

Figure 1. Represented image process: (a) original image; (b) smoothed; (c) threshold; and (d) binary.

5.3. Results and discussions.

5.3.1. Effects of post loading methods.

The chosen of the deposition technology is crucial step to realize the selective deposition of the nanorods. We firstly try with the spin coating technology, which gets great success in the literature.[5] However, in our case this method does not work out. As showed in Figure 2a, no selectivity towards to PS or P4VP is observed, the nanorods randomly spread over the whole area investigated by FESEM. Although the depth of the P4VP domains is around 30nm, and the diameter of the nanorods is less than that of the width of P4VP domains, the capillary force is still not enough to drive the loading of the nanorods into the gap during the spin coating process. In this case, another method, which is called site specific adsorption method, is employed. We know that the PEG/P4VP is fully miscible because of the special interaction between PEG/P4VP.[31] If the block copolymer films with P4VP domain are immersed into the solution containing PEG modified particles, the particles are expected to adsorb onto P4VP domains because of the specific interaction. As showed in Figure 2b, we achieve great success with this method. After dipping the same film into the same solution for 30 min, the PEGOH coated nanorods selectively adsorb onto P4VP domains. The selectivity towards to P4VP is ~100%, enlarged view of the sample shows that the nanorods self-assembly on the P4VP domains, its longitudinal direction orients parallel to that of the lamellae (Figure 2b, insert picture). The 3D view of SFM topographical image (Figure 2c) proves that almost all of the nanorods submerge into P4VP gaps. In this method we can exclude the contribution of the capillary force, since the loaded samples are rinsed immediately after they are taken from the solution: all of particles which are not adsorbed are removed immediately. The only driving force is the specific interaction between PEG/P4VP, which is probably hydrogen bond.[31]

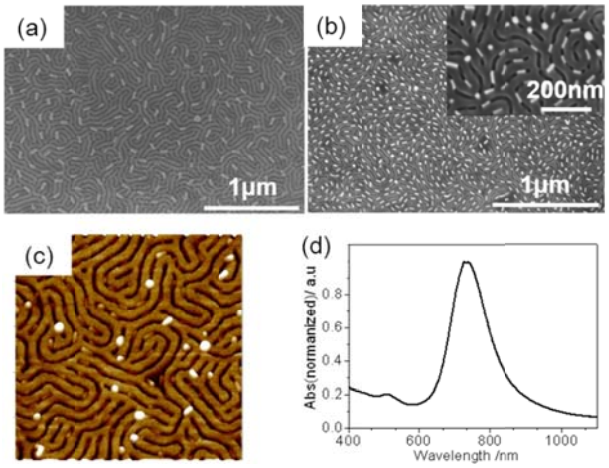

Figure 2. Morphology of PS_{390}-$P4VP_{140}(AOT)_{0.5}$ thin films loaded with PEGOH modified gold nanorods: (a) spin coating technology; (b) adsorption technology, insert picture is the enlarge view; (c) 3D topographical image, scan size 1×1μm; and (d) optical properties of the PEGOH modified gold nanorods on PS_{390}-$P4VP_{140}$; aspect ratio 3.3.

Another interesting thing is the selectivity of P4VP domains toward the spherical particles and nanorods. Limited amount of spherical particles is observed by FESEM and SFM, in strongly contrast to that of the mother solution, where ~30% of spherical particles is expected, indicating that nanorods adsorb onto that of the P4VP domains preferentially than that of the spherical particles. This is supported by UV-Vis spetra of the gold naoparticles loaded thin films. The optical property of the adsorbed nanorods is the change of the intensity ratio between the longitudinal (I_{long}) and transverse (I_{trans}) SPR peaks. The I_{long}/I_{trans} of the adsorbed nanorods is 7, which is larger than that of the nanorods in water (I_{long}/I_{trans} =3, data extrapolated from literature[36]), indicating more nanorods adsorb. This can be understood by the size effects. For our process, it is reasonable to expect that the adsorption/de-adsorption of the particles on the template take place at the same moment. When the polymer template is immersed into the solution, both of the spherical particles and nanorods can absorb onto it. The diameter of the spherical particle is around 30nm, which is much larger than that of the width of the P4VP domains, and the diameter of the nanorods is around 15nm, which is smaller than that of the block copolymer domains. When the particles adsorb onto the template, the nanorods can diffuse into the P4VP domain deeper, because it is smaller than that of the gap and larger contact area between PEG/P4VP can be achieved, which is energy favourable. However, the

spherical particles can adsorb onto the P4VP domains but cannot diffuse into the P4VP domains, since they are larger than that of the P4VP gap size. This is supported by the SFM, which showed that the nanorods come deeper into the P4VP gap, but the spherical particles are only on the surface. Therefore de-adsorption of the spherical particles is faster than that of nanorods.

5.3.2. Effects of surface modification of gold nanorods.

Another possible factor is the surface property of the gold nanorods. By changing of the end group of PEG, gold nanorods with same aspect ratio but with different functional group and surface charge can be fabricated easily.[36] The morphology of the template adsorbed with gold nanorods with different functionality is shown in Figure 3. The original CTAB coated gold nanorods have no adsorption on the template even after a long immersion time (5h), which can be ascribed to two reasons, the first reason is the missing of interaction between CTAB/P4VP, and the other is that the free CTAB in the solution adsorb onto PS-P4VP when the thin film is immersed into the solution, this adsorption layer blocks the adsorption of nanorods on the template. The $PEGNH_2$ coated nanorods is strong positively charged, and the amino group has no interaction with P4VP. It can selectively adsorb onto P4VP domains, (Figure 3b) with its longitudinal direction parallel to that of the lamellae wall, and the nanorods connect with an end-to-end configuration inside the P4VP domains. The surface coverage is estimated to be 31.8±5.5%. The PEGOH coated nanorods are weakly negatively charged, and the hydroxyl group has weak interaction with P4VP, which enhances the adsorption of the gold nanorods on P4VP. Surprisingly, the adsorption of the PEGOH modified nanorods does not show clear difference compare with $PEGNH_2$ coated nanorods (Figure 3c), similar orientation of nanorods in the P4VP domains with similar surface coverage (30.2±2.3%) are observed. This surface coverage is higher than that of the same gold nanorods with short immersion time (Figure 2b), indicating that the adsorption is strongly time dependent, which will be discussed in detail later in this paper. The adsorption can be enhanced if strong interaction is introduced, *i.e.* strong hydrogen bonging between carboxylic group and pyridine units.[37] As shown in Figure 3d and e, multilayer adsorption is observed in PEGCOOH coated nanorods with same immersion time. The gold nanorods lose the orientation towards to that of the lamellae wall, although

all of them still selectively go to P4VP domains. (Figure 3e). Well oriented nanorods pattern from this type of gold nanorods can be obtained, if the immersion time is reduced (*i.e.* 5min), the surface coverage is 30.1±1.0% (Figure 3f), which is closed to that of the same template immersed into $PEGNH_2$ and PEGOH modified nanorods solution for 80min.

It is very important to clarify the situation of P4VP in the nanorods solution. Changing of the surface functionality of the nanorods surface might change the pH value of the solution, too, which influences the status of the P4VP domains. P4VP is a polyelectrolyte, which responses to the pH of the solution. It is reported that the isoelectric point of P4VP is about pH=4,[38] it is positively charged and swollen if the pH is <4, and above that value the P4VP domains is neutral and clasped. In our case, it is extremely difficult to determine the pH values of the gold nanorods with different surface functionality, because of the disturbance of colour coming from the gold nanorods. It is estimated that the pH of all of the solutions used in this study is estimated to be close to 6-7, because the solution is extremely diluted (<1mg/ml), indicating that in all of the cases, the P4VP are clasped, which is supported by in-situ SFM, no changes are observed between the dry PS-b-P4VP thin films and PS-b-P4VP thin films in the nanorods solution (results not shown here). Therefore we can conclude that the specific interaction between the PEG/P4VP is the crucial driving force for directing the assembly of the nanorods. The end group of the PEG can enhance the adsorption if strong interaction is introduced, but this is not the crucial condition in the process.

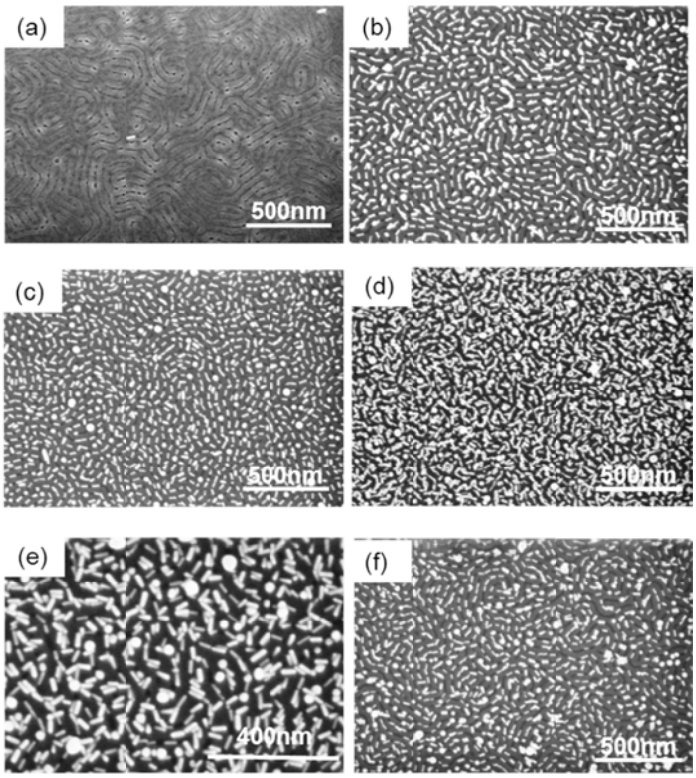

Figure 3. Morphology of PS_{390}-$P4VP_{140}(AOT)_{0.5}$ thin films loaded with gold nanorods modified with: (a) CTAB, 5h; (b) $PEGNH_2$, 80min; (c)PEGOH, 80min; (d) PEGCOOH, 80min, (e) enlarged view of (d); and (e) PEGCOOH, 5min; aspect ratio 3.3.

Last important issue is the selectivity of P4VP toward to that of nanosphere and nanorods. In all of the areas investigated, limited amount of nanophsere is observed, the ratio between the sphere/nanorods is much lower than that of the solution (~30%,[36]), indicating that in respect of the end group and surface charge, the P4VP has clearly selectivity to that of nanorods, which most probably comes from the size confinement effect. This size confinement effect is also believed to be the origin of the end-to-end configuration observed by FESEM. The width of the P4VP gap is 18nm, therefore the maximum deviation angle of the longitudinal direction from the lamellae wall is estimated to be 20°. In addition, such kind of end-to-end configuration and parallel alignment of the nanorods to that of the lamellae wall leads to the maximum contact area between PEG and P4VP, which maximized the interaction between PEG/P4VP. It also limits the number of the nanorods adsorbed on one side, only one nanorod is allowed to adsorb onto one domain.

5.3.3. Effects of P4VP domain size.

The size of the P4VP domains, especially the width of the P4VP, influences the adsorption of the gold nanorods. In this case, another template based on PS_{710}-$P4VP_{340}$ $(AOT)_{0.5}$ is used, the width of the P4VP domain is about 28nm, which is about 2 times of the diameter of the gold nanorods. The results of $PEGNH_2$ or PEGCOOH modified nanorods on this template are shown in Figure 4. As can be seen, similar to situation on the PS_{390}-$P4VP_{140}$ $(AOT)_{0.5}$ (Figure 3b), both of the nanorods can selectively adsorb onto P4VP domains in the template from PS_{710}-$P4VP_{340}$ $(AOT)_{0.5}$, the P4VP domains can be covered totally with the nanorods, depended on the immersion time and surface modification. The difference mainly comes from the configuration of nanorods inside the P4VP domains. On PS_{390}-$P4VP_{140}$ $(AOT)_{0.5}$ only an end-to-end configuration is observed for $PEHNH_2$ modified nanorods, but it is versatile on PS_{710}-$P4VP_{340}$ $(AOT)_{0.5}$. On some areas, the end-to-end configuration is observed, the nanorods follow the direction of the lamellae wall, but also other configurations, such as side-to-side or tilted end-to-end configurations, are also observed. Because of the strong interaction between the PEGCOOH and P4VP, the adsorption is fast, and a full coverage of the PEGCOOH modified nanorods has been achieved during the same immersion period, in general the longitudinal direction of the nanorods is parallel to the direction of the lamellae wall. High resolution FESEM image shows that in each domain the gold nanorods organize into buddle with the side-to-side configuration, these buddle structures assemble onto the P4VP domains and follow the direction of the lamellae with an end-to-end configuration. The gold nanorods form monolayer on the template, no second layer is observed in the deeper part of the template (Figure 4e).

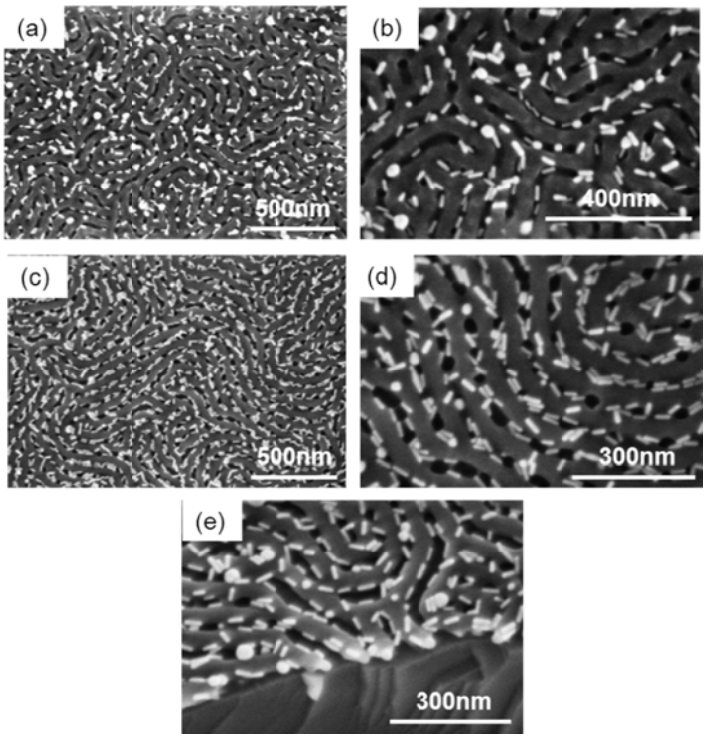

Figure 4. Morphology gold nanorods with different coatings on PS_{710}-$P4VP_{340}(AOT)_{0.5}$ thin films (a) $PEGNH_2$; (b) enlarged view of (a); (c) PEGCOOH; (d) enlarged view of (c); (e) FESEM cross-section view of (c), 45°; aspect ratio 3.3, 80min.

5.3.4. Effects of the aspect ratio of the nanorods.

Figure 5 shows the results of PEGOH coated gold nanorods with an aspect ratio of 5.2 assembled on the block copolymer thin films. As can been seen, this gold nanorods have the similar behavior like that of the nanorods with an aspect ratio of 3.3. It selectively adsorbs onto the P4VP domains in the thin films, the nanorods take the end-to-end configuration, and the longitudinal axis of the nanorods oriented parallel to that of the lamellae wall. The difference between the nanorods on two different polymers is that locally a side-to-side configuration is observed on the template of PS_{710}-$P4VP_{340}(AOT)_{0.5}$, and this side-to-side aggregated nanorods go to the P4VP domains, and with their longitudinal axis parallel to that of the lamellae wall.

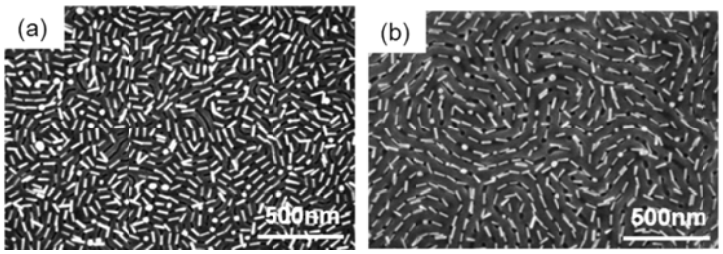

Figure 5. Morphology gold nanorods coated with PEGOH on thin films template (a) PS_{390}-$P4VP_{140}$ $(AOT)_{0.5}$; (b) PS_{710}-$P4VP_{340}$$(AOT)_{0.5}$; aspect ratio 5.2, loading time 80min.

5.3.5. Effects of immersion time.

The amounts of the adsorbed gold nanorods strongly depend on the immersion time. Figure 6 shows the results of $PEGNH_2$ coated nanorods adsorbed onto PS_{390}-$P4VP_{140}$ $(AOT)_{0.5}$ with different immersion time. The PS_{390}-$P4VP_{140}$ $(AOT)_{0.5}$ has a morphology of lamellae oriented perpendicular to that of the silicon wafer (Figure 6a), removing of AOT leads to the formation of gap like structure, the cross section view of the same sample proves that this structure goes through the whole film. The surface coverage of this P4VP gap is 35±1%. When this template is immersed into gold nanorods solution, the nanorods start to adsorb onto this template. The density of the gold nanorods is growing with increasing immersing time (Figure 6b-e and Figure 3b). At 10min, little amount of nanorods together with some spherical particles is adsorbed randomly on the template; locally the nanorods take the end-to-end configuration, and form line structure. Increase of the immersion time from 10 to 60min leads to higher amount of adsorption, and the nanorods have the end-to-end configuration on more areas, at 80min (Figure 3b), almost all of the P4VP domains are covered with end-to-end connected nanorods, with small amount of gold spheres, increasing of the immersion time further does not enhance the adsorption and ordering of gold nanorods, instead, on some areas the aggregation of the nanorods is observed. The surface coverage of the gold nanorods obtained from these FESEM pictures is shown in Figure 6f. It shows an exponential recovery behaviour, the adsorption rate of the gold nanorods decreases with increase adsorption time, a saturated region is observed around an immersion time of 80min. At the point, the surface coverage of the gold nanorods is 30.1±2.7%, which is closed to that of the surface coverage of P4VP

(36.2±0.5%,), indicating that on this template the gold nanorods can reach the maximum adsorption.

The exponential recovery behaviour of the adsorption can be understood as following, at the very beginning, there is no gold nanorods adsorbed onto the template, the template has the maximized active site (P4VP domains), therefore the gold nanorods adsorb onto the template very fast, with increasing of immersion time, more nanorods adsorb onto the template, and the active sites decreases, which reduce the adsorption rate, at the full coverage, the steric hindrance between PEG chain and the static electric repulsion between nanorods prevents the adsorption of more nanorods, therefore a plateau is expected.

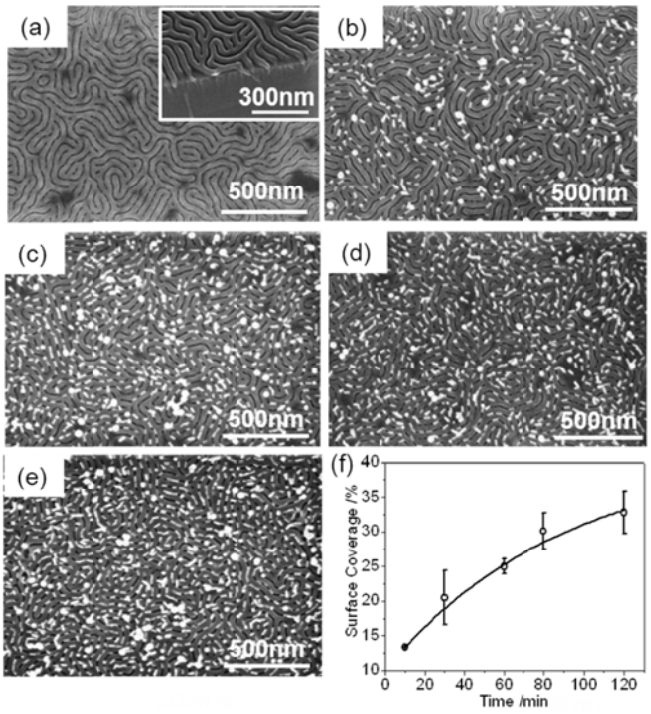

Figure 6. Morphology gold nanorods coated with $PEGNH_2$ on PS_{390}-$P4VP_{140}$ $(AOT)_{0.5}$ with different time: (a) 0min, insert showed the 45° view of cross section; (b) 10min; (c) 30min; (d) 60min; (e) 120min; (f) surface coverage extrapolated from FESEM images; aspect ratio 3.3.

5.3.6. Optical properties.

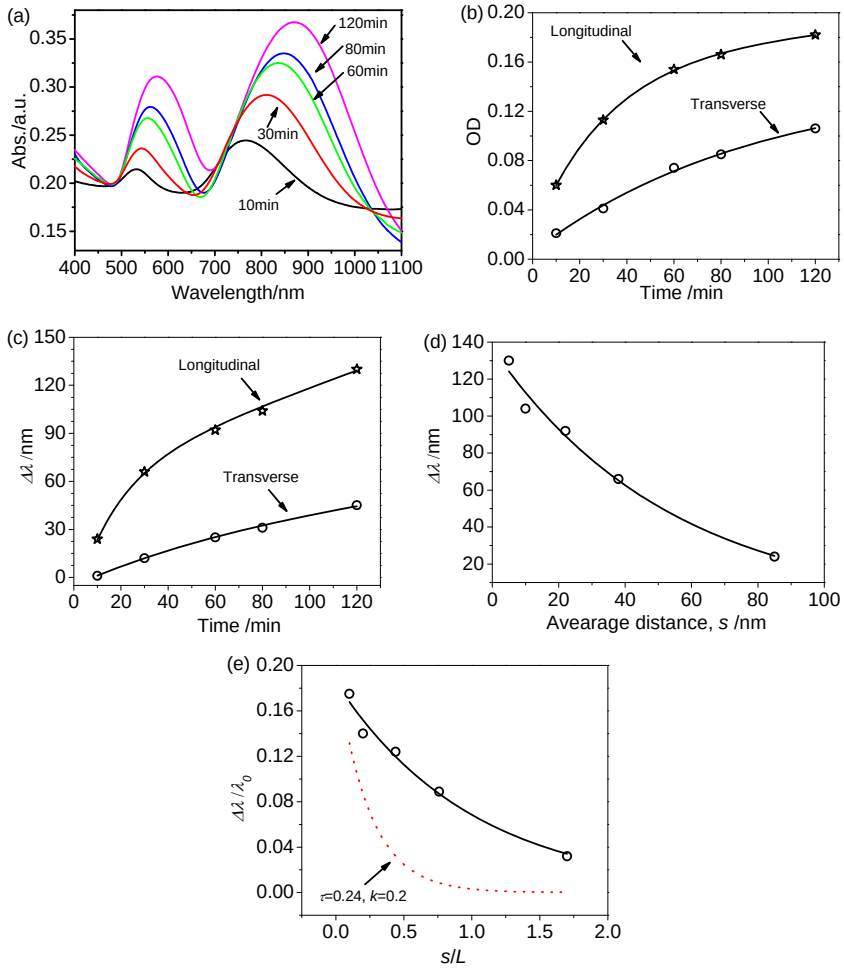

Figure 7. (a) UV-Vis spectra of adsorbed $PEGNH_2$ modified nanorods on PS_{390}-$P4VP_{140}(AOT)_{0.5}$; (b) optical density (OD) *vs.* time; (c) red shift of the LSPR ($\Delta\lambda$) *vs.* time; (d) $\Delta\lambda$ as a function of average distance (s), the solid line is a fitting of the model $\Delta\lambda=y_0+a\exp(-s/l)$, yielding a decay length of 54.1±26.1nm (R^2=0.982); (e) fractional shift vs. average distance (s)/nanorods length (L), the solid black line is fitted by a model of $\Delta\lambda/\lambda_0=k\exp(-(s/L)/\tau)$, the red dash line is simulated with gold nanorods of aspect ratio=3, τ=0.24, k=0.20[39].

FESEM is a local method, in order to get the kinetics of the adsorption process in a large scale, UV-Vis spectra of the samples immersed into the nanorods solution for various times are measured and the results are showed in Figure 7. As expected, increasing of the immersion time leads to a higher amount of adsorption, and the optical densities (ODs) of both longitudinal and transverse SPR peaks increase with increased immersion time (Figure 7a), ODs of both LSPR and TSPR show an exponential recovery behaviour (Figure 7b): the increase rate of the ODs decreases

with the increased immersion time, same behaviour is observed from the samples have same immersion time by FESEM (Figure5f).

Another interesting phenomenon is the red shift of both of LSPR and TSPR peaks with the longer immersion time (Figure 7a and c), compared to that of the single particle situation in solution (λ=740nm). The LSPR and TSPR shift to high wavelength region gradually with the immersion time (Figure 7a). The red shift of LSPR is much more obvious than that of the TSPR, a maximum absolute red shit of 130nm for LSPR, leading to λ of LSPR closing to 900nm, is observed, when the P4VP covers fully with the gold nanorods (Figure 7c). It is known that the coupling of the SPR of nanorods is depended on the distance between nanorods and the configuration of the multiparticles.[39-43] The end-to-end configuration leads to red shift, while the side-by-side configuration leads to blue shift of the SPR. As showed in FESEM section, on this template, the nanorods orient nearly end-to-end inside the P4VP domains, and on each position only one nanorod is possible. From these images the average end-to-end distance (s) can be estimated, and the absolute values of SPR red shift ($\Delta\lambda$) is plotted against the average distance (s), and the result is showed in Figure 7d, the data can be described by an exponential decay model,[39] and the decay length is 54.1±26.1nm.

The red shift of the SPR peaks with decreased inter-particle distance can be described by an one component exponential decay model (Eq. 5.1) for dimmer:[40, 44]

$$\Delta\lambda/\lambda_0 = k \times \exp(-(s/L)/\tau) \qquad (5.1)$$

where $\Delta\lambda/\lambda_0$ is fractional shift, which is defined by the scaling of absolute red shift ($\Delta\lambda$) to that of the SPR at single particle situation (λ_0), τ is the exponential coupling decay length, describing the length over which the combined field decays as the pair moved away from each other, k is a amplitude, its physical mean is maximum fractional shift which occurred at zero separation of the pairs, and is proportional to the maximum overlapping field of the two particles, and L is the length of the nanorods. This method describes the plasmonic coupling as a near-exponential function of separation, and is an attempt to simplify the convoluted coupling that occurred between not only plasmonic dipoles (which theoretically coupled as a function of separation such as s^3) but also higher order multipoles as the separation decreases. This method cannot only describe the size scaling of the symmetric nanoparticle (such as sphere), but also asymmetric particles (*e.g.* nanorods, spheroids), and an exponential decay length τ ~0.2L is found to be universal for all shapes of nanoparticles in both of theoretical

calculation and experiments. [45] This model also can be used to describe our experimental data, as showed by Figure 7e (solid line), the fitting is good and gives a value of k=0.19±0.01 and τ = 1.00± 0.12 (R^2=0.981). Compared with the literature which investigated gold nanorods dimmers with same aspect ratio[39] (red dash line in Figure 7e), the amplitude k value is close to the literature value, indicating that at zero separation the gold nanorods have similar maximum fractional shift, therefore similar maximum overlapping field in both of dimmers and lines with end-to-end configuration. However, the exponential coupling decay length τ deviates obviously from the literature value; the fractional shift decayed almost 1 time over the length of the nanorods, meaning that length over which the combined field decays as the pair moved away from each other is larger than that of sphere or nanorods dimmer. One needs to keep in mind that this empirical equation is developed to describe the coupling between dimmer of nanoparticles initially, and it is extended to describe the situation of trimmer of the symmetric nanospheres,[39-43] in these cases a universal scale of τ ~0.2 time over the length of the particles is found, however, this value can be varied in some shapes, large values are also reported for nanoprisms (τ ~0.4). [46]

5.3.7. Nanorods in cylindrical holes.

Above we show that the lamellae domains of block copolymer can be selectively adsorbed by nanorods and align nanorods parallel with an end-to-end configuration. Another important issue is to control of the orientation of the nanorods in vertical direction. Block copolymer thin film templates with cylinder hole are ideal candidates. Figure 8 shows the morphology of the gold nanorods coated with PEGOH on PS_{390}-$P4VP_{140}(AOT)_{0.33}$, which has cylindrical holes after removing of AOT.[47] As can be see, the gold nanorods selectively adsorb onto the P4VP domains, but it is difficult to achieve the perfect vertical alignment of gold nanorods in the cylindrical holes in larger scale. Locally some of the nanorods align perpendicularly to that of the silicon wafer (or parallel to that of the axis of cylinders), where only dot like morphology with a size of about 15nm is observed. In most of the areas the gold nanorods decline with various angles towards to that of the axis of the cylindrical holes, in this case the elongated nanorods are observed.

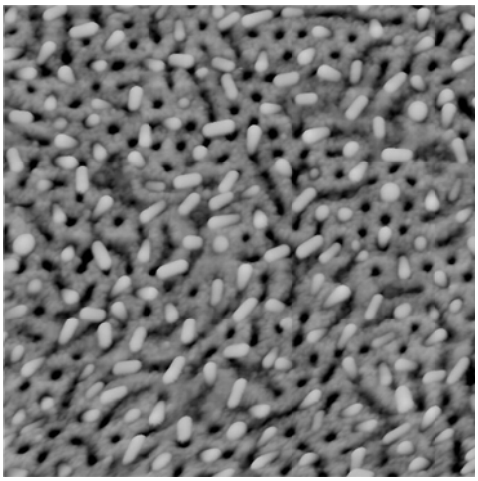

Figure 8. 3D topographical image of PEGOH modified gold nanorods on PS_{390}-$P4VP_{140}(AOT)_{0.33}$ thin film, scan size 1×1μm.

5.4. Conclusions.

The selective adsorption of nanorods onto one domain of block copolymer porous thin film templates is realized by using of the specific interaction between the particles and block copolymer. The porous thin film templates are prepared by washing out of ligand from the supramolecular PS_n-$P4VP_m(AOT)_{D/N}$ thin films in basic solution. The hydrogen bonding between PEG/P4VP is crucial for the selective loading of the gold nanorods into P4VP domains. The orientation of the gold nanorods is controlled by the morphology of the templates: the lamellae holes lead to the parallel orientation, while the cylindrical holes induce perpendicular orientation. The morphology of the nanorods is defined by the size confinement from that of the block copolymer. When the width of the lamellae is comparable to that of the nanorods diameter, single gold nanorod aligns parallel to that of the lamellae wall with an end-to-end configuration, when the width of the domains is larger than that of the particles diameter, the nanorods can assemble with a side-to-side configuration, and such kind of buddle self assemble inside the block copolymer domains with an end-to-end configuration, with their long axis parallel to that of the lamellae domains. Time dependent adsorption of the gold nanorods is confirmed by the FESEM and UV-Vis spectra. The optical properties can be tuned by changing of the immersion time in the nanorods solution, and it can be described by a single component exponential decay model, and a new decay scale of ~1*L* is obtained.

5.5. References.

[1] A. C. Balazs, T. Emrick, T. P. Russell, *Science* **2006**, *314*, 1107.

[2] Y. Lin, A. Boker, J. He, K. Sill, H. Xiang, C. Abetz, X. Li, J. Wang, T. Emrick, S. Long, Q. Wang, A. Balazs, T. P. Russell, *Nature* **2005**, *434*, 55.

[3] Y. Zhao, K. Thorkelsson, A. J. Mastroianni, T. Schilling, J. M. Luther, B. J. Rancatore, K. Matsunaga, H. Jinnai, Y. Wu, D. Poulsen, J. M. J. Frechet, A. Paul Alivisatos, T. Xu, *Nat. Mater.* **2009**, *8*, 979.

[4] X. Zhang, S. H. De Paoli Lacerda, K. G. Yager, B. C. Berry, J. F. Douglas, R. L. Jones, A. Karim, *ACS Nano* **2009**, *3*, 2115.

[5] M. J. Pavan, R. Shenhar, *J. Mater. Chem.* **2011**, *21*, 2028.

[6] X. Huang, S. Neretina, M. A. El-Sayed, *Adv. Mater.* **2009**, *21*, 4880.

[7] I. W. Hamley, *The physics of block copolymers* Oxford University Press Oxford 1998.

[8] J. G. Son, X. Bulliard, H. Kang, P. F. Nealey, K. Char, *Adv. Mater.* **2008**, *20*, 3643.

[9] Y. Hansik, L. Il-Min, I. Sang Hyuk, L. Seung-Yeol, L. Byoungho, *Nanotech.* **2012**, *23*, 015306.

[10] M. J. Misner, H. Skaff, T. Emrick, T. P. Russell, *Adv. Mater.* **2003**, *15*, 221.

[11] Q. Zhang, T. Xu, D. Butterfield, M. J. Misner, D. Y. Ryu, T. Emrick, T. P. Russell, *Nano Lett.* **2005**, *5*, 357.

[12] J. G. Son, W. K. Bae, H. Kang, P. F. Nealey, K. Char, *ACS Nano* **2009**, *3*, 3927.

[13] S. Niu, R. F. Saraf, *Nanotech.* **2007**, *18*, 125607.

[14] E. Ploshnik, A. Salant, U. Banin, R. Shenhar, *Adv. Mater.* **2010**, *22*, 2774.

[15] E. Ploshnik, A. Salant, U. Banin, R. Shenhar, *Phys. Chem. Chem. Phys.* **2010**, *12*.

[16] K. S. Iyer, B. Zdyrko, S. Malynych, G. Chumanov, I. Luzinov, *Soft Matter* **2011**, *7*, 2538.

[17] B. K. Kuila, E. B. Gowd, M. Stamm, *Macromolecules* **2010**, *43*, 7713.

[18] Q. Zhang, S. Gupta, T. Emrick, T. P. Russell, *J. Am. Chem. Soc.* **2006**, *128*, 3898.

[19] S. Watanabe, R. Fujiwara, M. Hada, Y. Okazaki, T. Iyoda, *Angew. Chem. Int. Edit.* **2007**, *46*, 1120.

[20] P. Mansky, Y. Liu, E. Huang, T. P. Russell, C. Hawker, *Science* **1997**, *275*, 1458.

[21] E. Han, K. O. Stuen, Y.-H. La, P. F. Nealey, P. Gopalan, *Macromolecules* **2008**, *41*, 9090.

[22] S. H. Kim, M. J. Misner, T. Xu, M. Kimura, T. P. Russell, *Adv. Mater.* **2004**, *16*, 226.

[23] C. Osuji, Y. Zhang, G. Mao, C. K. Ober, E. L. Thomas, *Macromolecules* **1999**, *32*, 7703.

[24] M. Anthamatten, P. T. Hammond, *J. Polym. Sci. Part B: Polym. Phys.* **2001**, *39*, 2671.

[25] W. H. de Jeu, Y. Séréro, M. Al-Hussein, *Adv. Polym. Sci.* **2006**, *200*, 71.

[26] J. Ruokolainen, R. Mäkinen, M. Torkkeli, T. Mäkelä, R. Serimaa, G. t. Brinke, O. Ikkala, *Science* **1998**, *280*, 557.

[27] O. Ikkala, G. ten Brinke, *Science* **2002**, *295*, 2407.

[28] W. van Zoelen, E. Polushkin, G. ten Brinke, *Macromolecules* **2008**, *41*, 8807.

[29] H.-L. Chen, J.-S. Lu, C.-H. Yu, C.-L. Yeh, U. S. Jeng, W.-C. Chen, *Macromolecules* **2007**, *40*, 3271.

[30] J. Kao, J. Tingsanchali, T. Xu, *Macromolecules* **2011**, *44*, 4392.

[31] K. Albrecht, A. Mourran, X. Zhu, T. Markkula, J. Groll, U. Beginn, W. H. de Jeu, M. Moeller, *Macromolecules* **2008**, *41*, 1728.

[32] Y. Lin, V. K. Daga, E. R. Anderson, S. P. Gido, J. J. Watkins, *J. Am. Chem. Soc.* **2011**, *133*, 6513.

[33] J. J. Chiu, B. J. Kim, G.-R. Yi, J. Bang, E. J. Kramer, D. J. Pine, *Macromolecules* **2007**, *40*, 3361.

[34] E. Ploshnik, A. Salant, U. Banin, R. Shenhar, *Phys. Chem. Chem. Phys.* **2010**, *12*, 11885.

[35] M.-C. Daniel, D. Astruc, *Chem. Rev.* **2003**, *104*, 293.

[36] M. Bartneck, H. A. Keul, S. Singh, K. Czaja, J. r. Bornemann, M. Bockstaller, M. Moeller, G. Zwadlo-Klarwasser, J. r. Groll, *ACS Nano* **2010**, *4*, 3073.

[37] J. Cho, J. Hong, K. Char, F. Caruso, *J. Am. Chem. Soc.* **2006**, *128*, 9935.

[38] D. Li, Q. He, Y. Cui, J. Li, *Chem. Mater.* **2007**, *19*, 412.

[39] P. K. Jain, M. A. El-Sayed, *J. Phys. Chem. C* **2008**, *112*, 4954.

[40] K. H. Su, Q. H. Wei, X. Zhang, J. J. Mock, D. R. Smith, S. Schultz, *Nano Lett.* **2003**, *3*, 1087.

[41] C. Tabor, D. Van Haute, M. A. El-Sayed, *ACS Nano* **2009**, *3*, 3670.

[42] A. M. Funston, C. Novo, T. J. Davis, P. Mulvaney, *Nano Lett.* **2009**, *9*, 1651.

[43] P. K. Jain, W. Huang, M. A. El-Sayed, *Nano Lett.* **2007**, *7*, 2080.

[44] W. Rechberger, A. Hohenau, A. Leitner, J. R. Krenn, B. Lamprecht, F. R. Aussenegg, *Optics Comm.* **2003**, *220*, 137.

[45] P. K. Jain, M. A. El-Sayed, *Chem. Phys. Lett.* **2010**, *487*, 153.

[46] C. Tabor, R. Murali, M. Mahmoud, M. A. El-Sayed, *J. Phys. Chem. A* **2008**, *113*, 1946.

[47] J. Wang, W. H. de Jeu, P. Müller, M. Möller, A. Mourran, *Macromolecules* **2012**, *45*, 974.

Chapter 6 Nanostructured TiO_2 Thin Films Templated from Co-assembly of Fully Miscible Block Copolymer Complex/Polymeric Precursors

6.1. Introduction.

Titanium dioxide (TiO_2) has attracted extensive research interests because of its oxidation strength, high photo-stability, and nontoxicity.[1, 2] These properties make the TiO_2 widely used as a pigment, protective coating and as a catalyst.[3-7] Porous TiO_2 coatings and membranes are also desirable for photovoltaic, as separators and as catalysts. Different routes have been developed for the preparation of TiO_2 nanostructures, [8-17] among them block copolymers (BCP) templates, in which microphase segregation directs the growth of the inorganic phase, are the most popular routes.[10-17] Generally, the block copolymer is dissolved in a selective solvent, at a concentration exceeding the critical micelle concentration (CMC).[18] Subsequently, the TiO_2 precursor is added so that it is partitioned inside the core or selectively "binds" to the periphery of the micelles. Controlled pre-condensation of the precursor through a sol-gel process leads to nanostructured TiO_2 powders or films featuring mesostructure of the parent block copolymer. Thermolysis sinters the TiO_2 and removes the organic template. The morphology of inorganic material generated during this process is defined by the property of the block copolymer aggregation in solution. For instance, micelle structure will lead to spherical nanoparticle. Varieties of block copolymers have been successfully used for the preparation of nanostructured TiO_2.[10, 13, 14, 16, 19, 20] As a drawback, it is difficult to fine-tune the morphology.[16, 17]

Another issue is related to the nanostructure of a thin film, which often requires control of the orientational order. It is well-known that block copolymer lamellae or cylinders orient preferentially parallel to the substrate plane.[21] Tremendous effort was dedicated to control the vertical alignment of the block copolymer nanostructures.[22] In the recent works, it has been shown that incorporation of mesogens through supramolecular interactions (complex) in block copolymer results

in a hierarchical structure – a feature which originates from the interplay between a liquid crystal state and microphase separation.[23-27] In particular, the microdomains can be controlled by the stoichiometry of the complex, while liquid crystalline (LC) - ordering acts on the orientational order of the domains. In thin films, smectic layers tend to align near the interface, which orients block copolymer interphase perpendicularly to the air/substrate interface. In one of our recent study, we have shown that sodium bis(2-ethylhexyl) sulfosuccinate (AOT) form ionic bonds with pyridine containing block copolymer, i.e. poly (styrene – b – 4-vinylpyridine) (PS-P4VP).[28]

The last issue is related to the chemical stability of the TiO_2 precursors. In principle, TiO_2 precursors are highly sensitive to moisture, as it reacts with traces of water to produce ill-defined titanium-oxo/hydroxo precipitates.[16, 17] The high reactivity originates from the low-electronegativity of Ti atom and a coordination number that is higher than its valence, this results in the so-called “coordination expansion".[29, 30]. Recently, a non-aqueous sol-gel technology has been developed to improve the stability of silicon dioxide precursors.[31] The precursor is hyper-branched polyethoxysiloxanes, proved to be stable in the ambient atmosphere for months. This concept was extended to the synthesis of TiO_2 precursor through polycondensation of titanium isopropyl oxide with acetic anhydride. The resulting educts is poly (titanium isopropyl oxide) (PAOT), a yellowish powder readily soluble in organic solvents. The precursor is stable in solution for several days while the monomer is several minutes in the same solvent.

Compared to silica precursor, [32] the morphology of blends based on TiO_2 precursor is more difficult to control due to the weak interaction with the block copolymer.[17] The sulfonate or sulfate groups have a Lewis base property, and are able to coordinate with titanium (IV) to form a stable complex.[33, 34] Such interaction is useful to make compatible blends of TiO_2-precursor and block copolymer complex, a prerequisite for influencing the mesostructure of inorganic thin films. [24, 28]

In the present contribution we report on a new non sol-gel route for the preparation of a thin nanostructured TiO_2 film by co-assembly of a block copolymer complex and PAOT. The structure directing agent is a complex of PS-P4VP and AOT.[28] First, we discuss the thin film property of PAOT and the resulting titanium dioxide. Second, we make use of the ionic complex P4VP(AOT) to prepare miscible blends of PAOT and

block copolymer complex. We demonstrate the key roles of the ligand (AOT) in (i) defining the morphology and orientational order of the block copolymer template, and (ii) enhancing compatibility of the block copolymer with TiO_2 precursor. As such, the molar ratio R of titanium to pyridine (Ti/Py), and the degree of protonation DN defined by the ratio of AOT to pyridine enable morphological control of the thin films structure.

6.2. Experimental sections.

6.2.1. Materials.

The block copolymer complex was PS_n-$P4VP_m(AOT)_{DN}$; in which the subscripts n, m denote degree of polymerization and DN denote the molar ratio of AOT/pyridine, respectively. The complex was prepared according to literature.[28] All the chemicals including solvents are analytical pure and purchased from VWR GmbH. Silicon wafer (100) was purchased from CrysTec GmbH, and the SiO_x coated TEM grids were purchased from Plano GmbH.

PAOT is synthesized in our lab, it is a new TiO_2 precursor. It is a yellowish powder, which can be dissolved into organic solvents, i.e. chloroform, toluene, hexane, *etc*., at any concentrations without precipitation or gelation. The solid content of the PAOT was measured as following: the PAOT was weighted into a ceramic pan in a glove box, and then it was hydrolysed with an ethanol/HCl/H_2O mixture. The solvent was evaporated under room temperature for 3 days. All of the possible organic residuals were removed by calcination at 400°C for 4h. The solid content was the ratio between the weight of final TiO_2 and initial PAOT. In order to get good accuracy the measurements were done at least three times and the average was reported. From the solid content of PAOT one can easily calculate the molar ratio of the titanium in the PAOT. The blend composition was defined by the molar ratio of titanium to the pyridine.

6.2.2. Sample preparation.

In separate vials, the PS_n-$P4VP_m(AOT)_{DN}$ and PAOT were dissolved in chloroform, a good solvent for both of the compounds, the concentration was fixed at 1 wt%. The solutions of the BCP-complex and PAOT were prepared by mixing a desired volume

of the respective solutions. Before use, the solutions were filtered through 0.2μm PTFE syringe filters. For TEM investigations, the solution was drop-cast directly onto the SiO_x -coated copper grids and the excess was soaked with filter paper below. The silicon wafers were cleaned by sonication in isopropanol for 5 min, dried with an air stream, and activated in UV/O_2 for 12 min. These treatments lead to a hydrophilic SiO_x having water contact angle of less than 5°. The films were prepared by spin-coating equipped with a homemade chamber to produce coating in an atmosphere saturated with chloroform. The spinning speed was 3000 rpm, and the time was 2 min. The film thickness was 30 nm measured by ellipsometry (MM-SPEL-VIS, OMT GmbH). The films were treated with hydrogen (H_2) plasma (Plasma System 100, PVA Tepla AG) to remove the organic moieties and convert the precursor to TiO_2. The typical plasma treatment conditions were: 200W, 1 mbar, and 30min. The calcination was done in a Muffle furnace. The plasma treated thin films were placed in the furnace and heated to 400°C under a heating rate of 2°C/min, then kept at that temperature for 4h, finally the furnace was cooled down to ambient temperature with a cooling rate of 2°C/min. For FT-Raman experiments, in order to minimize the influence of ambient moisture, the samples were sealed in the glove box in an aluminium pan with glass windows. For FTIR experiments, samples were prepared by spin coating the solution onto KBr plates and subsequently treated with hydrogen plasma.

6.2.3. Characterization methods.

Transmission Electron Microscopy (TEM) images were acquired using a Zeiss Libra120 with an accelerating voltage of 120 kV. Scanning Electron Microscope (SEM) experiments were performed using a Hitachi S4800 high resolution Field Emission Scanning Electron Microscope with an accelerating voltage of 1.5kV. Tapping model SFM experiments were performed on a NanoScope V multimode AFM (Digital Instruments Veeco Instruments, Santa Barbara, CA) under ambient conditions. Commercial available standard silicon cantilevers (PPP-SEIH-W from Nanosensors) with a spring constant of 5~37 N/m and an oscillation frequency of ~125 kHz were used. FT-Raman spectra were recorded by using a Bruker RFS 100/S FT-Raman Spectrometer with a Nd:YAG laser (wavelength 1064nm). The power of the laser was 200 mW and the resolution was 4 cm^{-1}. 500 scans were performed for

each spectrum. IR spectra (resolution of 4 cm^{-1}) were recorded by using a Nicolet NEXUS 670 Fourier Transform IR spectrometer. For each spectrum more than 200 scans were averaged to enhance the signal to noise ratio. Crystal structure of thin TiO_2 film (~150nm) was characterized by Grazing Incidence Wide Angle X-Ray scattering (GIWAXS). The experiment was carried out on a Powder Diffractometer with a focusing Ge- monochromator (Johann-type) PSD detector (Co-radiation) (STADI MP vertical from STOE, Darmstadt, Germany). Cobalt $K_{\alpha 1}$ radiation was used as the X-ray source and the experiments were done in Bragg-Brentano-Geometry. The focused beam was directed on the sample at an angle ω of 0.75°.

6.3. Results and discussions

First we discuss the film-forming properties of PAOT. Second, based on morphological studies by TEM, we demonstrate the miscibility of the pair block copolymer complex and PAOT. Third, the result of the plasma treatment is presented and discussed on the base of SFM investigation. The report ends with a discussion on the origin of the miscibility based on FT-Raman spectroscopy and on the analysis of the structure parameters.

6.3.1. Film properties of PAOT.

Figure 1a shows that the film thickness increases linearly with the concentration of PAOT in the solution. The coatings are uniform with the exception of films cast from a high concentration (≥ 200 g/L), wherein cracks evolves. This indicates that residual stress develops during the casting process, which becomes increasingly important with the film thickness. Such effect is ascribed to partial transformation of the precursor to TiO_2 by ambient humidity, and results in a volume contraction. However, in thin films, it is essentially a reduction in thickness. Hydrogen plasma treatment converts the precursor to TiO_2 and eliminates the organic fragments, these results in an extra contraction of the thickness of about 60%. Because the precursor contains 48.5±2.1% of TiO_2, films treated with plasma are denser (20%), as compared to untreated ones. Annealing the film at 400°C for 4h resultants in a further reduction of the thickness of about 18%, indicating the increase of the crystallinity. Furthermore,

FT-IR (Figure 1b) shows that after plasma treatment, the conversion is incomplete and traces of the organic residue are still present.

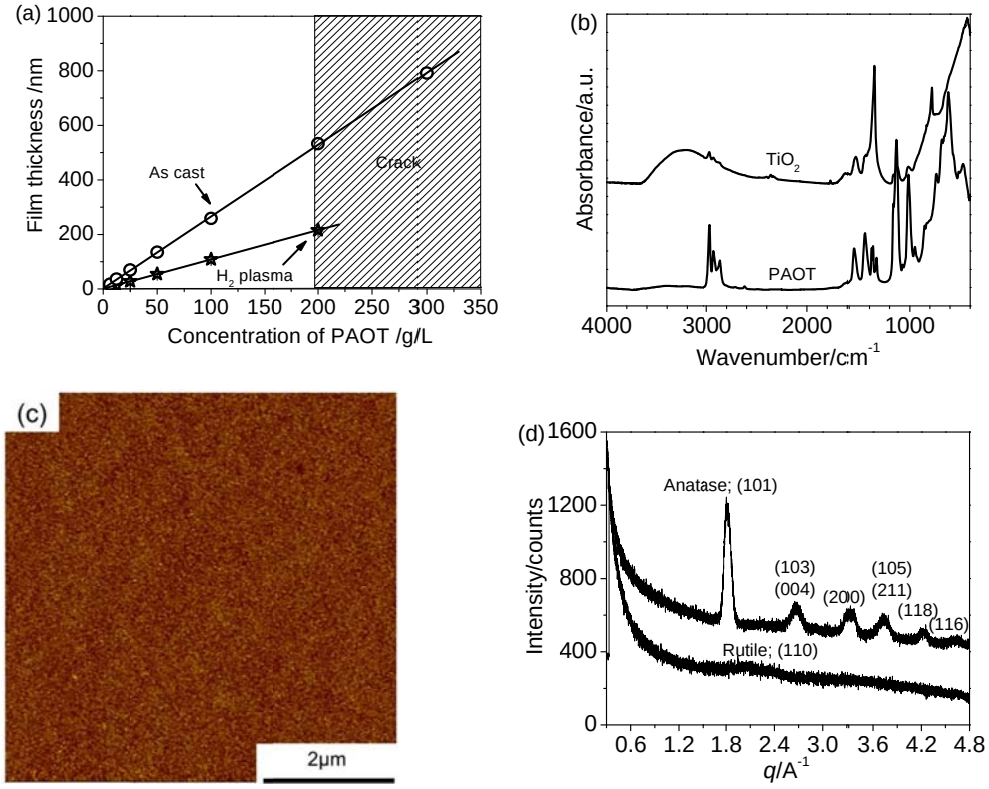

Figure 1. (a) Relationship between the film thickness and concentration of PAOT, before (circle) and after H_2 plasma (star); (b) FTIR spectrum of PAOT films: before conversion clearly indicates that spectra is dominated by the organic moieties and the TiO_2 is hardly visible; after H_2 plasma (upper spectra), Ti-O-Ti bands at 1350 and 780cm^{-1} become visible with some organic residue[35, 36]. (c) SFM height image of TiO_2 after exposure to H_2 plasma; (d) GIWAXS patterns of the H_2 plasma treated film (lower curve) and after thermal annealing for 4h at 400°C (upper curve).

FESEM (image not showed here) and SFM shows that the films are uniform and smooth over relatively large area with a mean roughness of about 0.78 nm (Figure 1c). Actually the crystallinity of the film is low, only a broad peak in the *q* range of 1.6-2.4 Å (Figure 1d), which can be assigned to the (110) reflex of the rutile form (JCPDS 88-1175). After thermal annealing, the film is well crystalline, which is proved by the pronounced GIWAXS diffraction peaks. The peak position (Figure 1d) proves the formation of anatase phase further (JCPDS 84-1286).

To conclude, PAOT can be processed to form smooth thin films, crack develops above certain thickness. Treatment with H_2 plasma eliminates the organic moieties, leading to TiO_2 with very low crystallinity. Sintering the film at high temperature leads to crystalline TiO_2 films with anatase phase.

6.3.2. Co-assembly of PS_n-$P4VP_m(AOT)_{DN}$ and PAOT.

The thin film morphology of block copolymer complex PS_n-$P4VP_m(AOT)_{DN}$ has been studied in details.[28] Here, we explore the morphology of block copolymer complex as a template for preparation of nanostructured TiO_2 films. This requires a selective miscibility of PAOT with one of the blocks. Below we show that the degree of protonation largely controls the partitioning of PAOT within the P4VP/AOT domains.

6.3.2.1. PS_{390}-$P4VP_{140}(AOT)_{1.0}$/PAOT.

In thin films, the block copolymer complex self-assembles into lamellae coexisting with PS-cylinders.[28] Figure 2 shows the morphology of the blends depending on the molar ratio of Ti/Py. The dark contrast is due to the high electron density of PAOT together with P4VP(AOT). Increasing the concentration of PAOT reduces the mass fraction of PS and leads to morphological change: PS lamellae gradually transforms into circular domains (gray) delimited by PAOT/P4VP(AOT) as the continuous phase (Figure 2a-c). Further increase of *R* from 10 to 20 widens the interspace between the PS domains without altering the domain morphology (see Figure 2c-d). It is essential to note that the molar ratio of Ti/Py, can be as high as ca. 20 without precipitation or gelation. This will be discussed later based on FT-Raman spectroscopy.

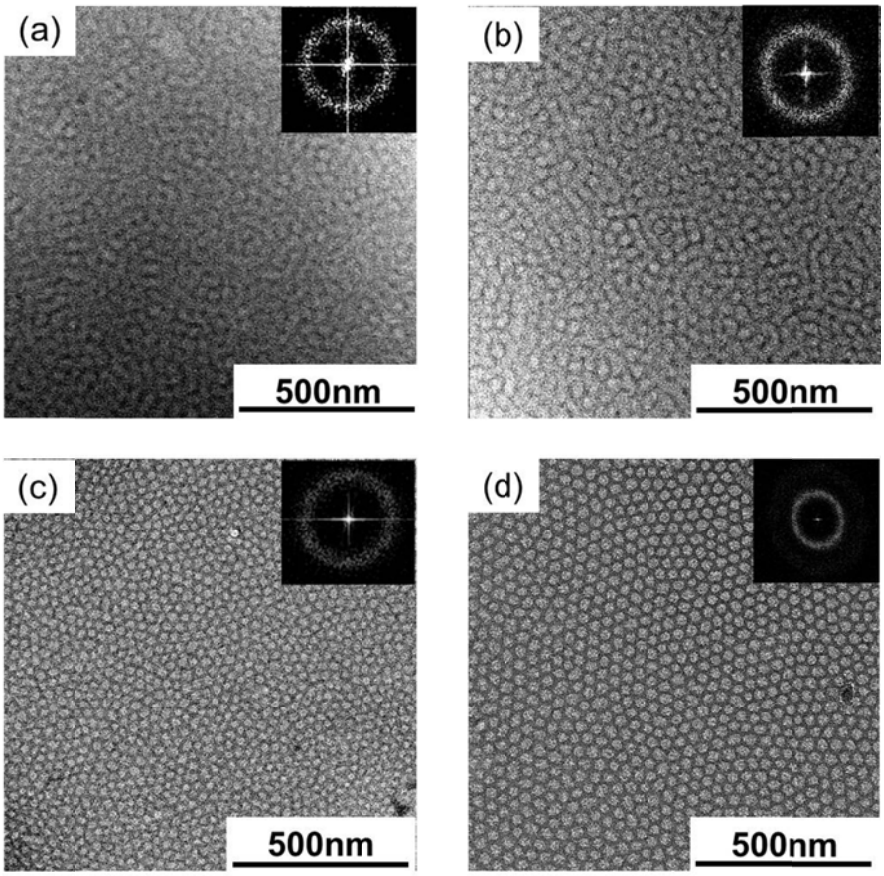

Figure 2. TEM-micrographs of blends of PS_{390}-$P4VP_{140}(AOT)_{1.0}$ / PAOT with different molar ratio R= (a) 1.3; (b) 5.1; (c) 10.2; (d) 20.3, the insert are the corresponding FFT images.

6.3.2.2. PS_{390}-$P4VP_{140}(AOT)_{0.5}$/PAOT.

With 50% protonation the neat block copolymer complex forms lamellae, in which the width of the $P4VP_{140}(AOT)_{0.5}$ is about 21 nm and the periodicity is 47 nm.[28] Figure 3 shows the morphology of the blends depending on *R*. Apparently, for $R \leq$ 15.2, the inter-lamellar space increases with PAOT concentration. Structural transition occurs when *R* is close to 30, leading to PS cylinders having a diameter and periodicity of about 25.1 ± 0.8 nm and 36 nm, respectively.

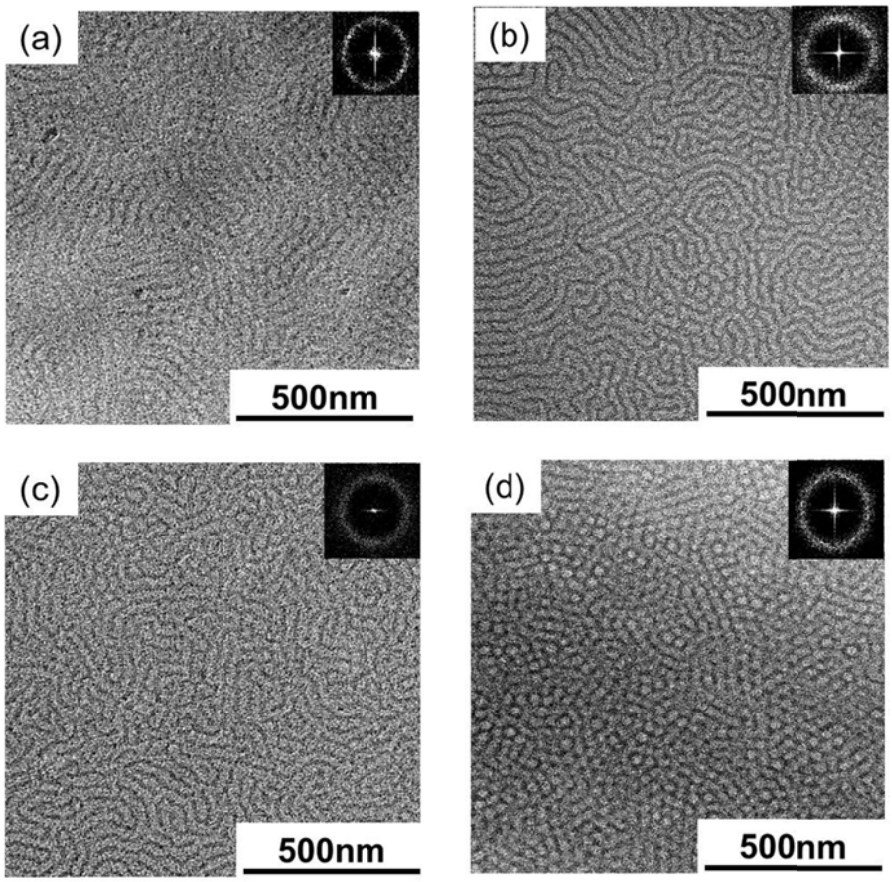

Figure 3. TEM-micrographs of a drop-cast solution of the mixture of PS_{390}-$P4VP_{140}(AOT)_{0.5}$/PAOT with different molar ratio *R*= (a) 1.9; (b) 7.6; (c) 15.2; (d) 30.5; the insert is the corresponding FFT images.

6.3.2.3. PS_{390}-$P4VP_{140}(AOT)_{0.33}$/PAOT.

In thin films, such a low degree of protonation leads to the lamellae coexisting with cylinders of $P4VP_{140}(AOT)_{0.33}$. [28] Addition of a small amount of PAOT, i.e. *R*= 2.6, reduces the mass fraction of PS to 0.42 and most likely lamellae morphology evolve (see Figure 4a). The variation of *R* from 2.6 to 20.4 only increases the inter-lamellar space (Figure 4a-c and 4e). For *R*= 40.9, a structural transition is observed, the PS domains (gray) are now delimited by the continuous phase (dark) (Figure 4d). This new structure has a periodicity of 32 nm, in which the diameter of the PS domain is of about 23.7±1.7 nm. Knowing that the mass fraction of PS is of about 0.11, it is probably a spherical morphology.

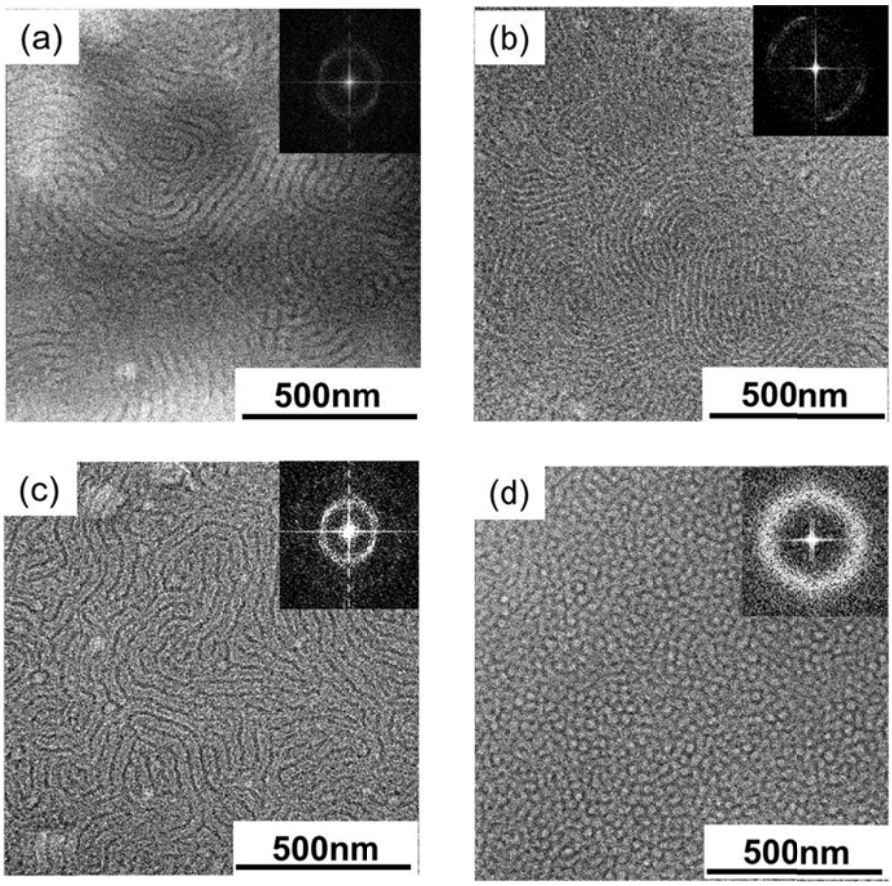

Figure 4. Morphology of PS_{390}-$P4VP_{140}(AOT)_{0.33}$/PAOT with different molar ratio *R*= (a) 2.6; (b) 10.2; (c) 20.4; (d) 40.9; the insert are the corresponding FFT images.

6.3.3. Nanostructured TiO_2 thin films.

In this section, films of defined thickness were prepared from a solution containing the mixture. The films were treated with hydrogen plasma (H_2 plasma), enabling transformation of PAOT to TiO_2 and simultaneously removing organic residues. For the sake of clarity and to avoid redundancy, we describe the morphologies of the films where the P4VP was fully protonated, we refer to SI for other compositions.

6.3.3.1. PS_{390}-$P4VP_{140}(AOT)_{1.0}$/PAOT.

Figure 5 summarizes the films morphology depending on *R* after H_2 plasma treatment. For *R*= 1.3, Figure 5a shows that the film morphology consist of a fine TiO_2 nanoparticle (~10nm) which cluster in a wire-like pattern with an average height of about 4nm. FFT-image gives a characteristic distance of about 49 nm. Increase of *R* to 5.1, leads to wire-like pattern and pores with an average period of about 45 nm and

a depth of 8 nm. For R = 10.2 or 20.3, the pores are well defined with a periodicity of about 42 nm and 38 nm respectively. An estimate of the pore diameter from the SFM images leads to a value of 24 nm, with a depth close to the film thickness, i.e. between 10 and 13 nm. Figure 5e shows a SEM image of the film cross section, which clearly indicates that the pores goes through the whole film. It is important to note that regardless of the composition, all films present a fine TiO_2 nanoparticle with an average diameter of about ~10 nm (cf. SI). In contrast, films of pure PAOT were smooth after plasma treatment (Figure 1).

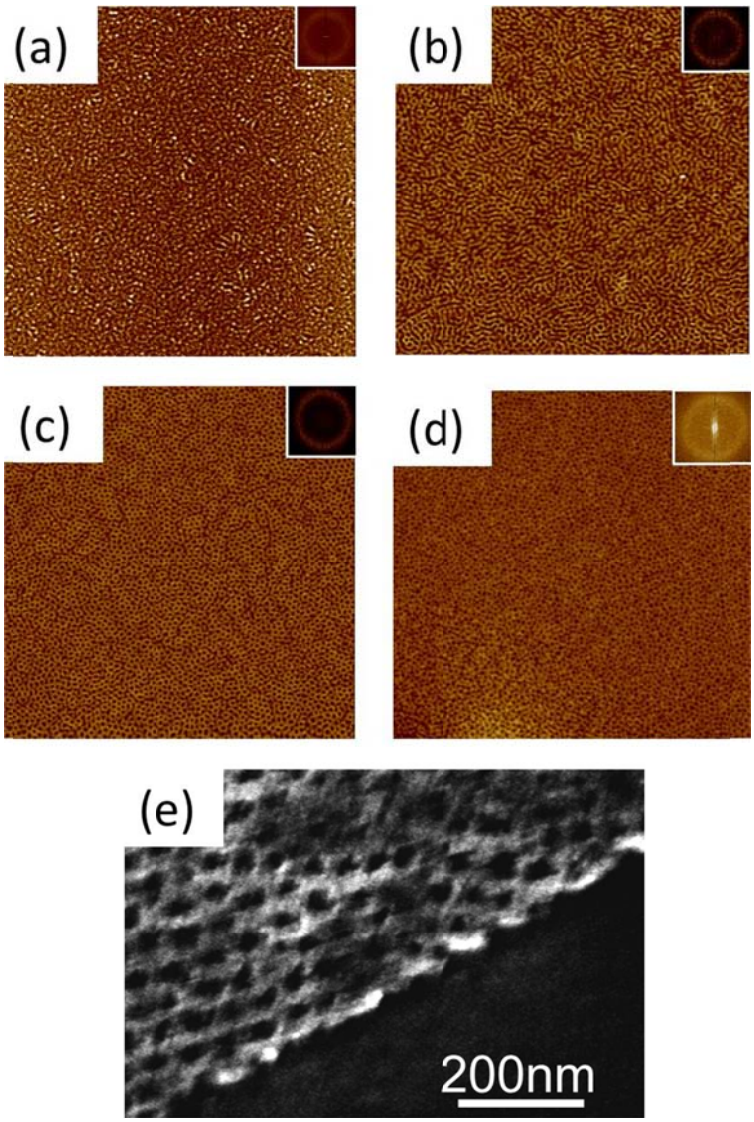

Figure 5. SFM height images of a thin film after treatment with H_2 plasma. The films were prepared from a mixture of PS_{390}-$P4VP_{140}(AOT)_{1.0}$ and PAOT with a molar ratio 1.3 (a), 5.1 (b), 10.2 (c), and 20.3 (d); (e) FESEM edge-view of a mechanically fractured films; the insert pictures in a-d are the corresponding FFT images, the scan size is $3\times3\mu m^2$.

6.3.4. Thermal stability of TiO_2 thin film.

The thermal stability of the TiO_2 films prepared by soft transformation (H_2 plasma) is an issue. In particular, porosity reduces resistance to stress generated by thermal expansion, or by thermal annealing induced post-crystallization. Often, the porous structure collapses at high temperature, which limits their application. [32]

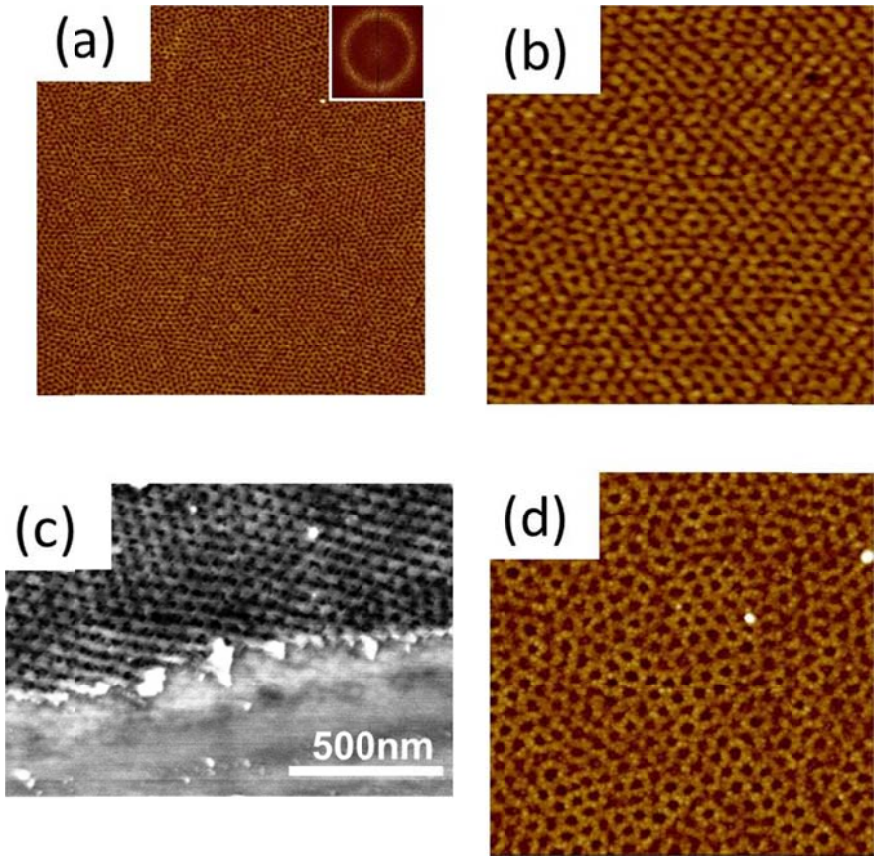

Figure 6. Morphology of TiO_2 templated from PS_{350}-$P4VP_{260}(AOT)_{1.0}$/PAOT: (a) topography image (3×3 μm^2); (b) enlarged view of (a) (1×1 μm^2); (c) FESEM images of an edge-view of a mechanically fractured films fractured; (d) topography image of (a) annealing at 400 °C for 4h (1×1 μm^2); the inserts are the corresponding FFT.

To investigate the stability of the nanostructure against the high temperature treatment e.g. 400°C, we chose a composition in which polystyrene form cylinder in a P4VP(AOT)/PAOT matrix. Based on our previous report, PS_{350}-$P4VP_{260}(AOT)_{1.0}$/PAOT fits this requirement. Figure 6 a-c show the film morphology after H_2 Plasma treatments. Indeed, the structure is porous with a pore diameter and a

periodicity of about 20 nm and 40 nm respectively. The pore depth is 10 nm, close to the film thickness.

The crystallinity of TiO_2 film is low when it is converted by H_2 Plasma, and thermal annealing leads to a transition of the low crystallinity TiO_2 to anatase phase (Figure 1d). After annealing at 400°C for 4h, the porous film remains optically homogenous without any cracks. Furthermore, the regular porosity of the film is preserved. Representative SFM height image is shown in Figure 6d, which indicates a periodicity of 40 nm, similar to the value before annealing. It also reveals the fine structure of the TiO_2 film after thermal annealing. Apparently, thermal treatment does not affect the fine nanoparticle, the morphology appears clearer and the average size is slightly larger, which is 12 nm. In addition, the pores depth and the film thickness are comparable, of about 8 nm. This value is 2 nm less than the thickness before annealing, indicating 20 % volume reduction. Similar reduction is found for TiO_2 thin film (18%) annealed in the same condition, meaning that the thermal annealing leads to more condensed TiO_2 film.

6.3.5. Miscibility mechanism.

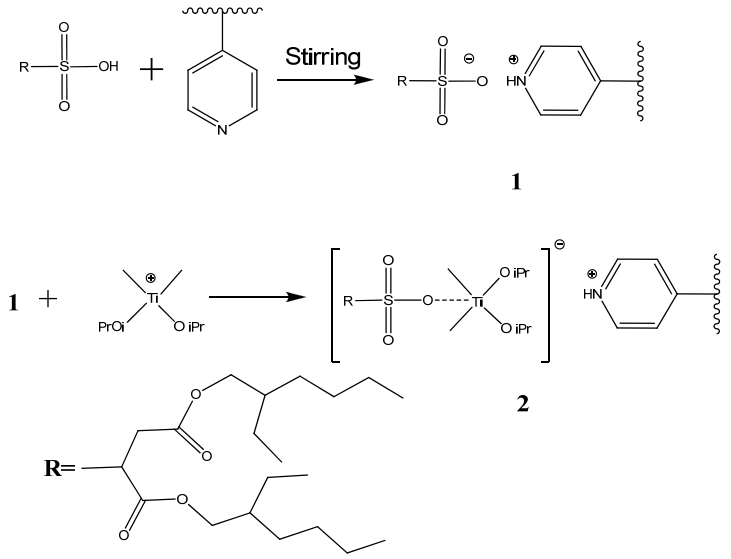

Scheme 1. Scheme of coordination interaction between the $P4VP_{100}$ $(AOT)_{1.0}$ complex and PAOT.

It is well-known that interaction between the pyridine units and titanium is weak, and limited amount of TiO_2 precursor can be incorporated into P4VP domains.[10, 20, 37]

Here we attempt to show that miscibility of precursor is due the supramolecular interactions while the polymeric structure is a key to enhance partitioning capacity of the template. Scheme 1 shows that the sulfonic acid group form ionic bond with pyridine units by proton transfer (compound **1**). The later can partially dissociate in polar solvent, like chloroform, into negatively charged ions (AOT-sulfate) and positive charged protons P4VP-H. The sulfonate, AOT-sulfate is a Lewis bases, can coordinate with PAOT through titanium (IV) and eventually form a *giant* stable complex (*giant* refer to macromolecule like precursor). Therefore we anticipate that complexation of the pyridine via a Lewis acid - Lewis base interaction take places, similar interaction has been reported for a complex of tetramethanesulphonate titanium (IV) and pyridine.[33] Such a complex is strong enough to account for the miscibility of the blend in the present system.[32]

FT-Raman is used to probe the supramolecular interaction between a P4VP homopolymer and PAOT complex. Figure 7 shows Raman spectra of the blend in the solid state with a mass ratio of 1:1. In the wavenumber range form 1570-1680 cm^{-1}, PAOT is Raman inactive, and P4VP shows a peak at 1597 cm^{-1}, assigned to the free pyridine ring. This peak is well-known to be sensitive to the environment, for instance, in case of ionic interaction, it shifts to 1637 cm^{-1},[38] for a metal coordination it shifts to ca.1620 cm^{-1},[39] or for hydrogen bonding it shifts to ca.1600 cm^{-1}.[40, 41] In the present study a shift from 1597 cm^{-1} to 1637 cm^{-1}, indicating the formation of ionic bond between sulfonic groups of AOT and pyridine units. In addition, presence of a shoulder at 1600 cm^{-1} suggests some hydrogen bond between AOT and P4VP. In a binary mixture of a non-protonated P4VP and PAOT, the peak position of the pyridine ring in the Raman spectrum is not affected at all. However, as discussed earlier, blends containing P4VP(AOT) shows two peaks characteristic of ionic and hydrogen bonding. Besides that, a new peak appears at 1620 cm^{-1}, which strongly indicates some interaction between sulfonate / PAOT group and pyridine. Yet sulfonate group of the complex $P4VP(AOT)_{1.0}$ coordinates with Ti(IV) of the PAOT, such a complex is positively charged and it is susceptible to bind with a negatively charged pyridinium, in a similar way to metal coordination interaction.

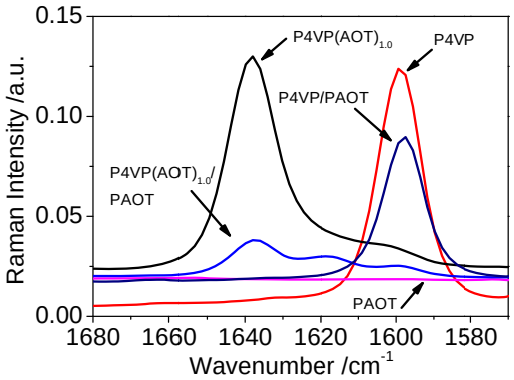

Figure 7. FT-Raman spectra of P4VP(AOT)$_{1.0}$ complex and PAOT mixture with a weight ratio of 1:1.

6.3.6. Morphology diagram.

Based on the TEM investigations, a diagram of the morphology of the blends is shown in Figure 8. The horizontal axis represents the ratio of the total mass of complex P4VP$_m$ (AOT)$_{DN}$, denoted as f_{comp}, and the vertical axis represents the molar ratio of Ti/pyridine, denoted as R.

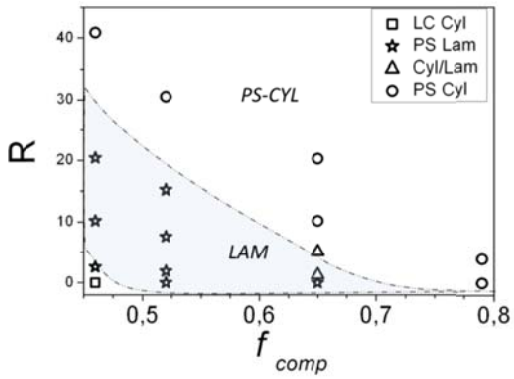

Figure 8. Tentative morphological of PAOT and PS$_{390}$-P4VP$_{140}$(AOT)$_{DN}$ as a function of the mass fraction of the complex (f_{comp}) and the molar ratio R.

So far, regardless the compositions of the mixtures, the solution does not show precipitation, nor a macrophase separation in films, even at very high molar ratio (R>40). Accordingly, morphological control of the blend becomes accessible because of the selective incorporation of PAOT guided by the microdomains structure. In principle variety of morphology are accessible, which is an advantage over the well-established sol-gel technology. Because the partitioning of the inorganic precursor is

limited to low molar ratio, and often, the high selectivity of the solvent results in precipitation/gelation of the block copolymer template.[16] It should be noted that the morphology are well-defined in particular at high protonation degree and concentration of PAOT. This is supported in the thin film investigation, in particular after removal of the organic moieties.

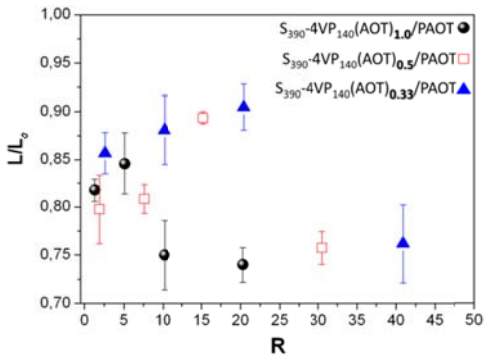

Figure 9. Summary of the variation of the ratio L/L_0 as a function of R, where L is the structural period of the blends and L_0 is the natural period of the pure block copolymer complex.

It is useful to plot the variation of the period depending on the composition of the blend. Figure 9 shows the variation of the ratio L/L_0 as a function of R, where L is the structural period of the blends and L_0 is the natural period of the pure block copolymer complex.[28] The graph demonstrates that, (i) L/L_0 is smaller than 1, suggesting that the miscibility is due to specific interactions of PAOT and P4VP(AOT), in agreement with FT-Raman analysis. Note that a different behaviour is observed in the case of swelling of block copolymer lamellae with a solvent or a homopolymer, in that case, the ratio is always greater than 1.[42] (ii) Monotonic increase of the period with R, ensue from incorporation of PAOT around the P4VP chain and assisted by AOT;[43] (iii) Structural change leads to a net reduction of the period whose occurrence depends strongly on the degree of protonation. For instance, at high degree of protonation a low amount of PAOT is required to alter the structure which clearly support the importance of the protonation on the localization of PAOT; (IV) Above the transition the long period depends weakly on R, this may indicate homogenous incorporation of PAOT within P4VP(AOT) domains.

The last issue is related to the structure of the films after H_2 Plasma. Regardless of the blend composition, presence of the complex generates a fine TiO_2 nanoparticle (~10nm). Since films prepared from pure PAOT are smooth, we assume that the complex catalyses or partially precondenses the PAOT. However, the origin of the well-defined size remains unknown and requires further investigations. Furthermore, to templates the block copolymer nanostructure requires a high degree of protonation, while the pattern morphology is defined by the PAOT concentration. For low protonation degree, a sparse pattern consisting of 10 nm TiO_2 particle is formed ordered structure evolve only for high concentration of PAOT. This is in agreement with the influence of PAOT on the periodic length as discussed above (cf. Figure 9).

6.4. Conclusions.

We have studied the properties of a poly(titanium isopropyl oxide) (PAOT) in thin films as a new precursor for TiO_2. We demonstrated that such a precursor can be processed with conventional spin-coating technique. H_2 plasma treatment leads to films that are smooth with a thickness ranging from a few nm to 100 nm, cracks develop for thicker films. High temperature annealing transforms the low crystalline TiO_2 rutile phase to highly crystalline anatase phase.

We have demonstrated a new way to prepare a nanocomposite from a miscible mixture of PAOT an ionic complex of a block copolymer containing pyridine and sulfonated surfactant AOT. The surfactant synergistically influences the morphology, orientational order of the template, enhances miscibility and selectivity of PAOT with P4VP(AOT) via coordination interaction between sulfonate/titanium(IV). Elimination of the organic moieties enables preparation of nanostructured TiO_2 thin films, such as discontinues or percolated nanoparticle, and nanopores, which replicates the morphology of block copolymer templates.

6.5. References.

[1] X. Chen, S. S. Mao, *Chem. Rev.* **2007**, *107*, 2891.

[2] O. Carp, C. L. Huisman, A. Reller, *Prog. Solid State Chem.* **2004**, *32*, 33.

[3] M. Gratzel, *Nature* **2001**, *414*, 338.

[4] A. Hagfeldt, M. Graetzel, *Chem. Rev.* **1995**, *95*, 49.

[5] A. L. Linsebigler, G. Lu, J. T. Yates, *Chem. Rev.* **1995**, *95*, 735.

[6] A. Mills, S. Le Hunte, *J Photochem. Photobiol. A* **1997**, *108*, 1.

[7] S. A. Bilmes, P. Mandelbaum, F. Alvarez, N. M. Victoria, *J. Phys. Chem. B* **2000**, *104*, 9851.

[8] X. Mingxia, Z. Qinglin, L. Hongxing, D. Guozhang, Y. Hongchun, W. Taihong, Z. Bingsuo, W. Yanguo, *Nanotechnology* **2009**, *20*, 055605.

[9] Y. Huogen, Y. Jiaguo, C. Bei, L. Shengwei, *Nanotechnology* **2007**, *18*, 065604.

[10] X. Li, K. H. A. Lau, D. H. Kim, W. Knoll, *Langmuir* **2005**, *21*, 5212.

[11] P. S. Chinthamanipeta, Q. Lou, D. A. Shipp, *ACS Nano* **2010**, *5*, 450.

[12] G. J. d. A. A. Soler-Illia, A. Louis, C. Sanchez, *Chem. Mater.* **2002**, *14*, 750.

[13] X. Li, H. Yang, C. Li, L. Xu, Z. Zhang, D. H. Kim, *Polymer* **2008**, *49*, 1376.

[14] E. L. Crepaldi, G. J. d. A. A. Soler-Illia, D. Grosso, F. Cagnol, F. Ribot, C. Sanchez, *J. Am. Chem. Soc.* **2003**, *125*, 9770.

[15] P. Yang, M. Yang, S. Zou, J. Xie, W. Yang, *J. Am. Chem. Soc.* **2007**, *129*, 1541.

[16] Y.-J. Cheng, J. S. Gutmann, *J. Am. Chem. Soc.* **2006**, *128*, 4658.

[17] S. H. Kim, O.-H. Park, F. Nederberg, T. Topuria, L. E. Krupp, H.-C. Kim, R. M. Waymouth, J. L. Hedrick, *Small* **2008**, *4*, 2162.

[18] I. W. Hamley, *The physics of block copolymers* Oxford University Press Oxford 1998.

[19] C.-C. Weng, K.-H. Wei, *Chem. Mater.* **2003**, *15*, 2936.

[20] A. H. Yuwono, Y. Zhang, J. Wang, X. H. Zhang, H. Fan, W. Ji, *Chem. Mater.* **2006**, *18*, 5876.

[21] M. J. Fasolka, A. M. Mayes, *Annu. Rev. Mater. Res.* **2001**, *31*, 323.

[22] A. P. Marencic, R. A. Register, *Annu. Rev. Chem. Biomol. Eng.* **2010**, *1*, 277.

[23] W. van Zoelen, E. Polushkin, G. ten Brinke, *Macromolecules* **2008**, *41*, 8807.

[24] K. Albrecht, A. Mourran, X. Zhu, T. Markkula, J. Groll, U. Beginn, W. H. de Jeu, M. Moeller, *Macromolecules* **2008**, *41*, 1728.

[25] J. W. Lee, C. Lee, S. Y. Choi, S. H. Kim, *Macromolecules* **2009**, *43*, 442.

[26] J. Kao, J. Tingsanchali, T. Xu, *Macromolecules* **2011**, *44*, 4392.

[27] H.-S. Sun, C.-H. Lee, C.-S. Lai, H.-L. Chen, S.-H. Tung, W.-C. Chen, *Soft Matter* **2011**, *7*, 4198.

[28] J. Wang, W. H. de Jeu, P. Müller, M. Möller, A. Mourran, *Macromolecules* **2012**, *45*, 974.

[29] J. Livage, M. Henry, C. Sanchez, *Prog. Solid State Chem.* **1988**, *18*, 259.

[30] U. Schubert, *J. Mater. Chem.,* **2005**, *15*, 3701.

[31] X. Zhu, M. Jaumann, K. Peter, M. Möller, C. Melian, A. Adams-Buda, D. E. Demco, B. Blümich, *Macromolecules* **2006**, *39*, 1701.

[32] Y. Wan, Zhao, *Chem. Rev.* **2007**, *107*, 2821.

[33] R. C. Paul, V. P. Kapila, S. K. Sharma, *J. Inorg. Nucl. Chem.* **1974**, *36*, 1933.

[34] I. n. Szilágyi, E. Königsberger, P. M. May, *Inorg. Chem.* **2009**, *48*, 2200.

[35] D. Lin-Vien, N. B. Colthup, W. G. Fateley, J. G. Grasselli, *The Handbook of Infrared and Raman Characteristic Frequencies of Organic Molecules*, Academic Press, 1991.

[36] V. Zeleňák, V. Hornebecq, S. Mornet, O. Schäf, P. Llewellyn, *Chem. Mater.* **2006**, *18*, 3184.

[37] N. Steunou, S. Forster, P. Florian, C. Sanchez, M. Antonietti, *J. Mater. Chem.* **2002**, *12*, 3426.

[38] J. Ruokolainen, M. Torkkeli, R. Serimaa, S. Vahvaselkä, M. Saariaho, G. ten Brinke, O. Ikkala, *Macromolecules* **1996**, *29*, 6621.

[39] J. Ruokolainen, J. Tanner, G. ten Brinke, O. Ikkala, M. Torkkeli, R. Serimaa, *Macromolecules* **1995**, *28*, 7779.

[40] H. Kosonen, S. Valkama, J. Ruokolainen, M. Torkkeli, R. Serimaa, G. t. Brinke, O. Ikkala, *Eur. Phys. J. E* **2003**, *10*, 69.

[41] J. Ruokolainen, G. ten Brinke, O. Ikkala, M. Torkkeli, R. Serimaa, *Macromolecules* **1996**, *29*, 3409.

[42] W. van Zoelen, G. Alberda van Ekenstein, O. Ikkala, G. ten Brinke, *Macromolecules* **2006**, *39*, 6574.

[43] S. Valkama, T. Ruotsalainen, H. Kosonen, J. Ruokolainen, M. Torkkeli, R. Serimaa, G. ten Brinke, O. Ikkala, *Macromolecules* **2003**, *36*, 3986.

Chapter 7 Biaxial Alignment of Block Copolymer - Complex Lamellae

7.1. Introduction.

Unidirectional sliding of a rod of polytetrafluoroethylene (PTFE) against a smooth and rigid surface (e.g. glass), results in a friction-deposited layer of single-crystalline PTFE oriented along the sliding direction.[1-3] The properties of the resulting surface are well documented and enable uniaxially oriented growth of organic material.[2-7] However, reports addressing the orientation of a coil-coil block copolymer (bcp) on such a transferred layer are still scarce. The difficulty is related to the physical properties of the block (coil structure) which is only weakly sensitive to the crystal structure of the underlying substrate. In this work this problem is mitigated by introducing small molecules (ligands) selected (i) to interact specifically with one of the blocks through hydrogen bonds,[8, 9] and (ii) to physically adsorb onto PTFE-rubbed substrate.[5] The interaction of the ligands with the substrate, i.e. the PTFE layer, controls the in-plane orientation of the microdomain structure, while the stoichiometry of the complex defines the block copolymer morphology. This possibility is of considerable interest. While orientation of block lamellae in a film along the substrate normal is by now well established,[10, 11] it is still difficult to obtain in addition azimuthal (in-plane) uniformity.

Two structurally different ligands were selected with a terminal carboxylic acid group to form a complex with the polybase P4VP, while as second block PS was used. In thin films, a degree of complexation of 0.75 generates lamellae. Because the ligands form stacks parallel to the SiO_2 substrate, the block copolymer lamellae orient perpendicularly to the film.[10] However they lack of azimuthal order in the plane of the film, resulting in a fingerprint texture. The friction-deposited PTFE layer consists of periodic stripes with an average height of about 4 nm. On such a substrate, the lamellae of the block copolymer complex remain orthogonal to the interfaces but additionally align uniaxially along the PTFE stripes.

In the following we give a comprehensive account of the results obtained. First, we discuss the morphology and orientational order of the lamellar ligands. We combine

Scanning Force and Field-Emission Electron Microscopy (SFM and FESEM) to assess the homogeneity and surface structure of films with a thickness of 40-100 nm. FE-SEM also provides side observation allowing a view of the internal structure of the lamellae and their orientation relative to the support. In the second part, we present the grazing-incidence small and wide angle X-ray scattering results (GISAXS and GIWAXS) for one of the samples. The combination of these techniques allows presenting a full quantitative model of the uniform film structure.

7.2. Experimental section

7.2.1. Materials.

Two block copolymers were investigated PS_{330}-$P4VP_{130}$ (M_w/M_n=1.07) and PS_{190}-$P4VP_{100}$ (M_w/M_n=1.12); in which the subscripts denote degree of polymerization. They were synthesized by living anionic polymerization, as described elsewhere.[26] All the chemicals and solvents are analytical pure and purchased from Sigma-Aldrich.

7.2.2. Synthesis of ligands.

The synthesis of ligand L**1** was described previously.[12] L**2** was prepared according to the following procedure. To a solution of 5-(2-octyldodecyl)-2,2'-bithiophene[27] (0.50 g, 1.5 mmol) in 100 mL dry THF *n*-BuLi (1.6 M, 0.95 mL, 1.52 mmol) was added dropwise at 0 °C. After 1 h the reaction mixture was cooled down to -78 °C and CO_2 was led into the solution over a period of 5 h. The mixture was then warmed up to room temperature and stirred overnight. 1M HCl was added dropwise, and the mixture was diluted with dichloromethane. The organic phase was dried over $MgSO_4$. After evaporation of the solvents the crude mixture was purified by column chromatography (SiO_2, *n*-hexane:ethyl acetate, 3:1 (v:v)) resulting 5'-(2-octyldodecyl)-2,2'-bithiophene-5-carboxylic acid (L**2**) as a brownish solid (0.16 g, 22%). ^{1}H NMR (400 MHz; $CDCl_3$): [ppm] = 7.74 (1 H, d, *J* = 4.0 Hz, *H4*), 7.12 (1 H, d, *J* = 3.6 Hz, *H3'*), 7.07 (1 H, d, *J* = 4.0 Hz, *H3*), 6.68 (1 H, d, *J* = 3.6 Hz, *H4'*), 2.72 (2 H, d, *J* = 6.8 Hz, CH-*CH_2*-T), 2.72 (1 H, bs *CH*-CH_2-T), 1.32-1.20 (32 H, m, alkyl *CH_2*), 2.72 (6 H, t, *J* = 6.8 Hz, *CH_3*). MS *m/z* (CI): 491 [M^+]. Anal. Calcd. for $C_{29}H_{46}O_2S_2$: C 70.97, H 9.45%. Found C 70.79, H 9.46%.

7.2.3.Complex preparation.

The complexes were prepared according to the literature procedure.[15] In brief, the block copolymer and the ligand were dissolved in chloroform and stirred in the dark overnight. Subsequently, the solvent was evaporated by rotary evaporation under reduced pressure. The solid was collected, re-dissolved in chloroform, and filtered with a 0.2 μm PTFE syringe filter. The final concentration of the solutions was controlled to 0.5wt% and stored in brown GC vials. Hydrogen bonding between the block copolymer and the ligand was assessed with infrared spectroscopy, for details see the supporting information. All solvents used were of analytical grade and bought from VWR GmbH, Germany. Silicon wafers (100) were purchased from Si-Mat GmbH.

7.2.4. Film preparation.

The films were prepared by spin coating a solution of the block copolymer complex in chloroform onto a pre-cleaned silicon wafer or onto a PTFE rubbed surface. The unidirectional rubbing was done manually at 300 °C. Annealing of the thin films was carried out in a closed vessel containing a small amount of benzene.

7.2.5. Characterization methods.

The morphology of the thin films was investigated by tapping mode SFM (NanoScope V, BrukerAXS) under ambient conditions. Scanning Electron Microscopy (SEM) was performed using a Hitachi S4800 high-resolution Field Emission Scanning Electron Microscope with an accelerating voltage of 1-1.5 kV. In order to avoid any artifacts no metal coating was used. To enhance the contrast the ligand was removed by washing the thin film in ethanol, a good solvent for the ligand but a bad one for PS. After washing the morphology of the micro-phase separation was still the same, though shrinking occurred of the domains in which the ligand was originally present.[16] Grazing incidence wide and small angle X-ray scattering (GIWAXS and GISAXS) measurements were performed at the synchrotron beamline BW4 of the DORIS III storage ring (HASYLAB at DESY) in Hamburg. The sample-detector distances were set to 107 and 2088 mm, respectively. In GIWAXS the incident angle was 0.2° and in GISAXS 0.4°. The scattering signal was recorded by a

2D detector (MARCCD, 2048x2048 pixels). The specular peak or the small angle scattering were blocked by a rod-shaped beam stop. Detailed GISAXS and GIWAXS setting description can be found elsewhere.[18-20] IR spectra were recorded using a Nicolet NEXUS 670 Fourier Transform IR spectrometer at a resolution of 4 cm^{-1}.

7.3. Results and discussions.

7.3.1. Structure of pure ligands and block copolymers

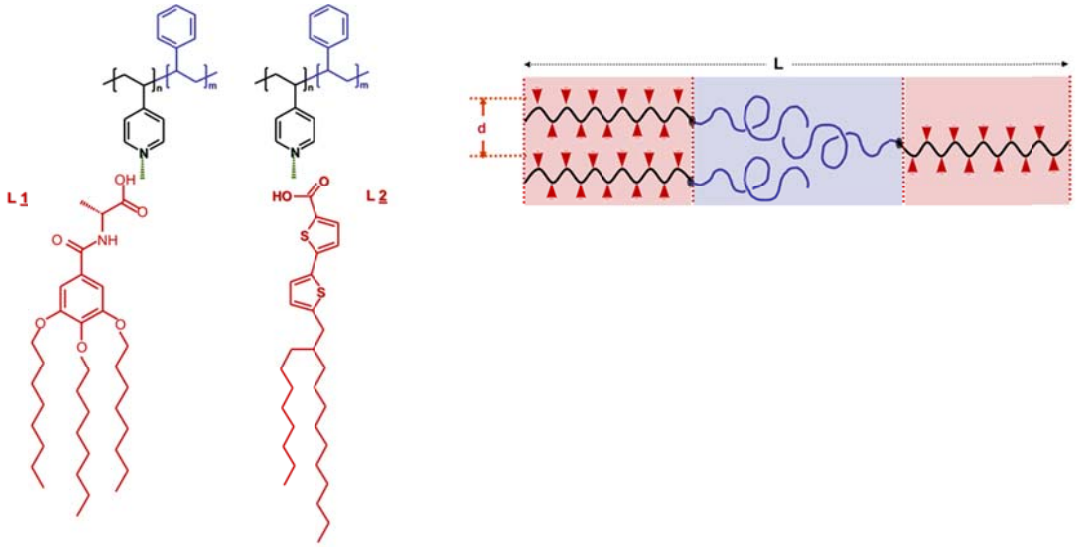

Scheme 1. Structure of the ligands 4´-(3´´,4´´,5´´-tris(octyloxy) benzamido) propanoic acid denoted as **L1** and 5'-(2-octyldodecyl)-2,2'-bithiophene-5-carboxylic acid denoted as **L2** with hydrogen bonds between P4VP and the ligands (a). Schematic illustration of the lamellar microphase-separated structure in the block copolymer complex (b), d is about 4 nm and L is about 40 nm.

The ligands are denoted as L**1** and L**2** (see Scheme 1). Both compounds crystallize in bulk with a melting temperature around 114 and 45 °C, respectively. In thin films the ligand self-assembles into dimers that in turn form cylinder (columnar) (L**1**)[12] or lamellar stacks (L**2**) (refer to Figure S1 and S2 in Supporting Information, respectively). The copolymer is poly (styrene- b -4-vinylpyridine) (PS-P4VP). The ligands readily bind to the pyridine unit through hydrogen bonds (refer to Figure S1 and S2 in Supporting Information).[8, 9, 13] However, depending on the strength of the hydrogen bonds, steric interaction limits the degree of complexation and phase

separation might occur at high degree of complexation.[14] A degree of complexation of 0.75 ensures that the block copolymer self-assemble in lamellae while the ligands form a smectic layer orthogonal the block copolymer interface. Here 0.75 is the number of ligand per P4VP unit, thus specifying the ligand/monomer ratio in the system. Scheme 1 illustrates schematically the hydrogen-bonded structure.

7.3.2. Morphology of block copolymers complex thin films on silicon wafer

Figure 1a shows an SFM height image of a thin film of the bcp complex PS_{330}-$P4VP_{130}$ (**L1**)$_{0.75}$ (subscribe denoted as the degree of polymerization) on bare SiO_2. The 2D-FFT of the height image is a halo indicating a short range orientational order with a lamellar period of about 45 nm. In addition, the side view on the edge of a fracture in Figure 1b clearly indicates that the lamellae are perpendicular to the substrate plane. The film thickness is about 80 nm, almost twice the bcp period. This also holds for another block copolymer complex PS_{190}-$P4VP_{100}$(**L1**)$_{0.75}$ with a lamellar period of 26 nm (see supporting information S4). For the present thicknesses confinement effects due to the surface field can be excluded: the perpendicular orientation of the lamellae is solely associated with the ligand organization.[15, 16] The false color orientation map of Figure 1c indicates an average domain size of about 500-700 nm.

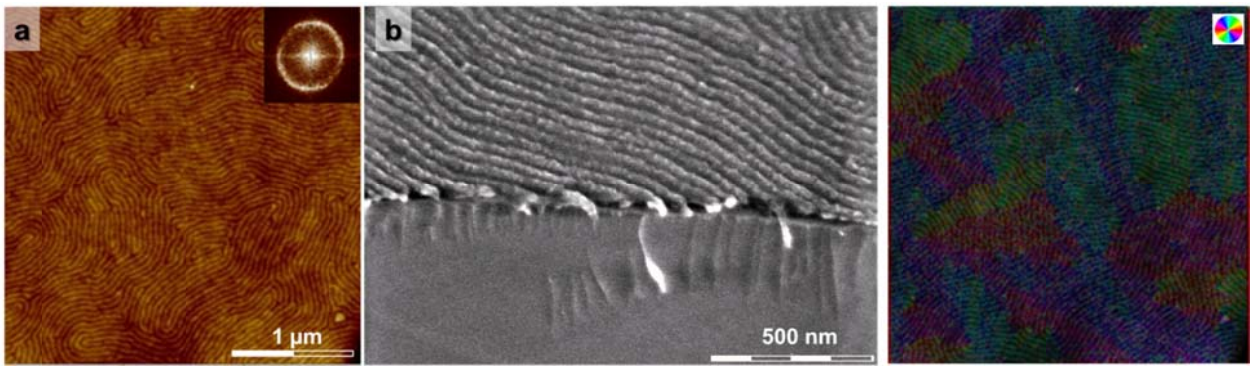

Figure 1. Thin film morphology of PS_{330}-$P4VP_{130}$ (**L1**)$_{0.75}$. (a) SFM height image, insert showed the 2D FFT which indicates an interlamellar spacing of about 45 nm; (b) tilted cross-sectional FESEM image (45°); (c) The false color orientation map of (a) indicates an average domain size of about 500-700 nm.

7.3.3. Morphology of block copolymers complex thin films on PTFE rubbing silicon wafer

Unidirectional sliding of a PTFE rod against a silicon substrate causes the transfer of regular lines having an average height of about 4 nm and a periodicity of about 65 nm (Figure 2). The structure of the resulting PTFE films has been well studied.[1, 6, 17] Such a surface has no effects on the orientational order of the pure block copolymer. Figure 3a shows that the pure block copolymer forms P4VP cylinders that are randomly oriented in the PS layers. Obviously, without the ligand the microdomain structure is insensitive to the underlying PTFE-lines. However, for the block copolymer complex remarkable alignment is observed. Figure 3b and 3c display uniaxial orientation of the lamellae parallel to the PTFE stripes. The 2D-FFT (inset in Figure 3c) shows well-defined peaks orthogonal to the rubbing direction. The peak position indicates a periodicity of 43 nm, the interlamellar period is not influenced by the underlying PTFE stripes. Moreover, a cross-sectional view of the film shows that the lamellae maintain their vertical orientation (Figure 3d). This will be made more quantitative below in the discussion of the GISAXS and GIWAXS data.

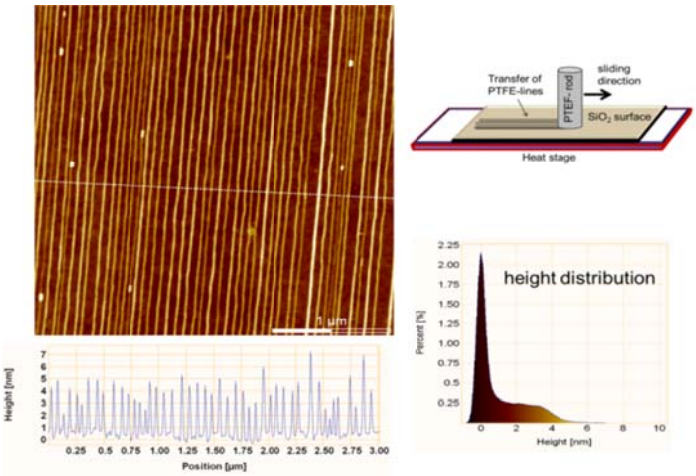

Figure 2. SFM height image of the friction-transferred PTFE stripes. The height distribution and the cross-section profile indicate a mean height and a periodicity of about 4 nm and 65 nm, respectively. The drawing illustrates the transfer process.

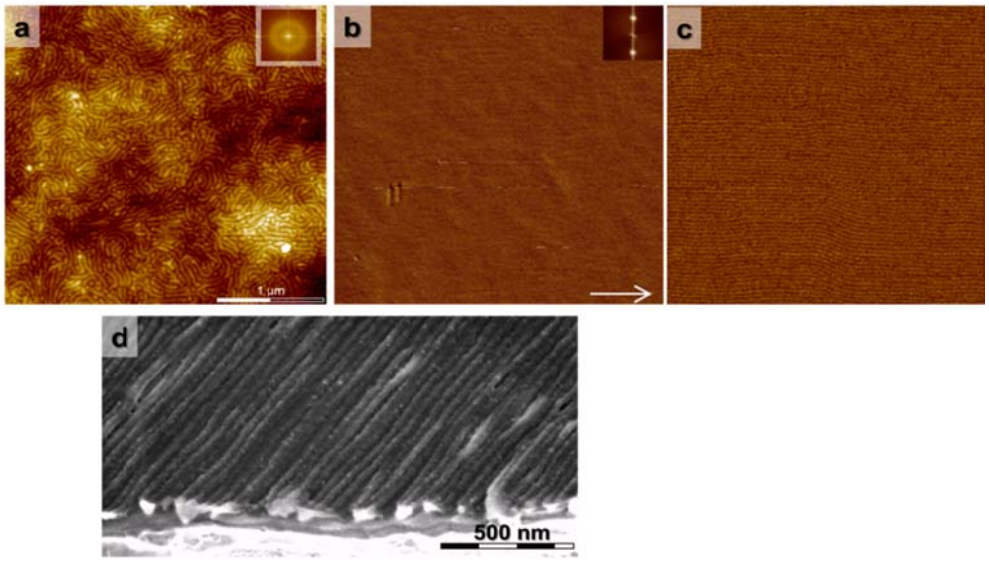

Figure 3. SFM height and phase image of a thin film deposited on PTFE stripes after annealing for 24 h in benzene vapor. (a) Cylindrical morphology of PS_{330}-$P4VP_{130}$ without ligands showing a random orientation insensitive to the underlying PTFE stripes. (b) Phase SFM image of the block copolymer complex PS_{330}-$P4VP_{130}$ $(\mathbf{L\underline{1}})_{0.75}$ on PTFE (scan size 10×10 µm^2 in 4480×4480 lines). The inset shows the corresponding 2D-FFT. (c) Enlarged view of (b) (scan size 3×3 µm^2 in 512×512 lines). (d) FESEM image of a cross-section viewed at a tilt angle of 45°. The arrow indicates the rubbing direction.

For the second compound PS_{330}-$P4VP_{130}(L\underline{2})_{0.75}$ (see Scheme 1) again a degree of complexation of 0.75 is required to form a lamellar phase. In thin films, the lamellae are orthogonal to the SiO_2/air interface without in-plane orientational order as for PS_{330}-$P4VP_{130}(L\underline{1})_{0.75}$. As expected, on a friction-deposited PTFE layer the lamellae align along the PTFE stripes (Figure 4) while the 2D-FFT (Figure 4, insert) indicates arcs orthogonal to the rubbing direction. The peak position indicates a periodicity of about 46 nm.

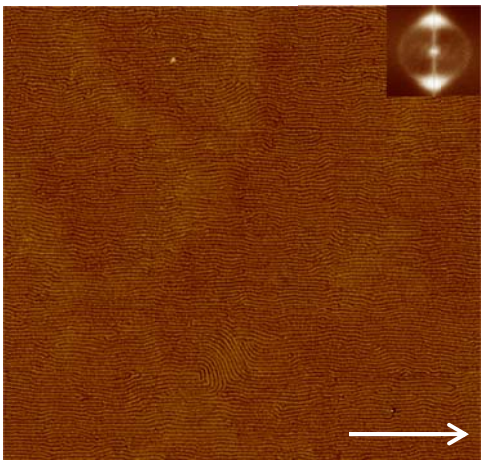

Figure 4. SFM phase images of PS_{330}-$P4VP_{130}$ (**L2**)$_{0.75}$ on PTFE (scan size 6×6 μm^2 in 4096×4096 lines), PTFE-lines, respectively. The arrow indicates the rubbing direction. Insert shows a 2D FFT of a 20×20 μm^2 images.

7.3.4. GISAXS and GIWAXS

Grazing-incidence wide and small angle X-ray scattering (GIWAXS[18] and GISAXS[19] was performed on films (about 40 nm thick) of PS_{330}-$P4VP_{130}$(**L2**)$_{0.75}$ at beamline BW4 at HASYLAB (Hamburg, Germany).[20] Both an unoriented sample and a sample aligned by PTFE were probed. In the latter case the X-ray beam was either parallel or perpendicular to the alignment direction (long direction of the PTFE fibers). The 2D GISAXS data and line cuts are shown in Figure 5 in the two directions parallel and perpendicular to the preferred long axis. The simplest feature is the peak corresponding to 41-43 nm, the block copolymer lamellar period (compare to about 45 nm from SFM). At larger angles we find two x-ray peaks/features at *q*-values corresponding to 3.4 and 4.4 nm, respectively. As both values occur simultaneously in the unaligned samples, none of them can originate from PTFE. The length of the **L2** ligand in a fully stretched conformation is about 1.8 nm. Hence, the first dimension is close to the length of a free ligand dimer (about 3.6 nm). The second dimension of 4.4 nm can be attributed to a double layer of two ligands attached in opposite directions to the P2VP chain. Indeed at the relevant 0.75 average complexation, free ligands can be expected to form a dynamic equilibrium with ligands bound to the polymer.[21, 22] Smectic demixing (without macroscopic phase separation) has been proposed earlier to explain the X-ray features of another system

with a hydrogen-bonded polymer with mesogenic side chains.[23] In that case the two proposed components are the combination of the polymer with bound mesogen and the 'solvent' composed of the mesogens in the liquid state.

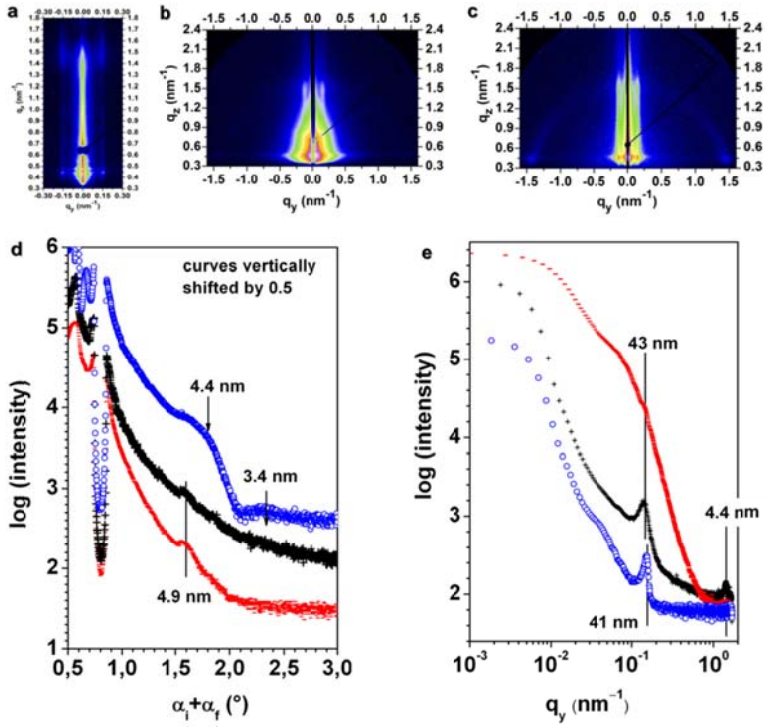

Figure 5. Top: 2D GISAXS data of PS_{330}-$P4VP_{130}$ (**L2**)$_{0.75}$ for an unoriented sample (a) and for oriented samples with the X-ray beam parallel (b) and perpendicular (c) to the preferred PTFE direction, respectively. Bottom: Detector cuts (d) and out-of-plane cuts (e). Curves with a bar, cross and circle symbols are for parallel PTFE orientation, perpendicular PTFE orientation and unoriented, respectively.

Regarding the orientation of the ligand lamellae we note that in the aligned sample a signal (corresponding to 4.4 nm, the smectic layer period) is only observed when the X-ray beam is perpendicular to the preferred PTFE direction. From this observation we can conclude to a rather simple structure, depicted in Figure 6 for a single block period. Both the block lamellae and the smectic layers are perpendicular to the substrate and mutually orthogonal. The origin of the ordering of the block copolymer lamellae is due to the ligands that want to be parallel to the PTFE stripes. Such an alignment of the ligands is very similar to the alignment of the nematic director to grooves in the substrates of liquid-crystal displays.[24, 25] This process in turn forces the block lamellae to align azimutally.

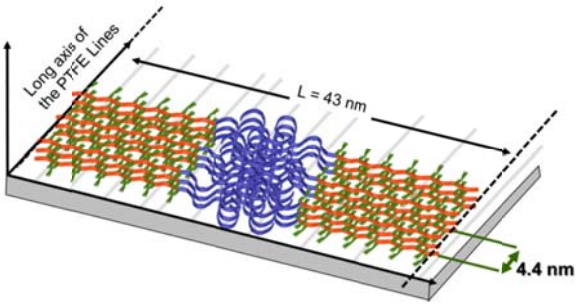

Figure 6. Model for the structure of PS_{330}-$P4VP_{130}$(**L2**)$_{0.75}$ on a PTFE covered substrate.

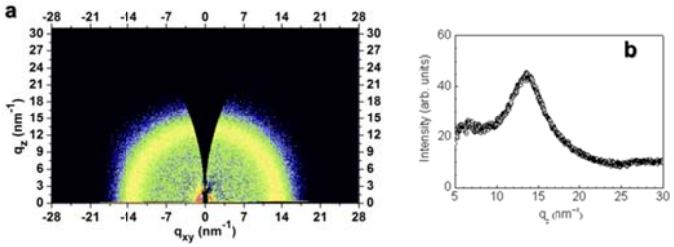

Figure 7. (a) 2D GIWAXS data of an unoriented sample of PS_{330}-$P4VP_{130}$(**L2**)$_{0.75}$. (b) Corresponding slice-integrated over 80-100°.

To determine the internal structure of the ligand lamellae GIWAXS is used (see Figure 7). For the unaligned sample the only feature is a broad ring with a maximum corresponding to 0.47 nm. The lineshape can be represented by a Gaussian with a FWHM of about 4 nm^{-1}. However, the limited dynamic range and complicated background do not allow much meaning to be assigned to this observation. Bulk WAXS on the strongly related homopolymer (P2VP(**L2**), not shown) give a similar strong broad ring at 0.46 nm. The obvious interpretation is a smectic-like structure consisting of stacked liquid layers. In the GIWAXS pattern of aligned samples (either with the X-ray beam parallel or perpendicular to the preferred direction, see supporting information Figure S5) we still observe the broad ring. In addition a multitude of discrete peaks is found that can be assigned to the underlying PTFE structure by comparing with GIWAXS data for a pure friction-deposited PTFE film.[17] There is no evidence for crystallinity inside the smectic layers of the ligands.

7.4. Conclusions.

We present a simple and convenient method to align block copolymer (bcp) lamellae perpendicular to the air/substrate interface with additionally a long-range in-plane orientational order. This is achieved by a combination of supramolecular liquid crystalline (LC) ordering in the block copolymer complex and a PTFE thin layer produced by the well-known friction-deposition techniques. Remarkably, the thickness of the aligning PTFE layer is only ca. 4 nm while the block copolymer film thickness is of about 100 nm. Wedge-shaped mesogens control the self-assembly of the block copolymer rendering vertical orientation of the microdomains. In addition the vertical lamellae orient parallel to the friction-deposited PTFE layer leading to long-range lateral ordering. This technique has the advantages of simplicity as compared to other approaches and creates new opportunities for manufacturing nanoscopic device components. Additional asset is the easy introduction of functionality by altering the structure of the ligand or by the selective disruption of hydrogen bonds; all this provides unique possibilities for block copolymer nanotechnology.

7.5. References

[1] J. C. Wittmann, P. Smith, *Nature* **1991**, *352*, 414.

[2] J. K. Krüger, M. Prechtl, P. Smith, S. Meyer, J. C. Wittmann, *J. Polym. Sci. . B: Polym. Phys.* **1992**, *30*, 1173.

[3] J. K. Krüger, B. Heydt, C. Fischer, J. Baller, R. Jiménez, K. P. Bohn, B. Servet, P. Galtier, M. Pavel, B. Ploss, M. Beghi, C. Bottani, *Phys. Rev. B* **1997**, *55*, 3497.

[4] A. M. van de Craats, N. Stutzmann, O. Bunk, M. M. Nielsen, M. Watson, K. Müllen, H. D. Chanzy, H. Sirringhaus, R. H. Friend, *Adv. Mater.* **2003**, *15*, 495.

[5] D. E. Hooks, T. Fritz, M. D. Ward, *Adv. Mater.* **2001**, *13*, 227.

[6] P. Dietz, P. K. Hansma, K. J. Ihn, F. Motamedi, P. Smith, *J. Mater. Sci.* **1993**, *28*, 1372.

[7] C. Y. Yang, Y. Yang, S. Hotta, *Mol. Cryst. Liq. Cryst.* **1995**, *270*, 113.

[8] J. Ruokolainen, R. Mäkinen, M. Torkkeli, T. Mäkelä, R. Serimaa, G. t. Brinke, O. Ikkala, *Science* **1998**, *280*, 557.

[9] O. Ikkala, G. ten Brinke, *Science* **2002**, *295*, 2407.

[10] W. H. de Jeu, Y. Séréro, M. Al-Hussein, *Adv. Polym. Sci.* **2006**, *200*, 71.

[11] I. W. Hamley, *Prog. Polym. Sci.* **2009**, *34*, 1161.

[12] D. V. Anokhin, J. Lejnieks, A. Mourran, X. Zhu, H. Keul, M. Möller, O. Konovalov, N. Erina, D. A. Ivanov, *ChemPhysChem* **2012**, *13*, 1470.

[13] J. T. Korhonen, T. Verho, P. Rannou, O. Ikkala, *Macromolecules* **2010**, *43*, 1507.

[14] C. O. Osuji, C.-Y. Chao, C. K. Ober, E. L. Thomas, *Macromolecules* **2006**, *39*, 3114.

[15] K. Albrecht, A. Mourran, X. Zhu, T. Markkula, J. Groll, U. Beginn, W. H. de Jeu, M. Moeller, *Macromolecules* **2008**, *41*, 1728.

[16] J. Wang, W. H. de Jeu, P. Müller, M. Möller, A. Mourran, *Macromolecules* **2012**, *45*, 974.

[17] D. W. Breiby, T. I. Sølling, O. Bunk, R. B. Nyberg, K. Norrman, M. M. Nielsen, *Macromolecules* **2005**, *38*, 2383.

[18] J. Perlich, J. Rubeck, S. Botta, R. Gehrke, S. V. Roth, M. A. Ruderer, S. M. Prams, M. Rawolle, Q. Zhong, V. Körstgens, P. Müller-Buschbaum, *Rev. Sci. Instrum.* **2010**, *81*, 105105.

[19] P. Müller-Buschbaum, *Anal.Bioanal.Chem.* **2003**, *376*, 3.

[20] S. V. Roth, R. Döhrmann, M. Dommach, M. Kuhlmann, I. Kröger, R. Gehrke, H. Walter, C. Schroer, B. Lengeler, P. Müller-Buschbaum, *Rev. Sci. Instrum.* **2006**, *77*, 085106.

[21] W.-T. Chuang, H.-S. Sheu, U. S. Jeng, H.-H. Wu, P.-D. Hong, J.-J. Lee, *Chem. Mater* **2009**, *21*, 975.

[22] X. Zhu, U. Beginn, M. Möller, R. I. Gearba, D. V. Anokhin, D. A. Ivanov, *J. Am. Chem. Soc.* **2006**, *128*, 16928.

[23] M. Gopinadhan, E. S. Beach, P. T. Anastas, C. O. Osuji, *Macromolecules* **2010**, *43*, 6646.

[24] D. W. Berreman, *Phys. Rev. Lett.* **1972**, *28*, 1683.

[25] Y. Kawata, K. Takatoh, M. Hasegawa, M. Sakamoto, *Liq. Cryst.* **1994**, *16*, 1027.

[26] S. Mössmer, Vol. PhD, University of Ulm, Ulm 1999.

[27] S. Ellinger, U. Ziener, U. Thewalt, K. Landfester, M. Möller, *Chem. Mater.* **2007**, *19*, 1070.

Chapter 8 Blue Light Emitted Thin Films from Supramolecular Assembly of Oligothiophene/Poly (2-vinylpyridine-b-ethylene oxide) Complex

8.1. Introduction

Oligothiophenes is an interesting family of functional materials because of its outstanding physical and chemical properties.[1] The well-established thiophene-chemistry renders them versatile structures, and provides unique opportunities to tune the properties in a wide range. Oligothiophenes can be used in organic light-emitting diodes (OLEDs),[2, 3] organic thin film transistors (OFETs),[4-7] sensors, [8] and electrochromic devices,[9] which directly relate to the transverse π-π coupling between neighbouring thiophene rings. The challenges are their strong tendency to crystallize and the dewetting in thin films, which are problematic for the applications, where uniform films are required. One important issue for the real applications like optoelectronics is the proper controlling the ordering of the oligothiophene molecules and the orientation of the microdomains in thin films.[10, 11] To effectively transport the charges between the microdomains and the electrodes, the vertical orientation of the microdomains is preferential.[10] Most important, the geometry of the device has drastic impact on the performance of the device. For example, for the organic photovoltaic's (OPVs), after photo-excitation and charge separation the electrons and holes are transported back to the appropriate electrodes. The accepting and donating domains have strict geometrical requirements: the periodicity of the interface between the donor-acceptor must be prevalent (~10 nm), in addition, the donor and acceptor domains must form continues pathways to the electrodes.[10, 11] Such kind of ~10 nm pattern is also crucial for high performance OLEDs, which reduce the charge injection barriers and quenching at the electrodes.[11] However, it is difficult to obtain 10 nm length scale pattern with conventional lithographic technology but is possible with the self-assembly of the block copolymer.[12] Block copolymer bearing two or more incompatible blocks can form well-defined versatile microdomains (e.g. sphere,

cylinder, lamellae), with typical size about tens of nanometers.[13] The rod-coil block copolymer are indeed well known to self assemble into highly ordered nanostructures with lateral periodicity of 1-10 nm.[14-16] The vertical orientation of the microdomains is successfully achieved by applying of external fields,[5, 17, 18] neutralization of the surface energy,[19] and liquid crystalline (LC) field.[20]

Supramolecular approach in block copolymers pioneered by Ikkala and his coworkers[21-23] is used to control the lateral ordering of the microphase separation and the orientation of the microdomains in thin films.[24-29] In this approach, the small molecular mesogens are grafted to the polymer backbone via secondary interaction (i.e. hydrogen bond, ionic interaction, metal ligation), form comb-coil block copolymers. The addition of the small molecular mesogen changes the conformation of the polymer backbone[30] and increases the volume ratio of the complex part. Thus, the morphology transitions of the block copolymer complex occur. The comb-coil complex forms well defined microstructures similar to that of coil-coil block copolymer. The small molecular mesogens order into smectic structure inside one of the domains, form hierarchical structure-*within*-structure morphology (typical size 1-10 nm). This type of LC field can be used to manipulate the orientation of the microdomain in thin films. The LC filed generated by smectic ordering of the mesogen takes place with layers orthogonal to the block interfaces, allowing effortless alignment of the block copolymer microstructure, e.g. cylinder or lamellae perpendicular to the air/substrate interfaces.[25, 28, 29] This concept can be extended to control the self-assembly of the semiconductor molecules into nanostructures in the thin films. The benefit of this approach is that it circumvents the difficulties associated with the synthesis of monodispersed conjugated block copolymers[31] and tailing of the properties without synthesizing new block copolymers. Recently this approach has been employed in the literature to control the ordering of the rod-coil block copolymer[32, 33] and coil-coil block copolymer,[34]. In both cases, nanostructured thin films can be obtained. Xu and co-workers[34] attached a quarterthiophene to the side chain of poly (4-vinylpyridine) via hydrogen bonding between pyridine group and hydroxyl group on one side of the quarterthiophene, which acts as *p*-type semiconductors in field-effect transistors. In thin films, the quaterthiophenes complex assembles into microdomains with tens of nanometers in size, oriented normal to the surface. Such nanostructured thin films exhibit the same

motilities as that of the quaterthiophene mesogen (10^{-4} $cm^2/(V \cdot s)$). Compared with the complex between coil-coil block copolymer and normal mesogen (i.e. 3-pentadecylphenol, PDP)[24, 25, 29] or surfactant (dodecylbenzenesulfonic acid, DBSA)[26], limited attention had been paid to this field[32-34] and less is known about the complex of the block copolymer/semiconductive molecules, although, this supramolecular approach is a promising method for the fabrication of functional nanostructured organic semiconductor thin films.

The present work is focused on the nanostructure formation and optical properties of the block copolymer/oligothiophene complex in thin films. Similar to previous study,[28] a fully miscible block copolymer poly (2-vinylpyridine-b-ethylene oxide) (P2VP-PEO) is used. A new asymmetric oligothiophene molecule is synthesized (Scheme 1, denoted as R_v-2T-COOH), it has bithiophene as core. One side of the molecule is substituted with a branched 2-octyldodecyl group and the other side with a carboxylic group, which proves the hydrogen bonding with pyridine. The reason why we chose the branched 2-octyldodecyl group is based on the previous publication: introducing of 2-octyldodecyl into the oligothiophenes give good solubility oligomers with up to seven thiophene rings and had a great impact on the packing properties of the molecules in bulk and thin film.[35] It renders the oligomers good properties for monolayer formation and very good mobility in monolayer (10^{-2} $cm^2/(V \cdot s)$). In addition, the bulky alkyl tail is hydrophobic, which is incompatible with PEO and will enhance the separation strength of the blocks after complexation. Structure-*within*-structure with different morphologies are observed by combination of scanning force microscope (SFM) and X-ray reflectivity (XRR). The optical properties of the thin films are investigated with the UV-Vis spectrometer and fluorescence spectrometer. As complementary, the bulk structure of the complex is also investigated by wide angle X-ray scattering (WAXS) and polarized optical microscope (POM).

8.2. Experimental section.

8.2.1. Materials.

P2VP homopolymer with an M_w of 37500 and PDI of 1.07 was purchased from Sigma-Aldrich. P2VP-PEO block copolymer with a monomer ratio of 180/560 and a PDI of 1.06 was synthesized by sequential anionic polymerization described

elsewhere.[28] The ligand R_v-2T-COOH (Scheme 1) was prepared in lab. Silicon wafers (100) were purchased from Si-Mat GmbH (Germany), and optical polished quartz was supplied by Heraeus Quarzglas GmbH (Germany). All of the solvents used were analytical grades and purchased from VWR GmbH (Germany).

8.2.2. Sample Preparation.

The preparation of the complex is similar to the literature.[28] In general, P2VP-PEO block copolymer or P2VP homopolymer and R_v-2T-COOH were dissolved into chloroform, stirred in the dark overnight, and dried by using a rotor evaporator under reduced pressure. The solid was collected and re-dissolved into chloroform, and filtrated with a 0.2 μm PTFE syringe filter. The final concentration of the solutions was controlled to 0.5 wt% and stored in brown GC vials. The complex was denoted as P2VP(R_v-2T-COOH)$_x$-PEO or P2VP(R_v-2T-COOH)$_x$ for the block copolymer and homopolymer, respectively, x was the molar ratio between carboxylic group and pyridine group. Thin films were prepared by spin casting (Convac 1001S, Germany) of the solutions onto freshly cleaned silicon wafer at a speed of 2000 rpm for 30 s, resultant in a film thickness of 40 nm (ellipsometry, MM-SPEL-VIS, OMT GmbH, Germany). Before spin coating the silicon wafer was cleaned by sonication in isopropanol for 5 min, dried with air stream, and activated in UV/O_2 for 12 min. Thermal annealing of the films was performed under vacuum (2×10^{-2}mbar) at 60°C for 2 days. After thermal annealing, the films were allowed to cool down to ambient temperature slowly. This temperature was chosen because both of the PEO and P2VP(R_v-2T-COOH)$_x$ were molten, and had enough mobility for reorganization to reach thermal dynamic stable state, and this temperature was also not too high to destroyed the hydrogen bonding between carboxylic group and pyridine group, and prevented the possible degradation of the ligand. Thin films used for optical properties were prepared on the quartz substrates and went through the same treatment as those on the silicon wafer.

8.2.3. Characterizations.

IR spectra (resolution of 4 cm^{-1}) were recorded by using a Nicolet NEXUS 670 Fourier Transform IR spectrometer. Samples were prepared by drying several droplets

of 0.5wt% solution onto KBr plates at room temperature. For each spectrum more than 200 scans were averaged to enhance the signal to noise ratio. DSC measurements were performed on a Netsch DSC 404 instrument purged with N_2 stream. For each measurement, ~5 mg of sample was sealed in an aluminum pan using an identical pan as a reference. Both of the samples were heated to isotropic temperature and kept at that temperature for 2 minutes to erase the thermal history, after that the sample was cooled and reheated with a rate of 10 °C/min. Polarized Optical Microscopy (POM) was done on a Carl Zeiss Axioplan 2 imaging polarizing microscope equipped with a Mettler Toledo FP82HT hot stage connected to a Mettler Toledo FP90 processor. The micrographs were recorded with a Carl Zeiss AxioCam MRc digital camera. The Small Angle and Wider Angle X-Ray scattering experiments were done on a powder diffractometer (STADI MP vertical from STOE, Darmstadt, Germany) with focusing Ge-monochromator (Johann-type) PSD and cobalt anode. The experiments were performed on powder samples under transmission geometry. The morphology of the complex thin film was investigated by a tapping model SFM (NanoScope V, Digital Instruments Veeco Instruments Santa Barbara, CA) under different temperature. The temperature was controlled with a hot stage controlled by a MMHTRS High Temperature Heater Controller (Digital Instruments, Veeco Instruments, Santa Barnara, CA). Commercial available standard silicon cantilevers (PPP-SEIH-W from Nanosensors) with a spring constant of 42 N/m and an oscillation frequency of ~320 kHz were used. The data were processed by using NanoScope software Analysis, version 1.10. XRR was performed at JCNS-2 and PGI-4, Forschungszentrum Jülich using a D8 Advance X-ray reflectometer from Bruker AXS (Karlsruhe, Germany). A Cu X-ray tube with a line source (focal spot 12×0.04 mm^2) provided Cu K_α radiation with λ=0.1542 nm. A parabolic graded multilayer system (Göbel mirror) converted the divergent beam into an almost parallel beam (divergence <0.03°) and suppressed the Cu K_β radiation. The scattering plane was vertical and the sample remained horizontal. After reflection at the sample stage the intensity was collected by a NaI scintillation detector. The intensity was measured as a function of the scattering vector $q = (4\pi/\lambda)\sin\theta$, in which 2θ was the scattering angle. The latter was fixed at twice the incident angle θ, which sets q along the film normal. The measured intensity was corrected for the footprint of the X-ray beam, which overflows the sample below θ=0.8°. The data were analysed using an iterative matrix formalism derived from the

Fresnel equations. Three parameters were allowed to vary during the fit: the thickness, the electron density, and surface roughness. The thickness, electron density, and roughness of native SiO_2 were predetermined and they were fixed for all of the fits. Absorption spectra of the complex, both in solution and thin films were measured with a JASCO V-610 UV-Vis Spectrometer (JASCO GmbH, Germany). The concentration was 10^{-5} mmolL^{-1}. Fluorescence emission spectra in both of solution and thin films were measured with a FLUROMAX-4P Spectrometer (HORIBA Jobin Yvon GmbH), The spectra were excited at the wavelength of the respective UV/Vis absorption maxima. The quantum yield of the complex thin films was measured on the same machine with an integral sphere method under transmission model.

8.3. Results and discussions.

8.3.1. Complex formation.

The selective interaction between the carboxylic acid of the ligand and pyridine units of P2VP is first investigated using FTIR. Figure 1 presents the spectra of P2VP(R_v-2T-COOH)$_x$-PEO in the region of 1550-1800 cm^{-1}. In this region, P2VP has a distinct absorption band at 1589 cm^{-1}, corresponding to the stretching vibration of free pyridine ring, and the free ligand has a main absorption band at 1649 cm^{-1} and a shoulder at 1658 cm^{-1}, which can be assigned to the dimmerized carboxylic group in the pure ligand. Two peaks mean that two situations of the hydrogen bonding formation in the pure ligand.[36] After mixing of the ligand with block copolymer, the positions of the pyridine and carboxylic group bands change: the one at 1589cm^{-1} (pyridine) shifts to 1601cm^{-1}. Two bands from carboxylic group disappear and a new broad band with a maxima of 1696cm^{-1} appear, indicating that the dimmerization between the ligand molecules is destroyed and dominated by the interaction between the carboxylic group of the ligand and pyridine rings of P2VP.[36] The position of the complexed pyridine indicates that the interaction is mainly hydrogen bonding.[37, 38] Interestingly, the peak area at 1589cm^{-1} decreases, and correspondently the peak area at 1601cm^{-1} increases gradually with increasing of the molar ratio between carboxylic acid group and pyridine ring. However, the band at 1589cm^{-1} does not disappear even at the theoretical stoichiometric point, indicating that the real degree of complexation (x') deviates from the theoretical degree of complexation (x). The overlapped peaks

can be separated by peak deconvolution. The areas of the two peaks under 1589 and 1601cm^{-1} are obtained by fitting the experimental data with Gaussian function. Insert of the Figure 1a shows the result of x=0.25 as an example. As it can be seen, the fit fits the experimental data very well. The real degree of complexation (x') can be estimated using Eq. 7.1:[38]

$$x' = \frac{A_{1601}}{A_{1601} + \frac{\alpha_{1589}}{\alpha_{1601}} A_{1589}} \tag{7.1}$$

where A and α are the peak areas and absorption coefficients at respective wavenumber. It is found that the hydrogen bonding formed between the carboxylic group and pyridine rings of P2VP does not change the absorption coefficient significantly. Therefore $\alpha_{1589}/\alpha_{1601}$ almost equals to 1.[38] The real degree of complexation (x') estimated from Eq 7.1 is shown in Figure 1b. The x' starts to deviate from the x significantly at x=0.75, and a saturation of the degree of complexation is estimated to be around x'=0.7. The saturation of x' can be explained as following. Despite the exact value of the ligand volume is not known, the closest ligand distance can be estimated from the closed methyl group of the alkyl tails. The van der Waals radius of methyl group is ca.0.2 nm,[39] therefore the minimal distance between two ligands is ca.0.4nm, since it has two tails. The distance between two consecutive pyridine units in the P2VP chain cannot exceed 0.25nm at the most extended trans planar zigzag conformation.[40] When the ligand is mixed with the block copolymer, the selectively interaction between carboxylic acid group of the ligand and the pyridine units of P2VP drives the ligand to the P2VP domain. At the low degree of complexation, the density of the ligand along the P2VP backbone is low, therefore the space is enough for all of the ligands attaching to that of the P2VP backbone. The steric hindrance between the ligand can be avoided by stretching of the P2VP backbone. However, at the high degree of complexation the situation is severe, the space is not enough to let all of the ligands to attach to the backbone even when the P2VP backbone is fully stretched and the ligands take up side and down conformation in the smectic layers. Previously it has been found that the strong ionic interaction can drive all of the ligands to the polymer backbone. [28, 30, 41] In case, the ligand is not too bulky, such as AOT, which also has one branch tail, the smectic ordering is kept, and mostly the ligand takes the conformation of upside and down.[41]

If the ligand is too bulky (i.e. wedged shaped molecules) then it has to arrange around the polymer backbone, forming columnar phase at high degree of protanation.[28, 30] The same observation is reported by Ikkala's group and Chuang *et al*., for small molecules surfactant[42] and a wedged shaped molecule[43], respectively, where the hydrogen bonding is involved, and the saturation concentration is about 0.7 in both cases.

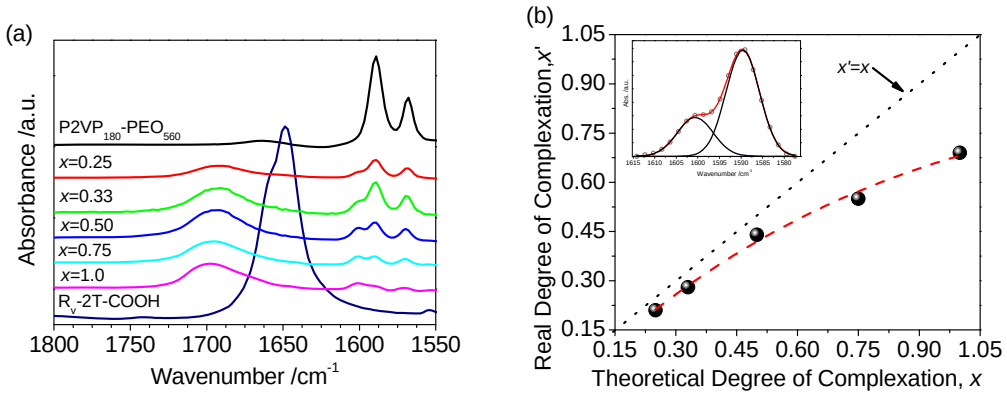

Figure 1. (a) FTIR spectra of P2VP(R_v-2T-COOH)$_x$-PEO in the region of 1550-1800cm^{-1}, and (b) theoretical degree of complexation (x) *vs.* the real degree of complexation (x'), the inserts show the peak deconvolution result of x=0.25 as an example, the open circles is the experimental data and the red line is the fitting.

The status of the free ligand in the block copolymer is crucial for the structure formation of the complex, either they dissolve in the block copolymer domain together with the bonded ligand, or precipitate and crystallize inside the block copolymer domain by themselves. These two situations can be discerned from the position of absorption band of the carbonyl group of the ligand. Lacking of the bands at 1649cm^{-1} and 1658cm^{-1} indicates that the ligands are in the dissolved state. In the following discussion, the values of theoretical degree of complexation x is used.

8.3.2. Bulk structure.

The bulk structure of the pure ligand and complex are investigated with POM and WAXS. Figure 2 and Table 1 present the results of the WAXS patterns of P2VP(R_v-2T-COOH)$_x$-PEO. In comparison, the results from the complex of P2VP homopolymer are also listed in the Table 1. The corresponding WAXS patterns are

shown in the support information (S.I. Figure S1a). The ligand shows lots of sharp peaks in both of small and wide angle region, indicating that it is crystalline at room temperature. The long period calculated from the most intensive peak at low angle region is *d*=2.28nm, with a possible second ordering at *d*=1.14nm. The ratio between the first and second ordering peaks is 1:2, indicating a possible layer structure in the crystals. The length of the R_v-2T-COOH in the fully stretched conformation is 1.8nm (MM2, ChemOffice). Therefore, the length of the dimmer is about 3.6nm, which is larger than the long period. It is reasonable to deduce that the ligand molecules tilt in the bulk. However, it is very difficult to estimate the tilting angle accurately without careful molecular simulation.

In general, the organization of the ligand in both of homopolymer and block copolymers is similar, here we focus on the block copolymer complex. The structure changes after complexation. All of the sharp peaks from the crystallization disappear and a new broader peak located at lower angle region appears in all of the compositions, indicating the formation of the liquid crystalline phase. In addition, a small shoulder peak is also observed, if one checks the patterns carefully. The faint second ordering peak means the low degree of ordering. The ratio between the first two peaks is 1:2, indicating the formation of the smectic layer structure in the complex. The *d* spacing of the first ordering peak is larger than that of the pure ligand, indicating that the P2VP chain penetrates into the middle of the ligand layer and swollen the double layer structures. The limited dependence of *d* on *x* means that the stretch effect of the ligand is very limited. It is very difficult to discern the type of the smectic ordering with the present 1D WAXS data. However, based on the primary molecular modelling we can deduce that most probably a Smctic C structure forms after complexation: the length of the P2VP segment is about 0.4nm (MM2), and the length of hydrogen bond between carboxylic acid group and pyridine is about 0.3nm,[44] therefore the thickness of the double layer when the P2VP is fully stretched conformation is about 4.2nm, which is larger than the measured thickness, therefore the ligand must tilt in the complex. The formation of the Smectic C phase in the block copolymer complex is proved by POM, from which schlieren texture with four arm brushes is observed (S.I. Figure S1b).

The first ordering peak is fitted with both of Gaussian and Lorentzian function and the latter gives better results. Interestingly, the smallest FWHM (largest domain size)

is obtained in the lowest degree of complexation, which is not expected. This can be explained by the existing of the free ligand in the samples with higher *x*, which has strong tendency to crystallize and disturb the LC ordering. In an extreme case, the crystallization of the ligand is observed in the P2VP homopolymer at *x*=1.0, and the FWHM is almost one order of magnitude higher than *x*=0.25.

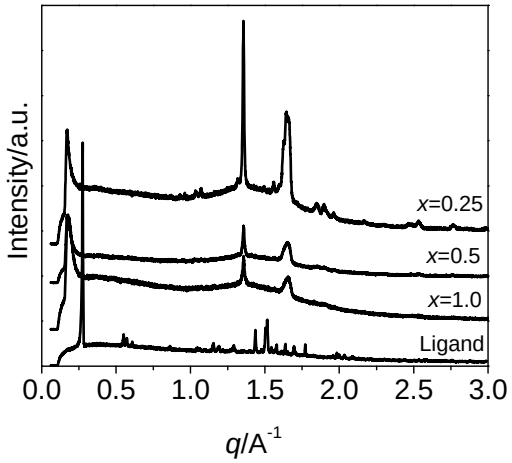

Figure 2. WAXS patterns of P2VP(R_v-2T-COOH)$_x$-PEO at room temperature.

Table 1. The parameters obtained from WAXS

x	P2VP(R_v-2T-COOH)$_x$				P2VP(R_v-2T-COOH)$_x$-PEO			PEO/nm
	d_1/nm	FWHM/nm^{-1}	d_2/nm	d_3/nm	d_1/nm	FWHM/nm^{-1}	d_2/nm	
0.25	3.66	0.0023	1.80	0.46	3.66	0.0028	1.74	
0.50	3.35	0.0037	1.72	0.46	3.66	0.0034	1.64	0.46/0.38
1.0	3.34	0.0153	1.72	0.46	3.47	0.0043	1.70	

The PEO crystallizes at room temperature in all of the compositions. Two main peaks are observed at *d*=0.46 and 0.38nm, indicating that it crystallizes into a monoclinic lattice. They can be assigned to the 120 reflection (at 0.46nm) and the overlaid $\bar{1}32$, 032, 112, $\bar{2}12$, $\bar{1}24$, $\bar{2}04$, 004 reflections (at 0.38nm), respectively.[45] The crystallinity of the PEO changes with *x*: at lowest *x* (0.25), the two main peaks are sharp. Additional peaks from other reflections of the monoclinic lattice are observed, meaning that the crystallinity of PEO is high. Increasing of *x* (0.5 and 1.0) leads to decrease of the intensity of the reflections. The additional reflections disappear, indicating that the crystallinity is decreased. However, the overlaying of

the reflections from PEO and the reflection from the lateral ordering of the ligand prevent the peak deconvolution. Therefore, it is difficult to determine the crystallinity of PEO accurately.

8.3.3. Morphology of thin films.

The morphology of the thin films before and after thermal annealing was investigated by using of SFM. Similar to the situation of our previous publications,[28, 41] the alkyl tail of the ligand preferentially wets the surface of the thin films. Due to its lowest surface energy compared to that of PEO and P2VP, a thin layer exists at the surface and blocks the direct observation of the morphology with SFM in the soft tapping made. Thus, the hard cantilever (force constant ~42N/m) is used and hard tapping mode is employed. In this situation, the tip can penetrate the thin layer and resolve the morphology of the complex beneath.

8.3.3.1. x=0.25 and 0.33.

Figure 3 shows the morphology of the P2VP(R_v-2T-COOH)$_x$-PEO at x=0.25. As showed before, this block copolymer is miscible and only crystal of PEO was resolved by SFM.[28] After incorporating of small amount of the ligand into this block copolymer (x=0.25), the PEO still crystallizes in the thin film, preventing the observation of the morphology at room temperature (Figure 3a). Heating the thin film above the melting point of the PEO helps to observe the microphase separation of the block copolymer, as shown in Figure 3b and c. Nanostructure is resolved at 65°C on both of the topography and phase images. However, the contrast is low on the phase image, which can be ascribed to the reason that both of the PEO and P2VP(R_v-2T-COOH)$_{0.25}$ are molten at this temperature, and the interaction between the tip and the different blocks is similar. On both of the images, the worm-like structure and dots like structure together with some feature-less areas are observed. Such kind of structure lacks of long rang order, only a very broad peak is observed on the PSD curve, which is very difficult to decide the periodicity of the structure. After thermal annealing, the structure does not change too much, but the long range ordering of the structure is improved, on PSD curve a sharp peak is observed, meaning that this structure has a periodicity of 42nm. It is very difficult to assign this morphology without further support information. The weight ratio of P2VP(R_v-2T-COOH)$_{0.25}$

(denoted as f_{comp}) is 0.62, therefore it might be that the dots like structure is the PEO cylinder oriented perpendicular to the surface and the worm like structure is the PEO laying parallel to that of the surface. In addition, there is no feature related to the self-assembly of the P2VP(R_v-2T-COOH)$_{0.25}$, from which the layer like structure is expected. The morphology of the thin films at x=0.33 is very similar to that of Figure 3d and e (results not shown here). The difference between them is the long range ordering of the nanostructure is enhanced, even at as cast film a sharp peak is observed on PSD. The periodicity of the nanostructure is 45 and 43 nm before and after thermal annealing, respectively.

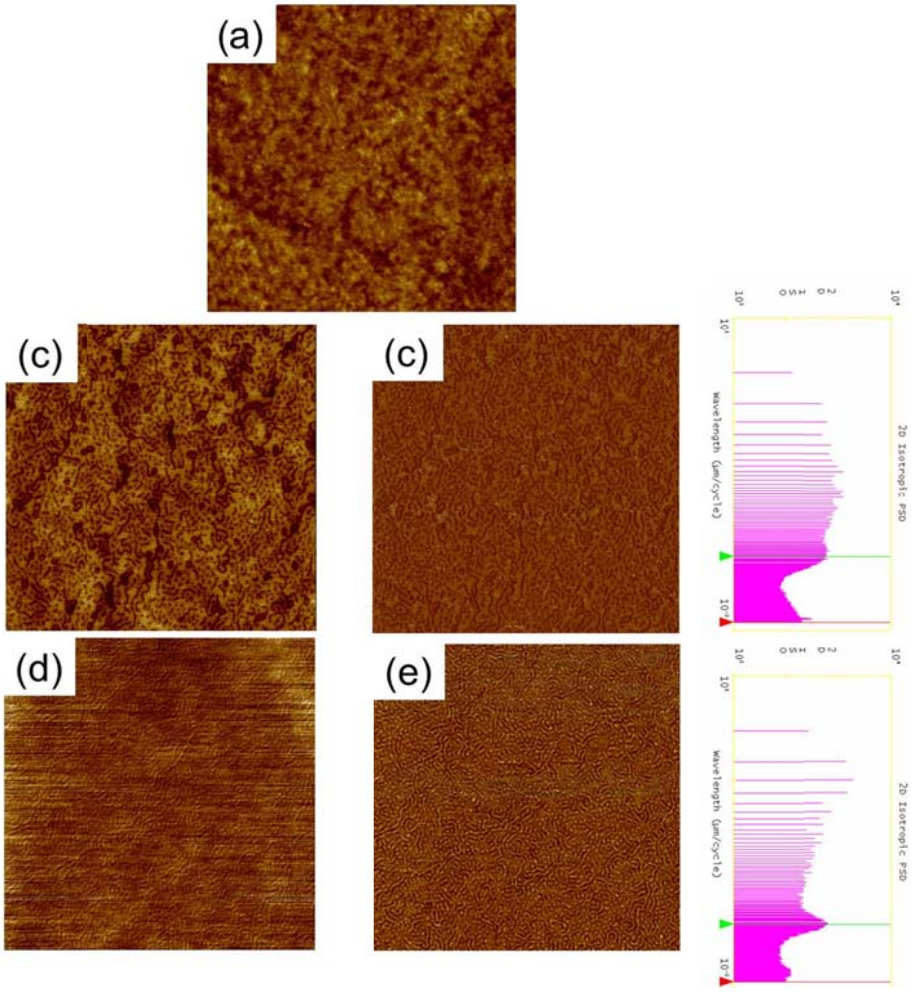

Figure 3. Morphology of P2VP(R_v-2T-COOH)$_{0.25}$-PEO thin films: (a) topography, as cast, at room temperature; (b) topography and (c) phase images of (a) at 65°C; (d) topography and (e) phase images of (a) annealed at 60°C for 2 days and heated to 65°C; scan size 3×3μm^2; the right images of (c) and (e) were the PSD curves of them.

Another important issue is the crystallization of PEO in the thin film. It crystallizes easily at room temperature from both solution casting and melt after long time

annealing. Even though the PEO is the minor phase in this complex, this is in strong comparison to the pure block copolymer. It is found that the crystallization of PEO can be suppressed totally during cooling from the melt when the weight fraction of PEO is less than 60%.[46] This can be explained as following: the ligand enhances the microphase separation because it has bulky alkyl tail, which is hydrophobic and immiscible with PEO, at low degree of complexation. The strength of microphase separation between P2VP(R_v-2T-COOH)$_{0.25}$ and PEO can be low, since the graft density of the ligand on the P2VP backbone is low. Therefore the ligand liberates the PEO from the dilution of P2VP. In addition, although we do not know the LC transition temperature of the complex at this composition, we can expect that there is no big difference between the transition temperature at x=0.25 and 1.0, and therefore the LC structure forms at room temperature. The ordering of the LC blcok and the crystallization of PEO happen at the same temperature region. The strength of microphase separation is not sufficient, therefore the nanoconfinement effects from the microphase separation is not strong enough to suppress the crystallization. Thus, PEO crystallizes freely at room temperature. This situation is similar to the so called "soft confinement" effect. [47] The long range ordering of the microphase separation at these two compositions is poor.

8.3.3.2. x=0.50 and 0.75.

Figure 4 presents the thin film morphology of P2VP(R_v-2T-COOH)$_{0.50}$-PEO before and after thermal annealing. At this degree of complexation, the weight ratio of the P2VP(R_v-2T-COOH)$_{0.50}$ is 0.72. When the complex is casted from chloroform solution, the microstructure from phase separation of the two blocks is already well developed. The contrast on the phase image is clear, indicating that the crystallization of the PEO is suppressed. A morphology of dots embedded in a continues matrix is observed on both of the topography and phase images. Such structure can be assigned to cylinder morphology perpendicular to that of the silicon surface. For some areas elongated structure is also visible, which can be ascribed to that of the coalesce of cylinders. The periodicity of the cylinder is 53nm. Another feature which can be seen on the topography image is the fluctuation of the height. The cross-section of the topography image shows that the fluctuation is the ill defined layer structure. The height is about 1.8nm (bottom of Figure 4a), which is close to the half of the bulk

period of the smectic layer. We believe that this feature comes from the organization of the P2VP(R_v-2T-COOH)$_{0.50}$.

Thermal annealing does not change the morphology too much, still the cylinder morphology with perpendicular orientation together with some elongated domains are resolved by SFM, and the periodicity of the microstructure is slightly reduced, which is 49nm after annealing. The organization of the P2VP(R_v-2T-COOH)$_{0.50}$ is better than that of before annealing. The topography image shows layer structure. The height of the layer is about 1.8nm, similar to the one before annealing. Most interesting thing is the contrast of the phase image after annealing. Now the contrast is very strong and it is reverse to that of the before annealing. The PEO domain is black (Figure 4d) instead of white (Figure 4b), indicating that the PEO domain is softer than that of P2VP(R_v-2T-COOH)$_{0.50}$ at room temperature. At room temperature the P2VP(R_v-2T-COOH)$_{0.50}$ is in the mesogenic state. The softer properties of the PEO domains indicate that PEO is amorphous or with very low crystallinity after thermal annealing. The average size of the cylinder domains is similar before and after thermal annealing, which is about 19nm. Therefore the confinement effect from the microphase separation is similar. The only explanation is that the crystallization processes from solvent casting and molten state are two different processes. During spin coating, a transition of disordered state (solution) to ordered state (thin film) happens. The solvent renders more mobility to the PEO, and the ill-defined microphase separation structure during the process cannot suppress the crystallization totally. Therefore the PEO can crystallize somewhat during the process. The crystallinity of the PEO depends on the competition between the speed of disorder-ordered transition and the crystallization kinetics of the PEO. However after thermal annealing, the cylinder structure is well defined, when the PEO is cooled down from the melt, the cylinder provides strong nanoconfinement towards to the crystallization, which suppresses the crystallization mostly. It has been shown that the 2D confinement from the cylinder is efficient to suppress the crystallization. Amorphous PEO is possible at room temperature with this geometry in PS-PEO,[48] PB-PEO[49] and a side chain liquid crystalline-PEO block copolymers[50] in bulk. This conclusion is supported by the DSC in the powder samples. A melting of PEO is observed on the first heating run after the sample is dried from chloroform, but it is difficult for PEO to crystallizes at room temperature cooling from the melt with phase separation structure (the cooling

curve in Figure S2), only a very small peak at 19.3°C is visible, and the crystallization mainly happens at -18.7°C. This indicates that not only the glassy polymer (e.g. polystyrene) can provide the nanoconfinement environment, but also the hierarchical ordering of supramolecular block copolymer complex can do the same. By incorporating of the ligand into the block copolymer, the LC field is introduced, which can not only control the orientation of the microdomain in thin film, but also tune the crystallization of PEO. As showed in this paper, this method is more versatile, different confinement environments can be introduced by changing the degree of complexation. For example, the "soft confinement" effect is obtained in x=0.25 and 0.33, then it shifted to "hard confinement" at x=0.5.

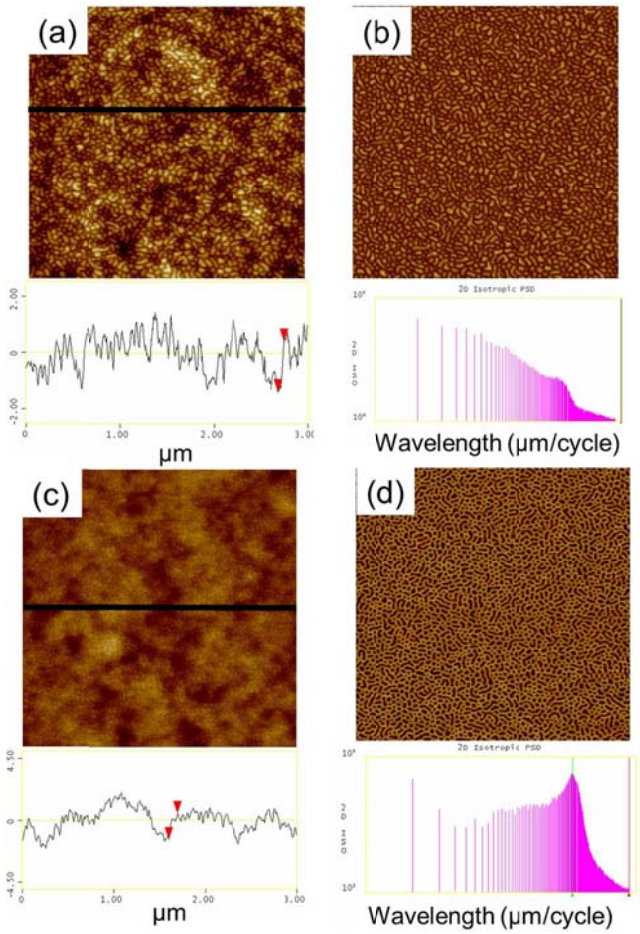

Figure 4. Morphology of P2VP(R_v-2T-COOH)$_{0.50}$-PEO thin films: (a) topography and (b) phase images of as cast film at room temperature; (c) topography and (d) phase images of (a) films annealed at 60°C for 2 days; scan size 3×3µm^2.

At x=0.75, the morphology (results not shown here) is similar to that of at x=0.5, a cylinder of PEO vertically oriented to that of surface is observed. The periodicity of the cylinder are 47nm and 49nm before and after thermal annealing, respectively. The layer structure comes from the organization of the P2VP(R_v-2**T**-COOH)$_{0.75}$ is observed, the height of such layer is 1.8nm, half of the bulk period. The main difference is the crystallization of PEO, the contrast of the phase images is strong in both of as cast and annealed thin films, and the PEO is softer than that of the P2VP(R_v-2T-COOH)$_{0.75}$, indicating that the crystallization of the PEO is fully suppressed, which can be ascribed to the stronger confinement from the P2VP(R_v-2T-COOH)$_{0.75}$, since its weight ratio increases to 0.78: less PEO in the cylinder domains reduces the chance of nucleation further, and therefore suppresses the crystallization more.

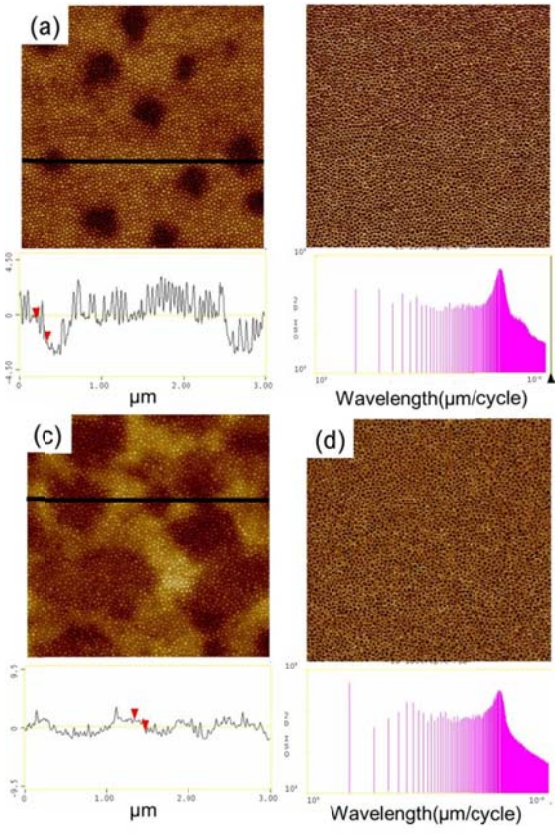

Figure 5. Morphology of P2VP(R_v-2T-COOH)$_{1.0}$-PEO thin films: (a) **t**opography and (b) phase images of as cast film at room temperature; (c) topography and (d) phase images of (a) films annealed at 60°C for 2 days; scan size 3×3μm^2.

8.3.3.3. x=1.0.

In this composition the weight ratio of P2VP(R_v-2T-COOH)$_{1.0}$ is 0.81, morphology of pure cylinder of amorphous PEO embedded inside the P2VP(R_v-2T-COOH)$_{1.0}$ matrix is observed, and the cylinder orients vertically to that of the surface(Figure 5), the periodicity of the cylinder are 43 and 44 nm before and after annealing, respectively, which is slightly smaller than that of x=0.5 and 0.75. The organization of the P2VP(R_v-2T-COOH)$_{1.0}$ is more pronounced in this composition. On the topography images for both of before and after thermal annealing terrace with defined height (1.9nm) is observed (Figure 5a and c), the value is slightly larger than the previous case. We know that there is free ligand inside the thin films from the FTIR, but no feature corresponding to that of macrophase separation between the block copolymer and free ligand is observed from both of the topography and phase images, indicating that the free ligand dissolved in the P2VP(R_v-2T-COOH)$_{1.0}$ domains in the molecular state.

8.3.4. XRR investigations.

The XRR is used to determine the possible layer structure stacked along the normal of the films. Figure 6 shows two XRR curves for two representative situations at x=0.25 (Figure 6a) and x=1.0 (Figure 6b) after thermal annealing. The Kiessig fringes at low q-values correspond to the total film thickness which is similar for both samples: 429Å for x=0.25 and 390Å for x=1.0. At x=0.25 (Figure 6a), the solid line is the fit of the experimental data with a three-layer model leading to the density profile shown in the insert and the result is listed in Table 2. The key parameters are an ordered top and bottom layer of high density and a homogenous middle layer. In this model, the well ordered bottom layer is crucial to fit the change in slope of the reflectivity curve around q=0.2-0.25 Å^{-1}, the top layer is not important for the fitting of the slope change but it improves the quality of the fit for most of the fringes. Most importantly, replacing the homogeneous middle layer by a stack of layers of alternating density (smectic period) decreases the quality of the fit, especially at the region q=0.2-0.25 Å^{-1}. Hence, we conclude that no evidence for smectic layers parallel to the substrate is found in this film. The thickness of the bottom layer is 14.4Å, which can be assigned to the monolayer of predominantly P2VP(R_v-2T-COOH)$_{0.25}$ is forced to be ordered on the silicon surface, with polar parts contacting SiO_2 and alkyl tails oriented towards the bulk of the sample. The thickness of the

bottom and top layer are commensurate with or half of the bulk smectic period, respectively. Films with x=0.33 has the similar situation and the result is not shown here.

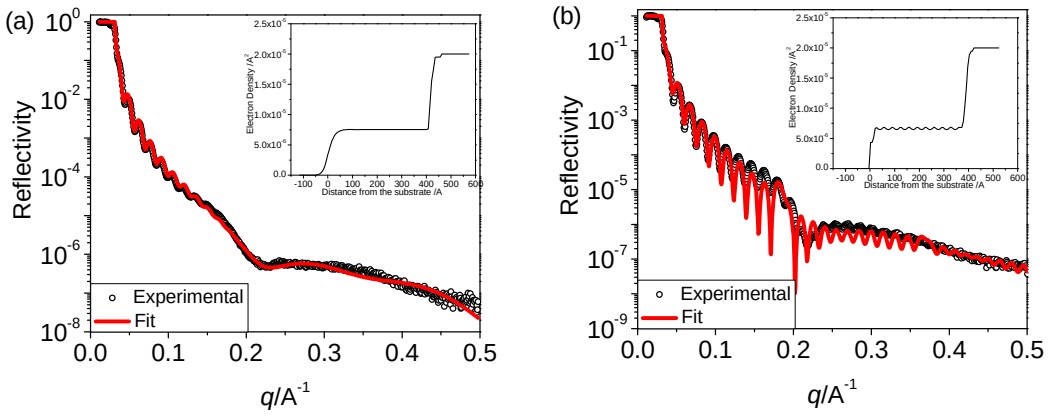

Figure 6. XRR intensity plotted as function of the scattering vector q $(Å)^{-1}$ of P2VP(R_v-2T-COOH)$_x$-PEO: (a) x=0.25 and (b) x=1.0. The inset was the density profiles in $Å^{-2}$ plotted as a function of film thickness Å in the direction normal to the sample surface.

Table 2. Structural details inferred from the fit of XRR data of film of P2VP(R_v-2T-COOH)$_{0.25}$-PEO.

Model	Thickness/ Å	Roughness/ Å	Electric density/ $Å^{-2}$
Top layer	38.9	17.4	$6.8x10^{-6}$
Middle layer	376	14.8	$7.5x10^{-6}$
Bottom layer	14.4	3.3	$1.6x10^{-5}$
SiO_2	29	2.6	$1.85x10^{-5}$

At the higher degree of complexation (x>0.33), the situation is somewhat different from that of the low degree of complexation. The slope changes at around q=0.2-0.3$Å^{-1}$, which is similar to that of low degree of complexation, however, the details of the slope change is different. For low degree of complexation (e.g. x=0.25), the slope changes at this region slowly, and the XRR curve is flatten after this area. However, the change of the slope for x=1.0 is drastically and some details is visible at this region. Afterwards, the Kiessig fringes are visible again, indicating that there is a

Bragg peak corresponding to a periodicity of about 34 Å presented in this sample (Figure 6b). Therefore, the model is replaced by a top layer, the alternative smectic layer, and the bottom absorption layers. The fit is given the Figure 6b (solid line), and the variation of the electron density along the samples normal is shown in the insert. The quality of the fit is moderated. The full model requires an absorbed bottom layer, eleven smectic layers parallel to the substrate, and a top layer. The results are listed in Table 3. The smectic layer period is 34Å, close to the bulk value, corresponding to the double layer of the ligand plus the P2VP chain in the middle. The small variation of the electron density for the smectic layers comes from the electron density difference between the thiophene plus P2VP (higher) and alkyl tail (lower). The thickness of the alky tail is 20.1Å, close to the thickness of the double layer (23Å)[35] indicates that the alkyl tail packed parallel in the thin films. The thickness of the top layer is 15.8Å, which is the single alkyl tail in this model. It is thicker than that of the alkyl tail inside the thin film, and the electron density is slightly higher, indicating a denser alkyl tail on the surface. The situation of the bottom layer in this model is different. It is not important for the fitting, just slightly improves the quality of the fitting. It is very thin but with highest electron density, indicating that the absorption layer is extreme dense and the interaction between the bottom layer and the silicon wafer is very strong. The situation of x=0.5 and 0.75 are similar and the results are not shown here.

Table 3. Structural details inferred from the fit of XRR data of film of P2VP(R_v-2T-COOH)$_{1.0}$-PEO.

Model		Thickness/ Å	Roughness/ Å	Electric density/ Å^{-2}
Top layer		15.8	0.001	$4.3x10^{-6}$
Smectic	Bithiophene	13.9	3.3	$6.9x10^{-6}$
layer	Alkyl	20.1	3.9	$6.5x10^{-6}$
Bottom layer		0.51	5.4	$1.4x10^{-5}$
SiO_2		29	2.6	$1.85x10^{-5}$

8.3.5. Optical Properties.

The absorption and emission properties of the P2VP(R_v-2T-COOH)$_x$-PEO in both of the solution and thin films are measured, Figure 7 shows some of the spectra, and Table 4 summarizes the results from Figure 7. The absorption peak position and

emission spectra of the thin films are similar before. After thermal annealing, the only change is the intensity of the photoluminescence. As we expected, the intensity decreases after thermal annealing, because of the ordering of the P2VP(R_v-2T-COOH)$_x$ is better. In the solution, R_v-2T-COOH shows a single absorption peak at wavelength of 347nm, coming from the bi-thiophene rings and corresponding to the band gap transition derived from the lowest π-π^* molecular transition. In the thin film state, it shows vibronic fine structure with two absorption peaks with the maximum at the wavelength of 374nm. Compared with that of the single molecular state in solution, the maxima of the absorption red shifts by $\Delta\lambda$=27nm. This is an indication that the bi-thiophene core is packed into *J* aggregates. This is also supported by the PL spectra. In the solution, it has an emission peak at 418nm, and the photoluminescence is not quenched totally in the thin film, still an emission peak at 509nm is observed. However, the intensity is 1-2 orders of magnitude lower than that of the single molecular state, meaning that the thiophene core has some organizations in the thin film. The HOMO-LUMO energy gaps (E_{gap}) are determined from the onset of the long-wavelength absorption part, and the results are shown in Table 4. As can be seen, in thin film the E_{gap} is smaller than that of the solution, proving that the thiophene core is ordered in the thin film.

The presence of the block copolymer has limited effects on the adsorption and emission properties of the ligand in solution. The complex has two absorption peaks in the UV region. The weak one is at wavelength of about 260nm,[30] coming from the π-π^* transition of the pyridine ring, and the absorption maxima appears at 345nm, originating from the π-π^* transition of the bithiophene core. The peak position is close to that of the pure ligand. The HOMO-LUMO energy gap E_{gap} is also very closed to that of the single molecular state of the pure ligand, and the peak position and E_{gap} does not change with the degree of complexation (*x*). In addition, the absorption increases with the increased degree of complexation (*x*), but it shows some kind of saturation at higher *x*. Similar trend is observed from the emission spectra. All of the complexes have the same emission maxima at 418nm, which is the same like the single molecular state of the pure ligand. The intensity of the spectra saturates at higher *x*, although more thiophene rings present in the higher *x*. The results of the absorption and emission of the complexes indicate that the ligand has some ordering in the solution, which reflects the structure of the ligand in thin films. It is proved by

FTIR that the ligand attaches to the pyridine with hydrogen bonding, in the solution this interaction still exists between the carboxylic acid group and pyridine, although it is weaken by chloroform. The chloroform is a good solvent for both of the P2VP and ligand, in the diluted solution the P2VP chain takes the conformation of the random coil, because of the hydrogen bonding interaction between the carboxylic group and pyridine, the ligand is absorbed to the surrounding of this random coil and forms some ordered structure, most probably the conformation of "ligand surrounded random coil morphology" exists in the solution, but the distance between the each bi-thiophene core is still far away from each other to let them have conjugation interaction. This can explain the quenching of the PL at higher degree of complexation. At higher *x*, more ligand presents in the solution and attaches to the surrounding of the P2VP backbone. Such kind of ordered structure leads the transformation of the energy from one thiophene core to other easier, which quenches the photoluminescence. From a previous publication,[30] ordered structures are observed in the solution of the complex of P2VP with complex 4-[3,4,5-tris(dodecyloxy) benzoyloxy] azobenzene-4-sulfonic acid or 4- [3,4,5-tris (octyloxy) benzoyloxy] azobenzene-4- sulfonic acid via ionic interaction, in that case, the ionic interaction between the ligand and P2VP or P4VP is so strong that well-ordered structure presents in the solution, and the conformation can be changed from "ligand-surrounded random coils" at lower degree of complexation into a true cylinder-shaped complex at high degree of protonation in the solution.

In the thin films, interestingly the absorption and emission maxima are the same to that of the solution, indicating that the molecular aggregation state of the ligand in the thin films is similar to that of the solution. On the absorption curves, two absorption peaks at 263 and 344nm are observed, originated from the π-π^* transition of pyridine and bi-thiophene core, respectively. In addition, The E_{gap} is somewhat smaller than that of the solution, indicating that the ordering of the bi-thiophene core is slightly better in the thin films than that of the solution. The emission spectra of the complex have only one maximum at about 420nm, which is again similar to that of the solution. However, the PL intensity of the complex is 1-2 orders of magnitude lower than that of the solution state. The intensity decreases with increasing of *x*. At low degree of complexation (e.g. x=0.25), the thin film has the highest intensity, and the photoluminescence is almost quenched by 2 order of magnitude at x=0.5 and 1.0.

From the results of SFM and XRR, we know that at lower *x*, the ordering of the P2VP(R_v-2T-COOH)$_x$ is poor, no clear evidence of the presence of smectic ordering is observed, however, when the *x* reach 0.5, more ordered smectic structure forms, such kind of structure change might response to the change of the PL intensity.

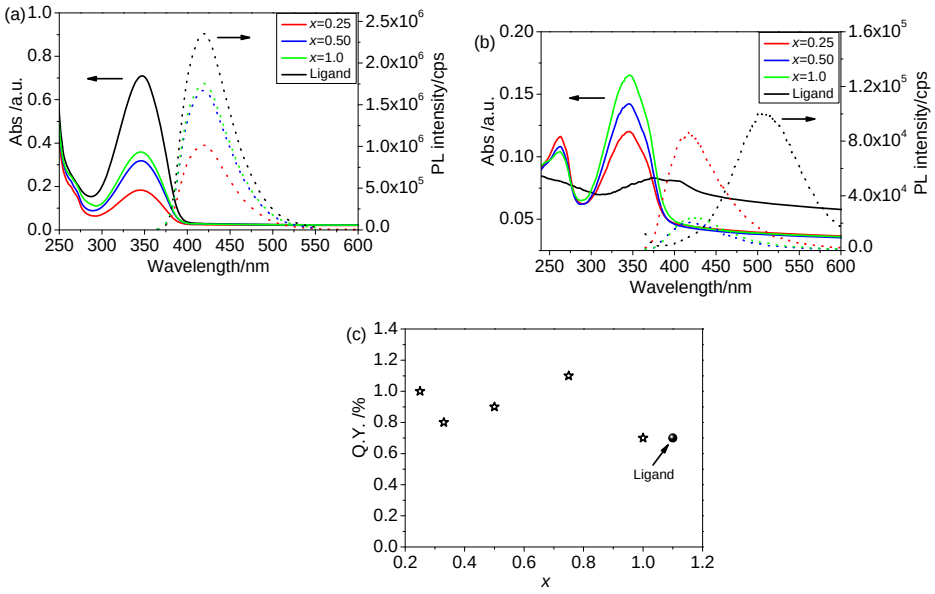

Figure 7. Optical of properties of the P2VP(R_v-2T-COOH)$_x$-PEO in (a) chloroform solution and (b) thin films annealed at 60°C for 2 days; the solid lines and dot lines were the absorption and photoluminences spectra, respectively.

Table 4. The optical absorption maxima (λ_{abs}), fluorescence emission maxima (λ_{FE}) and energy gap (E_{gap}) of P2VP(R_v-2T-COOH)$_x$-PEO

x	λ_{abs} /nm		λ_{FE}/nm		E_{gap}/eV	
	Solution	Films	Solution	Films	Solution	Films
Ligand	347	374, 404	418	509	3.13	2.76
0.25	345	344	418	417	3.18	3.11
0.5	345	344	418	420	3.18	3.11
1.0	345	345	418	420	3.18	3.11

For the application of the P2VP(R_v-2T-COOH)$_x$-PEO thin films as the blue light emitter, the quantum yield (*Q.Y.*) of the thin films are measured. *Q.Y.* reflects the light emission efficiency of the thin films illuminated by a particular wavelength, which is extremely important for the applications such as OLED. Here only the results of the

thin films after annealing are reported, since it reflects more about the thermal dynamic stable state of the thin films nanostructure. The *Q.Y.* of the pure ligand in thin film is about 0.7%, complexation of the ligand with the P2VP-PEO increases the *Q.Y.* somewhat, and it varies with the *x* slightly, the highest value is 1.2% at x=0.75, which is 70% higher than that of the pure ligand state. The change of the *Q.Y.* with *x* can be divided to three regions, corresponding to different organization state of the P2VP(R_v-2T-COOH)$_x$ in thin film.When x ≤0.33 where no evidence of smectic ordering of P2VP(R_v-2T-COOH)$_x$, the *Q.Y.* decreases with increasing *x*. When x is between 0.5 and 0.75, smectic ordering is observed. The *Q.Y.* increases with *x*, and the maximum value is obtained in this region at *x*=0.75. Further increasing of *x* to 1.0 does not change the smectic ordering of the P2VP(R_v-2T-COOH)$_x$. However, some free ligands are present and they dissolve in the P2VP(R_v-2T-COOH)$_x$ domain. In this situation the *Q.Y.* decreases, and the value is close to that of the pure ligand state.

8.4. Conclusions.

In the present study we report new asymmetric oligothiophene molecules with bi-thiophene as a core, which is substituted by carboxylic group and a branced alky tail on α and ω position, respectively. It crystallizes and no liquid crystalline phase is observed. The carboxylic group works as active group and it forms hydrogen bond with pyridine rings in the block copolymer of the P2VP-PEO. Thus, it provides the chance to tune the structure of both the ligand and block copolymer microphase separation, and introducing photoluminescence as functionality of the thin films. It is shown that the complexation induces formation of the liquid crystalline phase of the ligand. The structure depends on the degree of complexation. At high degree of complexation, the smectic ordering parallel to the surface is observed by both of XRR and SFM, but the structure is not clear at low degree of complexation in thin films. The complexation enhances the strength of the phase separation between P2VP and PEO. The parallel orientation of the smectic layer leads to effortless controlling of vertical orientation of the microstructure.

Most interestingly, the crystallization of the PEO in thin films can be tuned by the complexation. Depending on the degree of complexation, different hierarchical ordering presents in the thin films and the nanoconfinement changes with the hierarchical ordering. When *x* ≤0.33, the “soft confinement” effects is observed, the

ligand liberates the PEO and let it crystallize freely, in spite of the PEO is minor phase. At the higher *x* value, when the morphology of "PEO cylinders in LC matrix" is observed, the crystallization of PEO is difficult in the cylinder domains and much larger undercooling is necessary for the crystallization. At room temperature the amorphous PEO cylinder domains with vertical orientation can be obtained with this method, which is very interesting for some application like solid state electrochemical devices.

The optical properties of the complexes are discussed in both of the solution and thin films. The ligand alone shows a *J* aggregate behaviour, but it organizes to similar structure in both of the solution and thin film when it complexes with the block copolymer, although different structure is resolved by the SFM and XRR. Complexation also increases the efficiency of the light emission illuminated by a particular wavelength. The increase of the *Q.Y.* by 70% related to the pure ligand state in thin films is reported. The research provides a practical way for tuning the optical properties by using of the hierarchical ordering as a tool, which might provide another solution for high efficiency optical-electric devices.

8.5. References

[1] A. Mishra, C.-Q. Ma, P. Bäuerle, *Chem. Rev.* **2009**, *109*, 1141.

[2] D. Fichou, *J. Mater. Chem.* **2000**, *10*, 571.

[3] I. F. Perepichka, D. F. Perepichka, H. Meng, F. Wudl, *Adv. Mater.* **2005**, *17*, 2281.

[4] F. Garnier, R. Hajlaoui, A. Yassar, P. Srivastava, *Science* **1994**, *265*, 1684.

[5] H. Sirringhaus, T. Kawase, R. H. Friend, T. Shimoda, M. Inbasekaran, W. Wu, E. P. Woo, *Science* **2000**, *290*, 2123.

[6] B. S. Ong, Y. Wu, P. Liu, S. Gardner, *J. Am. Chem. Soc.* **2004**, *126*, 3378.

[7] S. A. Ponomarenko, O. V. Borshchev, T. Meyer-Friedrichsen, A. P. Pleshkova, S. Setayesh, E. C. P. Smits, S. G. J. Mathijssen, D. M. de Leeuw, S. Kirchmeyer, A. M. Muzafarov, *Organometallics* **2010**, *29*, 4213.

[8] B. J. Holliday, T. M. Swager, *Chem. Commun.* **2005**, 23.

[9] E. C. P. Smits, S. G. J. Mathijssen, P. A. van Hal, S. Setayesh, T. C. T. Geuns, K. A. H. A. Mutsaers, E. Cantatore, H. J. Wondergem, O. Werzer, R. Resel, M.

Kemerink, S. Kirchmeyer, A. M. Muzafarov, S. A. Ponomarenko, B. de Boer, P. W. M. Blom, D. M. de Leeuw, *Nature* **2008**, *455*, 956.

[10] J. Nelson, *Science* **2001**, *293*, 1059.

[11] R. A. Segalman, B. McCulloch, S. Kirmayer, J. J. Urban, *Macromolecules* **2009**, *42*, 9205.

[12] H.-C. Kim, S.-M. Park, W. D. Hinsberg, *Chem. Rev.* **2009**, *110*, 146.

[13] I. W. Hamley, *The physics of block copolymers* Oxford University Press Oxford 1998.

[14] M. Reenders, G. ten Brinke, *Macromolecules* **2002**, *35*, 3266.

[15] B. D. Olsen, D. Alcazar, V. Krikorian, M. F. Toney, E. L. Thomas, R. A. Segalman, *Macromolecules* **2007**, *41*, 58.

[16] N. Sary, R. Mezzenga, C. Brochon, G. Hadziioannou, J. Ruokolainen, *Macromolecules* **2007**, *40*, 3277.

[17] E. Huang, L. Rockford, T. P. Russell, C. J. Hawker, *Nature* **1998**, *395*, 757.

[18] S. H. Kim, M. J. Misner, T. Xu, M. Kimura, T. P. Russell, *Adv. Mater.* **2004**, *16*, 226.

[19] E. Han, K. O. Stuen, Y.-H. La, P. F. Nealey, P. Gopalan, *Macromolecules* **2008**, *41*, 9090.

[20] W. H. de Jeu, Y. Séréro, M. Al-Hussein, *Adv. Polym. Sci.* **2006**, *200*, 71.

[21] J. Ruokolainen, R. Mäkinen, M. Torkkeli, T. Mäkelä, R. Serimaa, G. t. Brinke, O. Ikkala, *Science* **1998**, *280*, 557.

[22] O. Ikkala, G. ten Brinke, *Science* **2002**, *295*, 2407.

[23] W. van Zoelen, G. ten Brinke, *Soft Matter* **2009**, *5*, 1568.

[24] S.-H. Tung, N. C. Kalarickal, J. W. Mays, T. Xu, *Macromolecules* **2008**, *41*, 6453.

[25] W. van Zoelen, E. Polushkin, G. ten Brinke, *Macromolecules* **2008**, *41*, 8807.

[26] B. Nandan, C.-H. Lee, H.-L. Chen, W.-C. Chen, *Macromolecules* **2006**, *39*, 4460.

[27] J. W. Lee, C. Lee, S. Y. Choi, S. H. Kim, *Macromolecules* **2009**, *43*, 442.

[28] K. Albrecht, A. Mourran, X. Zhu, T. Markkula, J. Groll, U. Beginn, W. H. de Jeu, M. Moeller, *Macromolecules* **2008**, *41*, 1728.

[29] J. Kao, J. Tingsanchali, T. Xu, *Macromolecules* **2011**, *44*, 4392.

[30] X. Zhu, U. Beginn, M. Möller, R. I. Gearba, D. V. Anokhin, D. A. Ivanov, *J. Am. Chem. Soc.* **2006**, *128*, 16928.

[31] G. Sauvé, R. D. McCullough, *Adv. Mater.* **2007**, *19*, 1822.

[32] N. Sary, F. Richard, C. Brochon, N. Leclerc, P. Lévêque, J.-N. Audinot, S. Berson, T. Heiser, G. Hadziioannou, R. Mezzenga, *Adv. Mater.* **2010**, *22*, 763.

[33] H.-S. Sun, C.-H. Lee, C.-S. Lai, H.-L. Chen, S.-H. Tung, W.-C. Chen, *Soft Matter* **2011**, *7*, 4198.

[34] B. J. Rancatore, C. E. Mauldin, S.-H. Tung, C. Wang, A. Hexemer, J. Strzalka, J. M. J. Fréchet, T. Xu, *ACS Nano* **2010**, *4*, 2721.

[35] M. Defaux, F. Gholamrezaie, J. Wang, A. Kreyes, U. Ziener, D. V. Anokhin, D. A. Ivanov, A. Moser, A. Neuhold, I. Salzmann, R. Resel, D. M. de Leeuw, S. C. J. Meskers, M. Moeller, A. Mourran, *Adv. Mater.* **2012**, *24*, 973.

[36] D. Lin-Vien, N. B. Colthup, W. G. Fateley, J. G. Grasselli, *The Handbook of Infrared and Raman Characteristic Frequencies of Organic Molecules*, Academic Press, 1991.

[37] H. Kosonen, J. Ruokolainen, P. Nyholm, O. Ikkala, *Polymer* **2001**, *42*, 9481.

[38] J. Y. Lee, P. C. Painter, M. M. Coleman, *Macromolecules* **1988**, *21*, 954.

[39] S. Suzuki, H. Onishi, T. Sasaki, K.-i. Fukui, Y. Iwasawa, *Catalysis Lett.* **1998**, *54*, 177.

[40] M. Puterman, F. J. Kolpak, J. Blackwell, J. B. Lando, *J. Polym. Sci. Polym. Phys.* **1977**, *15*, 805.

[41] J. Wang, W. H. de Jeu, P. Müller, M. Möller, A. Mourran, *Macromolecules* **2012**, *45*, 974.

[42] J. T. Korhonen, T. Verho, P. Rannou, O. Ikkala, *Macromolecules* **2010**, *43*, 1507.

[43] W.-T. Chuang, H.-S. Sheu, U. S. Jeng, H.-H. Wu, P.-D. Hong, J.-J. Lee, *Chem. Mater.* **2009**, *21*, 975.

[44] J. E. J. Mills, P. M. Dean, *Journal of Computer-Aided Molecular Design* **1996**, *10*, 607.

[45] L. Zhu, P. Huang, W. Y. Chen, Q. Ge, R. P. Quirk, S. Z. D. Cheng, E. L. Thomas, B. Lotz, B. S. Hsiao, F. Yeh, L. Liu, *Macromolecules* **2002**, *35*, 3553.

[46] M. Córdova, A. T. Lorenzo, A. J. Müller, P. Fragouli, H. Iatrou, N. Hadjichristidis, *Macromol. Sym.* **2010**, *287*, 101.

[47] L. Zhu, B. R. Mimnaugh, Q. Ge, R. P. Quirk, S. Z. D. Cheng, E. L. Thomas, B. Lotz, B. S. Hsiao, F. Yeh, L. Liu, *Polymer* **2001**, *42*, 9121.

[48] P. Huang, L. Zhu, S. Z. D. Cheng, Q. Ge, R. P. Quirk, E. L. Thomas, B. Lotz, B. S. Hsiao, L. Liu, F. Yeh, *Macromolecules* **2001**, *34*, 6649.

[49] R. V. Castillo, M. L. Arnal, A. J. Muller, I. W. Hamley, V. Castelletto, H. Schmalz, V. Abetz, *Macromolecules* **2008**, *41*, 879.

[50] Y. Zhou, S.-k. Ahn, R. K. Lakhman, M. Gopinadhan, C. O. Osuji, R. M. Kasi, *Macromolecules* **2011**, *44*, 3924.

Chapter 9 Morphological Investigation of Unique Onion-type Smectic Polymersome from Supramolecular Approach

9.1. Introduction.

It is well known that the natural phospholipids have the ability to self-assemble into vesicular structures (known also liposomes), in which the membranes are composed of bilayer of the corresponding phospholipids (Scheme 1a).[1] The morphology of the self-assembled objects is defined by the packing parameter: vesicular structure forms when the packing parameter is between 0.5 and 1. This molecularly thin membrane manifests itself a dynamic softness,[2] leading to poorly controlled membrane properties. Amphiphilic block copolymers have the same characters as phospholipids: they form vesicles when the ratio of hydrophilic to total mass is about 35±10%.[3] The model of block copolymer vesicles is shown in Scheme 1b: the hydrophobic blocks folds and ties in the wall, while the hydrophilic block swell in the water, providing large steric hindrance and stabilizing the vesicles.[4-6] Introducing of the liquid crystalline ordering (LC phase) to the hydrophobic block may change the self-assemble behaviour in water. The distinct LC ordering on the wall leads to high bilayer stiffness and high surface tensions, therefore giant vesicles form spontaneously.[7] The benefits of the LC ordering include more stabilization of the vesicles and highest ordering in membrane; the possible defects can self-heal because of the LC field.[7] LC vesicles can be obtained from different type of LC block copolymers (e.g. main chain LC block copolymers,[8] side chain block copolymers[9-17]) and different topologic structures[9, 10, 13, 16] within similar range of hydrophilic/total mass ratio of 18~33%.[10, 14, 16] As shown in Scheme 1c, this type of vesicle has the alternative packing of LC mesogen inside the wall, with the backbone perpendicular while the direction of the mesogen parallel to the surface of the wall. Interestingly the shape of the well order smectic vesicles (smecticsomes) shows sharp-edged[14] or ellipsoidal[16] morphology, which is believed to be the comprise between the smectic ordering and the stiffness of polymer backbone.

Until now most of the vesicles made from block copolymers are unilamellae,[4, 10, 15, 16] the hydrated hydrophilic blocks generates long range steric repulsion, preventing a

dense multilayer structure.[18] The onion type vesicles with closed packed layers are ubiquitous for low molecular weight surfactant.[19, 20] This type vesicle can be found in block copolymer only when the steric repulsion is overcame by introducing of strong interaction.[21] However the wall of the vesicles is still made from the alternative packing of hydrophobic/hydrophilic layers and the situation is still similar to Scheme 1b.

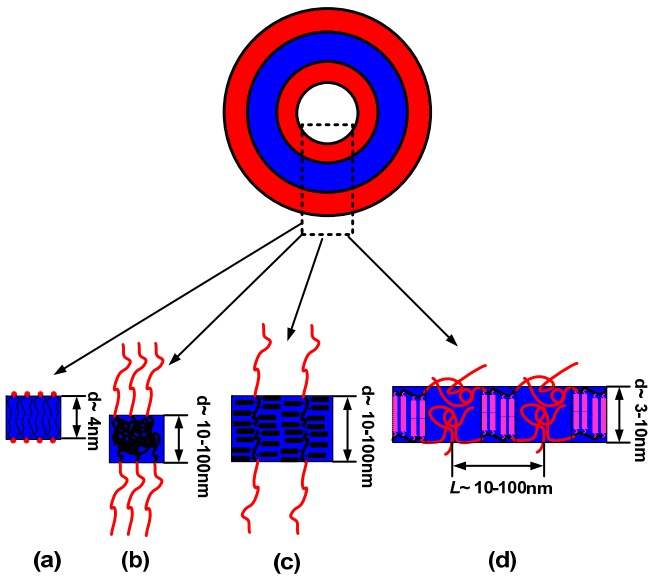

Scheme 1. Structure of the different type of vesicles: (a) liposomes; vesicles from (b) coil-coil block copolymers and (c) side chain liquid crystalline block copolymers; (d) onion type smectic vesicles.

The real challenge is how to prepare the vesicles shown in Scheme 1d: the polymer backbone on the wall orients parallel to the wall surface and contact with water directly, the hydrophobic pedant side group packs and forms bilayer structure, the alternative organization of parallel polymer backbone and side group composes the wall of the vesicles. Actually this situation is very similar to that of the small molecular surfactant, the repulsion with each other is very small, and therefore the close pack of the bilayers is possible and forming the onion type vesicles. Another hydrophilic block has to follow the conformation change of the hydrophobic block, it is not the corona of the vesicles shown in Scheme 1b and c, but embedding inside the wall. Depending on the aggregation number of the hydrophilic chain, it either forms

disordered structures on the wall (in the situation of unilamellar vesicles) or well-defined microphase separation structure (in the multilamellar vesicles).

In this paper, we provide a tailed way for the preparation of the onion type vesicles from block copolymers with structure illustrated in Scheme 1d. The block copolymer used is poly(2-vynyl pyridine-b-ethyl oxide) (P2VP-PEO), and the small molecular mesogens graft to the P2VP via secondary interaction: ionic interaction between sulfonic acid/pyridine, or hydrogen bonding between carboxylic acid/pyridine. By choosing of hydrophilic P2VP backbone, the parallel orientation of the chain is possible, and the complexation enhances the hydrophilicity of P2VP. The hydrophobic tail of the ligand behaves like the small molecular surfactant, which can form close packed structure. The PEO block is also hydrophilic and microphase separated from the P2VP/ligand complex. The vesicle is prepared by using a phase transfer method, which provides giant vesicles in the thermal dynamic stable state. The morphology of the vesicles is investigated by Cryo-electron microscope and optical microscope.

9.2. Experimental sections.

9.2.1. Materials.

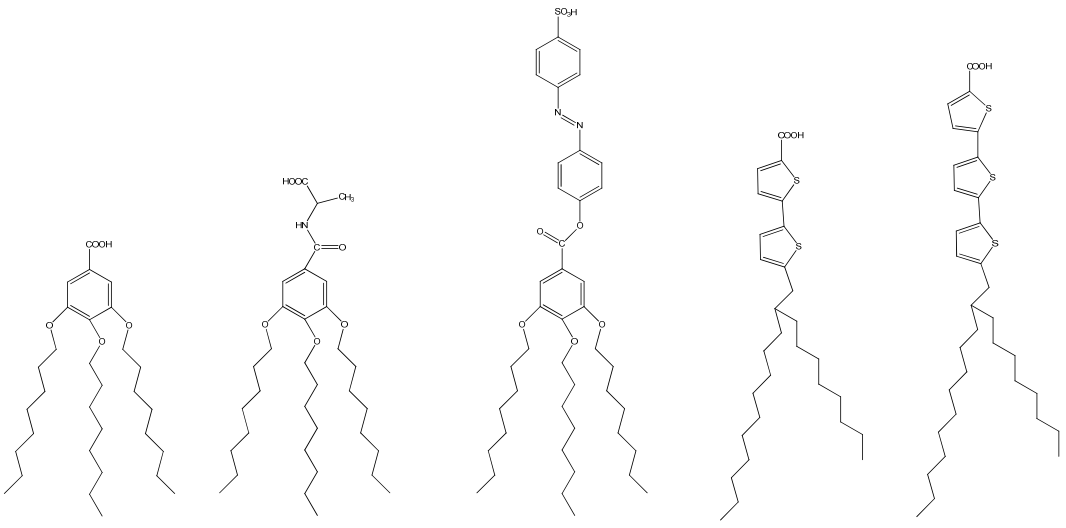

1 **2** **3** **4** **5**

Scheme 2. Chemical structure of the ligands.

Three block copolymers $P2VP_{180}$-PEO_{560} (PDI=1.18, numbers denote the degree of polymerization), $P2VP_{150}$-PEO_{550} (PDI=1.18), and $P2VP_{227}$-PEO_{254} (PDI=1.18) are

prepared by living anionic polymerization and the details is published elsewhere.[22] The ligands are three wedge-shaped molecules and one thiophene oligomers with bi-thiophene core. The structure of the ligands is shown in Scheme 2, and the preparation of the ligand is reported elsewhere.[23, 24] All of the solvents used are analytical pure grade and purchased from VWR GmbH (Germany).

9.2.2. Preparation of the vesicles.

The preparation of the block copolymer/ligand complex is reported elsewhere. The complexes are identified as $P2VP_n(\underline{\mathbf{L}})_x$-$PEO_m$, n, **L**, x and m are the degree of polymerization of PEO, the name of the ligand, degree of complexation and the degree of polymerization of P2VP, respectively.[25] The vesicles are prepared by using a phase transfer method and the procedure is outlined in Scheme 3: 0.5ml of the block copolymer/ligand complex solution (0.5wt%) was filled into a glass vessel and 5ml of MilliQ water was added into the same vessel immediately. The phase separation happens between the organic phase and the water phase, and the organic phase stays on the bottom of the vessel (below the water) because of the high density of the chloroform (1.48g cm^{-3}). About 1h later a gel like layer forms between the water phase and organic phase but each phase is still transparent, because of the slow evaporation of the solvent and amphiphilic nature of the block copolymer complex, the hydrophilic PEO contacts with water and is swollen by the water, and the hydrophobic LC block contacts with the chloroform. The glass vessel is stored in a dark hood, and the organic solvent is left to evaporate for long time without any disturbance, and the block copolymer complex will be transferred to the water phase slowly with the evaporation of the chloroform, after all of the organic solvent is evaporated, two phases is obtained: the up part semitransparent solution with some of the giant vesicles and the bottom white precipitation which is the sediment giant vesicles, they can be redispersed into the water phase easily if one shakes the vessel. The typical time range for this process is about 4 weeks, within such a long time range there is enough time to let the block copolymer to reorganize and reach the thermal dynamic stable state.

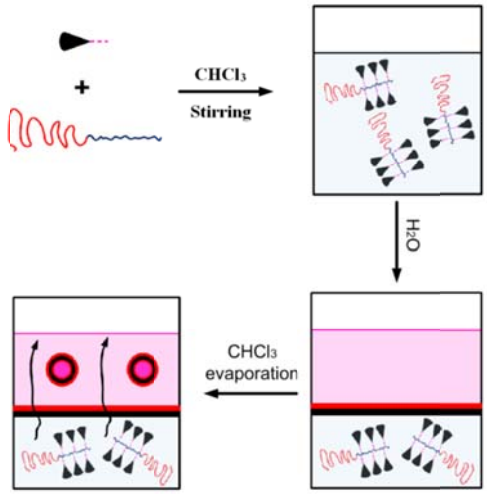

Scheme 3. General procedures for the preparation of vesicles by phase transfer method.

9.2.3. Characterization of the vesicles.

Cryo-TEM and Cryo-STEM were performed on a Philips CM 120 operated at 80 kV and Hitachi S-4800 Field Emission Scanning Electron Microscope at 30kV, respectively. The samples were prepared by putting a drop of the vesicles solutions on copper grid coated with hole-carbon film. The over excesses solution was absorbed by filter paper. The grid was dropped into the liquid nitrogen and transferred to the machine carefully to minimize the effects of the humidity. Cryo-FESEM was performed on the Hitachi S-4800 equipped with a Gatan Cryo-stage. For the sample preparation a drop of the solution was loaded into the copper holder, after that the holder together with solution was dropped into the liquid nitrogen to freeze the sample as fast as possible, after that the sample was transferred into the sample preparation stage under vacuum, and the sample was freeze-fractured by a knife in the vacuum, this freshly prepared surface was used for the observation, then the sample was transferred to the work stage. In order to enhance the contrast, the samples were sublimated under -90°C on the work stage for about 2min. The FESEM experiments were performed under 1 kV without any metal coating. The differential interferential contrast (DIC) optical microscopy was performed on a Zeiss Axioplan optical microscope in reflection model, coupled with a Zeiss Axiocam digital camera (Carl Zeiss MicroImaging GmbH).

9.3. Results.

9.3.1. The pyridine salts of the ligand (**L**-Py).

Before we go to the morphology of the block copolymer/ligand complex vesicles, we investigate the self-assembly of the monomer of the LC block, which is the corresponding pyridine salt of the ligand. The pyridine salts of ligand **1**, **2**, **4** and **5** do not form any visible structure in water, they precipitate after the evaporation of the organic solvent. Only the **3**-Py forms polydispersed giant vesicles (Figure 1), the size of the vesicles vary between 2-120μm, and most of them are in the range of 20-40μm. Two types of the vesicular structure are visible: the unilamellar giant vesicles and the giant vesicle-in-vesicle (multi-vesicle) structure.

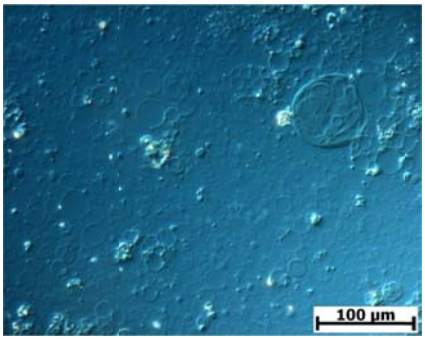

Figure 1. The optical microscopic image of **3**-Py in water.

9.3.2. Morphology of $P2VP_{150}$ $(\mathbf{1})_x$-PEO_{550}.

Figure 2 shows the typical morphology of fractured giant vesicles in ice. As can be seen, at low degree of complexation, *i.e.* x=0.25 (the weight ratio of PEO w_{PEO} is 0.41), two morphologies are observed: unilamellar giant vesicles with a typically diameter of *ca*. 30-50μm (Figure 2a), and multi-vesicles structure (Figure 2b). The multi-vesicles structure is composed of giant vesicles with smaller size (1-2 μm) encapsulated into one giant vesicle. Deep morphology investigation of the encapsulated giant vesicles reveals that they have complex internal structures: the normal unilamellar giant vesicles with similar morphology as that of Figure 2a but smaller size (results not shown here), and multilamellar (or onion type) vesicles (Figure 2c). The wall of onion type vesicles is composed of dense packed layer structures, Figure 2c shows one of the onion type vesicles as an example, 8 layers with similar wall thickness are clearly visible, limited by the resolution of the

technique, the layer thickness is not clear yet. When the degree of complexation is increased to 0.50 (w_{PEO}=0.31), the situation is very similar to that of x=0.25: the unilamellar vesicles co-exist with multilamellar vesicles, but the multilamellar vesicles dominate the structure, in most cases, the onion type vesicles are obtained. The structure of the unilamellar vesicles (pictures not shown here) is same as that of x=0.25. The morphology of the onion type vesicles are more defined, dense packed layer structure is observed from the outside to the centre of the vesicles (Figure 2d and e), between the layers small nanostructure with size of *ca*. 50nm is observed (Figure 2e), which is the self assemble of swollen PEO chains inside the wall of the vesicles. Further increase of degree of complexation suppresses the formation of the vesicles, only precipitation at the bottom of the vials is observed.

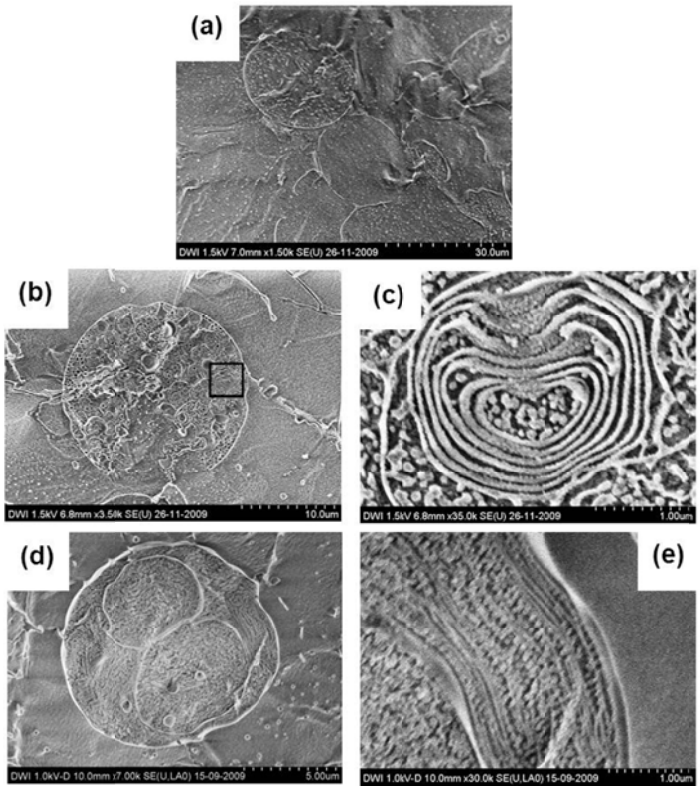

Figure 2. Cryo-FESEM micrographs of P2VP$_{150}$(**1**)$_x$-PEO$_{550}$: (a) x=0.25, unilamellar vesicles; (b) x=0.25, multi-vesicles;.(c) multilamellar vesicles, black box in (b); (d) x=0.50, multilamellar vesicles; and (e) enlarge view of the wall of (d).

9.3.3. Morphology of P2VP$_{150}$(2)$_x$-PEO$_{550}$.

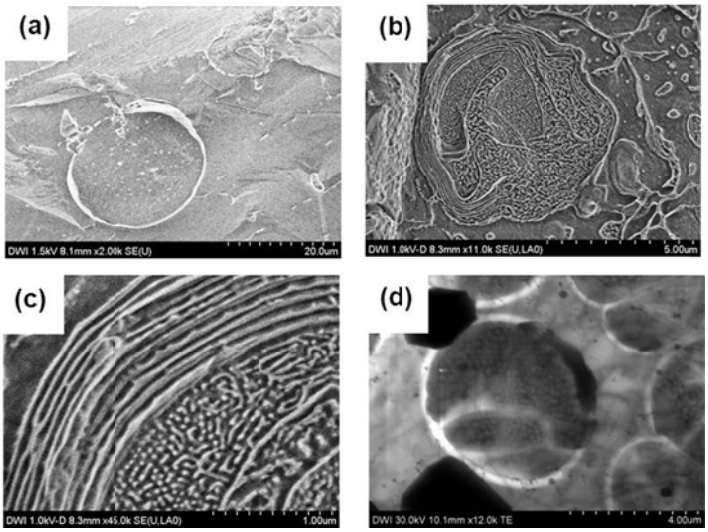

Figure 3. Cryo-FESEM micrographs of P2VP$_{150}$(**2**)$_x$-PEO$_{550}$: (a) x=0.33, unilamellar vesicles; (b) x=0.75, multilamellar vesicles; (c) enlarge view of (b); and (d) x=0.75, Cryo-STEM image.

When the head of the **1** is modified with alanine, although the interaction between the P2VP and ligand is not changed, which is still the hydrogen bonding, the self-assembly behaviour can be different from that of **1** because of extra hydrogen bonding between ligand is introduced. Figure 3 shows the typical morphology of P2VP$_{150}$(**2**)$_x$-PEO$_{550}$ in water with different degree of complexation. In all cases, the unilamellar vesicles co-exist with the onion type vesicles. The size of the unilamellar vesicles is about 30μm (Figure 3a), which is very close to that of the **1**, and they dominate the structure at low degree of complexation (x=0.25 and 0.33). When the degree of complexation is increased to 0.50 or 0.75, the onion type vesicles dominate the structure. As showed in Figure 3 b and c, the wall of the onion type vesicles are composed of closed packed layers, at least 11 layers with uniformed thickness are resolved by FESEM, between layers the protruded structures are observed, and on some areas where the wall are parallel to the fractured surface the dots like structure with a size of about 50nm is also observed, which can be assigned to the self assemble of PEO in the wall of the vesicles. Such kind of microphase separation structure on the wall of the vesicle is proved by Cryo-STEM, a morphology of white dots structure embedded in the continues phase is observed (Figure 3d), the size of the white dots

like structure is about 50nm. This structure can be assigned to the PEO phase, since it is swollen in the water therefore the density is smaller than that of the $P2VP_{150}(\underline{2})_{0.75}$.

9.3.4. Morphology of $P2VP_{227}(\underline{2})_x$-$PEO_{254}$.

The effect of the composition of the P2VP-PEO block copolymer is also considered. Figure 4 shows the morphology of $P2VP_{227}(\underline{2})_x$-$PEO_{254}$ self assembled in water. As can be seen, when x=0.25 (w_{PEO}=0.14) the morphology is dominated by the onion type vesicles (Figure 4a), and the size of these giant vesicles is about 5-10μm. On the wall of the onion type vesicles multi-layers adhere densely to each other, between the close packed layers dot-like structure is observed, which can be the microphase phase separation of PEO on the wall of the vesicle. Increasing of the degree of complexation leads to precipitation only.

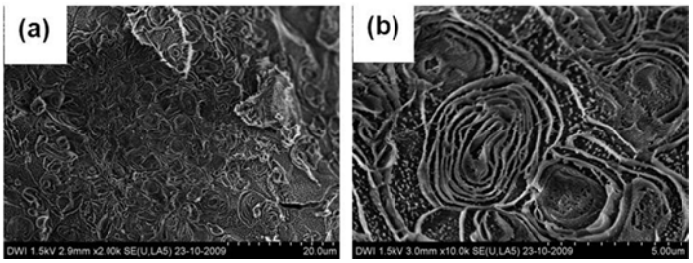

Figure 4. Cryo-FESEM micrographs of $P2VP_{227}(\underline{2})_x$-$PEO_{254}$: (a) x=0.25, multilamellar vesicles; and (b) enlarge view of (a).

9.3.5. Morphology of $P2VP_{180}(\underline{3})_x$-$PEO_{560}$.

Figure 5 shows the morphology of onion type vesicles from another wedge-shaped mesogen, which has sulfonic acid as the head. The interaction between the mesogen and P2VP backbone is changed to ionic interaction between sulfonic acid/pyridine via proton transfer. The morphology of this complex family in thin films has been reported.[25] The morphology and the orientation of the microdomains structure is controlled by the degree of protonation. The wedge-shaped molecule forms smectic layers parallel to the substrate interface while the block copolymer microdomains, *i.e.* PEO lamellae or cylinders, are normal to the smectic plane. When it is self assembled in water, the structure depends on the degree of protonation: they form giant vesicles (when $x \leq 0.5$) or precipitation (when x=1.0). Figure 5 shows x=0.25 as an example.

The size distribution of the giant vesicles is very broad, which varies from several micrometers to ~100μm (Figure 5a). The freezing-fractured FESEM image shows the multi-lamellar structure of this vesicle. On the wall the smectic structure parallel to the wall is clearly visible, which are the clear evidence of the formation of the onion type vesicles depicted in Scheme 1d.

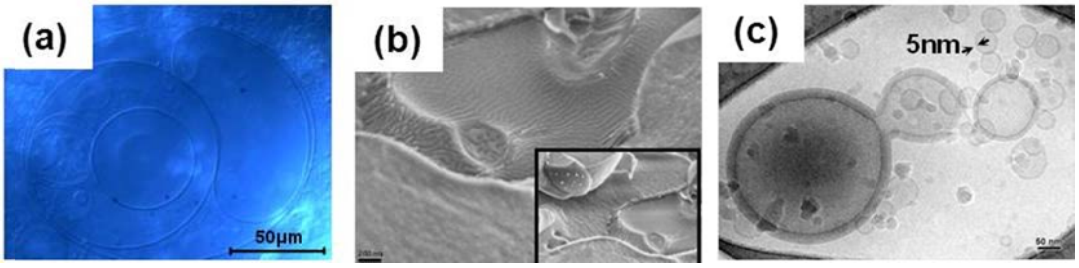

Figure 5. Morphology of $P2VP_{180}(\underline{3})_{0.25}$-$PEO_{560}$ in water: (a) optical microscope micrograph; (b) Cryo-FESEM micrograph; and (c) Cryo-TEM micrograph.

However, until now all of the evidences for the formation of unique onion type vesicles shown in scheme 1d are the close packing of the wall and the microphase separation of the PEO on the wall. Cryo-TEM provides direct evidence of the structure of the wall. As shown in Figure 5c, both of unilamellar and multilamellar vesicles present in the solution. The remarkable feature is that the thickness of the wall of the unilamellar vesicles is only 5nm, which agrees very well with the thickness of smectic layer consisting bilayer of the mesogen and P2VP backbone (5.6nm) in the solid state. If one checks the contrast of the Cryo-TEM micrograph carefully one can find that the variation of the dark and gray contrast on the wall, the dark contrast always appears on the water/wall interface and the body of the wall is gray, such kind of contrast originates from the contrast between hydrocarbon and sulphur, sulphur has slight higher electron density therefore it is dark, this directly proves that protonated P2VP are hydrophilic and it exposures to the water phase. In addition in the multilamellar vesicles variation of the dark and gray contrasts with a period of about 5nm is observed, proving that the multilamellar wall comes from the close packing of the smectic layers in a similar way to that of in the solid state.[23, 25]

9.3.6. Morphology of $P2VP_{180}(\underline{4})_x$-$PEO_{560}$ and $P2VP_{180}(\underline{5})_x$-$PEO_{560}$.

Two normal mesogens with carboxylic acid as head and thiophene rings as core are chosen as ligands, and the self-assembly behaviour of their complex with P2VP-PEO are investigated. The mesogen **4** forms stable complex with P2VP via hydrogen bonding in the solid state, while the complex of **5** are not stable for long time in the solid state at room temperature because of the strong tendency of the crystallization of **5**. However the structure formed in the solution is stable, no unexpected precipitation and structure change are observed during the investigation period (2-3 months), indicating that the interaction between carboxylic acid and pyridine is strong enough to prevent the crystallization of **5** in the vesicles. The self-assembly behaviour of the $P2VP_{180}(\underline{4})_x$-$PEO_{560}$ is investigated. The complex of **4** forms smectic phase at room temperature, and the morphology in the thin films and the orientation of the microdomains are controlled by the degree of complexation. (Chap. 8)

Depends on the degree of complexation, different morphologies form: for **4**, giant vesicles form with phase transfer method when $x<0.5$, while for **5**, until $x=0.75$ giant vesicles form but with some yellow precipitation in the bottom of the vial. FTIR results show that the saturated degree of complexation are between 0.5-0.75 and 0.33, for **4** and **5**, respectively (support information, Figure S1). Therefore the yellow precipitation is assigned to the crystallization of free **5** after the evaporation of the chloroform. Figure 6 shows the typical morphology of the giant vesicles from **4** and **5**. The size distribution of the giant vesicles are broad, it varies between 1-100μm. Different from that of mesogen **1** - **3**, the morphology of the giant vesicles forms in **4** and **5** is dominated by unilamellar vesicles, mutil-vesicles, and occasionally concentric vesicles. Another interesting feature is the shape of the vesicles. In the cases of **1** - **3**, the shapes of the vesicles are always round, the wall of the vesicles is fluffy, which deform with the water flow stream during the optical microscope observation. In the **4** and **5**, the wall is robust, no deformation is observed with the water flow stream. Some vesicles have the shaped edge (Figure 6a), which is similar to the situation of smecticsomes reported by Li *et al*.[10, 13, 15] This properties can be ascribed to the presence of ordered liquid crystalline phase and stiff polymer backbone as wall materials.[17]

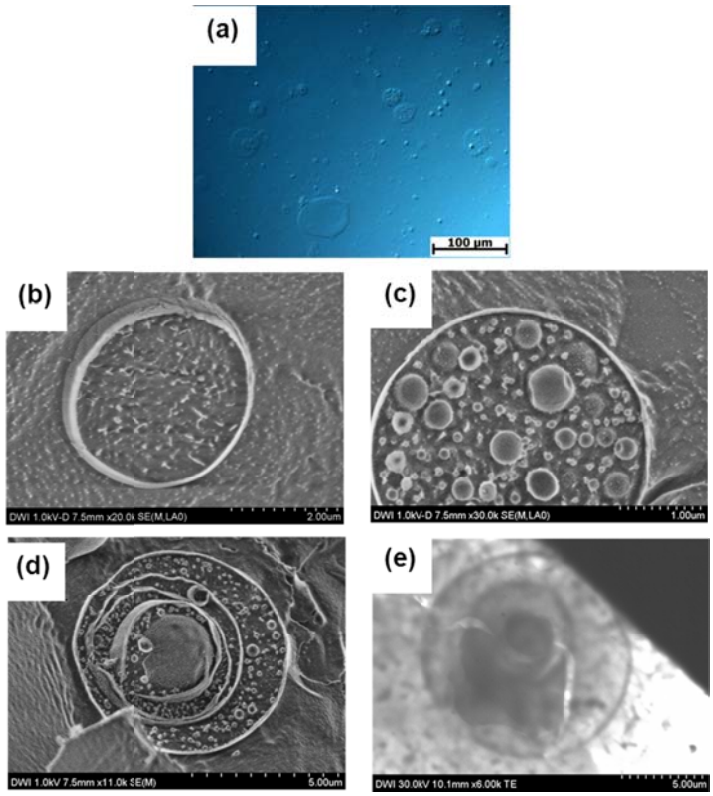

Figure 6. Morphology of P2VP$_{180}$(**L**)$_x$-PEO$_{560}$ in water: (a) **4**, x=0.33 optical microscope micrograph; CryoFESEM micrographs of (b) and (c) **4**, x=0.25; (d) **5**, x=0.33; and (e) **5**, x=0.33, CryoSTEM.

Cryo-FESEM technique proves the observation of the optical microscope. The unilamellar vesicles and multi-vesicles are clearly visible with this technique, and on the wall there is no clear evidence of microphase separation. The buzzing situation is from the concentric vesicles (Figure 6d), which is very close to that of multilamellar vesicles (i.e. Figure 3c and Figure 4d). However, if we compare these two situations carefully (Figure 6d and Figure 3c), two main difference can be found: (1) no microphase separation on the wall (STEM image, Figure 6e), and (2) most importantly the layers in the concentric vesicles are not close packed, and between layers smaller vesicles (particles) are observed (Figure 6d). It is known that liquid crystalline phase has a self-healing property,[26] any defects like the curvature generated by impurity (particle) will be eliminated by self-healing, leading to a wall with perfect ordering. In the present case, big particles observed between different layers, which can generate huge defects to the ordering of liquid crystalline phase, the presence of structure similar to that of Figure 5c will prevent the formation of the

particles between smectic layers. Therefore we can exclude the formation of onion type vesicles from these two mesogens, and mostly they generate the smecticsomes similar to Li's situation (Scheme 1c).

9.5. Discussions.

Now we discuss the reason for the formation of unique onion type vesicles. As shown in Figure 7, in a wide range of hydrophilic block ratio (w_{PEO}~0.17-0.42), vesicles form in water with the phase transfer method, this range is slightly broader than that of normal coil-coil block copolymers, where vesicles are found in the hydrophilic block ratio of 0.25-0.45.[3] In addition, depending on the surface area per PEO chain, different type of vesicles are found even in the same range of w_{PEO}: normal vesicles (Scheme 1c) at low surface area per PEO chain and unique onion type vesicles (Scheme 1d) at high surface area per PEO chain, indicating that this new type of vesicle may follow another formation mechanism.

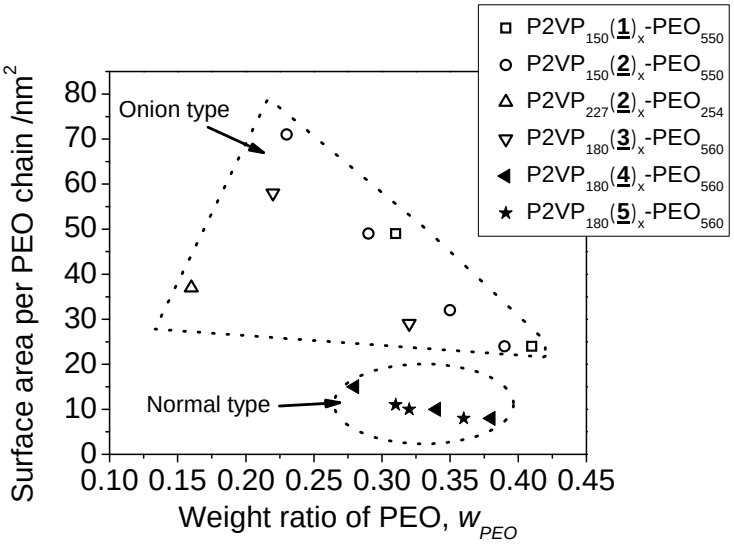

Figure 7. Morphology mapping of vesicles formed from $P2VP_n(\underline{L})_x$-PEO_m.

As shown above, the P2VP chain shows unique parallel orientation in the wall and contacts with water directly, and the bulk side group pack closely to form the wall, this situation is very similar to that of the phospholipids:[1] the hydrophilic head group contact with water, and the hydrophobic tail forms the wall, the alternative packing of the bilayer forms the onion type vesicles. P2VP is hydrophilic, and it can response to

water vapour,[27] or even water soluble if it is protonated.[28] In the present case, the ligand is attached to the P2VP either with hydrogen bond between carboxyl group/pyridine (**1**, **2**, **4**, **5**) or proton transfer between sulfonic group/pyridine, both of them increase the hydrophilicity of the P2VP chain, enhance the compatibility between the P2VP and water. Another issue is that if the P2VP/ligand complex wants to form similar structure shown in Scheme 1a, the size of the hydrophobic part (tail of the ligand) relative to the hydrophilic part (the P2VP and the head of the ligand) must fit a requirement: the value of v/al need to be between 0.5 and 1. In order to calculate the value, the interfacial area value of 0.64nm^2 is used for ligand of **1**, **2** and **3**, and 0.18nm^2 (estimated from the diameter of the thiophene) for **4** and **5**, respectively, the length of the hydrophobic part is calculate from the molecular length (MM2), and the volume of the hydrophobic tail is estimated by an assumption of the density of 1g/cm^3 for all of the ligand. The results are listed in Table 1. As can be seen, the wedge-shaped ligands **1**-**3** show a value between 0.5 and 1, indicating that they can form similar structure like liposomes, namely the alternative close packing of P2VP and ligand bilayer structure. Indeed onion type vesicles can form from the complex of wedge-shaped ligand/homopolymer poly (4-vynyl pyridine) (P4VP). The alternative assembles of the P4VP and mesogens generate the multilayer structure.[29] In comparison, the normal ligands used in the present research have packing parameter >1, indicating that they are too hydrophobic to form the structure similar to that of the liposome (Scheme 1a), therefore they cannot form the unique onion type vesicle (Scheme1d) but only the smecticsome (Scheme 1c), and the LC ordering on the wall leads to the formation of shaped wedge on the vesicles (Figure 6a).

Table 1. Packing parameters of the ligands

Ligand	l/nm	v/nm^3	p
1	1.6	0.84	0.82
2	1.7	0.96	0.88
3	2.8	1.27	0.71
4	1.7	0.81	2.80
5	1.9	0.95	2.94

Table 2. Summarization of the mass ratio of P2VP-PEO/ligand, x_g, area per PEO chain, and squared Flory radius R_F^2, depending on the degree of protonation.

Samples	Molar ratio x_g	Σ /nm^2	R_F^2	R_F^2/ Σ
P2VP$_{150}$(**2**)$_{0.25}$-PEO$_{550}$	0.027	24	238	10
P2VP$_{150}$(**2**)$_{0.33}$-PEO$_{550}$	0.020	32	238	7
P2VP$_{150}$(**2**)$_{0.50}$-PEO$_{550}$	0.013	49	238	5
P2VP$_{150}$(**2**)$_{0.75}$-PEO$_{550}$	0.009	71	238	3
P2VP$_{227}$(**2**)$_{0.25}$-PEO$_{254}$	0.017	29	94	3
P2VP$_{180}$(**4**)$_{0.25}$-PEO$_{560}$	0.022	8	243	30
P2VP$_{180}$(**4**)$_{0.33}$-PEO$_{560}$	0.017	10	243	24

Another point is the role of PEO in the formation of onion type vesicle and the origin of microphase separation of PEO on the wall. Based on the model (Scheme 1d) and on the molecular dimension, one may estimate the surface area per PEO chain for different degree of protonation with different ligand. This can be done by the way that the area per PEO chain (Σ) on the monolayer surface is set by the molar ratio x_g of P2VP-P2VP/ ligand, where Σ~(a_g/x_g) nm^2, a_g is a nominal area per ligand: 0.64nm^2 for wedge-shaped molecules and 0.18 nm^2 for the thiophene oligomers. Table 2 summarizes the results of ligand **2** and **4** as examples. For the wedge-shaped ligand **2**, when x=0.25 the surface area is 24 nm^2 per PEO chain, and it is increased to 49nm^2 when x is increased to 0.50. By comparison, the cross section (squared Flory radius, R_F^2) of swollen this PEO chain in dilute aqueous solution is R_F^2= ($aN_{PEO}^{0.6}$)^2=238 nm^2 when a=0.35nm and N_{PEO}=550. Thus the average area per PEO chain is significantly reduced to less than that of the squared Flory radius, indicating that the chain configuration of PEO is significantly restricted and it locates in the highly strength region.[18] Compared the situation of x=0.25 to that of 0.50, one can find that high degree of complexation increases the average area per chain, therefore the constriction is less and repulsion is weaker, as a consequence, the formation of onion type vesicle is facilitated at high degree of complexation. This is proved by factors that in the ligand **1**, and **2** onion type vesicle dominate at high degree of complexation. Reducing the degree of polymerzation of PEO chain also enhances the formation of the onion type vesicles, actually almost all of the vesicles observed in P2VP$_{227}$(**2**)$_{0.25}$-PEO$_{254}$ are

onion type vesicle, and as shown in Table 2, the R_F^2/Σ is significantly reduced to 3 at x=0.25.

In comparison, the thiophene oligomer with branched tail **4** shows much low value of area per PEO chain, indicating that the PEO chain is in more interactive region and therefore the repulsion between the PEO chain are much higher. It is almost 3 times larger than that of the wedge-shaped ligands at the similar degree of complexation with similar composition of original block copolymer. If one compares the value of R_F^2/Σ, this is another reason that onion type vesicle cannot form in these two ligands.

We interpret the in-plan structure of the PEO on the wall as the results of the osmotic pressure that arises from the local surface density of the PEO chains. Indeed, different conformation of the grafted polymer on a surface is discernible: (1) "mushrooms" when the mean distance between the grafting sites is larger than the polymer size R_F, (2) crossover region when the mean distance is comparable to R_F, and (3) highly strength region if the mean distance is smaller than R_F.[18] The situation (2) is also called mushroom-to-brush transition and is commonly used to signify the brush-like behaviour of the grafted polymer layer. The situation in the bilayer is slightly different from that of the solid surface, limited number of polymer chain can be grafted onto the bilayer because of: (1) the total repulsive interactions must equal to the water-oil surface tension, and (2) the lateral pressures of tethered polymers are a very sharply increasing function of the surface coverage and may lead to unstable films, *i.e.*, induced micelle formation.[30] In the present case, the conformation of the PEO chain is in the situation of (3), in which they strongly interact with each other (Table 2), therefore the phase separation is expected. Similar to that of block copolymer in the solid state, two situations are observed: (1) PEO shows disordered structure on the wall, where no phase separation is observed by the present technology, e.g., Figure 2a and Figure 3a, in these situations, unilarmellar vesicles are observed, the number of PEO chain is too low to form well defined structure, which is similar to the situation of block copolymer in extreme thin film; and (2) well order phase separation structure, e.g. Figure 3c and d, in these cases multilamellar vesicles with close packed wall structure is observed. This situation is quite similar to that of block copolymer in thin films.[31]

9.5. Conclusions.

In the present paper the onion type vesicle is prepared by the phase transfer method and the morphology of them are investigated in detail by using of Cryo-Electron Microscope. The block copolymer is constructed by grafting of ligand to the P2VP via secondary interaction: hydrogen bonding between carboxylic acid/pyridine and ionic bond between sulfonic acid/pyridine groups. These two types of interaction are strong enough to generate stable complex in water, and the structure of the vesicles depends on the degree of complexation, the length of PEO chain, and the geometry of the ligand. A unique onion type vesicle is obtained from the complex of P2VP-PEO/wedg-shaped ligand in a wide composition region of PEO. The wall of the onion type vesicle is made from alternative close packing of the P2VP and ligand bilayer, where the hydrophilic P2VP backbone is parallel to the wall and contact with water. The second block PEO forms well defined nanostructure on the wall when there are enough PEO chains in multilamellar vesicle, or disordered structure in the unilamellar vesicle. Actually the packing of the P2VP/wedge-shaped ligands is similar to that of phospholipids in liposome, the packing parameter of the three wedge-shaped ligands is between 0.7-0.9, which is predicted to forms vesicles. In comparison, the thiophene oligomers cannot form similar onion type structure even when the weight ratio of PEO locates in the same region as the wedge-shaped ligand, because of the packing parameter is far away from 1, which prevents the formation of the vesicle structure from the P2VP/ligand alone, indeed they form normal smecticsome in the water with PEO as corona.

9.6. References

[1] D. Lasic, D. Papahadjopoulos, *Science* **1995**, *267*, 1275.

[2] R. Lipowsky, E. Sackmann, *Structure and Dynamics of Membranes I. From Cells to Vesicles* North Holland, 1995.

[3] D. E. Discher, F. Ahmed, *Annu. Rev. Biomed. Eng.* **2006**, *8*, 323.

[4] A. Blanazs, S. P. Armes, A. J. Ryan, *Macromolecular Rap. Comm.* **2009**, *30*, 267.

[5] J. s. del Barrio, L. Oriol, C. Sánchez, J. L. Serrano, A. l. Di Cicco, P. Keller, M.-H. Li, *J. Am. Chem. Soc.* **2010**, *132*, 3762.

[6] D. E. Lonsdale, M. J. Monteiro, *J. Polym. Sci. Part A: Polym. Chem.* **2011**, *49*, 4603.

[7] M. Antonietti, S. Förster, *Adv. Mater.* **2003**, *15*, 1323.

[8] S. J. Holder, N. A. J. M. Sommerdijk, S. J. Williams, R. J. M. Nolte, R. C. Hiorns, R. G. Jones, *Chem. Commun.* **1998**, 1445.

[9] J. Yang, D. Levy, W. Deng, P. Keller, M.-H. Li, *Chem. Commun.* **2005**, 4345.

[10] J. Yang, R. Piñol, F. Gubellini, D. Lévy, P.-A. Albouy, P. Keller, M.-H. Li, *Langmuir* **2006**, *22*, 7907.

[11] R. Piñol, L. Jia, F. Gubellini, D. Lévy, P.-A. Albouy, P. Keller, A. Cao, M.-H. Li, *Macromolecules* **2007**, *40*, 5625.

[12] S. p. Boissé, J. Rieger, A. l. Di-Cicco, P.-A. Albouy, C. Bui, M.-H. Li, B. Charleux, *Macromolecules* **2009**, *42*, 8688.

[13] E. Mabrouk, D. Cuvelier, L.-L. Pontani, B. Xu, D. Levy, P. Keller, F. Brochard-Wyart, P. Nassoy, M.-H. Li, *Soft Matter* **2009**, *5*, 1870.

[14] B. Xu, R. Pinol, M. Nono-Djamen, S. Pensec, P. Keller, P.-A. Albouy, D. Levy, M.-H. Li, *Faraday Discuss.* **2009**, *143*, 235.

[15] M.-H. Li, P. Keller, *Soft Matter* **2009**, *5*, 927.

[16] L. Jia, A. Cao, D. Levy, B. Xu, P.-A. Albouy, X. Xing, M. J. Bowick, M.-H. Li, *Soft Matter* **2009**, *5*, 3446.

[17] H. Yang, L. Jia, C. Zhu, A. Di-Cicco, D. Levy, P.-A. Albouy, M.-H. Li, P. Keller, *Macromolecules* **2010**, *43*, 10442.

[18] P. G. de Gennes, *Macromolecules* **1980**, *13*, 1069.

[19] A. D. Bangham, R. W. Horne, *J. Mol. Biol.* **1964**, *8*, 660.

[20] J. Kuntsche, K. Westesen, M. Drechsler, M. H. J. Koch, H. Bunjes, *Pharmaceutical Res.* **2004**, *21*, 1834.

[21] J. A. Zupancich, F. S. Bates, M. A. Hillmyer, *Biomacromolecules* **2009**, *10*, 1554.

[22] K. Albrecht, Vol. PhD, RWTH Aachen University, Aachen 2007.

[23] X. Zhu, U. Beginn, M. Möller, R. I. Gearba, D. V. Anokhin, D. A. Ivanov, *J. Am. Chem. Soc.* **2006**, *128*, 16928.

[24] J. Lejnieks, Vol. PhD, RWTH Aachen University, Aachen 2011.

[25] K. Albrecht, A. Mourran, X. Zhu, T. Markkula, J. Groll, U. Beginn, W. H. de Jeu, M. Moeller, *Macromolecules* **2008**, *41*, 1728.

[26] P.-G. de Gennes, J. Prost, *The Physics of Liquid Crystals*, Oxford University Press, 1995.

[27] K. Albrecht, A. Mourran, M. Moeller, **2006**, *200*, 57.

[28] R. Varoqui, Q. Tran, E. Pefferkorn, *Macromolecules* **1979**, *12*, 831.

[29] D. Xie, M. Jiang, G. Zhang, D. Chen, *Chem. – A Euro. Journal* **2007**, *13*, 3346.

[30] K. Hristova, A. Kenworthy, T. J. McIntosh, *Macromolecules* **1995**, *28*, 7693.

[31] M. J. Fasolka, A. M. Mayes, *Annu. Rev. Mater. Res.* **2001**, *31*, 323.

Supporting Information I: Chapter 3 Structural and electrical properties of asymmetrically substituted sexithiophene monolayers

Experimental section

Materials. Solutions of *n*-butyllithium (*n*-BuLi) in hexane (2.5 mole L^{-1}), 2-bromothiophene, *N*-bromosuccinimide (Acros), 2-isopropoxy-4,4,5,5-tetramethyl-1,3,2-dioxaborolane, [1,1'-bis(diphenylphosphino) ferrocene]dichloropalladium(II) Pd(dppf)Cl_2 and *tetrakis*(triphenylphosphine) palladium(0) Pd(PPh_3)$_4$ (Aldrich) were used as received. THF and diethyl ether were dried by distillation over calcium hydride followed by distillation over lithium aluminum hydride. DMF was dried by distillation over BaO. Compound **3** and **5** were obtained as described in literature.[1, 2]

Characterizations. ^{1}H NMR spectra were recorded on a Bruker WP-250 SY spectrometer (250.13 MHz) using a signal of $CDCl_3$ (δ = 7.25) as the internal standard. ^{13}C NMR spectra were recorded on a Bruker Avance II 300 spectrometer at 75.48 MHz, while ^{11}B NMR spectra were recorded on a Bruker Avance II 300 spectrometer at 96.31 MHz. GPC analysis was carried out on a Shimadzu series 10-AVP System (Japan), equipped with a RID-10A refractometer and an SPD-M10AVP diode array matrix served as detectors, Phenomenex column (USA, 7.8x300 mm in size packed with the Phenogel sorbent with the pore size 500 Å) and THF as the eluent at 40 °C. All reactions, if not otherwise stated, were carried out under an inert atmosphere and in anhydrous solvents. The solvents were removed by evacuation (down to 1 Torr) on heating to 40 °C.

Synthesis. Synthesis of compound **2** was carried out according to **Scheme S1**. As a key step for this purpose a Suzuki reaction was chosen,[3] which was proved to be very effective for preparation of unsymmetrical oligothiophenes.[4, 5] Therefore, bromo-containing terthiophene derivative **4** and borolane-containing terthiophene derivative **7** have been prepared and sed in eth Suzuki coupling reaction. Compound **3** was used as the first initial compound,[1] which was brominated with N-bromosuccinimide in DMF solution in 91% isolated yield similar as described in literature.[6] Compound **5** was used as the second initial compound, which was

lithiated by *n*-butyl lithium in THF-hexane, followed by reacting with the $MgBr_2 \cdot Et_2O$ complex, prepared *in situ* from magnesium and dibromoethane in diethyl ether. The resulting magnesium derivative of compound **5** was used in Kumada coupling reaction with 2-bromothiophene in THF using [1,1'-bis(diphenylphosphino)ferrocene]dichloropalladium(II) ($Pd(dppf)Cl_2$) as a catalyst similar as described in the literature,[7] to yield compound **6** in 71% reaction and 58% isolated yield. Compound **6** was lithiated with *n*-butyl lithium in THF-hexane mixture followed by the reaction of the monolithium derivative thus formed with 2-isopropoxy-4,4,5,5-tetramethyl-1,3,2-dioxaborolane (IPTMDOB) to give compound **7** in 98.5% isolated yield. Compounds **4** and **7** were reacted under the Suzuki conditions using 2M aq. Na_2CO_3 as a base and toluene-ethanol mixture as a solvent similar as described in the literature.[8] After 54 h of reflux compound **2** was obtained in 88% reaction and 64% isolated yield. Purification of this and previous compounds was made by column chromatography (eluent - toluene) and recrystallization in toluene.

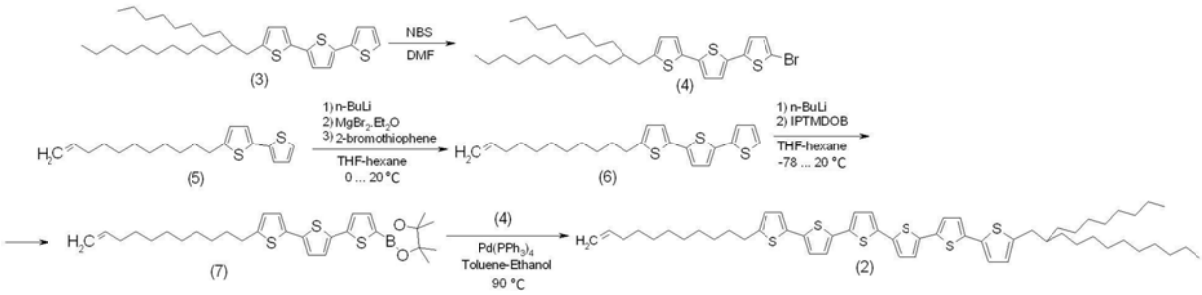

Scheme S1. Synthesis of 6T-oligomer with an undecyl spacer and a 2-octyldodecyl terminal group.

Compound ***4***. A solution of **3** (1.15 g, 2.17 mmol) in a mixture of 20 mL of toluene and 10 mL of DMF was cooled to -10 °C. In dark, a solution of N-bromosuccinimide (0.41 g, 2.28 mmol) in 8 mL of DMF was added dropwise during 10 min. After 10 min of stirring the cooling bath was removed and the reaction mixture was stirred at 22 °C for 12 h. The mixture was then poured into 200 mL of water and 300 mL of diethyl ether. The organic layer was isolated, washed with water and dried over sodium sulfate (referred to as the standard isolation below). After that the solvent was removed and the mixture was dried under vacuum (1 mbar) to yield 1.28 g of the crude product. It was purified by column chromatography on silica gel (eluent –

toluene : hexane mixture 1:3 v/v) to give pure compound **4**. Yield: 1.19 g (91%). ^{1}H NMR ($CDCl_3$, 250 MHz, δ ppm): 0.87 (t, 6H, *J* = 6.7 Hz, -C*H*$_3$), 1.17-1.38 (overlapped peaks with a max. at 1.25, 32H, -CH_2-C*H*$_2$-CH_2-), 1.61 (m, 1H, -CH_2-C*H*$(CH_2)_2$-), 2.72 (d, 2H, *J* = 6.7 Hz, -thiophene-C*H*$_2$-), 6.65 (d, 1H, *J* = 3.7 Hz, thiophene-H), 6.87 (d, 1H, *J* = 3.7 Hz, thiophene-H), 6.86-7.05 (overlapped peaks with a max. at 6.97, 4H, thiophene-H). Found (%): C, 63.19; H, 7.81; S, 15.79; Br, 13.10. Calc. for $C_{32}H_{47}BrS_3$ (%): C, 63.23; H, 7.79; S, 15.83; Br, 13.15.

Compound ***6***. THF (15 mL) was added dropwise to a 2.5 *M* solution (6.28 mL) of *n*-BuLi in hexane (15.7 mmol), maintaining the temperature below -10 °C. Then a solution of **5** (5.00 g, 15.7 mmol) in THF (15 mL) was added slowly, maintaining the temperature in the interval from -10 to 0 °C, after that the reaction mixture was heated up to 23 °C. An etheral solution of the complex of magnesium bromide with ether (freshly prepared from magnesium (0.456 g, 19 mmol) and dibromoethane (3.24 g, 17.3 mmol) in 20 mL of anhydrous ether) was poured to the obtained lithium derivative. The resultant Grignard reagent was added dropwise to a solution of the Pd(dppf)Cl_2 catalyst (0.057 g, 0.078 mmol) and 2-bromothiophene (2.82 g, 17.3 mmol) in THF (10 mL) at 10 °C. After heating to ~20 °C, the reaction mixture was stirred for 4 h. According to the GPC analysis, after the standard isolation the reaction mixture contained 71% of the product, purification of which was carried out by recrystallization in hexane. The yield of pure product was 3.65 g (58%). ^{1}H NMR ($CDCl_3$, 250 MHz, δ, ppm): 1.24-1.45 (overlapped peaks with a max. at 1.28, 14H, -CH-C*H*$_2$-CH_2-), 1.67 (m, 2H, *J* = 7.3 Hz, -thiophene-CH_2-C*H*$_2$-CH_2-), 2.03 (dt, 2H, J_1 = 7.3 Hz, J_2 = 6.7 Hz, =CH-C*H*$_2$-CH_2-), 2.77 (t, 2H, *J* = 7.3 Hz, -thiophene-C*H*$_2$-), 4.89-5.03 (m, 2H, C*H*$_2$=CH-), 5.73-5.89 (m, 1H, CH_2=C*H*-), 6.67 (d, 1H, J = 3.7 Hz, thiophene-H), 6.97 (d, 1H, J = 3.7 Hz, thiophene-H), 6.99 (d, 1H, J = 3.7 Hz, thiophene-H), 7.00 (dd, 1 H, J_1 = 3.7 Hz, J_2 = 4.9 Hz, thiophene-H), 7.04 (d, 1H, J = 3.7 Hz, thiophene-H), 7.15 (dd, 1 H, J_1 = 3.7 Hz, J_2 = 1.2 Hz, thiophene-H), 7.19 (dd, 1 H, J_1 = 4.9 Hz, J_2 = 1.2 Hz, thiophene-H). Found (%): C, 69.11; H, 7.12; S, 23.92. Calc. for $C_{23}H_{28}S_3$ (%): C, 68.95; H, 7.04; S, 24.01. ^{13}C NMR ($CDCl_3$, 75 MHz, δ, ppm): 28.91, 29.04, 29.11, 29.32, 29.44, 29.46, 30.16, 31.57, 33.80, 114.10, 123.31, 123.44, 123.65, 124.21, 124.65, 124.79, 127.80, 134.42, 135.44, 136.78, 137.26, 139.21, 145.55.

Compound **7**. 2.16 mL of a 2.5 *M* solution of *n*-BuLi (5.4 mmol) in hexane was added dropwise to a solution of 2.0 g (5.0 mmol) of compound **6** in 250 mL of THF, maintaining the temperature in the interval from -70 to -78 °C. The reaction mixture was stirred for 30 min at -78 °C, then the temperature was increased to 0 °C after that it was cooled down again to -78 °C and 1.18 mL (5.8 mmol) of 2-isopropoxy-4,4,5,5-tetramethyl-1,3,2-dioxaborolane was added. After stirring the mixture for 30 min at -78 °C, the cooling bath was removed and the stirring continued for additional 1.5 h. After the completion of the reaction, 200 mL of diethyl ether and 100 ml of ice water containing 5 mL of 1 N HCl were added to the reaction mixture. The organic phase was separated, washed several times with water until pH = 7, and dried over anhydrous sodium sulfate, after which the solvent was removed. According to the GPC analysis, the isolated mixture contained 91% of the product. After purification by column chromatography using a 1:3 mixture of toluene–hexane as the eluent 2.59 g of the pure product was obtained (yield 98.5%). ^{1}H NMR ($CDCl_3$, 250 MHz, δ, ppm): 1.23-1.43 (overlapped peaks with a max. at 1.34, 24H, - CH_2-C*H*$_2$-CH_2-, O-C-C*H*$_3$), 1.66 (m, 2H, *J* = 7.3 Hz, -thiophene-CH_2-C*H*$_2$-CH_2-), 2.03 (dt, 2H, J_1 = 7.3 Hz, J_2 = 6.7 Hz, =CH-C*H*$_2$-CH_2-), 2.77 (t, 2H, *J* = 7.3 Hz, -thiophene-C*H*$_2$-), 4.89-5.03 (m, 2H, C*H*$_2$=CH-), 5.73-5.89 (m, 1H, CH_2=C*H*-), 6.67 (d, 1H, *J* = 3.7 Hz, thiophene-H), 6.97 (d, 1H, *J* = 3.7 Hz, thiophene-H), 6.99 (d, 1H, *J* = 4.3 Hz, thiophene-H), 7.10 (d, 1H, *J* = 4.3 Hz, thiophene-H), 7.20 (d, 1H, *J* = 3.7 Hz, thiophene-H), 7.51 (d, 1H, *J* = 3.7 Hz, thiophene-H). Found (%): C, 66.18; H, 7.51; S, 18.15, B, 2.11. Calc. for $C_{29}H_{39}BO_2S_3$ (%): C, 66.14; H, 7.46; S, 18.27, B, 2.05. ^{13}C NMR ($CDCl_3$, 75 MHz, δ, ppm): 24.54, 24.72, 28.89, 29.03, 29.09, 29.30, 29.43, 29.45, 30.15, 30.90, 31.55, 33.79, 84.15, 114.09, 123.49, 123.59, 124.61, 124.83, 124.93, 134.31, 135.26, 137.46, 137.94, 139.20, 143.93, 145.75. ^{11}B NMR ($CDCl_3$, 96.3 MHz, δ, ppm): -22.28.

Compound **2**. 226 mg (0.194 mmol) of $Pd(PPh_3)_4$ was placed in a reaction flask under an inert atmosphere, then degassed solutions of 1.19 g (1.96 mmol) of compound **4** and 1.24 g (2.35 mmol) of compound **7** in 70 mL of toluene, 2.1 mL of a 2 *M* solution of Na_2CO_3, and 2.1 mL of ethanol were added; the reaction mixture was heated to boiling. After 54 h of stirring under reflux it was cooled down to 22 °C and poured into 250 mL of water and 250 mL of toluene. The organic layer was rinsed with water until pH = 7 and dried over anhydrous sodium sulfate; the solvent was removed *in vacuo*. As a result, 1.75 g of the raw product in 88% purity (GPC) was

obtained. The purification by column chromatography (eluent - toluene) followed by recrystallization yielded 1.16 g (64%) of pure compound **2**. ^{1}H NMR ($CDCl_3$, 250 MHz, δ, ppm): 0.87 (t, 6H, J = 6.7 Hz, -CH_2-CH_3), 1.16-1.45 (overlapped peaks with a max. at 1.25, 46H, -CH_2-CH_2-CH_2-), 1.61 (m, 1H, -CH_2-CH(CH_2)$_2$-), 2.72 (d, 2H, -thiophene-CH_2-CH(CH_2)$_2$-), 2.78 (t, 2H, -thiophene-CH_2-CH_2-), 4.89-5.03 (m, 2H, CH_2=CH-), 5.73-5.89 (m, 1H, CH_2=CH-), 6.66 (broad peak, 2H, Hz, thiophene-H), 6.94-7.09 (overlapped peaks with a max. at 7.06, 10H, thiophene-H). MALDI-MS, *m/z*: 926.68 (M^+, calc. 927.59). Found (%): C, 71.16; H, 7.97; S, 20.92. Calc. for $C_{55}H_{74}S_6$ (%): C, 71.22; H, 8.04; S, 20.74.

DSC peaks deconvolution.

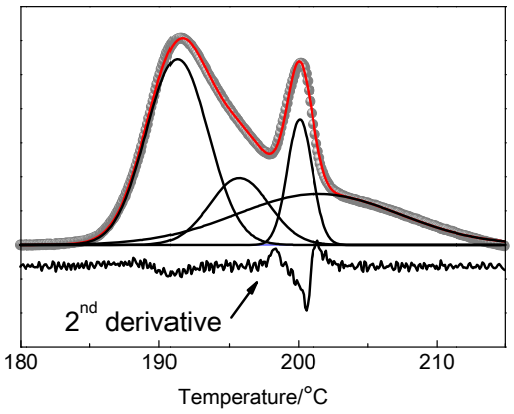

Figure S1. Peak deconvolution of the second heating curve of **2**

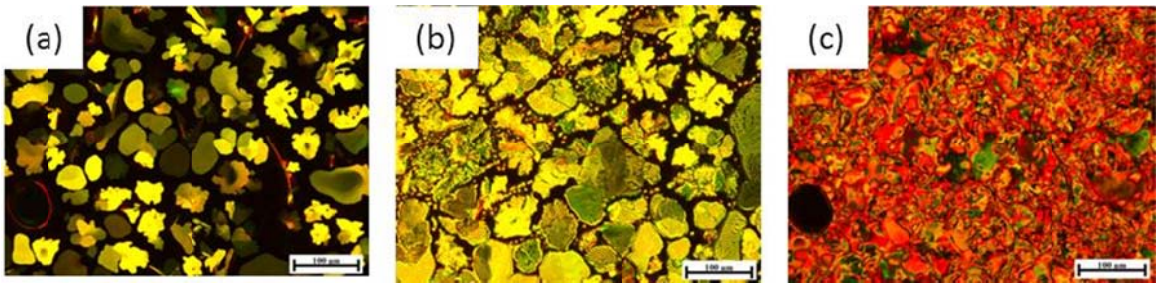

Figure S2. POM micrographs depicting the textures of molecule **2** upon cooling at 10 °C/min: (a) 200 °C; (b) 196 °C; (c) 195 °C.

Table S1. Model parameters from XRR for the asymmetric substituted 6T monolayer films.

Compounds	Model	Thickness/ Å	Electron density /eÅ^{-3}	Roughness/ Å
	Alkyl (top layer)	9.6	0.24	2.4
1	Thiophene core	24	0.46	2.4
	Alkyl (bottom layer)	12.5	0.36	3.8
	Alkyl (top layer)	9.6	0.15	1.6
2	Thiophene core	24.1	0.32	2.2
	Alkyl (bottom layer)	11.4	0.24	4.2

Table S2. GIWAXS parameters

Monolayer of compound 1			
(hk)	q_{xy} (nm^{-1}) exp	q_{xy} (nm^{-1}) theo	q_z (nm^{-1}) exp
(01)	12.6	12.6	5.1
(20)	16.6	16.5	10.4
(11)	15.6	15.0	0
(21)	18.7	20.8	5.3

Monolayer of compound 2			
(hk)	q_{xy} (nm^{-1}) exp	q_{xy} (nm^{-1}) theo	q_z (nm^{-1}) exp
(11)	12.08	12.04	6.78
(20)	9.25	9.24	12.95
(21)	14.50	14.46	12.88

Lines width analysis. The profiles of the degenerate peaks [(01) for compound **1** and (11) for compound **2**] were fitted to a Lorentzian and a Gaussian. In the in-plane direction a Lorenzian gives a better fit. This can be attributed to the well-know absence of long-range position order in infinite two-dimensional systems (See, for example, literature [9]). In that situation a Lorentzian function can serve to fit the wings of the x-ray peak that decay algebraically as $1/q^{2-\eta}$, while the central part can still be fitted to a Gaussian. Along the layer normal, the profiles clearly indicate a Gaussian distribution with a width σ=1.15 nm for compound 1 and σ=1.2 nm for compound 2, respectively. We assume that this distribution reflects the finite orientational order of the elongated molecules around their equilibrium direction.

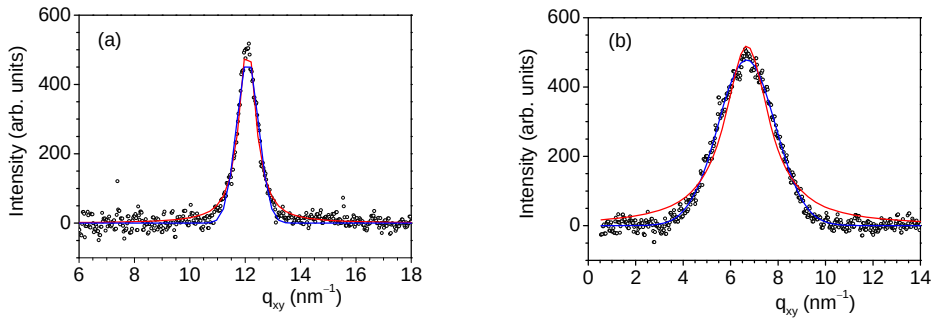

Figure S3. Line width analysis of the background-subtracted intensity of the (01) GIWAXS peak of sample 2 in (a) the longitudinal direction and (b) the transverse direction. Red lines: Lorentzian fit; blues Lines: Gaussian fit.

References.

[1] S. Ellinger, U. Ziener, U. Thewalt, K. Landfester, M. Möller, *Chem. Mater.* **2007**, *19*, 1070.

[2] S. A. Ponomarenko, O. V. Borshchev, T. Meyer-Friedrichsen, A. P. Pleshkova, S. Setayesh, E. C. P. Smits, S. G. J. Mathijssen, D. M. de Leeuw, S. Kirchmeyer, A. M. Muzafarov, *Organometallics* **2010**, *29*, 4213.

[3] A. Suzuki, *Acc. Chem. Res.* **1982**, *15*, 178.

[4] S. A. Ponomarenko, E. A. Tatarinova, A. M. Muzafarov, S. Kirchmeyer, L. Brassat, A. Mourran, M. Moeller, S. Setayesh, D. de Leeuw, *Chem. Mater.* **2006**, *18*, 4101.

[5] D. Didier, S. Sergeyev, Y. H. Geerts, *Tetrahedron* **2007**, *63*, 941.

[6] P. Bäuerle, F. Würthner, G. Götz, F. Effenberger, *Synthesis* **1993**, *1993*, 1099.

[7] S. A. Ponomarenko, S. Kirchmeyer, A. Elschner, N. M. Alpatova, M. Halik, H. Klauk, U. Zschieschang, G. Schmid, *Chem. Mater.* **2005**, *18*, 579.

[8] M. S. Polinskaya, O. V. Borshchev, Y. N. Luponosov, N. M. Surin, A. M. Muzafarov, S. A. Ponomarenko, *Mend. Comm.* **2011**, *21*, 89.

[9] P. M. Chaikin, T. C. Lubensky, *Principles of Condensed Matter Physics*, Cambridge University Press, Cambridge 1995.

Supporting Information II: Chapter 4 Thin Film Structure of Block Copolymer-Surfactant Complex: Strongly Ionic Bonding Polymer Systems

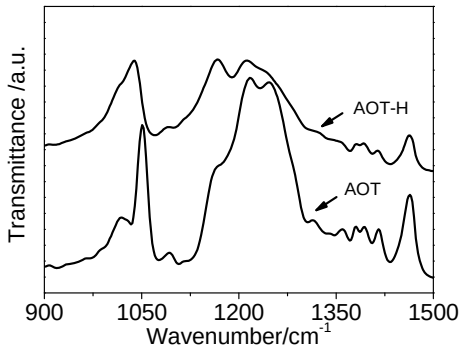

Figure S1. FTIR spectra of AOT and AOT-H

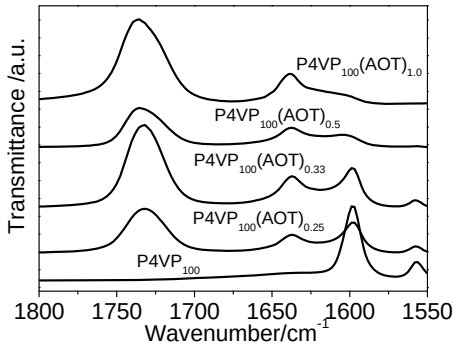

Figure S2. FTIR spectra of $P4VP_{100}(AOT)_{DN}$

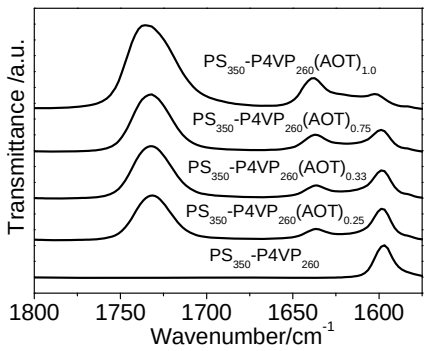

Figure S3. FTIR spectra of PS_{350}-$P4VP_{260}(AOT)_{DN}$

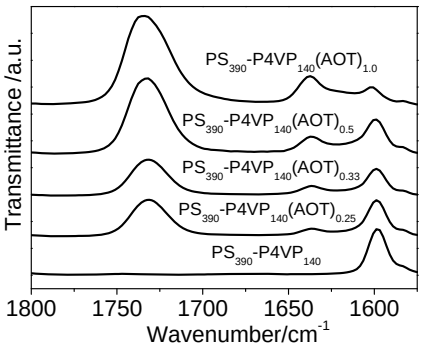

Figure S4. FTIR spectra of PS_{390}-$P4VP_{140}(AOT)_{DN}$

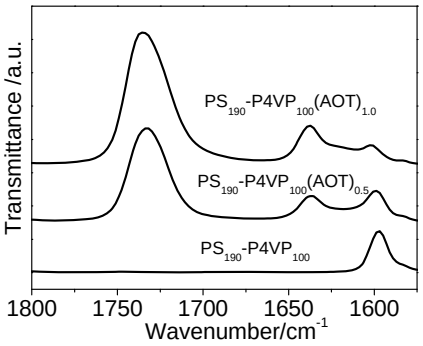

Figure S5. FTIR spectra of PS_{190}-$P4VP_{100}(AOT)_{DN}$

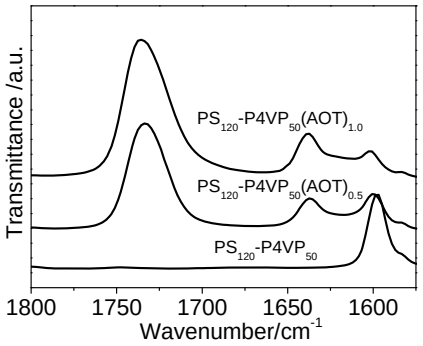

Figure S6. FTIR spectra of PS_{120}-$P4VP_{50}(AOT)_{DN}$

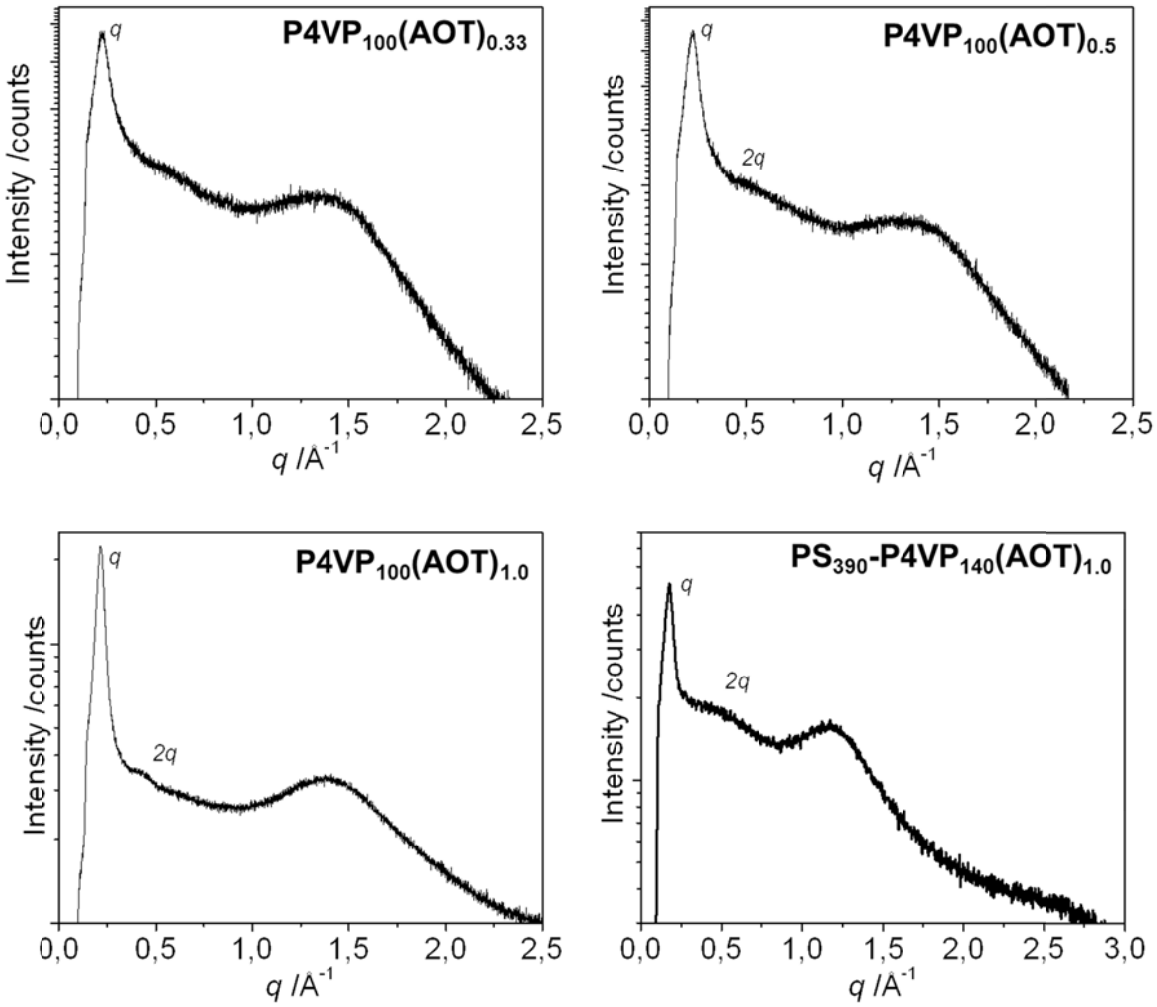

Figure S7. WAXS spectra for each homopolymer and copolymer complex note the faint second peaks (2q) which vanish at low protonation.

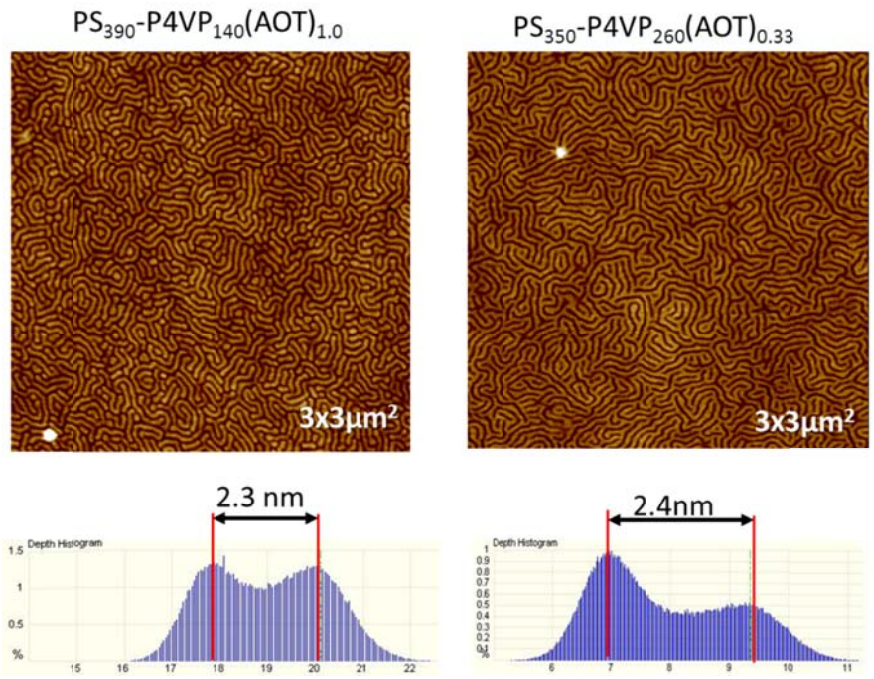

Figure S8. Representative height distribution and the corresponding height images.

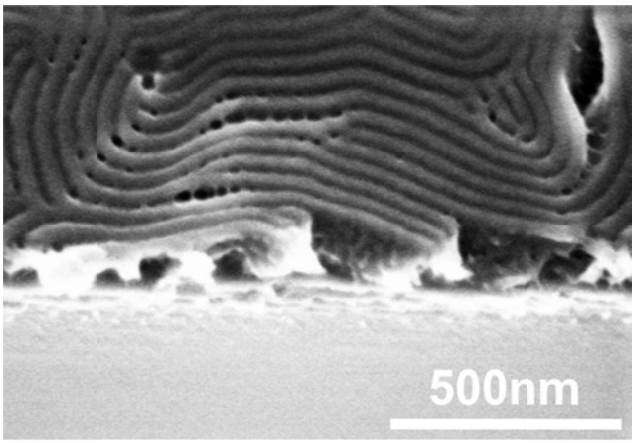

Figure S9. FESEM cross section of 1500Å thin films of PS_{390}-$P4VP_{140}(AOT)_{0.5}$. The film was imaged after immersion in diluted NH_3 solution for 30s, the viewing angle is 45°.

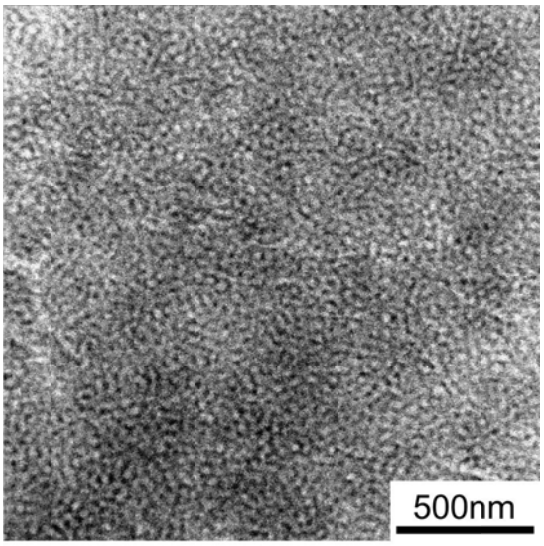

Figure S10. TEM image of PS_{390}-$P4VP_{140}(AOT)_{0.33}$, before washing with NH_3 solution.

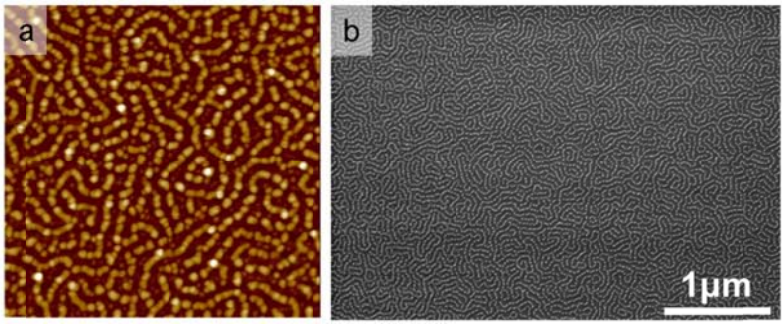

Figure S11. SFM and FESEM images of gold nanowires from PS_{390}-$P4VP_{140}(AOT)_{1.0.}$The scan size of the AFM image is $2\times2\mu m^2$. Interconnected gold nanoparticles with a diameter of ~150 Å, a height of ~200 Å, and a mean periodicity of 500 Å, which is similar to similar to the parent BC-complex template.

Supporting Information III: Chapter 6 Nanostructured TiO_2 Thin Films Templated from Co-assembly of Fully Miscible Block Copolymer Complex/Polymeric Precursors

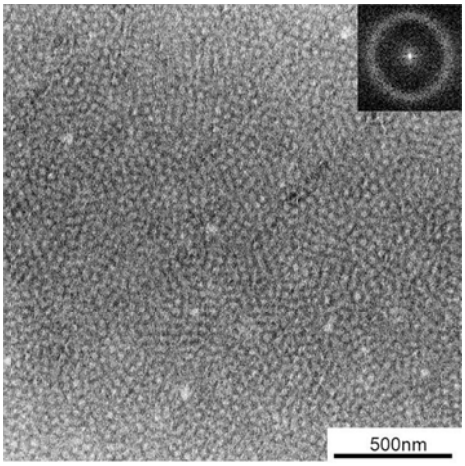

Figure S1. Morphology of PS_{350}-$P4VP_{260}(AOT)_{1.0}$/PAOT with Ti/Py molar ratio of 4.0/1; the insert pictures is the FFT of the same TEM image.

PS_{350}-$P4VP_{260}(AOT)_{1.0}$/PAOT. The PS_{350}-$P4VP_{260}(AOT)_{1.0}$ has a invert cylinder morphology, the PS cylinders are embedded inside the $P4VP_{260}(AOT)_{1.0}$ matrix, and it orients perpendicular to that of silicon surface in thin films.[1] Mixing with PAOT does not change the morphology. As shown in Figure S1, at Ti/Py=4.0/1, a gray dots embedded in dark matrix morphology is observed. Since the $P4VP_{260}(AOT)_{1.0}$/PAOT mixture has high density, it is dark and the gray dots can be the PS cylinders oriented vertically. The diameter of the PS domain is 24.2±1.0nm, and the periodicity is about 43nm.

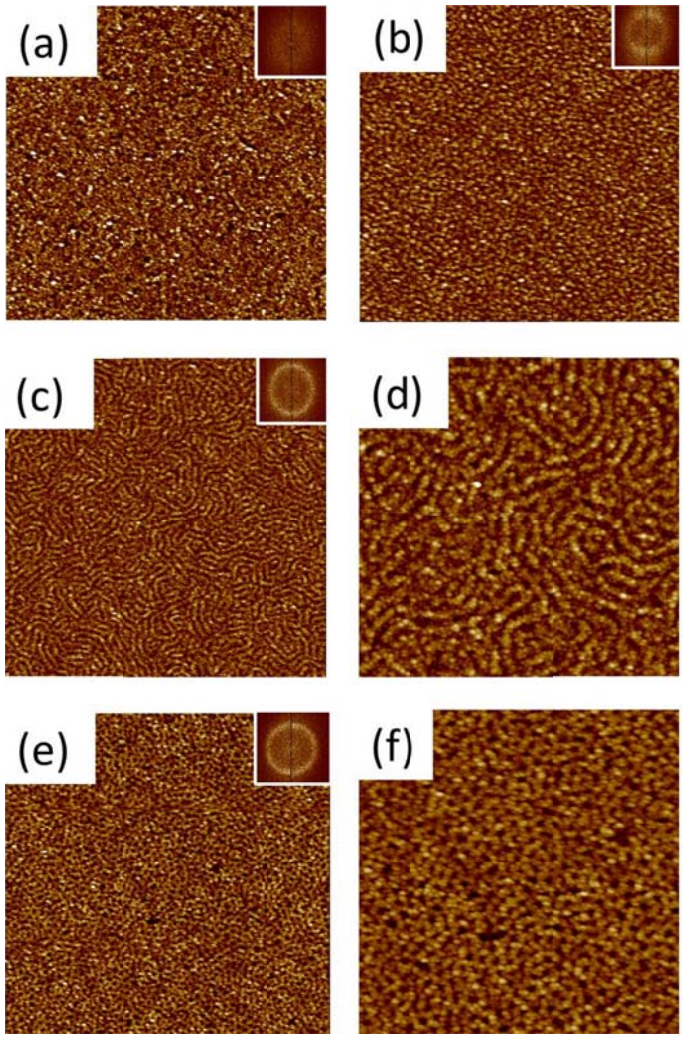

Figure S2. Topography images of TiO_2 templated from PS_{390}-$P4VP_{140}(AOT)_{0.33}$/PAOT: Ti/Py= (a) 2.6/1(scan size $3\times3\mu m^2$); (b) 10.2/1(scan size $3\times3\mu m^2$); (c) 20.4/1(scan size $3\times3\mu m^2$); (d) the enlarged view of (c) (scan size $1\times1\mu m^2$); (e) 40.9/1(scan size $3\times3\mu m^2$); and (f) the enlarged view of (e) (scan size $1\times1\mu m^2$); the insert pictures are the FFT of the same images

PS_{390}-$P4VP_{140}(AOT)_{0.33}$/PAOT. Figure S2 summarizes the films morphology depending on the molar ratio R (Ti/Py) after H_2 plasma treatment. For $R \leq 10.2$, the surface consists of a fine nanoparticle of TiO_2 (cf. Figure S2 a and b) with an average diameter and height of about 10 nm and 4 nm, respectively. Larger molar ratio ($R \geq 20$) leads to surface pattern similar to the parent templates. For R=20.4, a nanowire-like pattern (Figure S2 c and d) with an average period of about 44 nm comparable to TEM analysis (cf. Figure 4c). Figure S2 e and f show that the increase of R = 40.9 leads to a porous film with a depth comparable to the film thickness, i.e. 10 nm and an

in-plane period of about 37 nm, similar to TEM results (cf. Figure 4d). Note that, regardless of the composition the pattern is composed of fine-TiO_2 nanoparticles with an average diameter of about 10 nm (Figure S2d, S2f).

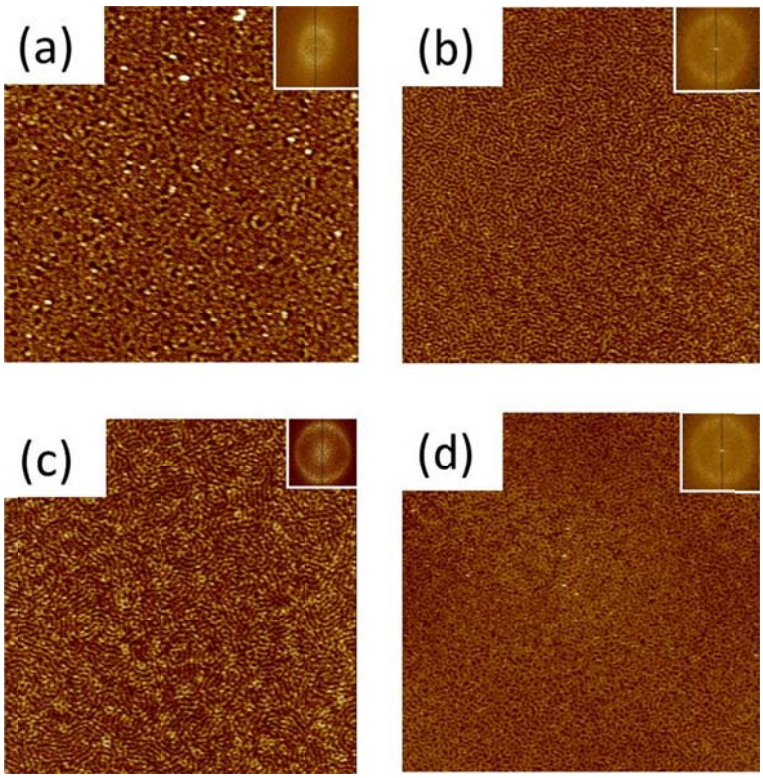

Figure S3. SFM height images of a thin film after treatment with H_2-plasma. The films were prepared from a mixture of PS_{390}-$P4VP_{140}(AOT)_{0.5}$ and PAOT with a molar ratio R= 1.9 (a), 7.6 (b), 15.2 (c) and, 30.5 (d); the insert are the corresponding FFT-images, the scan size is $3\times3\mu m^2$.

PS_{390}-$P4VP_{140}(AOT)_{0.50}$/PAOT. Figure S3a shows that for R=1.9, locally, fine nanoparticles forming a wire-like structure with poorly defined pattern, as suggested by the diffuse ring of the FFT-image. As R increase connected TiO_2 wire-like structure is formed for $7.6 \leq R \leq 15.2$. For R=7.6, the nanostructure exhibits a period and a height of about 42 nm and 6 nm respectively. Higher PAOT content, i.e. R=15.2, contour length of the wires-like increases, as shown in Figure S3 b and c. However, for R=30.5 porous structure develops with a periodicity of about 39 nm. The mean pore is of about 20 nm with a depth comparable to the film thickness, i.e. 10nm. High-resolution SFM image shows that nanostructure is composed of fine nanoparticles with a diameter of about 10 nm, similar to that of Figure S3d (image not shown here).

References.

[1] J. Wang, W. H. de Jeu, P. Müller, M. Möller, A. Mourran, *Macromolecules* **2012**, *45*, 974.

Supporting information V: Chapter 7 Biaxial alignment of block copolymer-complex lamellae

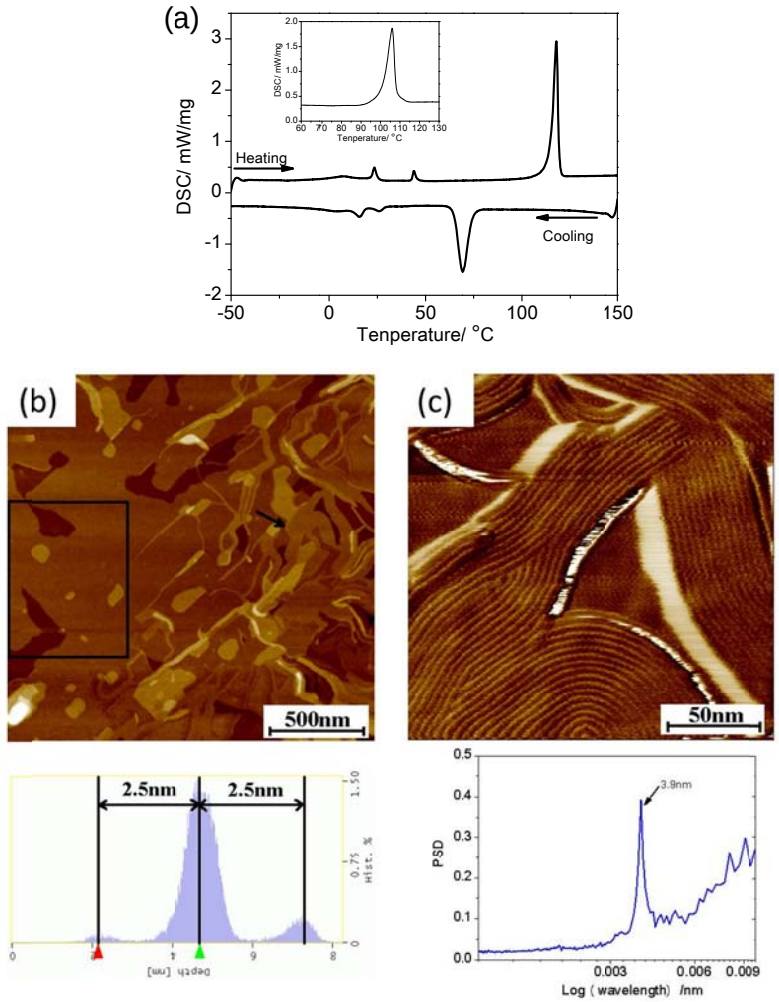

Figure S1. **(a)** Shows the thermogram of ligand **L1** indicating that the compound melts at around 114 °C and recrystallizes at around 69 °C with transition enthalpies of about 54 J/g, and 47 J/g, respectively. However, at low temperature, at least two thermal transitions are displayed, probably due to reorganization of the octyl-tails. We also noticed that if the sample is quenched from the isotropic state to room temperature and heated back, only one melting peak located at 105 °C with a transition enthalpy of 54 J/g occurred (see insert Figure S1a). SFM investigation of a thin film cast on SiO_2 shows that **L1** self-assembles in two distinct coexisting

morphologies. **(b)** Shows a layer-like structure with a depth of about 2.5 nm, as indicated by the black rectangle and the corresponding height distribution. **(c)** is an enlarged area indicated by the arrow in **(b)**, the image shows a strip-like structure with an in-plane periodicity of about 3.9 nm. Apparently, the ligand crystallizes in two polymorphs, which may coexist depending on the thermal history of the sample. The simplest model to explain the structure of the two polymorphs would be in one case formation of a dimer forming stacks parallel to the substrate plane. Tilting of the long axis of the molecule relative to the plane of the layers is required as the length of **L1**, in the extended conformation (ca. 1.7 nm), is greater than the layer thickness, while stripes result from formation of a columnar phase (possible formation of multiple H-bonds) in which the in-plane periodicity corresponds to the diameter of the column laying parallel to the substrate plane.[1] Note that it was not possible to prepare films of the ligand on PTFE rubbed SiO_2 since the material spontaneously dewets on the substrate.

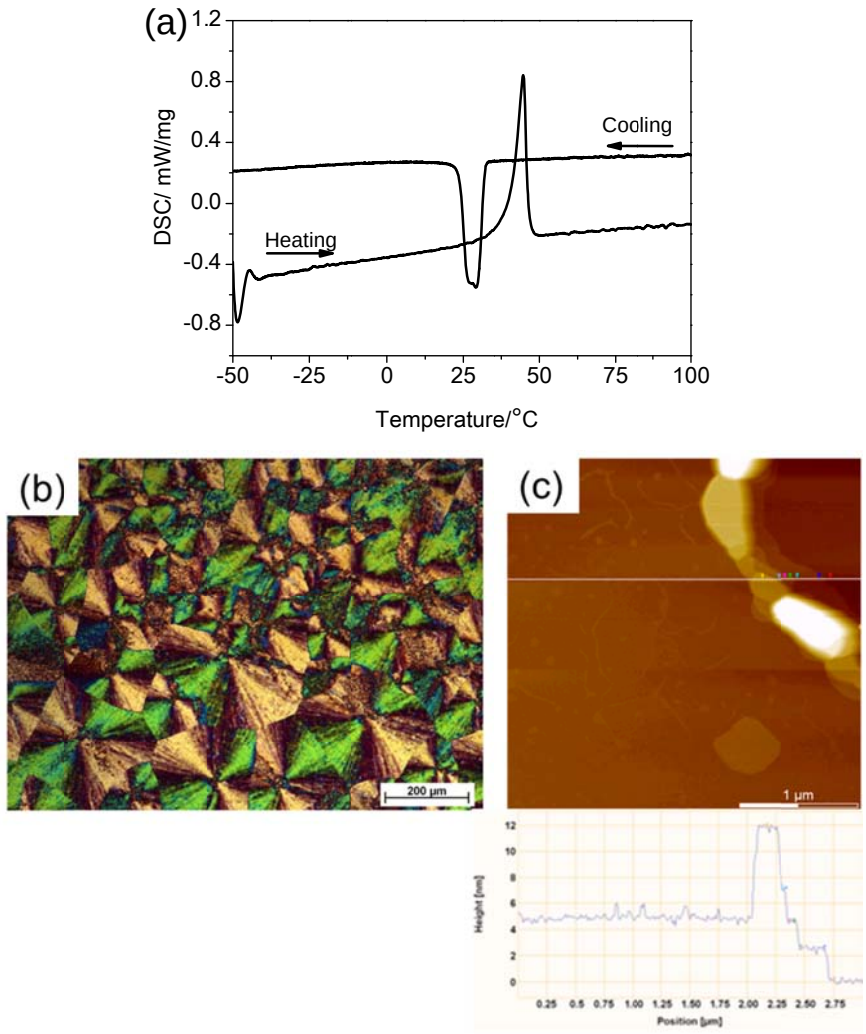

Figure S2. (a) Shows a typical thermogram of ligand **L2** indicating a single melting peak at around 45 °C and recrystallizes at around 29 °C with transition enthalpies of about 31.2 J/g, and 30.8 J/g, respectively. **(b)** Optical micrograph of **L2** recorded at room temperature under cross-polarized light, the image shows a spherulitic texture commonly observed for crystalline compounds. (**c**) SFM height image of a thin film of **L2** on a silicon oxide support, **L2** forms a layered structure with an average step height of about 2.4 nm.

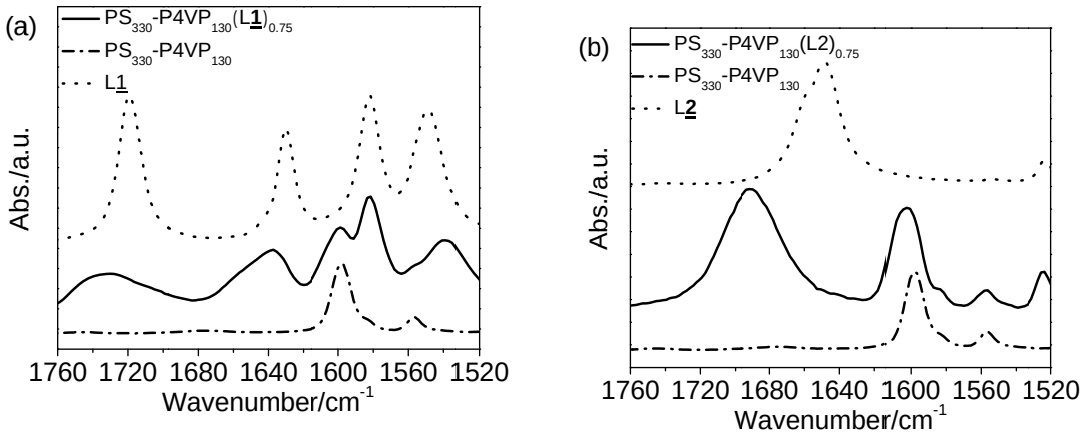

Figure S3. FTIR of (a) PS_{330}-$P4VP_{130}$(**L1**)$_{0.75}$ and (b) PS_{330}-$P4VP_{130}$(**L2**)$_{0.75}$ in the wavenumber region of 1520-1760 cm^{-1}. On both spectra the absorption band of carboxylic groups (C=O) of the pure ligand shifts to higher wavenumber region (from 1720 cm^{-1} to 1730 cm^{-1} for **L1**, and from 1650 cm^{-1} to 1690 cm^{-1} for **L2**) and becomes broader, while the absorption band associated to the free pyridine ring (C=N, 1597 cm^{-1}) shifts to ca. 1602 cm^{-1}, indicating the formation of hydrogen bonds between the carboxylic groups and the nitrogen atoms of the pyridine units.[2] There is no hint for the presence of free ligand in the complex within the accuracy of IR spectroscopy although it cannot be excluded as the absorption band of the carboxylic groups is quite broad. For a similar system, it has been reported that saturation is achieved for a degree of complexation of about 0.7-0.75.[3, 4]

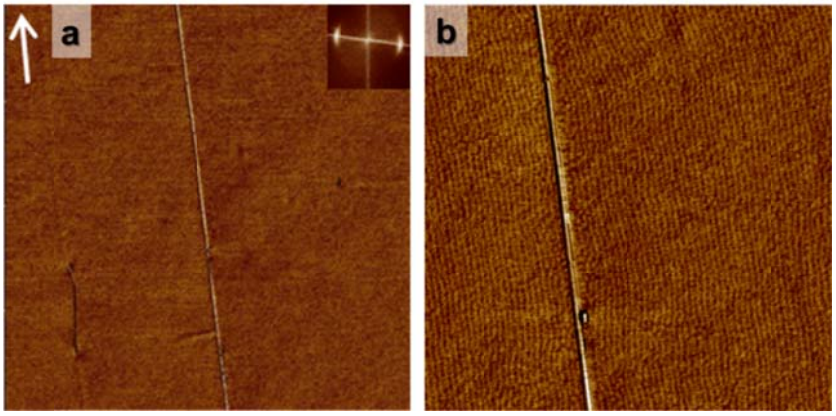

Figure S4. SFM phase images of a thin film deposited on rubbed PTFE stripes after annealing in benzene vapor for 24h: (a) PS_{190}-$P4VP_{100}$ (**L1**)$_{0.75}$ on PTFE (scan size 6 μm^2 in 4096×4096 lines), insert of (a) shows the 2D FFT. (b) Enlarged view of (a)

(scan size 2×2 μm^2 in 512×512 lines). The film thickness is 80 nm and the lamellar period is 26 nm. The arrow indicates the rubbing direction.

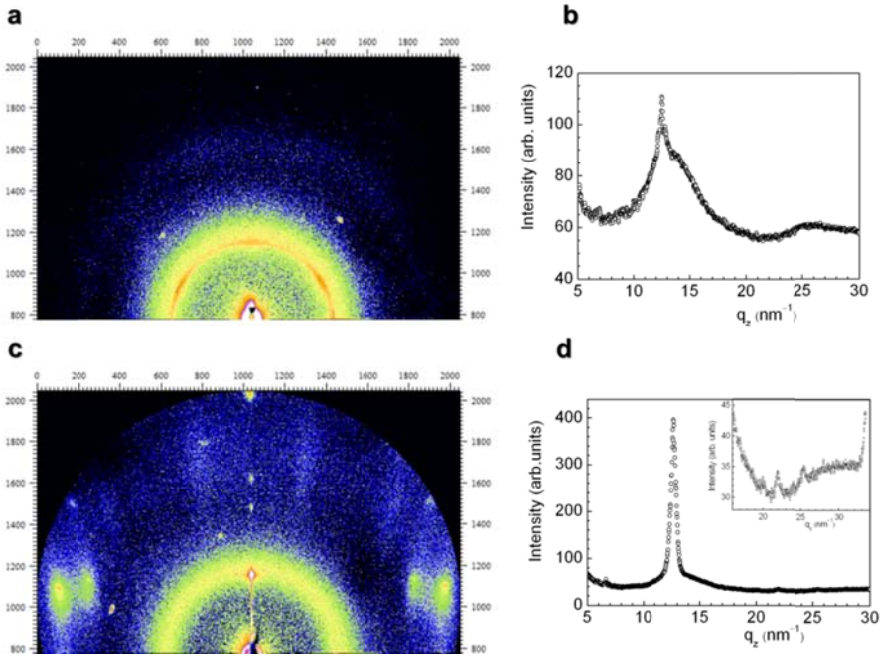

Figure S5. Left: GIWAXS of PS_{330}-$P4VP_{130}$(**L2**)$_{0.75}$ with at the right corresponding slice-integrated results over 80-100^o. Oriented samples with the x-ray beam parallel (a, b) and perpendicular (c, d) to the preferred PTFE direction, respectively. The broad band is due to the ligands, similar as in the non-oriented sample. The additional peaks are attributed to the underlying PTFE structure, as highlighted by the hexagonal structure in (a) and in the insert in (d). In (b) the positions of the center of the broad peak and the narrow one from the PTFE structure are 13.6 and 12.8 nm^{-1}, respectively.

References.

[1] D. V. Anokhin, J. Lejnieks, A. Mourran, X. Zhu, H. Keul, M. Möller, O. Konovalov, N. Erina, D. A. Ivanov, *ChemPhysChem* **2012**, *13*, 1470.

[2] J. Y. Lee, P. C. Painter, M. M. Coleman, *Macromolecules* **1988**, *21*, 954.

[3] W.-T. Chuang, H.-S. Sheu, U. S. Jeng, H.-H. Wu, P.-D. Hong, **J**.-J. Lee, *Chem. Mater* **2009**, *21*, 975.

[4] J. T. Korhonen, T. Verho, P. Rannou, O. Ikkala, *Macromolecules* **2010**, *43*, 1507.

Support informations IV: Chapter 8 Blue Light Emitted Thin Films from Supramolecular Assembly of Oligothiophene/Poly (2-vinylpyridine-b-ethylene oxide) Complex

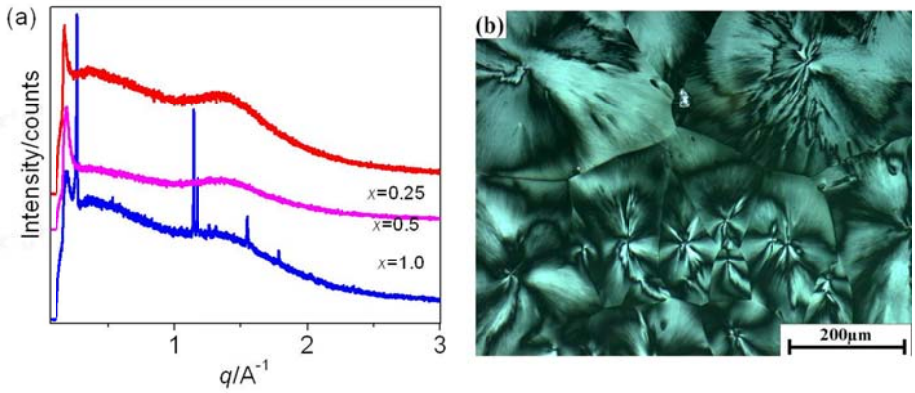

Figure S1. (a) The WAXS patterns of P2VP(R_v-2T-COOH)$_x$ and (b) POM picture of P2VP(R_v-2T-COOH)$_{1.0}$-PEO at room temperature

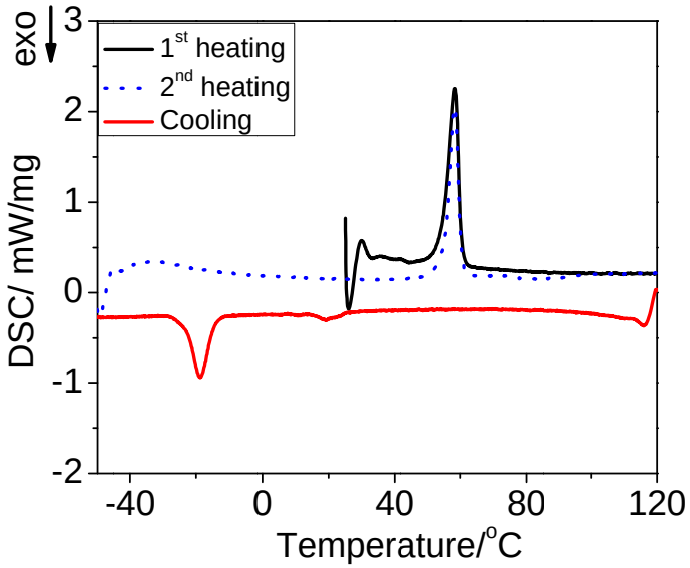

Figure S2. The DSC curves of P2VP(R_v-2T-COOH)$_{0.50}$-PEO at a rate of 10°C/min

Support Informations VI: Chapter 9 Morphological Investigation of Unique Onion-type Smectic Polymersome from Supramolecular Approach

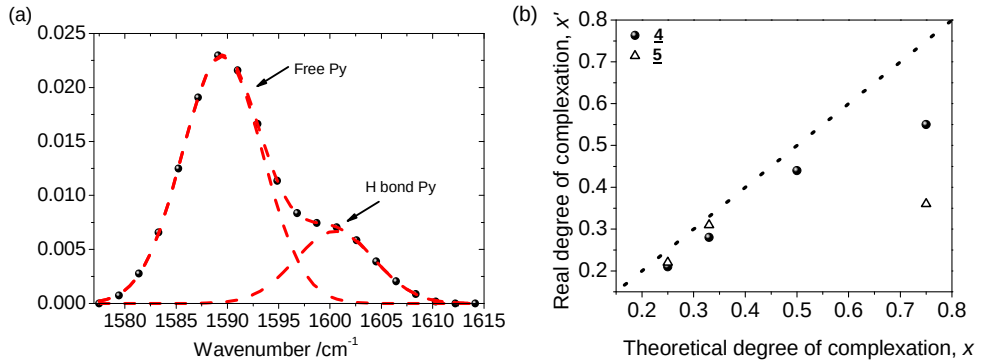

Figure S1. (a) Peak decomvolution of FTIR spectra of $P2VP_{180}(\underline{\mathbf{4}})_{0.25}$-$PEO_{560}$ in the region of 1570-1610cm^{-1}, and (b) theoretical degree of complexation (x) *vs.* the real degree of complexation (x'), the circles are the experimental data and the red dash lines are the fitting.

The overlapped peaks can be separated by peak decomvolution. The areas of the two peaks under 1589 and 1601cm^{-1} are obtained by fitting the experimental data with Gaussian function. Insert of the Figure S1a shows the result of x=0.25 as an example, as can be seen, the fit fits the experimental data very well. The real degree of complexation (x') can be estimated using Eq. S1:

$$x' = \frac{A_{1601}}{A_{1601} + \frac{\alpha_{1589}}{\alpha_{1601}} A_{1589}} \qquad \text{(S1)}$$

where A and α are the peak areas and absorption coefficients at respective wavenumber. It is found that the hydrogen bonding formed between the carboxylic group and pyridine rings of P2VP does not change the absorption coefficient significantly, therefore $\alpha_{1589}/\alpha_{1601}$ almost equals to 1. The saturated degrees of complexation are 0.5-0.75, and 0.3-0.4 for ligands **4** and **5**, respectively.

Lebenslauf

Persönliche Daten

Name	Wang
Vorname	Jingbo
Geburtstag	29.6.1982
Geburtsort	Taicang, Jiangsu
Staatsangehörigkeit	China

Qualifikationen

07/2001 Shaxi Middle School, Taicang, Jiangsu;

09/2001 – 07/2005 Nanjing University of Technology, Bachelor of Engineering;

09/2005 – 07/2008 Nanjing University of Technology, Master of Engineering: Master thesis with associate Prof. Dr. Qiang Dou in College of Materials Science and Engineering, Nanjing University of Technology, title: "Nucleation and Clarification of Polypropylene: Preparation, Structure and Performance";

09/2008 – 10/2011 PhD student in Makromolekulare Chemie with Prof. Dr. M. Möller am DWI an der RWTH Aachen e.V., topic "Hierarchical Ordering: Self-Assembly of Block Copolymers in Active Liquid Crystalline Matrices";

11/2011- to date, R&D Department, Borealis Polyolefin GmbH;

Publikationen

Papers:

1. Lejnieks Janis, Zhu Xiaomin, **Wang Jingbo**, et al. Self-assembly of a low-symmetry monodendron containing two asymmetrically linked molecular wedges. Chemphyschem, 2010, 11, 3638-3644.
2. Defaux Matthieu, Gholamrezaie Fatemeh, **Wang Jingbo**, et al. Solution-Processable Septithiophene Monolayer Transistor. Adv Mater, 2012, 24, 973-978.

3. **Wang Jingbo**, de Jeu Wim H., Müller Paul, et al. Thin film structure of block copolymer–Surfactant complexes: strongly ionic bonding polymer systems. Macromolecules, 2012, 45, 974-985.
4. Agina Elena V., Usov Ivan A., Borshchev Oleg V., **Wang Jingbo**, et al. Formation of Self-Assembled Organosilicon-Functionalized Quinquethiophene Monolayers by Fast Processing Techniques. Langmuir, 2012, 48, 16186-16195.
5. **Wang Jingbo**, de Jeu Wim H., Speiser M., et al. Biaxial alignment of block copolymer-complex lamellae. Soft Matter, accepted. **DOI:** 10.1039/C2SM27209A.

Conference Contributions

Wang Jingbo, Dou Qizheng, et al. Block copolymer complex as true liquid crystal template. 239th ACS National Meeting & Exposition, 2010, San Francisco.